The metallicity dependence of maser emission and mass loss from red supergiants and asymptotic giant branch stars

Steve Goldman
B.S. Physics St. Lawrence University

Thesis for Doctor of Philosophy

Department of Physics, University of Keele.

December 2017

Abstract

Asymptotic Giant Branch (AGB) stars and red supergiants (RSGs) are some of the largest contributors of dust and material back to the Universe. While a substantial amount of RSG dust will be destroyed by the subsequent supernova, the dust from AGB stars will be injected into the Interstellar Medium. Understanding the contribution of these stars and how it is affected by changes in stellar parameters is critically important to determining stellar lifetimes, constraining stellar models, and understanding the evolutionary paths of core-collapse progenitors and their subsequent supernova.

This study has discovered four new circumstellar masers in the Large Magellanic Cloud (LMC), and increased the number of reliable wind speeds found outside of our galaxy from 5 to 13. Results have been used to develop a relation for the wind speed as a function of luminosity and metallicity. A further analysis of the spectral energy distributions of these and Galactic OH/IR stars has led to the development of a robust empirical mass-loss prescription that uses luminosity, pulsation period and gas-to-dust ratio, a measure of metallicity. These results suggest that mass loss in this phase is (nearly) independent of metallicity between a half and twice solar metallicity.

A radio survey of evolved stars in the Small Magellanic Cloud (SMC) has found that none of the most luminous sources expected to show OH maser emission, do so. While sources may lie just below both the detection threshold and/or the required OH column density, a number of sources should still exhibit OH maser emission. It is possible that the OH masing phase of lower metallicity massive AGB stars and RSGs is cut short.

New observations in the radio, optical and infra-red have been used to constrain the location and mass-loss rate of the prominent dust producing LMC RSGs, IRAS 05280−6910 and IRAS 05346−6949. These results suggest that these sources may exhibit a dusty torus geometry, but confirmation will require further high angular resolution studies. The results of this work have made progress in understanding the wind driving and mass loss mechanism, and have set the stage for much larger upcoming surveys with the SKA and its pathfinders ASKAP and MeerKAT.

Dedication

To Susan Foster, an inspiration for curiosity

Acknowledgements

I would like to thank Jacco van Loon for all of his help in every part of this thesis. He has been an excellent teacher, collaborator, mentor, and friend, and his patience, dedication, and encouragement have far surpassed his duties as a supervisor. I would like to thank all of my collaborators for their meaningful contributions to the success of this work. And, I would also like to acknowledge the examiners of this thesis, Raphael Hirschi and Anita Richards, who have truly taken it to a higher level.

I would also like to thank Phillip Edwards for his faith in this research and to the staff at ATNF for helping with observations and being excellent hosts. I also owe a debt of gratitude to Hiroshi Imai, Iain McDonald, and Pierre Lasaffre for being excellent hosts and giving me the opportunity to share this work with the world.

In addition to the people that have directly contributed to the success of this thesis are the people who have made the last four years worth while. To my friends scattered across the globe from the department, around campus, and from conferences, thanks.

I would never have started this work if it wasn't for a curiosity, and I credit Susan Foster, a passionate and enthusiastic educator, for that gift. I also would never have had the confidence to pursue a career in astronomy if it wasn't for Aileen O'Donoghue and her years of encouragement.

Lastly, I would be nothing without the support of my family and friends back home who have kept me sane, motivated and laughing. Every postcard and package meant the world to me.

To all of the people who have made this work possible, cheers.

Publications

- McDonald I., Zijlstra A. A., Lagadec E., Sloan G. C., Boyer M. L., Matsuura M., Smith R. J., Smith C. L., Yates J. A., van Loon J. Th., Jones O. C., Ramstedt S., Avison A., Justtanont K., Olofsson H., Blommaert J. A. D. L., **Goldman S. R.**, Groenewegen M. A. T., 2015, MNRAS, 453, 4324 "*ALMA reveals sunburn: CO dissociation around AGB stars in the globular cluster 47 Tucanae*"

- Groenewegen M. A. T., Vlemmings W. H. T., Marigo P., Sloan G. C., Decin L., Feast M. W., **Goldman S. R.**, Justtanont K., Kerschbaum F., Matsuura M., McDonald I., Olofsson H., Sahai R., van Loon J. Th., Wood P. R., Zijlstra A. A., Bernard-Salas J., Boyer M. L., Guzman-Ramirez L., Jones O. C., Lagadec E., Meixner M., Rawlings M. G., Srinivasan S., 2016, A&A, 596, A50 "*The ALMA detection of CO rotational line emission in AGB stars in the Large Magellanic Cloud*"

- **Goldman S. R.** van Loon J. Th., Zijlstra A. A., Green J. A., Wood P. R., Nanni A., Imai H., Whitelock P. A., Matsuura M., Groenewegen M. A. T., Gómez J. F., 2017, MNRAS, 465, 403 "*The wind speeds, dust content, and mass-loss rates of evolved AGB and RSG stars at varying metallicity*"

- Orosz G., Imai H., Dodson R., Rioja M. J., Frey S., Burns R. A., Etoka S., Nakagawa A., Nakanishi H., Asaki Y., **Goldman S. R.**, Tafoya D., 2017, AJ, 153, 1190 "*Astrometry of OH/IR stars using 1612 MHz hydroxyl masers. I. Annual parallaxes of WX Psc and OH138.0+7.2*"

- **Goldman S. R.**, van Loon J. Th., Goméz J. F., Green J. A., Zijlstra A. A., Nanni A., Imai H., Whitelock P. A., Groenewegen M. A. T. and Oliveira J. M. 2017, arXiv:1710.02184 "*A dearth of OH/IR stars in the Small Magellanic Cloud*"

Contents

Abstract . . . iii
Dedication . . . iv
Acknowledgements . . . v
Publications . . . vi
1 Introduction . . . **1**
1.1 The Evolution and Fate of a Star . . . 1
1.1.1 Low and intermediate mass stars . . . 1
1.1.2 High mass stars . . . 4
1.2 Stellar pulsations . . . 6
1.3 Stellar dust . . . 7
1.3.1 Carbon-to-Oxygen ratio . . . 9
1.3.2 Silicates . . . 12
1.4 Wind-driving mechanism . . . 14
1.4.1 Dust-driven wind theory . . . 14
1.4.2 Alternative wind-driving forces . . . 15
1.5 Masers . . . 17
1.5.1 OH Masers . . . 18
1.5.2 Pumping mechanisms . . . 18
1.5.3 Circumstellar masers . . . 19
1.5.4 SiO and H_2O masers . . . 20
1.6 CO line emission . . . 22
1.7 Metallicity and luminosity . . . 23
1.7.1 Metallicity distributions . . . 24
1.7.2 Star formation history of the Magellanic Clouds . . . 26
1.7.3 Dust within the Magellanic Clouds . . . 28
1.8 Mass-loss . . . 31
1.8.1 Mass-loss regimes . . . 31
1.8.2 Mass-loss example: IRAS 04498−6842 . . . 36
1.9 Research aims . . . 38
2 Methodology . . . **41**
2.1 Single dish radio techniques . . . 43
2.1.1 The Parkes radio telescope . . . 43
2.2 Interferometric radio techniques . . . 47
2.2.1 Interferometry . . . 47
2.2.2 The Australia Telescope Compact Array . . . 48
2.2.3 Observational techniques . . . 50
2.2.4 Data reduction . . . 51

2.3 Mid-infrared spectroscopic techniques . . . 54
2.3.1 Very Large Telescope . . . 55
3 LMC Maser results . . . 59
3.1 LMC maser sample . . . 59
3.1.1 Parkes observations . . . 60
3.1.2 The Australia Telescope Compact Array observations . . . 61
3.1.3 Parkes and ATCA combined H I Maps . . . 65
3.2 LMC maser results . . . 65
3.3 Individual maser sources . . . 69
3.4 Stellar velocities from optical spectra . . . 84
4 Determining the gas-to-dust ratio . . . 89
4.1 The DUSTY code . . . 89
4.2 LMC sample . . . 89
4.3 Galactic samples . . . 92
4.3.1 Gas-to-dust ratios in the LMC . . . 101
4.4 The Geometry of WOH G64 . . . 106
4.5 The Geometry of IRAS 05280−6910 . . . 106
5 Wind speeds and mass-loss rates . . . 110
5.1 Circumstellar wind speed . . . 110
5.2 VVV pulsation periods . . . 113
5.3 A new mass-loss prescription . . . 116
5.3.1 Interpretation of the Goldman et al (2017) mass-loss prescription 122
5.4 Comparison to previous prescriptions . . . 126
5.5 Fundamental stellar parameters and mass-loss . . . 129
5.6 LMC Conclusions . . . 133
6 Extending to lower metallicity environments . . . 134
6.1 The SMC . . . 134
6.1.1 Previous searches for oxygen-rich dusty stars in the SMC . . . 134
6.2 Description of the Sample . . . 137
6.2.1 Observations . . . 137
6.2.2 Data reduction . . . 140
6.3 Results . . . 141
6.4 Discussion . . . 146
6.4.1 A dearth of OH masers in the SMC . . . 146
6.4.2 OH/IR populations in the Magellanic Clouds . . . 151
6.4.3 Isolating the OH/IR sample . . . 152
6.4.4 Maser strength . . . 156
6.4.5 Mass-Loss and evolutionary phase . . . 162
6.4.6 Future prospects . . . 169
6.5 Conclusions . . . 170

7 Unveiling the dustiest RSGs in the LMC . . . 172
7.1 IRAS 05280−6910 and WOH G347 . . . 172
7.2 VISIR observations . . . 175
7.3 Results . . . 176
7.3.1 The SEDs of IRAS 05280−6910 and WOH G347 . . . 176
7.4 Source location . . . 179
7.5 IRAS 05346–6949 . . . 182
7.6 The IR colours of the most luminous LMC RSGs . . . 187
7.7 Conclusions . . . 187
8 Conclusions . . . 189
8.1 Discussion . . . 189
8.1.1 How is circumstellar expansion velocity affected by other stellar parameters? . . . 189
8.1.2 How is mass loss affected by other stellar parameters? . . . 190
8.1.3 How does metallicity affect maser emission and the circumstellar environment? . . . 191
8.1.4 An explanation for multiple populations in globular clusters . . . 192
8.1.5 Constraining the final stages of stellar evolution . . . 192
8.1.6 Open questions . . . 193
8.2 The next generation of instruments . . . 193
8.2.1 The Australian Square Kilometre Array Pathfinder . . . 193
8.2.2 MeerKAT . . . 194
8.2.3 The Square Kilometre Array . . . 195
8.2.4 The James Webb Space Telescope . . . 195
8.3 Future work . . . 196
8.3.1 Obtaining metallicities for LMC OH/IR stars . . . 196
8.3.2 Measuring silicate dust in the Galactic bulge . . . 197
8.3.3 Resolving stellar populations in M31 with Hubble . . . 197
8.4 SED fitting with a goodness of fit . . . 198
8.5 Final remarks . . . 198
Appendix . . . 200
A Important mechanisms . . . 200
B Galactic OH maser sources . . . 201
C Mainline OH spectra . . . 205
D Past SMC maser targets . . . 214
E YSO OH maser spectra . . . 216
Bibliography . . . 231

List of Figures

1.1 HR diagram 2
1.2 RSG structure just before core-collapse 5
1.3 A K-band lightcurve from an evolved AGB star 6
1.4 Mass loss of stellar objects 8
1.5 The circumstellar environment and chemistry 10
1.6 An optical spectrum of an oxygen-rich evolved star 11
1.7 The 10 μm silicate feature 13
1.8 OH ground state maser transitions from Cimerman & Scoville (1980). . 19
1.9 OH maser detection of IRAS 05298−6957 20
1.10 The Milky Way Galaxy 25
1.11 The Magellanic Clouds 26
1.12 LMC photometric metallicity map 27
1.13 The luminosity distributions of OH/IR samples. 29
1.14 Mass loss versus pulsation period for dust-drive wind 33
2.1 The sensitivity of an N-band spectroscopic observation of a standard star 41
2.2 The 16cm RFI map of the ATCA 42
2.3 The 64-metre Parkes Radio Telescope 44
2.4 The Australia Telescope Compact Array 48
2.5 One of the six Australia Telescope Compact Array dishes 49
2.6 The delay of a two element interferometer 50
2.7 The Very Large Telescope 55
2.8 The results of chopping an nodding 57
3.1 LMC observation fields 61
3.2 OH 1612-MHz maser emission from IRAS 04407−7000 70
3.3 OH 1612-MHz maser emission from IRAS 04498−6842 72
3.4 OH 1612-MHz maser emission from IRAS 04509−6922. 73
3.5 OH 1612-MHz maser emission from IRAS 04516−6902 74
3.6 The FWHM ATCA fields used to observed IRAS 04516−6902 75
3.7 OH 1612-MHz maser emission from IRAS 04545−7000. 76
3.8 OH 1612-MHz maser emission from IRAS 04553−6825. 77
3.9 OH 1612-MHz maser emission from IRAS 05003−6712. 78
3.10 OH 1612 and 1665-MHz maser emission from IRAS 05280−6910. 80
3.11 OH 1612-MHz maser emission from IRAS 05294−7104. 81
3.12 OH 1612-MHz maser emission from IRAS 05558−7000. 82
3.13 OH 1612-MHz maser emission from MSX LMC 807. 83
3.14 OH 1612-MHz maser emission from MSX LMC 811 (IRAS 05329−6708) 85
3.15 OH 1612-MHz nondetection from MSX LMC 815 86
3.16 The cross-spectrum fitting of IRAS 04407−7000 and IRAS 04516−6902 88

4.1 The LMC spectral energy distributions . . . 93
4.2 The Galactic Centre spectral energy distributions . . . 97
4.2 The Galactic bulge spectral energy distributions . . . 100
4.3 The polarised 1612- and 1665-MHz maser detections of IRAS 05280−6910 108
5.1 The observed wind speed as a function of luminosity . . . 112
5.2 The observed wind speed as a function of gas-to-dust ratios . . . 114
5.3 The observed wind speed as a function of mass-loss rate and pulsation period . . . 115
5.4 Fit pulsation periods for Galactic bulge sources . . . 116
5.5 The derived and predicted mass-loss rates as a function of luminosity . 118
5.5 The derived and predicted mass-loss rate as a function of pulsation period 119
5.5 The derived and predicted mass-loss rate as a function of gas-to-dust ratio 120
5.6 A comparison of mass-loss prescriptions . . . 121
5.7 The mass-loss rate as a function of gravity . . . 124
5.8 The mass-loss rate divided by luminosity against pulsation period . . . 125
5.9 The observed wind speed as a function of luminosity with RSGs . . . 127
5.10 The observed mass-loss rates as a function of luminosity with RSGs . . 128
6.1 SMC observation fields . . . 138
6.2 SMC OH 1612-MHz maser observations . . . 143
6.3 The SMC luminosity as a function of $J - K$ colour . . . 148
6.4 The expected maser peak flux distribution of the SMC . . . 150
6.5 The 24 μm flux density versus [3.6]−[8.0] colour for LMC sources in the fields . . . 153
6.6 The 24 μm flux density versus [3.6]−[8.0] colour for SMC sources in the fields . . . 154
6.7 Expected maser efficiency . . . 160
6.8 The SMC spectral energy distributions . . . 164
6.9 Luminosity distributions of the stellar samples . . . 167
6.10 The SMC mass-loss rate as a function of luminosity and pulsation period 168
7.1 SOFI and HST observations of NGC 1984 . . . 173
7.2 The SEDs of IRAS 05280−6910 and WOH G347 . . . 175
7.3 The VISIR and IRS N-band spectra of IRAS 05280−6910 . . . 177
7.4 The SEDs of IRAS 05280−6910 and WOH G347 . . . 178
7.5 *Hubble*, *Spitzer*, and *Herschel* mosaic of IRAS 05280−6910 and WOH G347 . . . 180
7.5 continued . . . 181
7.6 The spectral energy distribution and 1612-MHz spectrum of IRAS 05346−6949 . . . 184
7.7 1420-MHz continuum image of IRAS 05346−6949 . . . 185
7.8 The 24μm flux density versus [3.6]-[8.0] colour for the LMC RSGs . . . 186
B1 OH 1612-MHz maser emission from Galactic sources . . . 202

C1 ATCA mainline OH maser observations of IRAS 00483−7347 206
C2 ATCA mainline OH maser observations of BMB-B75 207
C3 ATCA mainline OH maser observations of MSX SMC 018 208
C4 ATCA mainline OH maser observations of IRAS 04498−6842 209
C5 ATCA mainline OH maser observations of IRAS 04509−6922 210
C6 ATCA mainline OH maser observations of IRAS 04516−6902 211
C7 ATCA mainline OH maser observations of MSX LMC 811 212
C8 ATCA mainline OH maser observations of MSX LMC 815 213
E1 Parkes 1612-MHz OH maser observations of IRAS 01039−7305 and IRAS 01042−7215 217

List of Tables

1.1 Stellar parameters of IRAS 04498−6842 37
1.2 Prescription mass-loss rates 37
3.1 Radio observations of circumstellar masers in the LMC 63
3.2 The LMC maser target sample characteristics 64
3.3 Results of recent maser searches in the LMC 67
4.1 Results of spectral energy distribution fitting for the LMC sample . . . 102
5.1 The resolution of the radio observations in the Galaxy and LMC 111
6.1 The SMC maser target sample characteristics 136
6.2 SMC observation fields 139
6.3 The upper limits, maximum maser efficiencies, and likelihood-of-detection for maser emission in the SMC sample 149
6.4 Results of spectral energy distribution fitting for the SMC sample . . . 161
7.1 The best-determined positions for the VISIR, ATCA, and HST observations 182
7.2 The pointing accuracy and angular resolution of the observations targeting the most luminous LMC RSG 182
7.3 Results of spectral energy distribution fitting for the LMC RSGs . . . 183
B1 Results of Galactic maser observations. 204
D1 Targets from the 1612-MHz OH maser survey by Wood et al. (1992). . 215

1 Introduction

1.1 The Evolution and Fate of a Star

All low-to-intermediate-mass stars (0.8 $M_\odot \lesssim M_{\rm initial} \lesssim 8\ M_\odot$) will eventually become red giants and then Asmptotic Giant Branch (AGB) stars while the higher mass stars will become a RSGs. The closest star, the Sun, is no exception. In roughly five billion years, the Sun will inflate and engulf the inner planets of the solar system. The sun will then go through periods of expansion and contraction due to the activating of fusion in both hydrogen and helium, as well as a period of intense mass-loss, right before it loses its outer shell, and is left a white dwarf cinder. This is the life destined for the very common sun-sized stars. One of the more remarkable phases in this evolution, is the transformation that the star will undergo at the termination of the AGB phase. A star will lose up to 85% of its initial mass at a rate of up to 10^{-4} solar masses per year (van Loon et al., 1999). These stars, and to a lesser degree red supergiants, contribute a significant amount of dust and chemically enriched material to the interstellar medium (ISM) (Herwig, 2005). This evolutionary stage is the critical and brief moment that this study has focused on.

1.1.1 Low and intermediate mass stars

The AGB phase is the final stage of evolution for low-to-intermediate mass stars. After their formation and brief existence as pre-main sequence stars, they will follow a path on the famous Hertzsprung-Russell (hereafter HR) diagram as core hydrogen-burning main sequence stars (Fig. 1.1). As hydrogen fusion deposits helium within the core, hydrogen core fusion ceases and triggers gravitational contraction. This contraction then increases core pressure until it is counteracted by the force of electron degeneracy pressure. As pressures and temperatures rise, this allows for hydrogen shell burning around a helium core. This change is represented in the HR diagram as a move toward the Red Giant

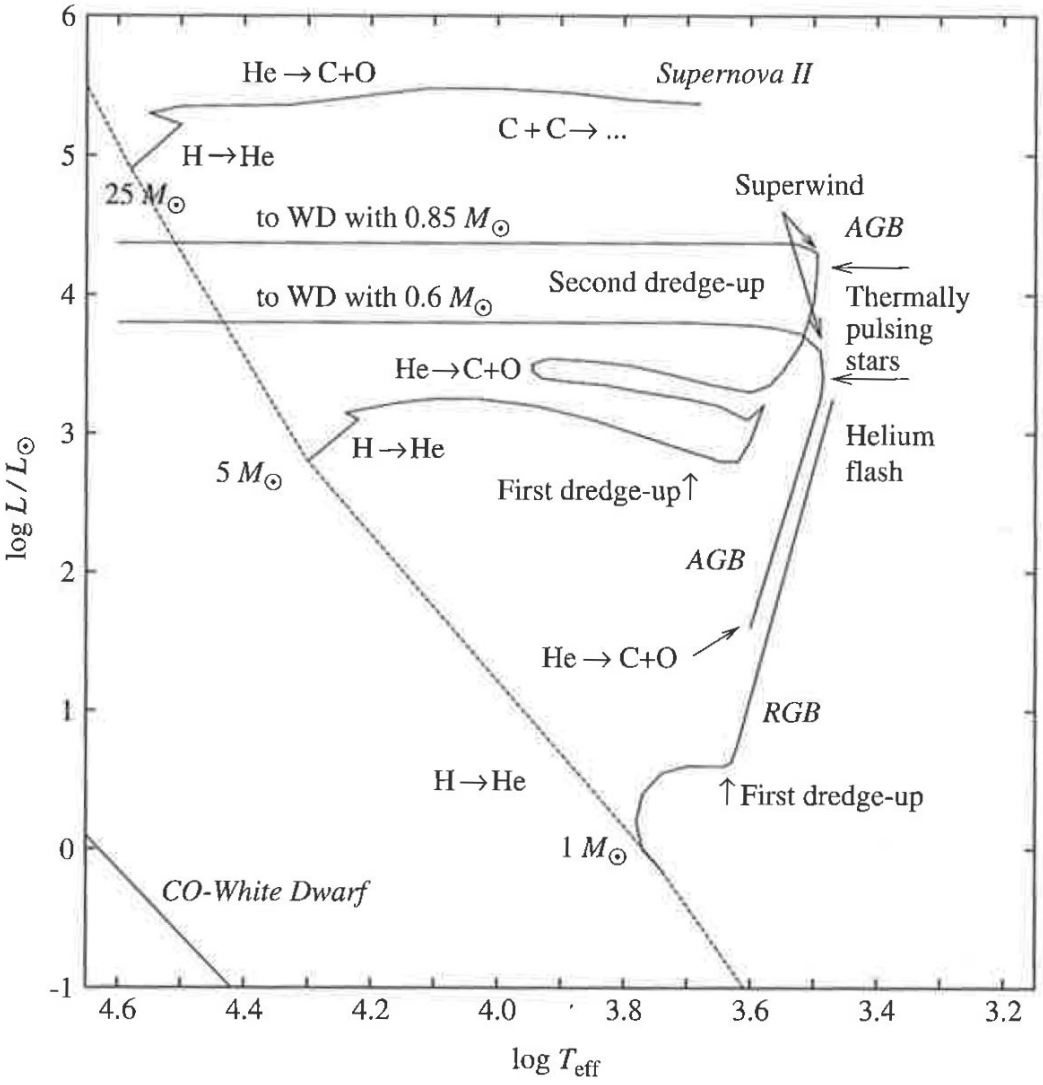

Figure 1.1: HR diagram from Gail & Sedlmayr (2014)

Branch (RGB).

As the inert helium core of the star contracts and heats, the luminosity of the source increases. As a result, the circumstellar envelope expands and cools, and becomes convective. This is described as the first ascent of the RGB within the HR diagram. As the core reaches temperatures in excess of 10^8 K, helium fusion begins producing carbon through the triple-alpha process. Within the electron-degenerate core, the outward force is dependent not on thermal pressure but quantum mechanical pressure. As temperatures

increase from helium fusion, and degeneracy keeps volume constant (as it is unaffected by increases in temperature), this increases the fusion rate and consequently the temperature. The cycle creates a runaway process which results in a sudden ignition known as the helium flash. This is only true for low mass stars, as stars between $1.8 - 8$ $M_\odot$ do not exhibit an electron-degenerate helium core or helium flash, rather initiate helium fusion in non-degenerate conditions due to higher temperatures within the core. After helium core fusion ceases, hydrogen and helium shell fusion begin, marking the beginning of the AGB phase.

The Asymptotic Giant Branch At the beginning of the AGB stage, a star will have an inert degenerate carbon-oxygen core and will undergo nuclear fusion primarily within the helium shell, producing C and O through the triple-alpha process. The helium shell is surrounded by a small helium-rich intershell region, a hydrogen shell, and then a convective outer envelope. As fusing material is depleted within the helium shell, helium shell burning ceases and the star enters the thermally pulsing AGB or TP-AGB phase.

Once the helium shell is depleted, pressure increases, and hydrogen shell fusion takes over. The helium by-product of this reaction creates a thin shell of helium over time, which grows until it ignites violently. This explosion is known as a helium shell flash. The explosion causes the star to expand and cool halting hydrogen fusion. Once the star contracts, helium shell burning reaches the edge of the hydrogen shell, and the helium flash has finished, hydrogen fusion reignites and the TP-AGB cycle starts over; this calmer phase of stable hydrogen shell burning is known as the interpulse period (Iben & Renzini, 1983). During the TP-AGB the star will lose a significant amount of mass until hydrogen in the outer envelope is depleted. The star will then transition to bluer colours, and reach temperatures high enough to ionize the circumstellar ejecta and become a planetary nebula. Following the planetary nebula phase, the remaining material is locked away in a CO white dwarf cinder.

1.1.2 High mass stars

Super-AGB Stars with initial masses 6 $M_\odot \lesssim M \lesssim 9\ M_\odot$ are thought to be massive enough to initiate carbon fusion within the core or "carbon-burning" (Jones et al., 2013). These stars undergo a similar evolution as their lower mass counterparts, yet their fate, expected to be an ONe(Mg) white dwarf or electron-capture supernova, is still unclear (Doherty et al., 2015). As carbon is fused, the star is left with a degenerate core made up of oxygen and neon rather than carbon and oxygen. These stars are known as super-AGB stars. Super-AGB stars have not been studied in the same detail as AGB or RSG stars, as they are difficult to model and it is still unclear how to identify them observationally. Nevertheless, they are an important link between the lower- and upper-mass regimes.

Red supergiants RSGs exhibit several similar stages of evolution as AGB stars but follow a different evolutionary path. RSGs start their life as hot OB stars on the main sequence. They fuse hydrogen within the core until there is no material left for fusion. The star will then expand and cool, and move horizontally on the HR diagram to cooler temperatures, with a roughly constant luminosity. The star will then begin to fuse elements like helium and carbon similar to higher-mass AGB stars. Unlike AGB stars however, massive stars will continue to fuse heavier elements in concentric shells from oxygen up to silicon (Fig. 1.2). A limit is reached when iron ash is deposited within the core reaches above the Chandrasekhar mass and the core can no longer support itself by electron degeneracy pressure and releases a shockwave. This process is known as a Type II or core-collapse supernova, which then leaves a neutron star or black hole depending on the mass. These stars are thought to be the progenitors of the most common supernova, the Type II-P supernova (Smartt, 2009). There is a substantial amount of evidence to suggest RSGs as the progenitors with numerical hydrodynamical models (Chevalier, 1976) and analytic solutions (Arnett, 1980) requiring large initial radii, as well as progenitor data on several well studied SNe (e.g. SN2003gd, SN2005cs, SN2008bk; Smartt, 2009). In addition to Type II-P SNe, mass loss can deplete the star's mantle moving it toward bluer colours where it may explode as a Type IIb or possibly Type Ib supernova, yet no

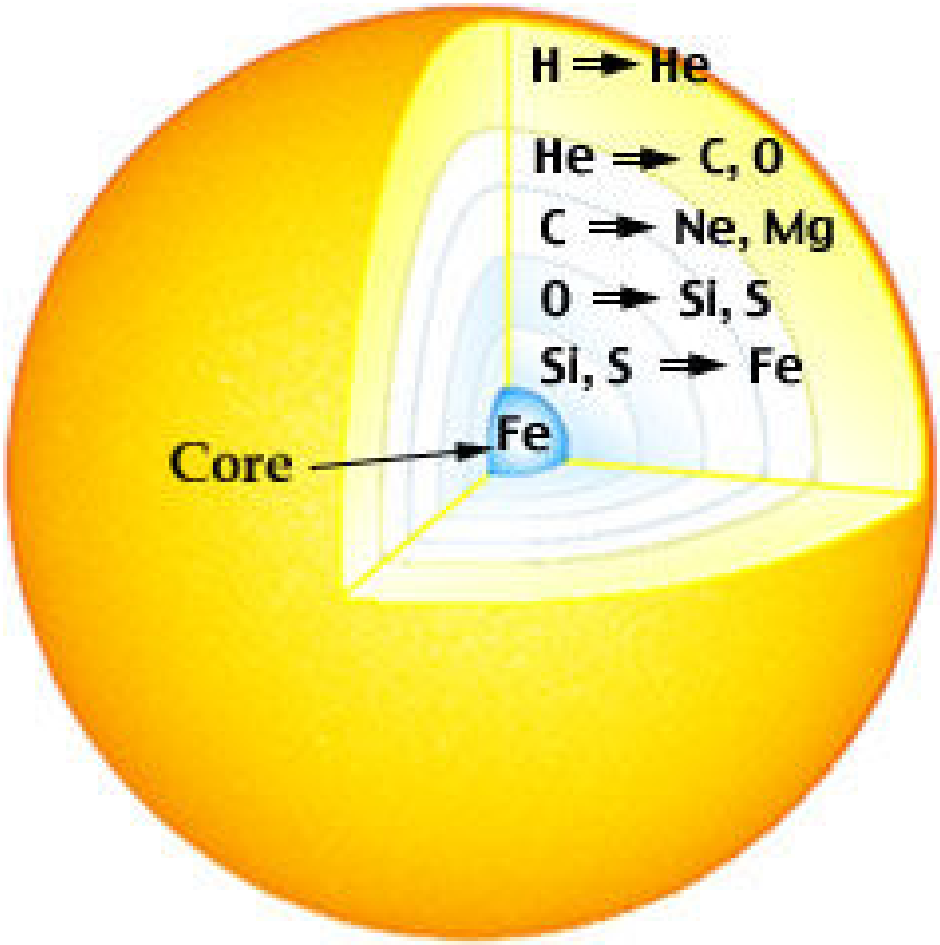

Figure 1.2: RSG structure just before core-collapse. Credit: NASA Observatorium Aeronautics

observations of the progenitors of these supernova exist.

Stars are the crucibles responsible for creating the majority of elements in the Universe heavier than helium. Consequently, understanding the contribution of stars in these specific phases of their evolution, constrains the composition and origin of the material that makes up the Universe.

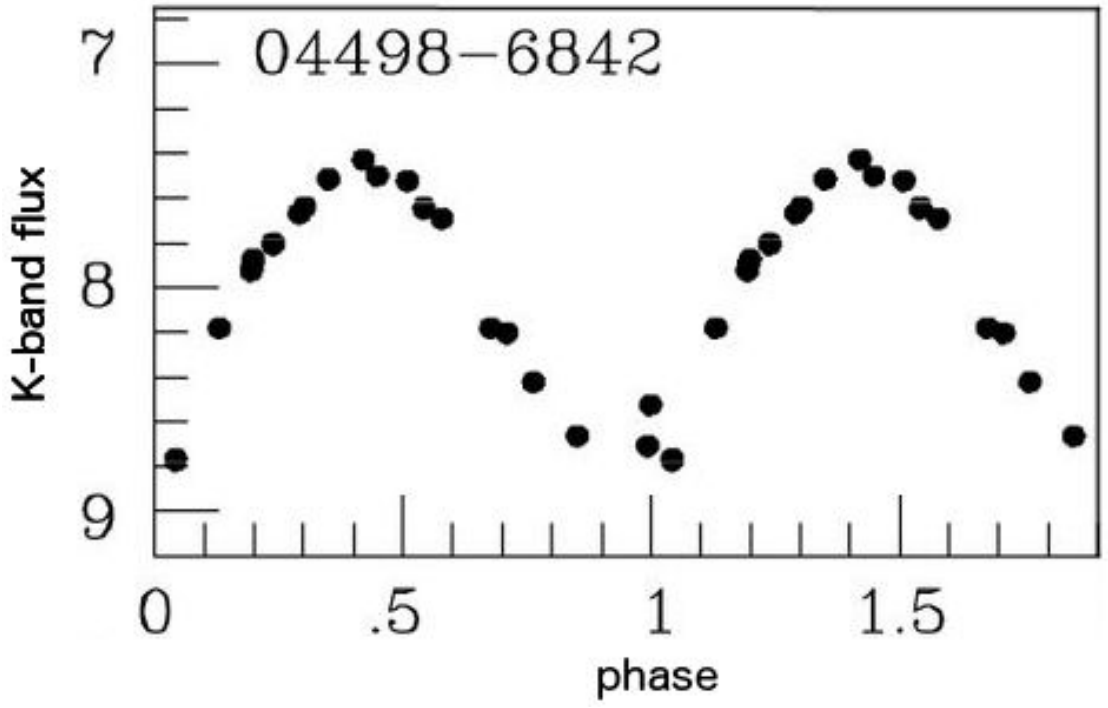

Figure 1.3: A K-band lightcurve from the evolved AGB star IRAS 04498−6842 (adapted from Whitelock et al., 2003).

1.2 Stellar pulsations

Towards the end of there evolutionary phase, lower mass Mira variable AGB stars (named after the star Mira or O Ceti) and larger mass evolved AGB stars will undergo pulsations. These pulsations can last between hundreds and thousands of days, changing in brightness by up to 2.5 magnitudes in the V-band. An example of such a source is the TP-AGB star: IRAS 04498−6842, shown in Figure 1.3. These pulsations are due to the κ mechanism.

The κ mechanism is driven by changes in opacity, a stellar parameter commonly denoted using κ. In a main sequence star, as an atmosphere is compressed, temperature and density increase, which consequently leads to a decrease in the opacity. This keeps the system in a state of equilibrium, where compression does not lead to an increase in radiation pressure. In dusty evolved stars, when the atmosphere is compressed and hydrogen and helium are partially ionised, this leads to an increase in opacity. As

temperature, density, and opacity increase, this increases radiation pressure and pushes the atmosphere outward. Material expands and cools, opacity decreases, and the cycle starts again. These pulsations are thought to be critical to levitating material out to large radii, and enhancing mass loss (further discussed in 1.4). Recent work has shown that refractory species like Aluminium oxides can form close to the star with silicates forming further at a radius of ~ 5 $R_{\odot}$ (Höfner et al., 2016).

1.3 Stellar dust

Understanding dust and the recycling of material within the Universe requires first an understanding of how it is produced, transformed, and destroyed. AGB stars are recognized as one of the major producers of stellar dust in the Universe (Fig. 1.4), along with Supernovae (SNe), RSG, and Wolf-Rayet stars (Gehrz, 1989; Sloan et al., 2008). How different environments affect the chemical composition of this dust is still unclear with few high resolution mid-IR spectroscopic studies outside of the Galaxy (Cherchneff, 2013). The collective net contribution of dust from all AGB stars is expected to be larger than that of SNe (Fig. 1.4). This is considering that SNe destroy not only their own dust, but more importantly, pre-existing dust from progenitors and the ISM (Lakićević et al., 2015; Temim et al., 2015). The net contributions of SNe are still controversial as the significance of shocks and high energy particles is still unclear (Dunne et al., 2003; Dwek, 2004; Krause et al., 2004; Bianchi & Schneider, 2007; Schultheis et al., 2014; Matsuura et al., 2011; Gomez et al., 2012). The dominant destruction process of this dust is the reaction of dust with hydrogen molecules, referred to as chemisputtering (Gail & Sedlmayr, 1999). To a lesser degree, dust is destroyed through sublimation by the heating of the dust grains from the absorption of stellar radiation.

Within AGB stars, the initial process of dust formation is still unclear. The nucleation of dust grains is challenging to model (e.g. Salpeter, 1977; Nanni et al., 2013), and models typically start from seed-nuclei that become the cores of larger dust grains. Adding to this challenge, the composition of the dust grains will depend on the

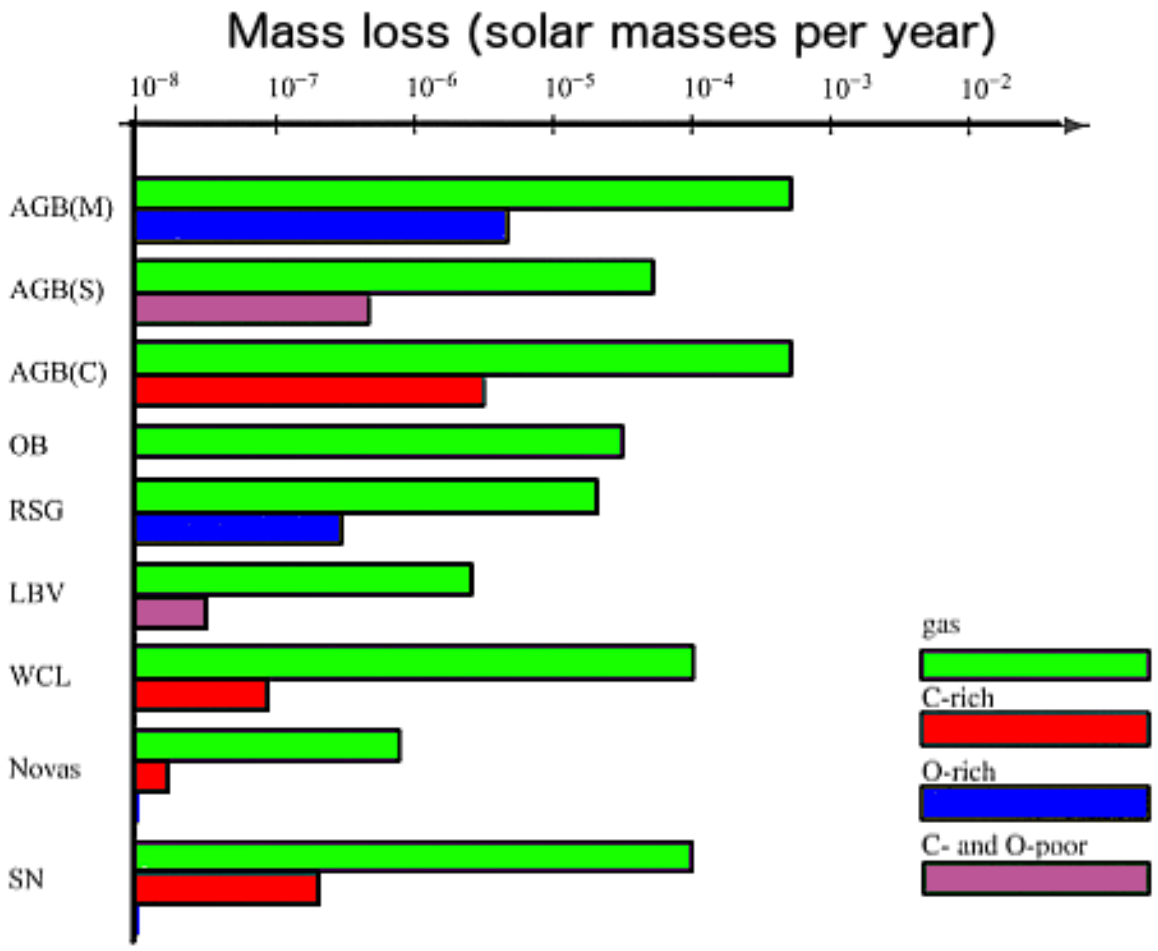

Figure 1.4: Mass loss of stellar objects (adapted from Gail & Sedlmayr, 2014).

circumstellar environment from which they form. This study focuses on oxygen-rich sources which produce silicate dust grains as opposed to carbonaceous dust grains.

1.3.1 Carbon-to-Oxygen ratio

There are two paths set for AGB stars that will depend on the ratio of carbon-to-oxygen (C/O ratio) and will impact the circumstellar chemistry (Fig. 1.5). An AGB star can be designated as an oxygen-rich (C/O < 1), carbon-rich (C/O > 1), or S-type star (C/O ~ 1). The C/O ratio will determine whether the ejected material will form circumstellar dust made up of either silicate or carbonaceous dust grains, and whether the star will exhibit maser transitions (further discussed in §1.5).

The chemical composition of an AGB star's circumstellar envelope will depend highly on initial mass. It is known that the helium shell flash and halting of hydrogen burning within the TP-AGB leads to strong convection in the region between the hydrogen and helium shells. This allows carbon as well as s-process elements to be brought up to the surface, consequently altering the star's surface composition. This is known as a Third-Dredge Up (TDU) event, and the process transforms the outer layers of an AGB star from oxygen-rich to carbon-rich[1].

A competing phenomenon that decreases the surface abundance of carbon is known as Hot-Bottom Burning (HBB). Stars with initial masses $\gtrsim 3$ M$_\odot$ will undergo HBB after a TDU event within the much longer interpulse period. In these stars, the base of the convective envelope will reach temperatures high enough for hydrogen burning reactions to aid in transforming carbon into nitrogen through the CNO cycle (Boothroyd, Sackmann & Ahern, 1993). HBB stars can have luminosities above the level governed by the core mass and break the 'classical' AGB limit which is set by the highest stable core mass. The decrease in C/O ratio from HBB confines all higher mass evolved stars to oxygen-rich stars, with lithium as one of the by-products. Lithium has been used in the past as an indicator for HBB, and a way of distinguishing HBB AGB stars and RSGs.

[1]For more details on the internal stellar processes and mechanisms discussed in this Chapter, see Appendix A.

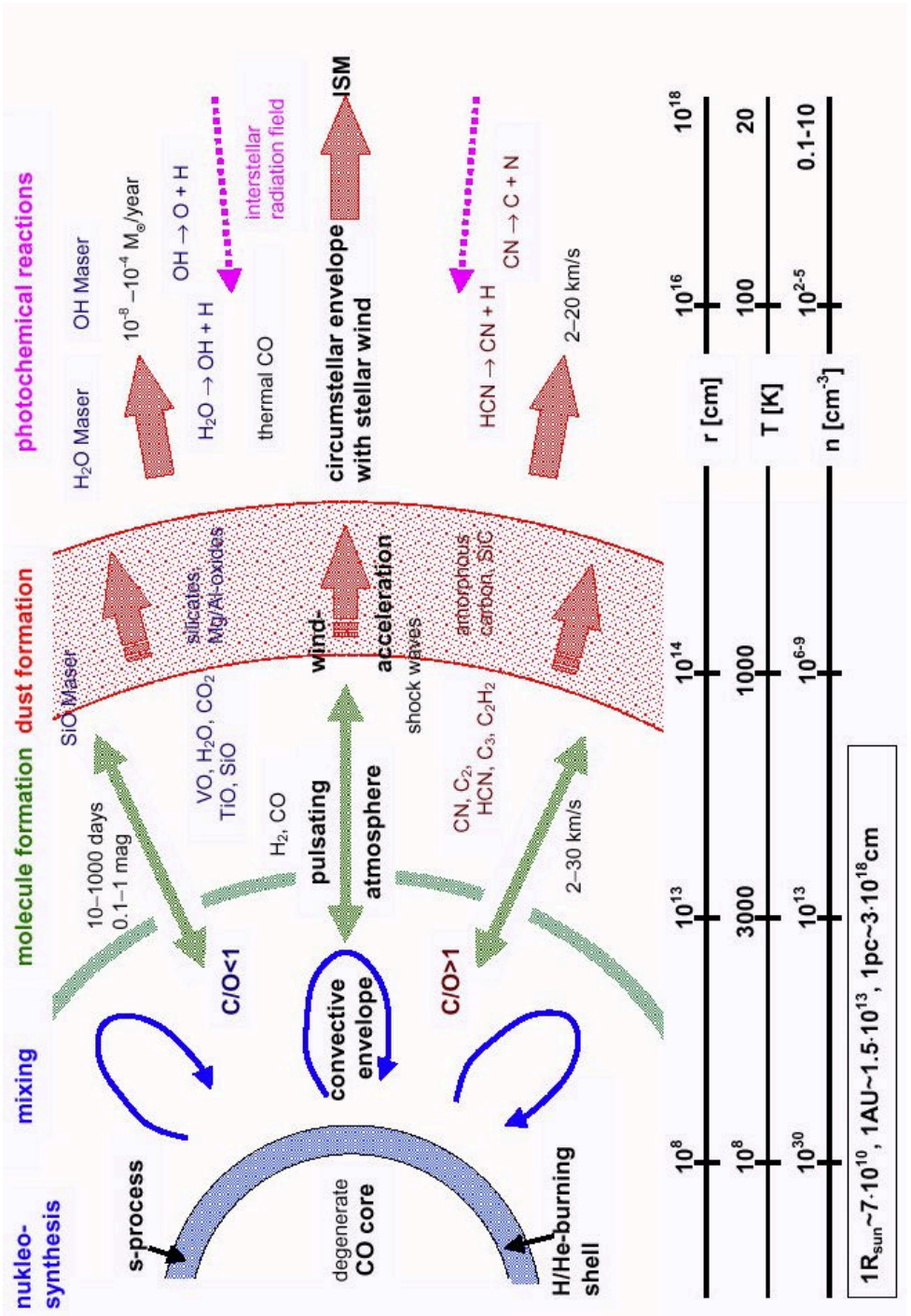

Figure 1.5: A diagram of the circumstellar environment and chemistry of AGB stars (made by Josef Hron).

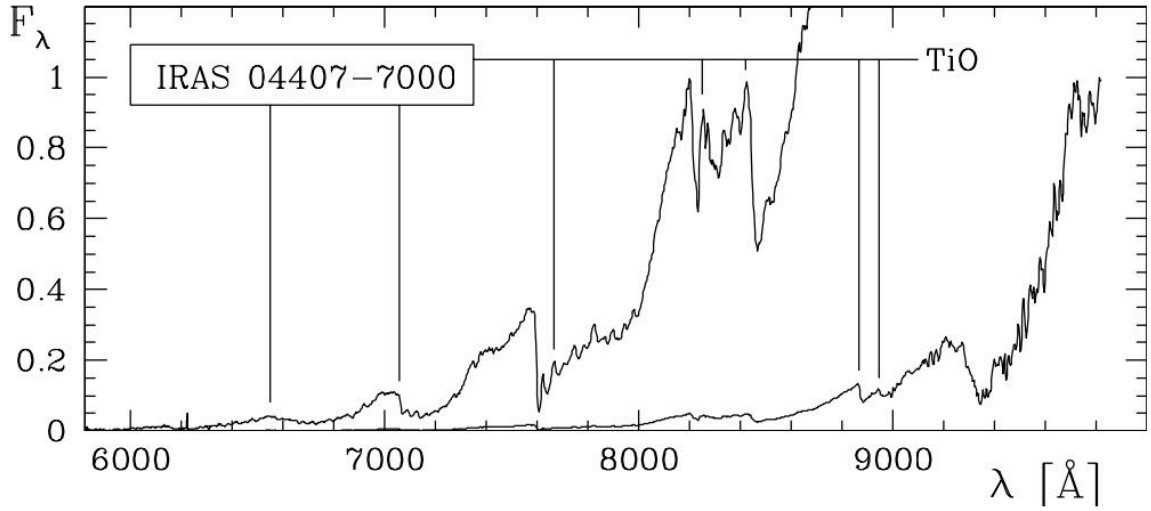

Figure 1.6: An example of an optical spectrum of a cool oxygen-rich evolved AGB star (adapted from van Loon et al., 2005). Shown are TiO features indicative of a late-M spectral type and low effective temperature. The spectrum is shown on two normalised scales to exploit the full dynamic range of the data.

This study focuses on oxygen-rich AGB stars (the more common AGB stars) covering both lower mass sources within the galaxy, and higher mass sources that have undergone HBB, within the Magellanic Clouds (Fig. 1.13; shown later). The gap in luminosity between these samples is where carbon-rich AGB stars are expected to lie, but they have been omitted from this study for reasons that will be explained in §1.5. As opposed to hotter stars, cool evolved AGB stars can create more fragile molecules within their atmospheres. Oxygen-rich evolved stars in particular are known for harbouring molecules like TiO. The optical spectra of late-M type stars is dominated by prominent TiO bands (Fig. 1.6), and observations of these bands as well as those from other molecules are used to determine stellar effective temperatures (e.g. van Loon et al., 2005).

1.3.2 Silicates

Mid-IR spectroscopy is typically used to determine the chemical composition of the dust around an evolved star as either oxygen or carbon rich. Within oxygen-rich silicate dust, the stretching vibrations of the Si-O bond in a SiO_4 tetrahedron create a prominent feature at 10 μm[2] (Fig. 1.7), which is typically used to categorise the source as oxygen-rich. Conversely, carbon stars have several features between 3 and 12 μm as a result of the bending and stretching of carbon and hydrogen bonds. The silicate dust is expected to be made up of a combination of types of pyroxene ($MgSiO_3$), olivine (Mg_2SiO_4), quartz (SiO_2), corundum (Al_2O_3), and iron (Fe). The contribution of each of these species in the dust of a typical AGB star is still unclear, but serious work is being done to resolve the issue (Decin et al., 2017; Nanni, 2013; Jones, 2013).

The inclusion of iron in circumstellar dust is still a matter of debate. Iron has been invoked to explain the discrepancy in the calculation of momentum-transfer. Dust grains without iron tend to be too transparent at 1 μm to drive stellar outflows seen in the Galaxy. Yet models have shown that iron is too unstable to form at small radii (Woitke, 2006), and iron grains at larger radii cannot drive an outflow or efficient mass-loss. As iron has no spectral features, directly confirming the contribution or existence of iron within these grains has presented an observational challenge.

Recent work has explored the possibility of grain size as a possible explanation for the wind-driving. Höfner (2008) has shown that iron-free Mg_2SiO_4 grains can grow to sizes between 0.1 and 1 μm in dynamical atmospheres. These grains can gain significant momentum by scattering stellar photons of wavelength comparable to their size (Höfner, 2015). Synthetic photometry and spectra have been computed using these models and have been found to be in good agreement with observations (Bladh et al., 2013).

[2]The bending vibrations of the O-Si-O bond also create a less defined feature at $\sim$18μm.

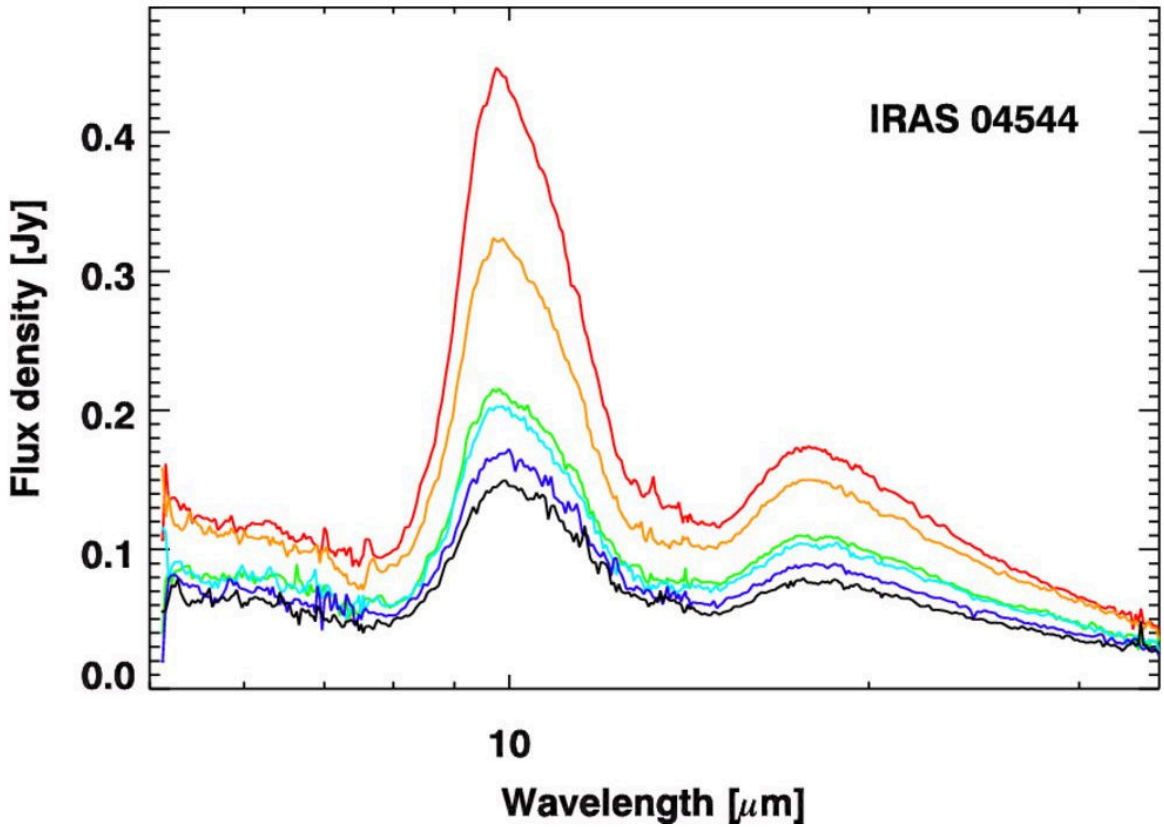

Figure 1.7: The 10 μm silicate feature of the AGB star IRAS 04544−6849 shown in emission (adapted from Jones et al., 2014). Displayed are observations taken at different times showing the variability of the silicate feature over time.

1.4 Wind-driving mechanism

1.4.1 Dust-driven wind theory

The dominant theory for the driving of circumstellar outflows in cool evolved stars is dust-driven wind theory. During stages of dense mass-loss, stars exhibit a lower effective temperature, a higher luminosity, and large pulsations. A correlation between the dust content and pulsation amplitude led to the conclusion that these pulsations are critical to driving the wind (Jura, 1986; Habing, 1987). Since this realisation, it has become generally accepted that pulsations are the dominant mechanism for levitating material from the stellar surface. As Höfner (2015) describes, it is expected that wind acceleration works like a 2-stage rocket. The first stage levitates dust-free gas out to a few stellar radii, after which the gas condenses into dust and radiation pressure forms the propulsion for the second stage. It is expected that radiation pressure on these dust grains forces the grains radially outward and, as they are forced out, drag along hydrogen gas through friction. For a simplistic view of the system, the gravitational acceleration (Eq. 1.1), and the radiative acceleration (Eq. 1.2), can be combined to calculate the ratio of outward acceleration (Γ), shown in Eq. 1.3.

$$F_{grav} = \frac{GMm}{R^2} \tag{1.1}$$

$$F_{rad} = \frac{L}{c}\frac{\kappa m}{4\pi R^2} \tag{1.2}$$

$$\Gamma = \frac{F_{rad}}{F_{grav}} = \frac{\kappa L}{4\pi GMc} \tag{1.3}$$

This shows the dependence on luminosity as the outward driving force, on opacity (κ) a measure of the dust, and on the current mass of the source. When the outflow reaches its maximum momentum transfer, the source is said to be within the “superwind”

phase (as will be discussed in §1.8). Wind speeds for these stars can vary, ranging from a few km s^{-1} to 25 km s^{-1} (Engels & Bunzel, 2015), with more luminous sources having higher wind speeds[3] (Wood et al., 1992; Marshall et al., 2004, §5.1). Stars within this evolutionary stage will have escape velocities at the stellar surface of typically between 43−48 km s^{-1} (e.g Marshall et al., 2004), but with the aid of stellar pulsations, can be overcome. It has been shown, using water maser observations, that this occurs at radii between $\sim$ 5−15 $R_{\odot}$ (Richards et al., 2012).

The idea of a superwind was originally introduced by Iben & Renzini (1983). Since then, a significant amount of work has been done in trying to understand how it is affected by other stellar parameters. It is possible that circumstellar outflows are enhanced by other forces such as magneto-acoustic or magneto-hydrodynamic waves. It has been shown that dustless stars typically lose their mass via magneto-acoustic waves within their chromosphere (Hartmann & MacGregor, 1980; Dupree, Hartmann & Avrett, 1984; McDonald & van Loon, 2007).

1.4.2 Alternative wind-driving forces

There are several forces that have shown to be effective drivers of stellar outflows. There are two main types of wind-driving processes that can be separated by their method of momentum transfer. First there are radiation-driven winds, where radiative momentum is transferred by radiation on circumstellar dust or molecules. And second, there are pressure-driven winds, like acoustic or magneto-hydrodynamic (Alfvén) waves, that accelerate material through the dissipation of mechanical energy created by the star. The following sections, based on the review by Gail & Sedlmayr (2014), will describe each of these in turn.

Radiation-driven winds Radiation pressure on molecules has shown to contribute to the radiative acceleration of a circumstellar outflow (Jørgensen & Johnson, 1992). Using

[3]The additional impact of metallicity on the expansion velocity will be discussed further in Chapter 5

a grid of photospheric models, Jørgensen & Johnson (1992) showed that this mechanism may be a viable aid to circumstellar outflows. The effect on the outflow is minor, of the order of a few percent of the gravitational force in the stellar atmosphere, yet it is unaffected by modest changes in the effective temperature and mass, which may make it more important in less evolved, warmer sources. This mechanism has however shown to be highly dependent on the metallicity and C/O ratio, producing higher acceleration for metal- and carbon-rich sources.

Pressure-driven winds Pressure waves, like sound waves, have been proposed as a possible aid to circumstellar outflows. These waves would push material out to a point where dust driven winds would accelerate the material further. However Wood (1990) has questioned the potential of these waves to survive stellar pulsation as they would likely be reflected or destroyed by stellar pulsations of the star. As Wood (1990) states, a Mira variable will have material falling inward at a speed of 10-15 km s^{-1} onto a shock front moving $\sim$ 10 km s^{-1} outward, sound waves would presumably be reflected back toward the star.

Alfvén waves Another possibility is magneto-hydrodynamic Alfvén waves. As a conducting liquid in a constant magnetic field creates an electromagnetic force, random motions of material at the stellar surface create waves that travel outward and interact with the ionised plasma within the chromosphere. This has been proposed in the past as strong candidate for aiding stellar outflows (Judge & Stencel, 1991; Schröder & Cuntz, 2005). Schröder & Cuntz (2005) have derived a mass-loss prescription, using chromospheric energy as a measure of the driving force of the wind, and that relies on Alfvén waves to transfer momentum. This prescription was calibrated using mass-loss rates of nearby less-evolved Galactic RGB stars and remains a well-used prescription for AGB stars.

These mechanisms while unlikely to be the dominant driving force behind massive AGB outflows may be important aids in wind driving. They may become particularly

important in regimes where dust-driving becomes less effective, for example, at lower metallicities, higher effective temperatures, or for less evolved stars.

1.5 Masers

Masers are excellent tools for understanding the physical conditions associated with areas of dense gas and dust. The term maser refers to 'Microwave Amplification by Stimulated Emission of Radiation.' Under certain conditions maser pumping can occur in which a higher energy level of a molecule becomes overpopulated with respect to a lower level, known as a population inversion. This can be caused by incident radiation or collisions with molecular hydrogen. An incident photon of wavelength matching the wavelength of the transition between these levels stimulates the emission of another photon as a molecule drops from the higher to the lower level. Thus one photon becomes two, then four and so on. Masing also requires sufficient velocity coherence along the direction of radiation propagation for the photon wavelengths to be similar (within the thermal or microturbulent dispersion). Depending on the size of the population, this may allow for amplification well over the intensity of a thermal line transition, making it a valuable tool for probing distant sources.

The first recorded detection of an astrophysical maser was made by Weaver et al. (1965), in which they unknowingly observed an OH maser emanating from a molecular cloud. This keystone discovery led to the further search and development of masers and maser theory. The masers' high brightness temperatures and very narrow line-widths led researchers to correctly assume the radiation was being amplified in the same way as a terrestrial laser. These masers have become important stellar probes especially for evolved stars. These are referred to as circumstellar masers. The strongest circumstellar masers occur in oxygen-rich evolved stars as opposed to carbon stars, which is why this study will focus exclusively on oxygen-rich evolved stars.

1.5.1 OH Masers

There are four known ground-state OH maser transitions at 1612, 1665, 1667, and 1720 MHz. The 1612-MHz maser occurs within the outer reaches of the circumstellar envelope of evolved AGB and RSG stars. The main-line 1665- and 1667-MHz transitions also occur within the inner regions of the circumstellar envelopes of evolved stars, but also occur near Young Stellar Objects (YSOs). The final 1720-MHz transition primarily occur in areas where Supernova Remnants (SNRs) interact with molecular clouds. The diversity of phenomena in such a small range of frequencies has allowed for multi-purpose observations to yield a range of positive results.

The most important maser transition for evolved stars is the 1612-MHz maser transition. These masers typically occur at distances from $10^{16} - 10^{17}$ cm, at the point where stellar winds arrive at their final velocity (Elitzur, 1992). Goldreich & Scoville (1976) suggested that the OH needed for maser emission is formed by interstellar UV radiation penetrating the circumstellar envelope and photodissociating water. However clumpiness and possibly stellar radiation itself among other things, may affect the maser emission.

Masers can only occur in a certain radius range within a circumstellar envelope. If masers occur inside this range (around several hundred au), densities are so high that collisions rapidly depopulate the upper transition which "quenches" the maser. Outside of this range (a few thousand au), lower densities are not enough to sustain the pump rate and the maser can no longer be maintained (Elitzur, 1992; Vlemmings et al., 2006)[4].

1.5.2 Pumping mechanisms

The 1612-MHz transition is a result of the fine and hyperfine structure of the OH molecule. The fine structure is the division of spectral lines due to the magnetic moment of the electrons in the molecule. This is dependent on the angular momentum and orbital spin

[4]For more see Cohen (1989) and Gray (2012).

of the electrons. The hyperfine structure is a division of the spectral lines, an order of magnitude weaker, that is caused by the magnetic moment created within the nucleus of a molecule. When ground state OH in a circumstellar envelope is excited by incident 35 and/or 53 μm infrared photons (produced by circumstellar silicate-rich dust), the molecules are excited to a higher energy rotational level of the ground vibrational state or 'pumped' (Elitzur, Goldreich & Scoville, 1976). From this state they then decay into a meta-stable state. At this point, the molecules need additional energy to overcome the energy barrier, and return to the ground state. Once a population is in this meta-stable state, all it takes is a high energy photon or spontaneous emission to cause a chain reaction that inverts the entire population, amplifying 1612-MHz photons that correspond to the energy difference of the states, and creating the maser (Fig. 1.8).

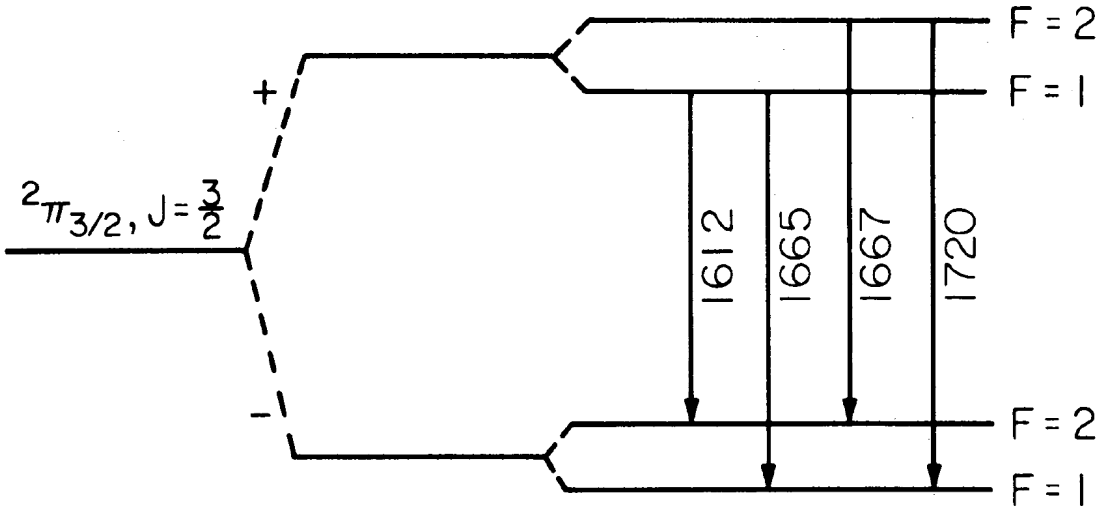

Figure 1.8: OH ground state maser transitions from Cimerman & Scoville (1980).

1.5.3 Circumstellar masers

An ideal maser detection will yield a double-peaked or 'double-horned' structure as is shown in Figure 1.9. This structure is what grants astronomers the ability to calculate

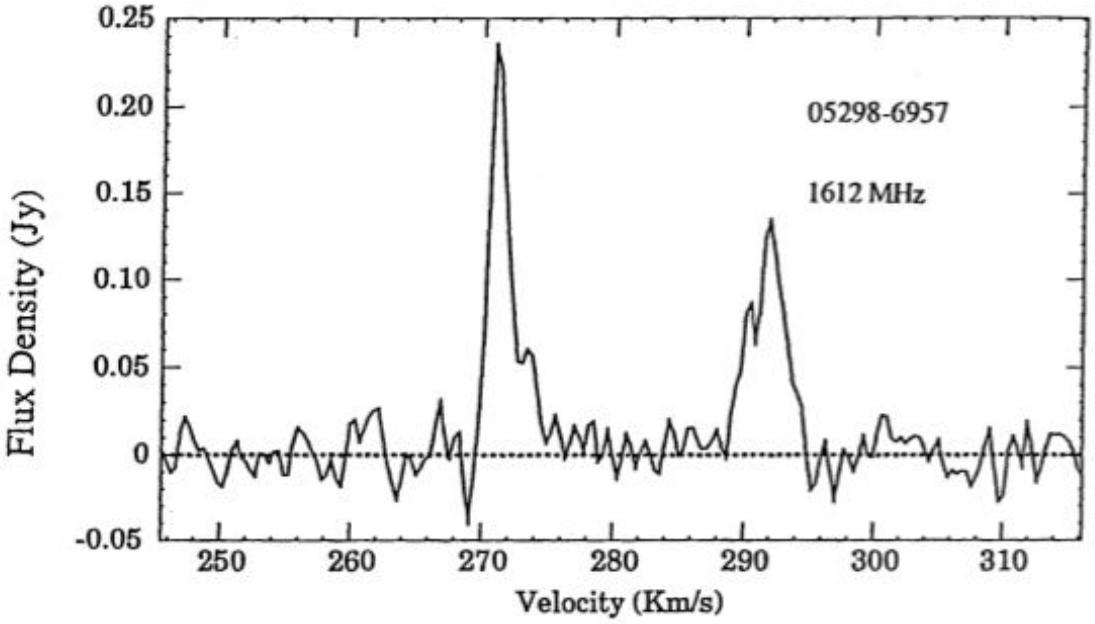

Figure 1.9: OH maser detection of IRAS 05298−6957 made by Wood et al. (1992).

the radial wind speed. What the two horns represent are the red-shifted and blue-shifted amplified radiation that is coming from regions moving toward and away from Earth, respectively. By taking half the frequency distance between the two peaks, or the distance from the centre of the peaks (the systemic velocity) to either peak, a final radial wind speed can be established. By assuming the star is spherically symmetric, it can be assumed that this is the wind speed in all directions. Often within the maser profile, the blue maser peak is brighter than the red maser peak. This has been suggested to be due to contribution or blocking effect from the parent AGB or RSG star (Sivagnanam et al., 1988; Takaba et al., 1994; Marshall et al., 2004). In practice, a distinct double-horned structure is not always attainable as a result of deviations from spherical symmetry and thus velocity coherence.

1.5.4 SiO and H_2O masers

While OH masers may be the most useful for studying stellar wind speeds, the 43-, 86-, and 129-GHz SiO maser and the 22-GHz water maser can be instrumental in interpreting

OH maser detections. These masers are especially important when the signal of an OH maser does not yield a distinguishable structure. SiO masers occur closer to the star and are thought to be pumped collisionally in the inner zones of the upper stellar atmospheres where substantial dust has yet to form ((e.g. Wittkowski et al., 2007)), at around a few stellar radii $\sim 10^{14}$ cm (e.g. McIntosh et al., 1989). They occur from rotational transitions in excited vibration states of the SiO molecules and give a measure of the systemic velocity as a result of being amplified tangentially. Water masers are also helpful as they act as probes in areas of accelerating winds. These masers are thought to be pumped collisionally and occur in the warm inner parts of the circumstellar envelope between the SiO and OH masers at distances around 10^{15} cm (Elitzur, 1992), and are amplified both radially and tangentially.

The amplification direction of the maser emission is determined by the velocity coherence of the populations. In the 1612-MHz maser, the population is coherent in the radial direction where the winds have reached their final expansion velocity. For the SiO maser, high velocity gradients limit radial amplification. The populations do however have a sufficiently large path length of velocity coherent molecules to beam tangentially, seen as a ring-like structure (e.g. Yi et al., 2005).

For both types of these masers to occur, sufficient temperature and density must be sustained. For a SiO maser, a density of SiO molecules more than 10^7 cm^{-3} and a temperature of roughly 1770 K is required (Elitzur, 1982). For a water maser, a gas density of $10^7 - 10^9$ cm^{-3} is required, as well as a kinetic temperature of $300 - 1000$ K (Benson & Little-Marenin, 1996). As is the case with OH masers, the inner limit marks the point at which high population densities result in rapidly increased collisional depopulation, quenching the maser, and the outer limit marks the point where the maser can no longer be sustained due to low population densities.

Detections of these masers have greatly assisted previous studies of OH masers. As was the case for the red supergiant WOH G64 (IRAS 04553−6825), the initial detection of an OH maser, made by Wood et al. (1992), gave an inaccurate value for the expansion velocity. Subsequent detections by van Loon et al. (2001a) of water and SiO emission, indicated a systematic velocity outside of the velocity range of the original OH maser

profile. After further analysis it was found that the OH profile showed an additional peak, which more than doubled the star's derived wind speed (Marshall et al., 2004). This is shown later in Figure 3.8 and will be further discussed in Chapter 3.

1.6 CO line emission

In addition to the 1612-MHz OH maser, thermal CO rotational line emission can be used to derive the circumstellar wind speeds of evolved stars. Observations have been successful in detecting CO in hundreds of oxygen-rich (Kerschbaum & Olofsson, 1999; Olofsson et al., 2002) and carbon-rich (Groenewegen et al., 2002) AGB stars within the galaxy. As CO emission is a thermal line emission, it is not amplified. Thus a greater sensitivity is needed to use CO emission as a viable tool in more distant environments. CO is one of the most abundant molecules in circumstellar envelopes. The strength of CO is in its ability to measure the circumstellar expansion velocity while also providing an independent estimate of the mass-loss rate. While the width of the CO line yields the expansion velocity, modeling the shape and strength of the feature gives an estimate of the mass-loss rate, because it is a thermal line and the intensity depends on the temperature.

As of now, only a handful of CO line detections have been made outside of the galaxy from evolved stars with two red supergiants, four carbon-rich AGB stars, and one oxygen-rich AGB star successfully detected (Groenewegen et al., 2016; Matsuura et al., 2016). The oxygen-rich sources (WOH G64, IRAS 05280−6910, and IRAS 04545−7000) have all been previously observed in OH and will be discussed further in Chapter 3. Attempts have also been made to observe CO line emission in the nearby Globular Cluster 47 Tucanae (McDonald et al., 2015). While unsuccessful, the results have been used to quantify the intensity of the interstellar UV radiation, responsible for photo-dissociating circumstellar CO molecules.

1.7 Metallicity and luminosity

In studying the winds of evolved stars it is assumed that they are primarily dust-driven winds. This assumes that the driving mechanism of the wind is radiation pressure on circumstellar dust grains that drag along gas through friction. Several studies have analysed the relationship between expansion velocity and other observable stellar parameters (van Loon et al., 2001a; Marshall et al., 2004). They found that the dominant parameters are metallicity and luminosity. As the amount of radiation pressure (i.e. luminosity) and the amount of dust (i.e. metallicity) are expected to affect the wind-driving, this is consistent with expectations. It has also been suggested that multiple scattering of photons will increase the driving force of the wind (Gail & Sedlmayr, 1986).

The effects of these parameters on the overall mass-loss of the star has also been studied (e.g. van Loon et al., 2005). Constraining these uncertainties is critical to accurately predicting the contribution of AGB stars back to the ISM. There are three major mass-loss regimes that will be discussed in §1.8, but the most prominent mass-loss regime is within the superwind phase. It has been theorised that within this phase, mass-loss will be affected by luminosity as it is the driving force of the winds carrying material away.

Analysing the wind-driving and mass-loss mechanisms requires studying stellar samples with different luminosities and that reside within different metallicity environments. By studying evolved stars not only within the Galaxy, but also within the Large and Small Magellanic Cloud dwarf galaxies, with metallicities of a half and a fifth solar respectively, the effects of metallicity on the expansion velocity and mass-loss rates of AGB stars can be further studied and tested. The proximity of the LMC and SMC at 50 (Feast, 2013) and 60 kpc (Szewczyk et al., 2009), respectively also make them ideal 'nearby' environments for further study.

1.7.1 Metallicity distributions

The Galaxy The closest stellar samples of evolved stars lie within the Galaxy. While the view of the Galaxy from within the Galactic disk is obscured by dust (Fig. 1.10), it still provides researchers with the brightest sources to study. Typical Galactic sources have chemical abundances, metallicities, and gas-to-dust ratios similar to that of the Sun around $Z = 0.0196$ (von Steiger & Zurbuchen, 2016), where Z is the fractional percentage of elements not hydrogen or helium. The most metal-rich sources reside within the Galactic Centre, at around 8 kpc (Eisenhauer et al., 2003), where most stars will have metallicity at or above solar metallicity (Wood, Habing & McGregor, 1998). However, a small population of lower metallicity sources has been discovered within the central parsec of the galaxy (Wood, Habing & McGregor, 1998; van Loon et al., 2003; Do et al., 2015). Within the Galactic bulge, sources typically peak at a near solar value, with a sharp cut-off just above solar, and a tail towards lower metallicity (Zoccali et al., 2003; Ness & Freeman, 2015). A radial metallicity gradient has also been discovered within the Galaxy from below solar metallicity in the outskirts to supersolar within the central 5 kpc (Feltzing & Chiba, 2013; Lépine et al., 2011). These samples provide a range of metallicity around solar to better understand the effects of metallicity. However distances to these sources are very uncertain and thus yield uncertain luminosities. In order to probe lower metallicities and a range of more accurate luminosities it is important to leave the Milky Way and study more distant stellar samples.

The Magellanic Clouds The LMC and SMC (Fig. 1.11) provide excellent nearby stellar samples for testing the effects of a range of various stellar parameters. The range of metallicities within the Magellanic Clouds can be used to draw conclusions about metallicity environments even lower than the Galaxy, characteristic of an earlier epoch of the Universe. The average metallicity of the LMC has been found to be around $[\mathrm{Fe/H}] = -0.38$ dex (or around half solar) with the LMC Bar hosting the highest metallicity stars (Choudhury, Subramaniam & Cole, 2016). Using their photometric metallicity map, they also found a number of deviations from the average (Fig. 1.12) and a shallow radial

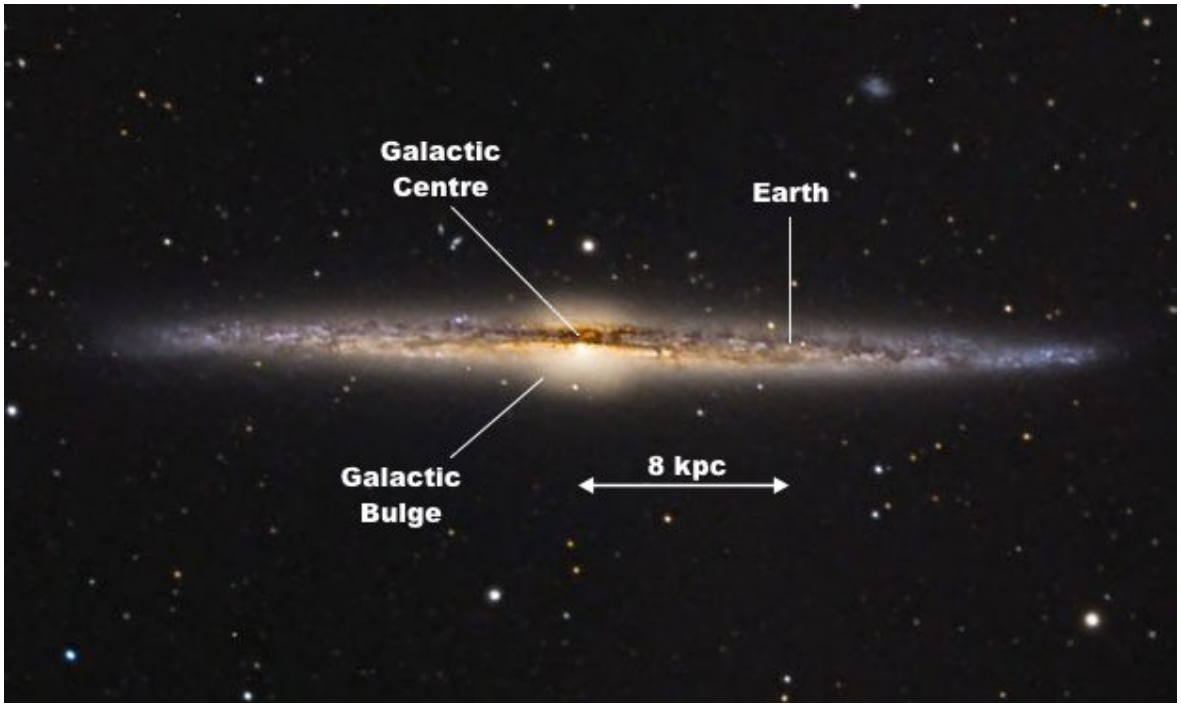

Figure 1.10: An adapted image of the edge-on spiral galaxy: NGC545a, depicting the Milky Way Galaxy.

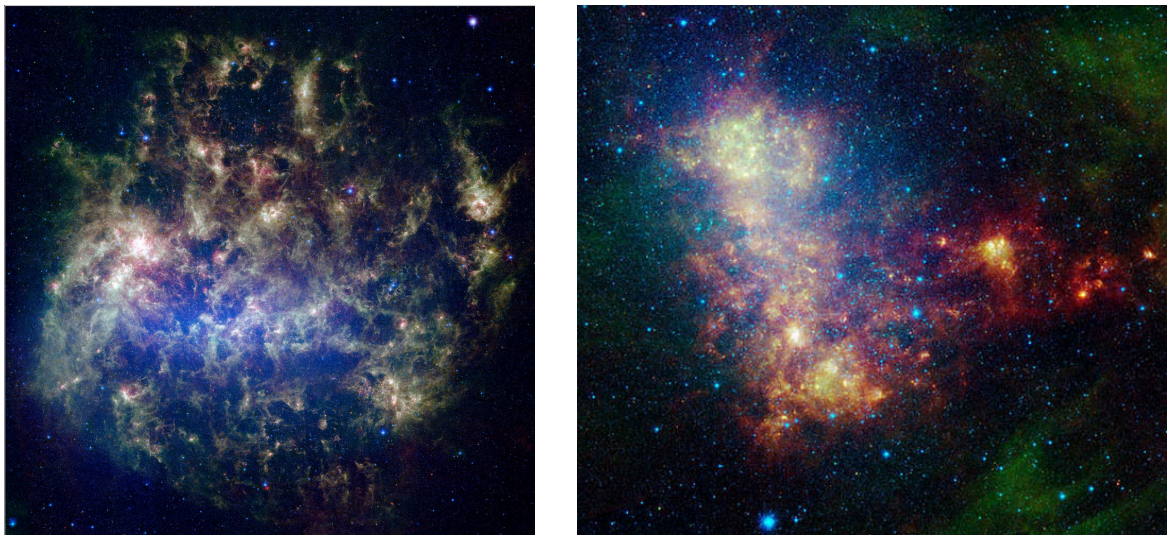

Figure 1.11: Spitzer colour images using all IRAC and MIPS bands of the Large and Small Magellanic Clouds (not to scale), from Meixner et al. (2006) and Gordon et al. (2011), respectively.

metallicity gradient out to around 4 kpc. These results were based on spectroscopic data of a large sample of RGB stars. While a gradual age-metallicity relation will exist, for stars with $M_{initial} \gtrsim 4\ M_{\odot}$ and ages $\lesssim 200$ Myr, a similar half solar metallicity can be assumed.

The SMC has an average metallicity of around [Fe/H] $= -0.68$ dex (Luck et al., 1998), corresponding to a metallicity of around one fifth solar. While there are other differences within these samples, something that will be described further in the coming chapters and especially in Chapter 6, observations in the Magellanic Clouds will be used to probe processes within evolved stars such as the wind-driving and mass-loss mechanisms.

1.7.2 Star formation history of the Magellanic Clouds

The Magellanic Clouds have considerably different AGB populations resulting from different star formation histories (SFHs). The SMC, with a stellar mass of $3.7 \times 10^8\ M_{\odot}$ (Skibba et al., 2012), is nearly a quarter of the stellar mass of the LMC at $1.7 \times 10^9\ M_{\odot}$

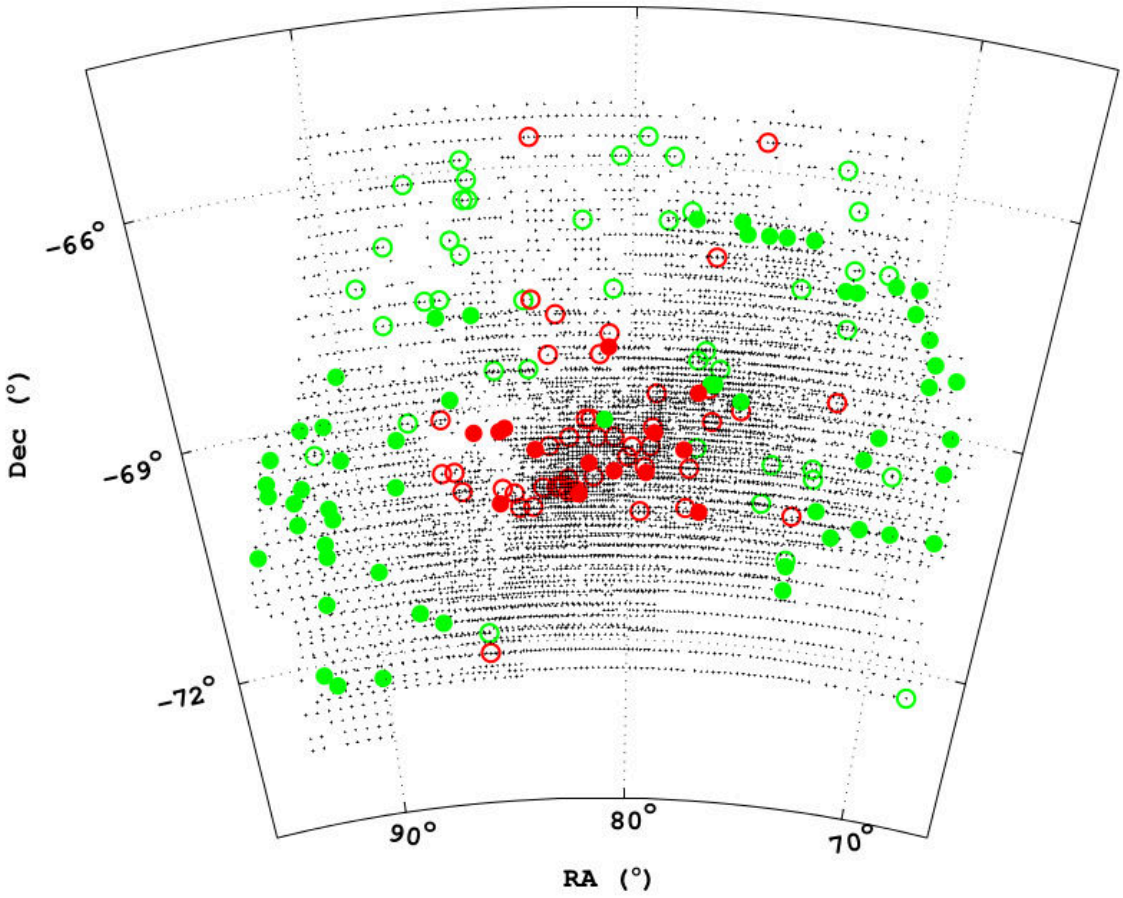

Figure 1.12: LMC photometric metallicity map from Choudhury, Subramaniam & Cole (2016). The subregions show large deviation from mean metallicity. In red, significantly metal-rich regions ~ 0.7 $Z_\odot$ ([Fe/H] $\gtrsim -0.15$ dex) and in green, the significantly metal-poor regions ~ 0.2 $Z_\odot$ ([Fe/H] $\lesssim -0.65$); filled circles are from OGLE III (Udalski et al., 2008), and open circles from MCPS (Zaritsky et al., 2004).

(Harris & Zaritsky, 2004, 2009). Within the LMC, a peak in star formation around 100 Myr ago (Harris & Zaritsky, 2009) has resulted in favourable conditions for bright maser emitting sources. Moreover, according to the recent work by Slemer et al. (2017) based on the stellar evolutionary tracks computed with PARSEC (Bressan et al., 2012) and COLIBRI (Marigo et al., 2017) codes, the minimum mass of a HBB star is ~ 4.2 $M_{\odot}$ for $Z = 0.006$, where the exact value of the mass will depend on the metallicity and on the underlying stellar model. As a consequence, given the 100 Myr evolution time of $5 - 6$ $M_{\odot}$ stars, this has resulted in a disproportionally large population of sources undergoing HBB (Dell'Agli et al., 2015; Slemer et al., 2017). Conversely, the SFH of the SMC derived by Harris & Zaritsky (2004) shows a minimum in star formation around 100 Myr ago, which has likely resulted in a smaller population of massive oxygen-rich AGB stars within the SMC. Even if the minimum in the star formation rate (SFR) is not confirmed by the most recent SFH derived by Rubele et al. (2015), the SFR by Harris & Zaritsky (2004) is in good agreement with the one derived by Rubele et al. (2015) about 100 Myr ago. More recent SFRs are difficult to constrain using *Hubble Space Telescope* data as it requires a wide survey area (Weisz et al., 2013). Regardless this work has investigated a number of lower mass oxygen-rich sources in the galaxy as well as several higher mass sources in the Magellanic Clouds that have undergone HBB (Fig. 1.13).

1.7.3 Dust within the Magellanic Clouds

It is expected that dust production may differ in lower metallicity environments and at higher redshifts. In the LMC, it has been suggested that carbon stars produce more dust than their oxygen-rich counterparts (Boyer et al., 2011; Matsuura, Woods & Owen, 2013; Sloan et al., 2016). Silicates form the bulk of the dust around oxygen-rich stars with thick circumstellar envelopes, but these probably cannot form close to the star, and the nucleation of refractory metal oxides is required, producing heterogeneous dust. In contrast, carbon compounds can both nucleate and grow at lower metallicities, and as a result, carbon stars may dominate the injection of dust into the ISM at low metallicities. Conversely evidence has been shown that carbon dust formation is also less efficient at

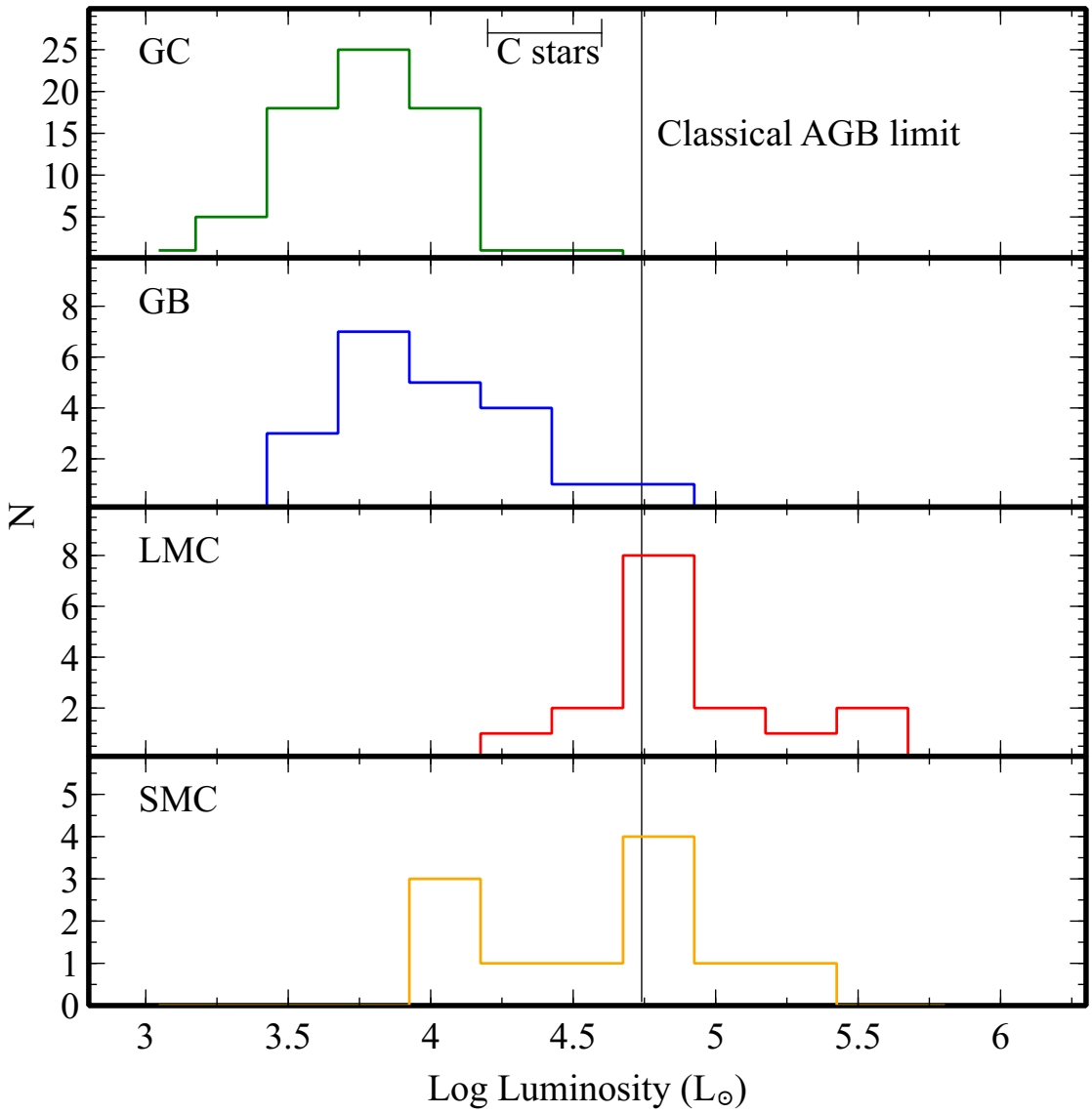

Figure 1.13: The luminosity distributions of the OH/IR samples in the Galactic bulge, Galactic Centre, and LMC (described in Chapter 4), as well as the SMC target OH/IR stars in the SMC (described further in Chapter 6). Sources with luminosities around 20,000 $L_{\odot}$ are expected to be carbon stars (C stars), stars which have been omitted from this study.

lower metallicity (van Loon et al., 2008). Comparing their results from spectroscopic studies of the 3.1 and 3.8 μm C_2H_2 absorption features in the SMC with a previous sample of LMC carbon stars (van Loon et al., 2006a), the stronger dust veiling of these absorption bands in the LMC has led to the conclusion that carbon dust formation may also scale with metallicity. However, the difference in pulsation periods within the samples may also be affecting the dust production (Sloan et al., 2016). The finding that the reduced dust production found in metal-poor Galactic Halo carbon stars show low wind speeds (Groenewegen, Oudmaijer & Ludwig, 1997; Lagadec et al., 2010) adds evidence to the idea of a lower efficiency of dust formation at lower metallicity. In addition to the efficiency, lower metallicity environments also have younger stellar populations, which results in a lower frequency of carbon stars. This should result in less dust in lower metallicity environments. The importance of AGB dust in the earlier universe has been shown from studies of dust at high redshifts (Valiante et al., 2009). Yet, at high redshifts, populations may not have had enough time to evolve a significant AGB population, a regime where RSGs may dominate the oxygen-rich dust production.

Comparing circumstellar dust content in the LMC and SMC provides some indication of the possible effect of metallicity on the dust composition. Analysis of mid-IR spectra of evolved stars has led to a number of important conclusions. Instruments like the *Spitzer Infrared Spectrograph* (IRS) have provided valuable insight into the chemical composition of circumstellar dust by looking at the silicate features at 10 and 18 μm and the crystalline silicate features between 20 and 35 μm. Silicate emission, as well as crystalline silicate features, have been observed within the SMC, yet no evolved stars within the SMC have ever been found to have silicate in absorption or self-absorption. As opposed to the Galaxy or the LMC, evolved stars in the SMC have shown to have less circumstellar dust (van Loon, 2000; van Loon et al., 2006b, 2008; Bonanos et al., 2010). The strong 3 μm water features of SMC sources may suggest that less oxygen is being locked in dust, which would be in agreement with the decreased dust content. This dust also shows a lower abundance of alumina (Sloan et al., 2008; Kraemer et al., 2017) and higher abundances of amorphous (as opposed to crystalline) silicates (Kraemer et al., 2017). Jones et al. (2012) have shown that lower metallicity dust has also been found to

have a higher fraction of enstatite ($MgSiO_3$) over forsterite (Mg_2SiO_4). Observations have revealed evolved stars with late-M spectral types in both the LMC and SMC. In the LMC, spectral types have been seen as late as M8−M10 (van Loon et al., 1998b, 2005), and in the SMC as late as M8 (Groenewegen & Blommaert, 1998).

1.8 Mass-loss

The intense mass-loss of these stars is hard to quantify, as most of the mass lost is in the form of gas. Additionally, as most of the gas is molecular hydrogen (H_2), a homonuclear molecule, it has no permanent dipole moment and, as a result, does not emit in radio frequencies. Neutral hydrogen (H I) does emit in radio frequencies, but can be confused with H I from the ISM. Methods of measuring the mass-loss of these stars have been developed and refined as well as models predicting the mass-loss of stars based on observational parameters.

1.8.1 Mass-loss regimes

The discussion of mass-loss regimes has been organised into pre-dust, dust-driven, and superwind. These three regimes probe different intensities of mass-loss, where the driving forces may differ. Past mass-loss prescriptions have been based on samples or assumptions associated with a certain mass-loss regime and each will be discussed in turn. This list is not exhaustive but mentions some of the more prominent prescriptions in each of these regimes.

Pre-dust phase A pioneering work that has contributed immensely to the understanding of the mass-loss of evolved stars was the work by Reimers (1975). This prescription, known as the classical Reimers' law, was derived using a scaling relation based on a small sample of red giants and supergiants, and gives a measure of the mass-loss in the less

intense pre-dust phase. In this phase, dust has yet to form in the outer atmospheric layers of the star, or at least has insufficient dust to drive an outflow. The relation is as follows:

$$\dot{M}^{R75}_{predust} = 10^{-13}\eta_R \frac{L}{gR}\,\mathrm{M}_\odot\,\mathrm{yr}^{-1} \tag{1.4}$$

where $\eta_R = 4$ and is a scaling parameter which sets the efficiency of the mass loss, L is luminosity, g is surface gravity and and R is stellar radius. More recently an updated model of the Reimers' law was proposed by Schröder & Cuntz (2005) which incorporates additional stellar parameters i.e. effective temperature ($T_{\rm eff}$) and initial mass (M), but has a similar dimensional dependence.

$$\dot{M}^{SC05}_{predust} = \eta \frac{LR}{M}\Big(\frac{T_{\rm eff}}{4000\,\mathrm{K}}\Big)^{3.5}\Big(1 + \frac{g_\odot}{4300g}\Big) \tag{1.5}$$

The efficiency parameter for this relation is set as $\eta = 8 \times 10^{-14} M_\odot$ yr^{-1}, a value calibrated using RGB stars in two nearby globular clusters; $g_\odot$ is solar surface gravitational acceleration. The Reimers' law is often scaled up arbitrarily and applied to the dust-driven mass-loss regime, where it is unlikely to be valid.

Dust-driven phase The next regime of mass-loss is the dust-driven regime where the mass-loss rate increases exponentially with pulsation period. Within this phase, the mass-loss is greatly enhanced by long stellar pulsations. These pulsations are expected to levitate material out to a radius where it is cool enough for the gas to condense into dust grains. These dust grains are then pushed radially outward by radiation pressure from the star, and the dust grains then drag along the gas through friction. A prescription known

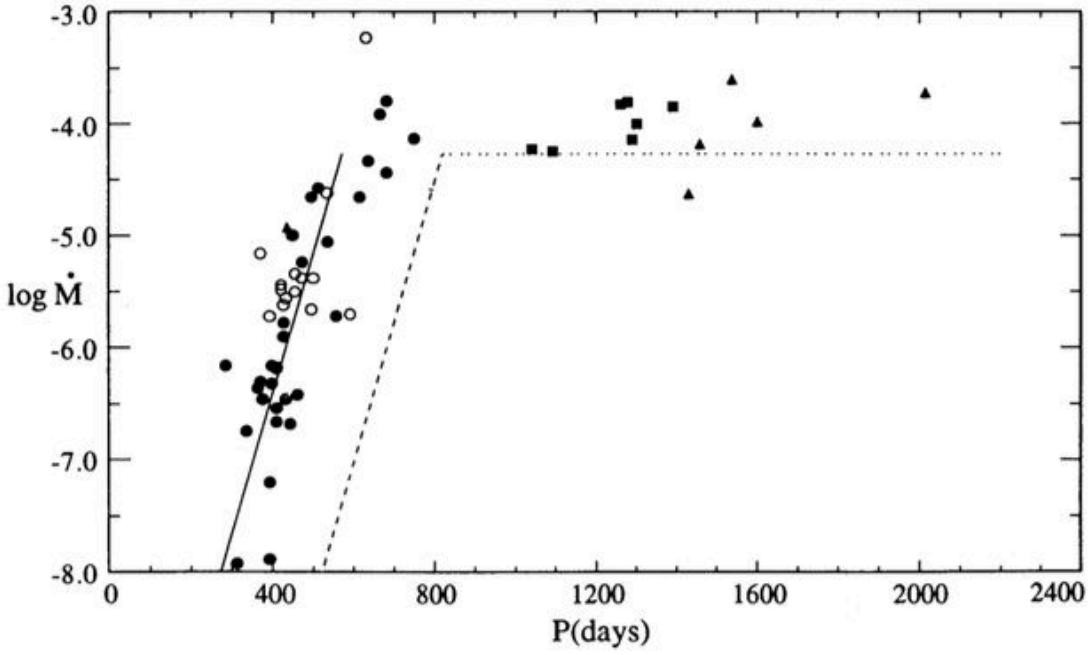

Figure 1.14: Mass loss versus pulsation period from Vassiliadis & Wood (1993) for sources exhibiting a dust-driven wind.

for accurately describing this phase is the Vassiliadis & Wood (1993) mass-loss prescription:

$$\log \dot{M}_{dust}^{VW93}(\mathrm{M}_{\odot}\, yr^{-1}) = -11.4 + 0.0125(P - 100(M/\mathrm{M}_{\odot} - 2.5)) \qquad (1.6)$$

where P is the pulsation period in days. This prescription is empirically derived based on CO observations and shows a rapid rise in mass-loss with pulsation period up to pulsation periods of around 500 days, at which point the mass-loss levels off (Fig. 1.14). At this point, the wind reaches the superwind phase. The subsequent levelling off will be discussed further in Chapter 5, as new results suggest that the pulsation period will still affect the mass loss for P $\gtrsim$ 500. It is expected that this is the point at which maximum momentum transfer is reached and the source enters the superwind phase.

The Blöcker (1995) mass-loss prescription has been based on the dynamical

theoretical study of the atmospheres of Mira-like variables by Bowen (1988). The prescription is based upon the pulsation models and fit to observed initial-final mass relations. The prescription has two formalisms that use either the main sequence mass or the current mass depending on if the pulsation is less than or greater than 100 d respectively. The prescription is found in terms of the Reimers' law mass-loss rate:

$$\dot{M}_{dust}^{B95} = 4.83 \times 10^{-9} M^{-2.1} L^{2.7} \frac{L}{gR} \tag{1.7}$$

The de Jager, Nieuwenhuijzen & van der Hucht (1988) mass-loss prescription is a commonly used mass-loss prescription that was based on 271 Galactic sources (hot and cool) along the HR diagram. The prescription uses effective temperature and luminosity but has been found to rely primarily on L (Mauron & Josselin, 2011). It is however hard to see this dependence as the prescription uses Chebyshev polynomials. According to de Jager, Nieuwenhuijzen & van der Hucht (1988) the prescription has an uncertainty of around a factor of 3. An updated version of the prescription was developed by Nieuwenhuijzen & de Jager (1990) which also includes current mass, but which has little effect on the mass loss. Assuming the mass as a constant ~ 13 $M_\odot$ (see Mauron & Josselin, 2011) the formula can be simplified to the following:

$$\dot{M}_{dust}^{NJ90} = 5.6 \times 10^{-6} \left(\frac{L}{10^5 \, L_\odot} \right)^{1.64} \left(\frac{T_{\rm eff}}{3500 \, K} \right)^{-1.61} \tag{1.8}$$

Superwind phase The most intense mass-loss regime of evolved stars is the superwind phase. During this phase a star will respond to reduced mass and gravity by expanding, creating larger pulsations and exhibiting a longer pulsation period ($\gtrsim 500$ d) at a near constant luminosity. A number of mass-loss prescriptions have been developed and refined to probe this phase. The Baud & Habing (1983) relation uses the results of

maser detections to calculate the mass-loss and is calibrated using a sample of Galactic disk OH/IR sources. The following is a form presented by van der Veen & Rugers (1989)

$$\dot{M}^{BH83}_{super}(\mathrm{M}_{\odot}\,\mathrm{yr}^{-1}) = 1.8 \times 10^{-7}\sqrt{F_{\mathrm{OH}}}V_{\mathrm{exp}}D \tag{1.9}$$

where F_{OH} is the 1612-MHz maser peak intensity in Jy, and D is the distance in kpc. The prescription relies on the assumption that the OH maser is saturated and operating at maximum pumping efficiency. The theoretical maximum pumping efficiency of converting 35 μm infrared photon to 1612-MHz maser photon is 25% (Elitzur, 1992). Under this assumption they argue that the peak flux density will depend on the abundance of OH molecules undergoing the population inversion.

An updated model was proposed by Zijlstra et al. (1996):

$$\dot{M}^{Z96}_{super}(\mathrm{M}_{\odot}\,\mathrm{yr}^{-1}) = 1.6 \times 10^{-10}F_{\mathrm{OH}}V_{\mathrm{exp}}D^{2} \tag{1.10}$$

They made the point that the pumping efficiency will not depend on the abundance of OH but rather the infrared flux at 35 μm which pumps the maser, assuming the momentum transfer is isotropic. This means that the maser does not measure the OH abundance but rather the infrared radiation from circumstellar dust. As a result, the prescription calculates the dust mass-loss rate whereas the other prescriptions discussed have calculated a gas mass-loss rate. As will be discussed further in Chapter 6, the maser efficiency will not always reach its maximum efficiency which is likely a result of the circumstellar environment. Measurements of the efficiency will also show a range of values above and far below this maximum due to the variability of these sources and the different times when the measurements were taken.

Another commonly used mass-loss prescription is that of Salasnich, Bressan & Chiosi (1999). This relation is based on the mass-loss prescription by Feast (1992) both of which use only the luminosity as an input. The prescription calculates the mass loss under the assumption that the gas-to-dust ratio will increase with luminosity.

$$\dot{M}_{super}^{S99} = 1.00 \times 10^{-4} (L/10^5 \mathrm{L}_{\odot})^{2.1} \tag{1.11}$$

Another mass-loss prescription that probes the superwind phase of mass-loss is that by van Loon et al. (2005):

$$\log \dot{M}_{super}^{vL05} = \alpha + \beta \log\left(\frac{L}{10^4 \mathrm{L}_{\odot}}\right) + \gamma \log\left(\frac{T_{\mathrm{eff}}}{3500\,\mathrm{K}}\right) \tag{1.12}$$

where $\alpha = -5.65 \pm 0.15$, $\beta = 1.05 \pm 0.14$, and $\gamma = -6.3 \pm 1.2$ for M-type stars. This is an empirically fitted relation based on a spectroscopic sample of AGB and RSG stars within the LMC. This derivation utilises the more accurate luminosities from the LMC, a result of more accurate distances, as a measure of the radiation pressure.

1.8.2 Mass-loss example: IRAS 04498−6842

A comparison of the mass-loss prescriptions has been conducted using the LMC AGB star: IRAS 04498−6842. The stellar parameters derived for this source are shown in Table 1.1, and the mass-loss rates calculated using the previously described mass-loss prescriptions is shown in Table 1.2. Also shown is a new mass-loss prescription that will be described further in §5.3. It should be noted that IRAS 04498−6842 is a luminous evolved star within its superwind phase and thus several of the mass-loss prescriptions are not appropriate for this phase of evolution; this is clearly illustrated with the range

Table 1.1: Stellar parameters of IRAS 04498−6842.

Stellar parameter	Symbol	Value	Reference
Luminosity	L	97,000 $L_\odot$	§4.2
Surface gravity**	$\log g$	-1.1	
Radius	R	1,660 $R_\odot$	Marshall et al. (2004)
Effective temperature	$T_{\rm eff}$	2,500 K	van Loon, Marshall & Zijlstra (2005)
Initial mass	M	8 $M_\odot$	Marshall et al. (2004)
Pulsation period	P	1292 d	Whitelock et al. (2003)
Maser flux*	$F_{\rm OH}$	29.4 mJy	§4.2
Expansion velocity	$V_{\rm exp}$	13 km s^{-1}	§4.2
Distance	D	50 kpc	Feast (2013)

Notes: *Value derived from peak maser flux intensity resampled to 1.17 km s^{-1}, the resolution used in Baud & Habing (1983). **Value derived from M and R listed.

Table 1.2: Mass-loss rates of IRAS 04498−6842 using past mass-loss prescriptions previously described as well as a new mass-loss prescription (Goldman et al., 2017) described in Chapter 5.

Prescription	Mass-loss rate
Reimers (1975)	3.1×10^{-10} $M_\odot$ yr^{-1}
Schröder & Cuntz (2005)	3.0×10^{-7} $M_\odot$ yr^{-1}
Blöcker (1995)*	5.5×10^{-7} $M_\odot$ yr^{-1}
Nieuwenhuijzen & de Jager (1990)	9.2×10^{-6} $M_\odot$ yr^{-1}
Salasnich, Bressan & Chiosi (1999)	9.4×10^{-5} $M_\odot$ yr^{-1}
Zijlstra et al. (1996)	1.5×10^{-4} $M_\odot$ yr^{-1}
Goldman et al. (2017)	1.6×10^{-4} $M_\odot$ yr^{-1}
van Loon et al. (2005)	2.0×10^{-4} $M_\odot$ yr^{-1}
Baud & Habing (1983)	6.3×10^{-4} $M_\odot$ yr^{-1}
Vassiliadis & Wood (1993)	7.5×10^{-3} $M_\odot$ yr^{-1}

Notes: *Calculation uses the first formalism mentioned and thus the initial mass.

of mass-loss rates spanning seven orders of magnitude.

As was previously mentioned the Reimers law is meant for sources void of dust and provides a mass-loss rate unrealistically low for IRAS 04498−6842. The Vassiliadis & Wood (1993) prescription is not meant for sources that have reached their superwind phase. Assuming continued exponential growth in mass loss after $\gtrsim$ 500 d ignores the observed leveling off and produces a unrealistically high mass-loss rate.

Several of these mass-loss prescriptions have been based on similar samples, assumptions, or sets of parameters; the use of L/gR is common in several of these prescriptions. The methods used to derive prescriptions is either through fitting observable stellar parameters, fitting initial-final mass functions, or using models based on the mechanisms of mass loss. Of the previous mentioned mass-loss prescriptions, the Baud & Habing (1983), Zijlstra et al. (1996), and Salasnich, Bressan & Chiosi (1999) prescriptions make assumptions for the abundance of OH (or effects of metallicity) but none of them isolate it explicitly. Whether mass loss is affected by metallicity is still under debate. Mauron & Josselin (2011) found a metallicity dependence when analysing RSGs in the LMC and SMC, yet other recent studies find no correlation (e.g Groenewegen et al., 2009; De Beck et al., 2010; Matsuura et al., 2016).

These prescriptions have been shown to illustrate several different approaches to quantifying the complex mechanism of stellar mass loss. These prescriptions will be investigated further in Chapter 5.

1.9 Research aims

The main question driving my thesis research is:

How are the wind-driving and mass-loss mechanisms within evolved stars affected by other stellar properties?

The largest uncertainties within both of these processes are the effects of metallicity

and luminosity. In understanding these relationships, the underlying mechanisms involved can be better understood, and more accurately and quantitatively modelled.

Understanding these stellar relationships have broad implications for understanding the contribution of these stars to the interstellar medium and the source of all dust and gas in the Universe. By probing the effect of metallicity in particular, mass-loss and wind-driving can be better understood in environments characteristic of an earlier epoch. The results will give constraints on the expected mass boundaries of core-collapse supernovae, and the measurements of expansion velocities in lower metallicity environments may be able to explain multiple stellar populations within Globular clusters, as a result of slow expansion velocity and self-enrichment. The samples analysed in the following chapters contain low mass AGB stars within the galaxy, and higher-mass AGB and RSG stars within the LMC, all of which have shown 1612-MHz OH maser emission. The difference in the samples may complicate the ability to disentangle individual stellar parameters but can still be used as comparable samples. The subsequent chapters are organised as follows:

Chapter 2 describes the observational techniques and data reduction methods used for collecting and analysing the data.

Chapter 3 details the Large Magellanic Cloud circumstellar maser sample. This sample includes a number of new observations and discoveries using the Parkes and Australia Telescope Compact Array radio telescopes.

Chapter 4 describes a new method of determining the ratio of gas and dust using the radiative transfer code DUSTY and results from maser observations.

Chapter 5 discusses the results of chapters 3 and 4 in a broader context, specifically on their implication for the relationships between stellar parameters and the wind-driving and mass-loss mechanisms. The chapter also discusses the implications for more fundamental stellar parameters.

Chapter 6 describes results from searches of maser emission in the SMC and the implications for the effects of metallicity on circumstellar envelopes.

Chapter 7 reports on recent VLT mid-IR observations of the LMC RSG: IRAS 05280−6910 and how they have used to constrain its location and mass-loss rate.

Chapter 8 summarises the major conclusions of this work and outlines future work.

2 Methodology

This study focuses on sources at multiple wavelengths, within the optical, infrared, and radio. In each of these regimes, different techniques are required for reducing the effects of undesired signal. Reducing deviations over a large portion of the bandwidth can be done by taking an exposure or integration of a background or baseline and subtracting it from the signal. For smaller scale deviations, the data may need to be flagged or ignored in order to get accurate results from the untainted data.

The bear of optical and infrared astronomy is dealing with the interfering effects of molecules within the atmosphere. Different observing techniques can reduce instrumental noise significantly, but these techniques cannot compensate for the wall of turbulent molecules between the instrument and the source. The sensitivity of IR detectors is greatly affected by the atmosphere especially around 9.5 and 12.5 μm as was seen in a recent Very Large Telescope N-band spectroscopic observation which will be discussed in Chapter 7 (Fig. 2.1).

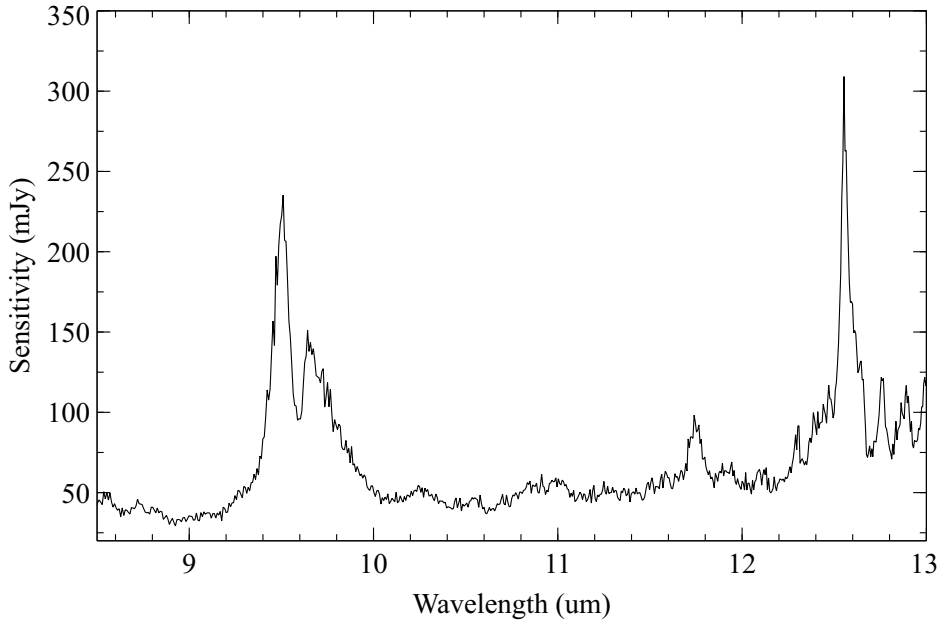

Figure 2.1: The sensitivity of an N-band spectroscopic observation of the standard star ϵ Psc. The large spikes are a result of the atmospheric emission.

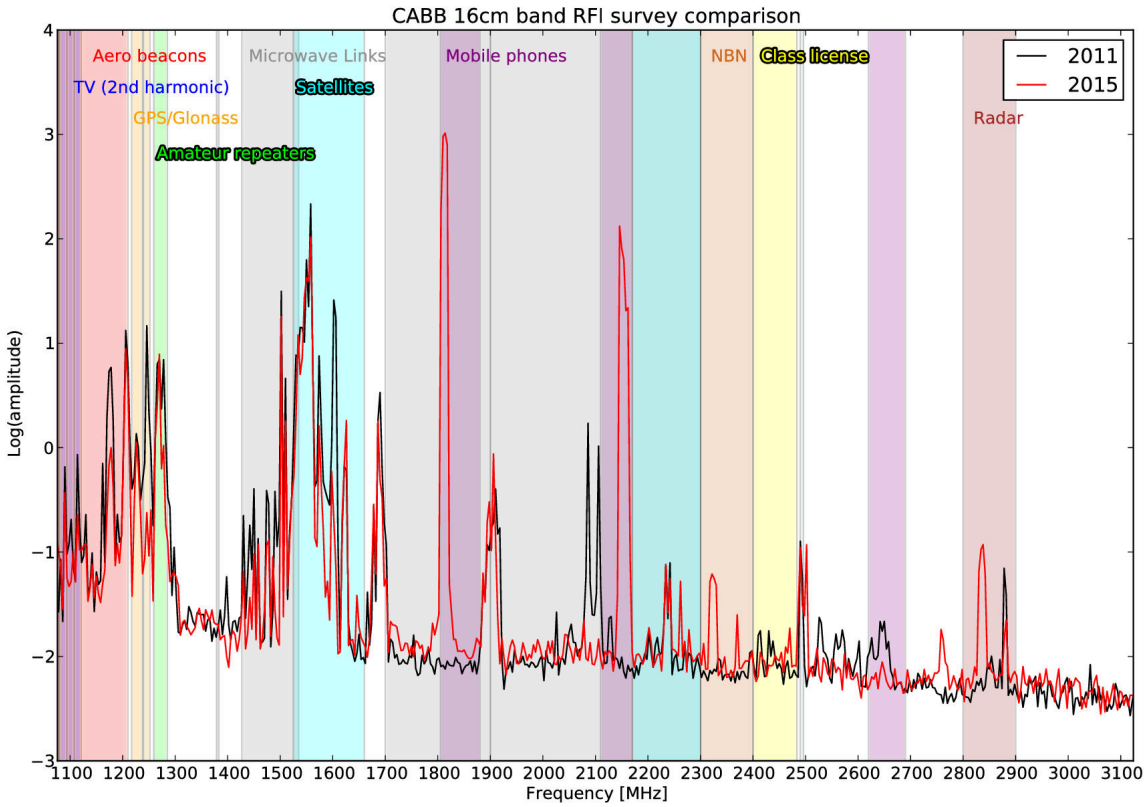

Figure 2.2: The 16cm RFI map observed from two RFI surveys in 2011 and 2015 with the ATCA (ATCA Users Manual v1.5).

The challenge in radio astronomy is overcoming man-made interference. Considering all of the devices and technologies currently used that operate at radio frequencies, it is a daunting task to target these same frequencies in distant stars and galaxies. Surveys of man-made radio interference with the ATCA have shown a range of different devices near important astronomical transition frequencies (Fig. 2.2). The techniques used to mitigate unwanted signal or "noise" will depend on the use of either a single dish or multiple element (interferometric) instrument.

Both single dish and interferometric instruments have their strengths and weaknesses. A single dish instrument will provide good sensitivity with a much simpler calibration, observation, and data reduction. Conversely an interferometric instrument will have far superior angular resolution. This allows for an additional spatial analysis, which can

be crucial when discovering or confirming emission. The necessity for either types of instrument will depend on the observing goals and thus both have been used in this analysis.

2.1 Single dish radio techniques

2.1.1 The Parkes radio telescope

The Parkes radio telescope is a 64m parabolic dish telescope located in Parkes, Australia and is the second largest movable telescope in the Southern Hemisphere. It has a large collecting area and provides a typical 'field-of-view' or Full Width at Half Maximum (FWHM) primary beam size of $29'$ at 18 cm. As a telescope does not respond uniformly to the sky, the size of the collective response beam is approximated by ~ 1.2 times the wavelength, divided by the diameter of the telescope. The wide dish has a large surface for collecting photons which provides the sensitivity needed for targeting maser candidates. As opposed to a radio interferometer, single-dish telescopes cannot disentangle spatially coincident sources within the primary beam of the telescope. However instruments like Parkes are ideal for targeting isolated maser candidates with known positions, and has been used in the discovery of nine of the thirteen LMC circumstellar maser detections.

The Telescope uses a fleet of 'front-end' receivers that are mounted in an aerial cabin supported by three large beams (Fig. 2.3). A signal that is received is fed through the Parkes conversion system and then to one of the correlators or 'back-end' units where the signal is amplified, and digitised. The receiver and correlator typically used for 18 cm or L-band observations have changed over the years. The Multibeam receiver and (until its decommissioning in 2016) the Multibeam correlator (MBCORR) have been used for L-band observations since they were installed in 1997. The H-OH receiver and the Digital Filter Bank mark IV (DFB4) correlator are now used for these types of observations. The steps for calibrating this data will be described in the following sections.

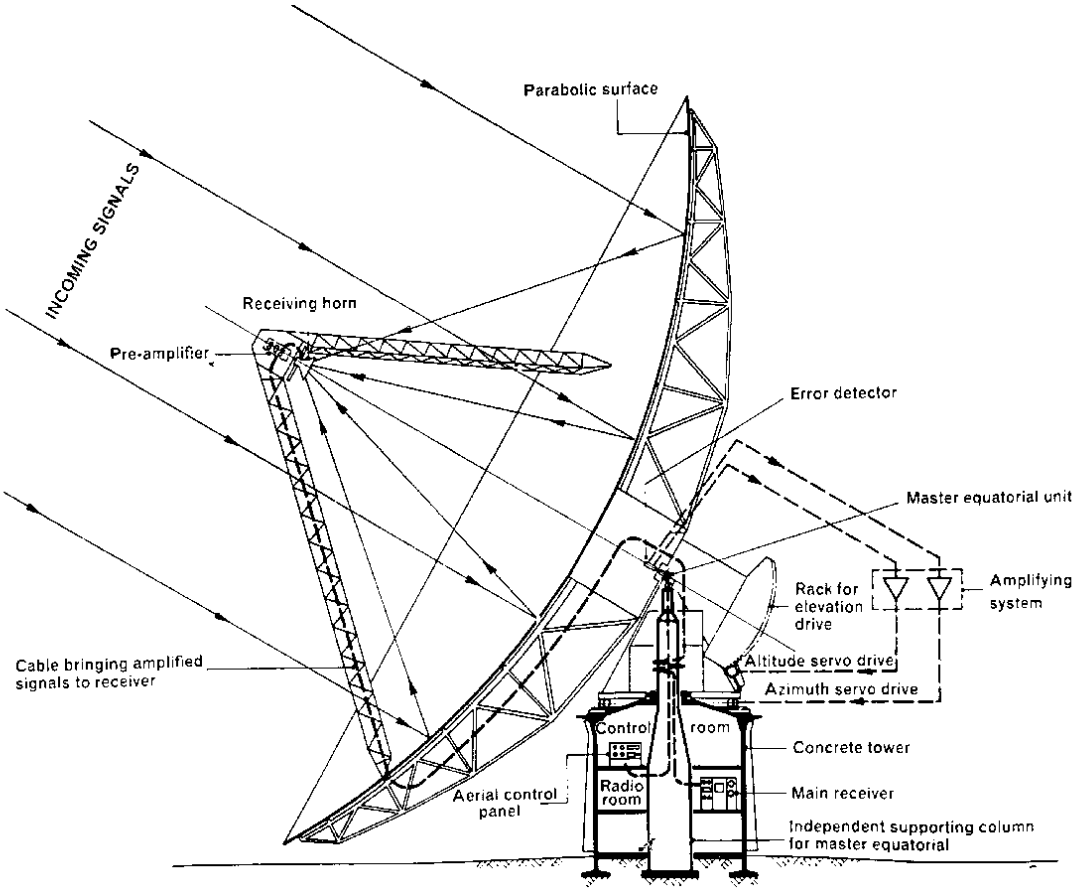

Figure 2.3: The 64-metre Parkes Radio Telescope

Bandpass calibration: There are several methods of calibrating the shape of the overall received signal also referred to as bandpass calibration. The two options used for the Parkes radio telescope are frequency-switching and position-switching. By aiming the telescope briefly off-source and taking a short observation, the "empty sky" signal can be subtracted from the on-source signal to obtain a flattened baseline. The same idea is used in frequency-switching mode, but alternatively an "out-of-band" frequency-throw is used instead of an off-source scan. These methods rely on the assumption that the off-source/out-of-band signal is truly empty, which is not always the case. Knowledge of the angular size and velocity of the source are important factors for determining the best calibration strategy (O'Neil, 2002). The strength of position-switching as opposed to frequency-switching is that no knowledge of the radial velocity of the source is required. For frequency-switching, if the source falls in the out-of-band frequency range, the source will be removed from the baseline at the velocity of the source minus the throw frequency. The benefits of frequency-switching are that it is much faster, without the need to move the telescope, and can be done more frequently. An alternative to both methods, is to use the total power spectrum without a bandpass calibration. This was done for several sources that will be discussed in Chapter 3, where the bandpass calibration did little to flatten the baseline. The baseline can then be manually fitted for each scan using a low-order polynomial. This allows for a more sensitive measure of the total flux from the source, at the cost of a less flattened baseline. The broad ripples in the bandpass can span the length of the bandwidth ($\gtrsim 300$ km s^{-1}) whereas maser emission is typically two peaks with widths on the order of 1 km s^{-1} and separated by between a few to 50 km s^{-1}. While this may affect the fluxes to a small degree, the widths of the peaks are not at risk of being affected by baseline fitting. Once this step is complete, the shape of the line-free channels will be flattened but will still contain a number of spurious and unwanted spikes.

Removing noise: Most observations will contain a number of narrow spikes that are a result of undesired man-made, instrumental or astronomical signals. These narrow and

highly non-gaussian spikes can be removed manually by flagging them or zeroing the flux within the specified spectral channel within the data file. Removing more broad noise features can be more challenging.

Parkes data reduction: The Parkes data described in Chapters 3 and 6 have been reduced using the CASA ASAP toolkit (McMullin et al., 2007). The data have been inspected manually for quality and for radio frequency interference (RFI) and the resulting scans were then bandpass calibrated using either off-scan or out-of-band baseline subtraction. For sources that used the total power spectrum, a line-free baseline was fitted and subtracted using a low-order polynomial for each scan. The scans were then averaged and reduced separately for each epoch. Additionally, the collective data for each target were averaged and reduced. All scans were aligned in velocity, weighted by the noise or the inverse square root of the system temperature ($T_{\rm sys}^{-2}$), and fitted with another low order polynomial, which was then subtracted. Any bad data spikes were determined visually and removed from within the file. As the flux of a maser source should not change over the observations, any spikes that changed dramatically in different scans were considered noise. All spectra were Hanning smoothed by varying degrees to extenuate any potential maser peaks. Hanning smoothing uses a running average over a symmetrical triangular kernel with a central pixel at 1/2 flux and adjacent pixels at 1/4 flux, and is useful as smoothing small deviations while preserving overall flux. This was done to varying degrees for each spectrum, but should be implemented with more systematic criteria in the future. This process has yielded spectra for each target from the 2003, 2005, and 2016 observing sessions, as well as spectra with the combined data.

2.2 Interferometric radio techniques

2.2.1 Interferometry

Radio Interferometry is a powerful tool that can be used to increase the angular resolution of an observatory without needing to increase the size of the physical aperture. This is achieved by using multiple telescopes in tandem. For a single dish telescope, angular resolution goes as: $\theta \propto \lambda/D$, where θ is angular resolution, λ is wavelength, and D is the diameter of the dish. When using more than one telescope, this value D becomes B, the longest baseline, or greatest distance between elements. This means that a massive virtual dish can be created at a fraction of the cost of a single dish telescope of that size.

Similar to the single-dish telescope, an array telescope using more than one antenna collects the radiation and creates a digital signal. Unlike single dish observations however, the different telescope signals are then used to generate interference patterns using the correlators. As each wavefront is added, an image becomes more clear and the interference pattern is lost. The data are received as a Fourier transform of the sky brightness distribution or 'complex visibilities' and make up the uv plane[5]. The uv plane is mapped as a Fourier transform of a two-dimensional plane perpendicular to the direction of the antenna.

It is important that the information is Fourier transformed as the spatial information received by the telescope is encoded in the cross-correlation of the Fourier-transformed response of each antenna[6]. While there are several extra steps that need to be taken in order to get an image, as opposed to single dish radio or optical telescope, the methods of radio interferometry have revealed tremendously detailed structures of distant objects with spatial resolutions impossible with single-dish telescopes. Angular resolutions of sub-milliarcsecond precision have been achieved at L-band ($1 - 2$ GHz) frequencies using satellite-based radio interferometry (see Middelberg & Bach, 2008). Advances in space-based interferometry will continue to achieve even higher resolutions and revealing

[5]This is not to be confused with the Ultra-Violet (UV) wavelength regime.
[6]For more details on radio interferometry see Thompson, Moran & Swenson (2001)

Figure 2.4: A satellite image of the Australia Telescope Compact Array (along horizontal line). Within the image, the array's five movable dishes lie near the centre of the Culgoora radio-heliograph, which traces the large circle, with the sixth dish stationary at the far left of the figure.

the cosmos in even more detail.

2.2.2 The Australia Telescope Compact Array

The Australia Telescope Compact Array or ATCA (Fig 2.4) is a radio interferometer located in Narrabri, Australia. It is composed of six identical 22m dishes (Fig. 2.5), five of which can be moved on tracks, with the sixth dish located 6km from the beginning of the track. This maximum separation of 6km allows for the creation of a simulated dish 6km wide, with an angular resolution or "synthesized beam" of $7''$ at 1612 MHz. This excellent angular resolution coupled with the $28'$ FWHM primary beam, set by the aperture of the individual dishes, has allowed observations to target multiple isolated maser candidates within the same field.

The array configuration used for the observations in this work was the 6km setup[7]. Longer baselines are more desirable for compact source observations as they

[7]This excludes the observation of MSX LMC 815 and one of the observations of IRAS 04516−6902,

Figure 2.5: One of the six Australia Telescope Compact Array dishes

improve angular resolution. This improved angular resolution allows us to differentiate unresolved sources. The correlator used for the observations was the 2-GHz Compact Array Broadband Backend (CABB) correlator. It allows for 2048 1-MHz channels that, when combined with the sensitivity of the 6km setup, make the ATCA an excellent instrument for observing compact narrow line-width sources like OH masers. The CABB correlator allows for the use of up to 16 'zoom-bands' which provide a narrower spectral range within each frequency band, allowing for much finer sampling. The correlator thus allows for multiple spectral lines to be observed at once, allowing for multi-purpose observations over a wide spectrum. This makes it possible to observe all ground-state OH transitions and 1420-MHz H I simultaneously, allowing the ATCA to probe a range of astronomical phenomena, in a single observation.

which used the 1.5C array configuration. This configuration uses dishes located closer to the centre, with a maximum baseline of 4.5 km

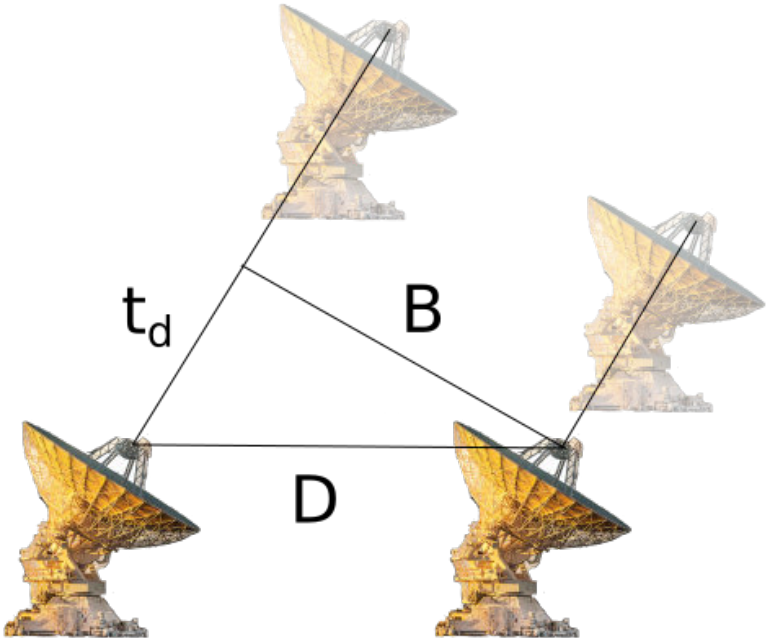

Figure 2.6: The delay of a two element interferometer with distance (D), effective baseline (B) and time delay (t_d).

2.2.3 Observational techniques

Delay calibration With a multi-element instrument, the relative distances between an element and the source will be (ever so slightly) of different lengths. To combine the individual signals, the distance or shift in frequency must be uniform. To correct for this, the data are delay calibrated. This step is critical as an incorrect calibration can result in useless data. Small deviations from the delay can be corrected for in post-processing, but if the delay moves correlation data outside of the bandwidth, the information is lost and the data cannot be correlated. This procedure calculates the correct time delay between the dishes that would simulate the dishes all being equidistant to the source (Fig. 2.6). This delay is much shorter (if not zero) with the source at the zenith. The calibration is done by observing a bright source ($\gtrsim$ 1 Jy) usually the radio-bright galaxy, PKS 1934−638. The delay for each dish is adjusted to maximize coherence, and the initial calibration continues.

Bandpass calibration The bandpass is the bandwidth frequency range allowed through the bandpass filter. The radio signal entering the receiver is truncated to correspond to one or more spectral windows covering the required frequency range and divided into spectral channels in the correlator. The bandpass, i.e. the phase and amplitude response as a function of frequency channel, needs to be corrected so that the response to a continuum source is as flat as possible (allowing for the spectral index). frequency. This was done using the same source as the previous calibration (PKS 1934638).

Amplitude calibration An initial calibration of the amplitude is done using the same source as the previous calibrations (also PKS 1934−638) by scaling the amplitude response of the telescope to that of a source with known flux. This then ensures an initial measure of the absolute flux of the targets.

Gain calibration The telescope gain can be affected over an observation by atmospheric effects, structural deformation, and aperture illumination (blockage of the signal to the receiver). By periodically observing a bright source with an accurate position and model (usually a point source), which is angularly close enough to the target to be seen through the same atmospheric conditions, these changes can be corrected for after the observation is complete, in the data reduction phase. This phase reference source is used to calculate gain solutions for amplitude and phase as a function of time, with typically a two minute integration every twenty minutes to ensure adequate temporal coverage.

2.2.4 Data reduction

Miriad The ATCA data described in Chapters 3 and 6 were inspected, flagged, and calibrated, using the MIRIAD package (Sault, Teuben & Wright, 1995). After loading the data, and separating it by targeted source, the visibilities were inspected within the time domain to look for large spikes in flux, using the task PGFLAG. After automatically and

then manually flagging any spikes for the target and calibrators, the visibilities were inspected in phase space and again in the time domain using the task BLFLAG. The automatic flagging routines used were a sum-threshold routine that removes bad visibility points above 7 times the median absolute deviation of the visibility point, and a 'blow away the dust' routine that removes visibility points without three 'good neighbours', using a nearest-neighbour algorithm. Any remaining outliers were then removed and the resulting visibilities were calibrated.

The first step in properly reducing the data is to do a bandpass calibration on the target using the flux/bandpass calibrator (usually PKS 1934−638). Using the task MFCAL, the flux density of the calibrator (with respect to frequency, not time, as the calibrator does not significantly change) is used to correct the shape of the baseline of the observation. The target is then gain calibrated throughout the observation with a secondary gain calibrator.

Once the target visibilities have been successfully calibrated and checked, they are transformed into three-dimensional data cubes by interpolating values for the gaps in uv coverage. Data cubes, the size of the FWHM of the primary beam, are created with a typical velocity range of 150 km $^{-1}$ and 0.1 km s^{-1} channels. Each visibility is weighted 'naturally' to minimize noise over the data cube, weighting the visibilities inversely proportional to the noise variance. The alternative is to weigh the data cube uniformly, or inversely proportional to the sampling density function. This results in an overall increase in noise as you move farther from the beam centre. This noise increases dramatically when approaching the Full Width at Half Maximum (FWHM) of the primary beam but remains a better approach for reducing data with larger scale structure as it reduces the effects of non-uniformity in the telescope response function (side-lobes). After creating the data cubes (or 'dirty maps), they are inspected using CASA. However, for successful maser detections, the sources go through an additional process of deconvolution or 'cleaning' to ensure an accurate sampling of the 'true' sky.

The Hogbom algorithm was used for the deconvolution of the radio data. The cleaning process looks for the brightest pixel outside of a specified target region. The position of each pixel is recorded within a 'clean list' and the number of pixels added to

the list is set by the number of iterations desired. The list is then used to replace each pixel response with an 'ideal' pixel response of the pixel signal convolved with a gaussian. This process removes 'sidelobes' which are the result of the incomplete uv coverage. The incomplete uv coverage is the result of gaps in the collecting area between the dishes.

In a simple two element interferometer, the received signal is an interference pattern. As more antennas are added to the interferometer, the interference pattern is slowly lost and the response becomes increasing similar to a Gaussian function at the centre of the beam. The sidelobes are a result of incomplete coverage and will affect the measured flux of any source caught within the side-lobe.

If, during an observation, the phase or delay begins to deviate significantly and the dishes need to be recalibrated, the resulting data need to be reduced separately, and thus the data reduction process will need repeating in its entirety for each re-calibration.

CASA Once the 3D data cubes are created they are viewed using CASA. For the target, as well as any other potential candidates, the map is cleaned excluding these regions and a spectrum is extracted for the target regions the size of the synthesized beam. The regions not containing the target are cleaned as a strong source that happens to fall within the field may create sidelobes, affecting the measured flux of the target. Cleaning must be done carefully to avoid over-cleaning faint targets, but if the source is so faint that any side-lobes would be below the noise level, cleaning is not necessary. Given a promising spectrum, the channel maps at the peak velocities are checked for a point source distribution. If this is the case, the spectrum is then smoothed to accentuate the shape of the maser profile, typically to a resolution between 0.4 and 1 km s^{-1}, and then further analysed. The smoothing typically uses is either median or Hanning smoothing, or both. Median smoothing takes a running median over the specified number of channels and Hanning smoothing takes a running mean across spectral channels with a triangular smoothing kernel.

Duchamp The source-finding package DUCHAMP (Whiting, 2012) was used to search for maser sources within the 28′ full width at half-maximum of each of the fields. The code uses a sum-threshold algorithm over each plane in a data cube and returns the positions of flux peaks above the set threshold. After tuning the value of the threshold to result in 10−15 peaks, a spectrum for each of the targets was extracted using CASA and any promising candidates were cross-referenced with AGB catalogues (e.g. Boyer et al., 2011; Riebel et al., 2012, 2015) and the SIMBAD database.

2.3 Mid-infrared spectroscopic techniques

Within this work, mid-IR spectroscopy has been used to investigate one of the largest dust producers in the LMC, the red supergiant: IRAS 05280−6910 (Chapter 7). Observing in the mid-IR comes with challenges different from those in the radio. Ground based-instruments, as opposed to space-based instruments, are easier to construct and maintain. This is why ground-based mid-IR instruments currently have more capabilities than space-based instruments. This work used spectroscopic and photometric data from the *Spitzer Space Telescope* to model the spectral energy distributions of evolved stars. While the instrument has a high sensitivity and is useful for isolated targets, it is less useful in crowded fields like the Galactic Centre. Instruments like the VISIR spectrograph at the Very Large Telescope (VLT) and *Michelle* at Gemini North can achieve higher spatial and spectral resolutions than space-based instruments as a result of their much larger-diameter instruments. However these instruments have severely limited sensitivities as a result of the high levels of thermal radiation from the sky as well as the instruments themselves.

The Earth's atmosphere is host to a significant amount of dust and a number of molecular features in both emission and absorption. Species like H_2O, O_3, CO_2, N_2O and CH_4 dominate the mid-IR spectrum creating a forest of telluric lines above 2.3 μm (Mason et al., 2008). In addition, Wien's law states:

Figure 2.7: The Very Large Telescope (Credit: ESO/José Francisco Salgado)

$$\lambda_{max} = b/T \tag{2.1}$$

where λ_{max} is the peak wavelength of a blackbody, T is the temperature (in K) and b is Wien's displacement constant ($b = 2900\,\mu$m·K). This means that a temperature of $\sim$ 27°C, a temperature commonly found on Earth, reaches its maximum intensity around 10 μm, where the flux of silicate emission from cool evolved stars peaks.

2.3.1 Very Large Telescope

The Very Large Telescope (VLT) is a telescope facility in Northern Chile run by the European Southern Observatory (ESO). The facility is located at the Paranal observatory which sits high in the Atacama Desert at 8,645 feet. The telescope is composed of four 8.2 m unit telescopes (UTs) with a suite of optical and infrared instruments (Fig. 2.7).

VISIR This work has made use of data from the VLT spectrometer and imager for the mid-infrared (VISIR) on the Melipal telescope (UT3). VISIR is capable of spectroscopy and imaging in the M-band (5 μm), the N-band (8−11 μm), and Q-band (17−20 μm). The long-slit spectroscopic mode of VISIR can also have a range of resolving powers from 150 to 30,000.

Chopping and Nodding To compensate for the atmosphere as well as changes in sensitivity of different parts of a telescope, imperfections within the primary mirror, as well as any other excess low frequency noise, mid-IR observations often use a method of chopping and nodding. Chopping is the rapid tilting of the telescopes secondary mirror off of the target by several arcseconds and is typically done several times a second. Chopping gives on- and off-source observations that can be used to remove unwanted signal that changes over time and gives a background subtracted image. Alternating the placement of the slit on the target between two positions or 'nodding', in addition to chopping, allows for the suppression of the residual background image. This creates a second set of on- and off- source observations (Fig. 2.8), that can be subtracted from each other to produce the final image.

VISIR pipeline The VISIR data that are used in Chapter 7 have been reduced using the REFLEX software (version 2.8.5) VISIR pipeline (version 4.3.1). The pipeline takes the raw spectroscopic data and executes a full spectroscopic reduction chain which includes stacking exposures, removal of optical distortions, wavelength calibration and spectrum extraction. One step not included in this pipeline is flux calibration using a telluric standard star, which must be done manually.

After stacking the chopped and nodded frames, the data are calibrated. VISIR uses curved slits to cancel the distortion of the pre-slit optics. This however adds distortions along the direction of the dispersed light. The magnitude of the optical distortion is known analytically and the VISIR pipeline corrects for each pixel by interpolating the distortion corrected pixels using the source pixels. After correcting for the optical

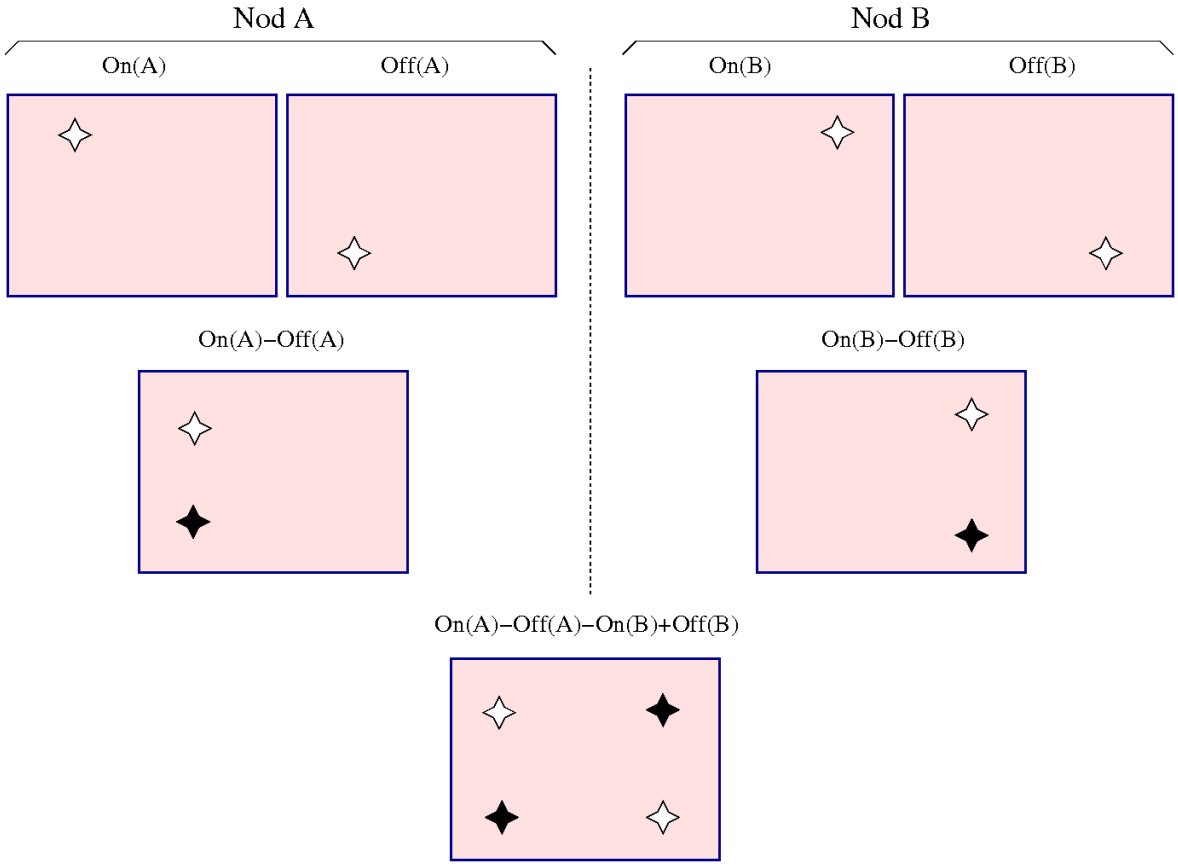

Figure 2.8: A diagram showing the results of chopping an nodding adapted from an image made by the Observatorio del Roque de los Muchachos (http://www.gtc.iac.es/instruments/canaricam)

distortion, the data are wavelength-calibrated.

Using a model based on the atmospheric emission (similar to that in Fig. 2.1) the pipeline fits the spectral signature that maximizes the cross-correlation. The model assumes a black body of 253 K and is multiplied by the emissivity of the atmosphere, Gaussian smoothed, and then multiplied by the detector quantum efficiency. This model is then fitted to the brightest spectral signature. The calibrated spectrum is then extracted using an optimal extraction method. This method takes the level of noise along the dispersion direction into account and weights the final spectrum by this value. The calculation of the standard deviation ignores pixels above 3σ, excluding them from the final extracted spectrum.

Next, the data need to be flux calibrated. This can be done by scaling the extracted spectral flux, in analogue-to-digital units (ADUs) per second, using a standard star. Using the ratio of ADUs s^{-1} from the standard star observations to a model of the known flux of the standard star in Jy, the target flux can be scaled to get the final flux in Jy.

3 LMC Maser results[8]

3.1 LMC maser sample

Circumstellar OH masers have been discovered within the Galaxy, as well as the LMC (Table 3.1). The Hamburg Database (Engels & Bunzel, 2015) has compiled thousands of OH maser detections within the Galaxy, yet few have been discovered in the LMC. Previous OH maser searches in the LMC have been completed by Wood et al. (1992), van Loon et al. (1998b), van Loon et al. (2001a) and Marshall et al. (2004) using IRAS data for selection criteria. These searches were biased against objects in molecular cloud regions which require better resolution. LMC searches of other maser types have supplemented these searches, including the SiO maser search by van Loon et al. (1996, 2001a) and the water maser searches by van Loon et al. (1998a) and Imai et al. (2013).

Following the successful selection method adopted by (Marshall et al., 2004), with the added benefit of existing mid-IR spectra obtained with the *Spitzer Space Telescope* (Buchanan et al., 2006; Kemper et al., 2010; Woods et al., 2011), the brightest oxygen-rich (silicate dust) mid-IR sources (which pump the OH maser) with the reddest optical and near-IR colours known in the LMC were selected. These have luminosities $L \gtrsim 20,000$ $L_{\odot}$. Despite the superior angular resolution of *Spitzer*, all targets are exclusively *IRAS* or MSX sources, suggesting that a few (if any) luminous OH/IR stars were missed. Indeed, none other was found in a recent search for extremely dusty luminous red supergiants in the LMC (Jones et al., 2015) based on the *Herschel Space Observatory* far-IR survey HERITAGE (Meixner et al., 2013).

Additionally, stars that pulsate with very long periods and large amplitudes were

[8]The following three chapters are based on published work entitled '*The wind speeds, dust content, and mass-loss rates of evolved AGB and RSG stars at varying metallicity*'; Goldman S. R., van Loon J. Th., Zijlstra A. A., Green J. A., Wood P. R., Nanni A., Imai H., Whitelock P. A., Matsuura M., Groenewegen M. A. T., Goméz J. F., 2017, MNRAS, **465**, 403-433.

All work was conducted by myself.

targeted, ignoring normal Mira variables which have shorter periods, thinner shells, and weaker OH emission. Typical LMC sources pulsate with periods $P \gtrsim 1000$ d and with K-band (~ 2.2 μm) amplitudes $\Delta K \geq 1.2$ mag as shown in Table 3.2. As a consequence of their thick envelope of circumstellar dust, these stars are obscured at short wavelengths and are bright in the mid-IR ($F_{25\mu m} \gtrsim 0.5$ Jy).

In order to determine how the dusty wind depends on stellar parameters, two comparison samples of OH/IR stars in the inner Milky Way were collected. These samples are described in detail in §4.3, but it suffices to highlight here some of their relevant similarities and differences. Like the LMC sample, both the Galactic Centre and Galactic bulge samples have relatively uniform and well-known distances, OH maser detections, and IR photometry. The Galactic Centre sources have more reliable pulsation periods; for the Galactic bulge sources, they have been determined for the first time in this work (§5.2). By virtue of their OH detection, these represent the most extreme OH/IR populations in those stellar samples. However, because they are dominated by relatively old, low-mass stars – and more massive stars are just too rare to yield examples of the briefest, most extreme phases of evolution – their luminosities are typically lower than those of the LMC sample, $L \sim 10,000$ $L_\odot$. The same selection bias will also have predominantly selected metal-rich stars, which are not present in the LMC.

3.1.1 Parkes observations

Targeted observations were done with the 64-m Parkes radio telescope in New South Wales, Australia. The targeted regions (along with those of the ATCA observations) are shown in Figure 3.1. The observations were done in 2003 from August 14 to 22 (Marshall et al., 2004), in 2005 (new) from July 8 to 9, and from August 13 to 22, observing the 1612-MHz OH satellite line (Project P433; PI: Jacco van Loon). The multibeam receiver used a dual polarisation setup with 8-MHz bandwidth and 8192 channels yielding 0.18 km s^{-1} channel^{-1} velocity resolution. The observations used a $12'$ primary beam and an 8-MHz bandwidth. Most observations were done in frequency-switching mode except for the 2003 observations of IRAS 04498−6842, IRAS 04509−6922, and IRAS 04553−6922,

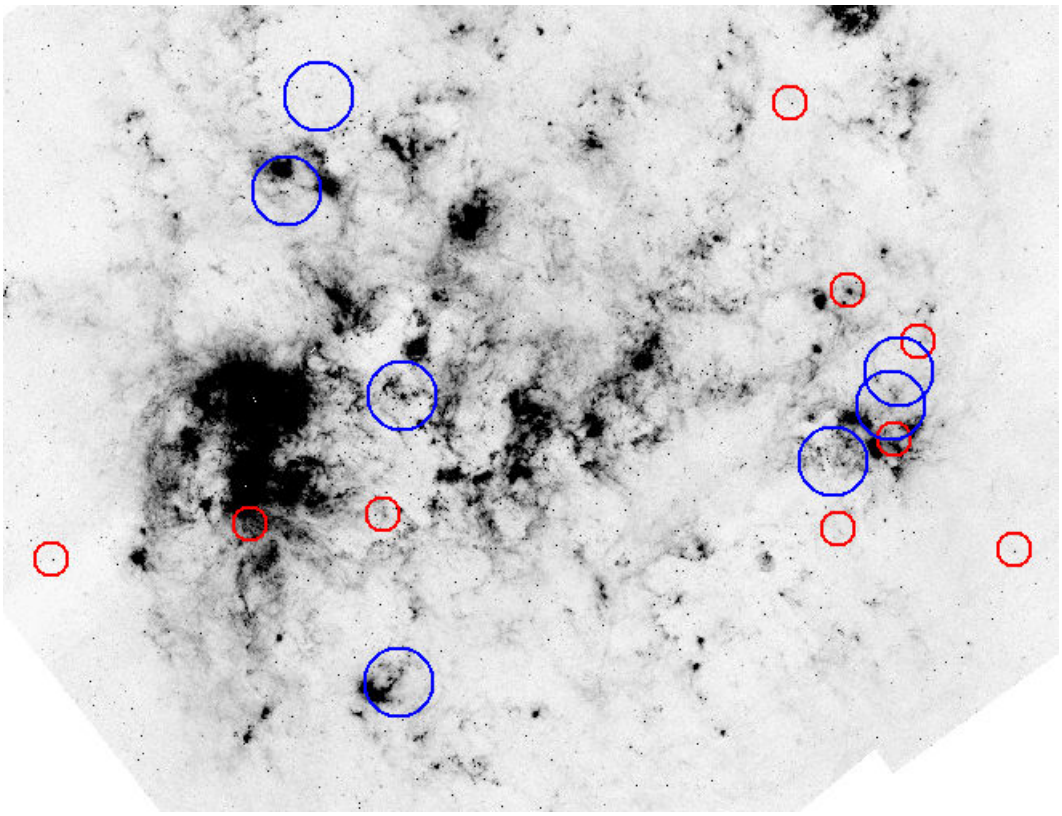

Figure 3.1: The *Spitzer* MIPS 24 μm image of the LMC (Meixner et al., 2006), overlaid with the FWHM fields at 1612-MHz of the Parkes (red) and ATCA observations (blue).

which were done in position-switching mode; integration times for observations are listed in Table 3.3. Within the table, the integrate flux was calculated using a peak width that was determined visually. For the Parkes observations the noise level was determined using the spectra and for the ATCA observations the noise level was determined using a region the size of the beam over all frequencies within the datacube.

3.1.2 The Australia Telescope Compact Array observations

The data were taken between March 6 and 8 in 2015, on June 11 in 2015, and between February 21 and 26 in 2016 (Project C2996; PI: Goldman), using the 6C, 6A, and 6B array configurations of the ATCA, respectively. Targeted integrations observing all four OH transitions (1612, 1665, 1667, and 1720 MHz) were done using the CFB 1M-0.5k

correlator configuration with zoom bands. The observations used a synthesized beam of around 7″ and a velocity range of 465 km s^{-1}. During the first two observations, the telescope was aimed directly at the primary targets (MSX LMC 807 and MSX LMC 815). The third observation used a position-switching technique to get full uv coverage of the third primary target, IRAS 04516−6902, while getting partial coverage on two secondary targets, IRAS 04509−6922 and IRAS 04498−6842. The two secondary sources could not fit within the primary beam of a single pointing, thus the need to alternate fields to observe with coverage similar to that of the shape of a Venn diagram yielding a final mosaicked image with pointings separated by $\sim 13'$ (shown later in Fig. 3.6). The fourth observation was split, observing the faint detection of IRAS 04516−6902, and the non-detection MSX LMC 815. The fifth, sixth, and seventh observations were aimed directly at the primary targets (IRAS 04553−6933, IRAS 05294−7104 and IRAS 05280−6910).

The observing programme has targeted sources with known but unclear OH maser profiles, as well as sources which are deemed good candidates. In general, highly luminous and reddened AGB and RSG sources with long pulsation periods and large pulsation amplitudes were targeted. Within the current sample, IRAS 04407−7000 and IRAS 05003−6712 only exhibit one maser peak. As these sources and their maser emission are highly variable (Harvey et al., 1974), subsequent observations are much more likely to yield a double-horned maser profile and expansion velocity.

The LMC is expected to harbour several thousand OH masing sources (Dickey et al., 2013). This much smaller observed sample likely indicates a sensitivity limit. OH masers are predicted to be excited by line overlapping of far-IR OH lines (e.g. Elitzur, Goldreich & Scoville, 1976; Bujarrabal et al., 1980). To excite OH masers, these far-IR OH lines are required to be optically thick. Therefore, only the most luminous, high mass-loss rate AGB stars and RSGs can produce OH masers detectable with current instruments; the ability to sustain these masers will also depend on metallicity (OH abundance and dust emission). The LMC AGB stars are also dominated by carbon-rich chemistry, decreasing the population of OH masing sources. OH/IR stars of low enough mass not to become carbon stars will also be less luminous, thus restricting the expected

Table 3.1: The LMC target sample, including the detections from Wood et al. (1992), van Loon et al. (1998b) and Marshall et al. (2004); J2000 positions are taken from 2MASS and ATCA observations. Also listed are the previously detected OH masers, and whether OH maser emission was detected here (no entry means that the target has not been attempted).

Object	Alternative	2MASS position (J2000)		ATCA position (J2000)		Previous	This work
name	names	RA	Dec.	RA	Dec.	OH	OH
IRAS 04407−7000	LI-LMC 4	04 40 28.5	−69 55 14			Yes[2,1]	Yes
IRAS 04498−6842	LI-LMC 60	04 49 41.5	−68 37 52	04 49 40.9	−68 37 50	Yes[1]	Yes
IRAS 04509−6922	LI-LMC 77	04 50 40.5	−69 17 32	04 50 40.3	−69 17 35	No[3]	Yes
IRAS 04516−6902	LI-LMC 92	04 51 29.0	−68 57 50	04 51 29.6	−68 57 47	No[1]	Yes
IRAS 04537−6922	WOH S 60	04 53 30.9	−69 17 50				No
IRAS 04545−7000	LI-LMC 159	04 54 10.1	−69 55 58			Yes[3]	Yes
IRAS 04553−6825	WOH G064	04 55 10.5	−68 20 30			Yes[3,1]	Yes
IRAS 04553−6933	LI-LMC 183	04 55 03.1	−69 29 13				No
IRAS 05003−6712	LI-LMC 297	05 00 19.0	−67 07 58			Yes[1]	Yes
IRAS 05280−6910	NGC 1984-IRS1	05 27 40.1	−69 08 05	05 27 41.3	−69 08 02	Yes[3]	Yes
IRAS 05294−7104	LI-LMC 1153	05 28 48.2	−71 02 29	05 28 48.9	−71 02 32	No[1]	Yes
IRAS 05298−6957	LI-LMC 1164	05 29 24.6	−69 55 14			Yes[3]	
IRAS 05329−6708	LI-LMC 1286	05 32 52.3	−67 06 26			*Yes[3]	No
IRAS 05346−6949	LI-LMC 1341	05 34 14.3	−69 47 20				No
IRAS 05402−6956	LI-LMC 1506	05 39 44.8	−69 55 18			Yes[3]	
IRAS 05558−7000	LI-LMC 1790	05 55 21.0	−70 00 03			Yes[1]	Yes
MSX LMC 807	LI-LMC 1280	05 32 37.2	−67 06 56	05 32 37.3	−67 06 57		Yes
MSX LMC 811		05 32 51.3	−67 06 52	05 32 51.3	−67 06 52	Yes[3]	Yes
MSX LMC 815		05 35 14.1	−67 43 56				No
MSX LMC 1207	LI-LMC 182	04 55 06.5	−69 17 09				No

References: [1]Marshall et al. (2004) [2]van Loon et al. (1998b) [3]Wood et al. (1992)

* Original detection was not from IRAS 05329−6708 but unresolved emission from MSX LMC 807 and MSX LMC 811.

Table 3.2: The LMC sample with bolometric magnitudes $M_{\rm bol}$, pulsation periods P, K-band peak-to-peak pulsation amplitudes ΔK, mean K-band magnitudes and $J-K$ colours from Whitelock et al. (2003). *Spitzer* 8.0-μm (F_8) and 24-μm (F_{24}) flux densities are from the SAGE project (Meixner et al., 2006), which use IRAC (Fazio et al., 2004) and MIPS (Rieke et al., 2004), respectively, on board the *Spitzer Space Telescope* (Werner et al., 2004). Spectral types are from van Loon, Marshall & Zijlstra (2005), except where noted otherwise; a distance to the LMC of 50 kpc is adopted (Feast, 2013).

Object name	$M_{\rm bol}$ (mag)	P (d)	ΔK (mag)	K (mag)	F_8 (Jy)	F_{24} (Jy)	$J-K$	Spectral type
IRAS 04407−7000	−7.11	1264[e]	1.23	8.79	0.51	0.68	2.34	M7.5
IRAS 04498−6842	−7.72	1292	1.30	8.08	0.78	0.69	1.86	M10
IRAS 04509−6922	−7.28	1292	1.45	8.59	0.37	0.86[h]	2.21	M10[k]
IRAS 04516−6902	−7.11	1165[e]	1.41	8.72	0.30	0.55[h]	2.32	M9[k]
IRAS 04537−6922				8.06[b]	0.04	1.30	1.27[b]	M3[c]
IRAS 04545−7000	−6.56	1216	1.57	10.13	0.17	0.38	5.70[n]	
IRAS 04553−6825	−9.19[j]	841	0.34	7.09	5.30	13.53[h]	2.60[h]	M7.5
IRAS 05003−6712	−6.20	942[e]	1.59	9.95	0.14	0.19	2.95	M9
IRAS 05280−6910	−7.75[n]			12.87[m]	1.03	24.18[l]		
IRAS 05294−7104	−6.79	1079	1.20	9.21	0.23	0.25	2.97	M8
IRAS 05298−6957	−6.72[n]	1280[n]	2.00[n]	10.29[n]	0.59	1.05	3.54[n]	
IRAS 05402−6956	−6.77	1393	1.80	10.40	0.62	1.00	4.46[n]	
IRAS 05558−7000	−6.97	1220	1.42	9.25	0.33	0.49	3.27	
MSX LMC 807	−6.08[d]			11.93[a]	0.33	0.45		
MSX LMC 811	−6.71[d]			11.12[b]	0.76	1.25	5.2[g]	
MSX LMC 815	−8.00[d]	590[f]		8.14[a]	0.19	0.20[i]	1.36[a]	M4
MSX LMC 1207				11.50	0.12		2.87	

References: [a]Buchanan et al. (2006) [b]Cutri et al. (2003) [c]Humphreys (1978) [d]Jones et al. (2012) [e]Kim et al. (2014) [f]Pierce, Jurcevic & Crabtree (2000) [g]Sloan et al. (2008) [h]Trams et al. (1999) [i]van Aarle et al. (2011) [j]van Loon et al. (1999) [k]van Loon et al. (1998b) [l]van Loon et al. (2001a) [m]van Loon, Marshall & Zijlstra (2005) [n]Wood et al. (1992)

detectable sample to the much rarer massive AGB stars ($\gtrsim 4M_{\odot}$). In order to further understand the mass-loss mechanism and the effects of varying metallicity and luminosity, sources need to continued to be discovered in the LMC, and more information about the current sample is needed. The fact that observations have resulted in additional serendipitous discoveries means that more OH masers must be awaiting detection at the current sensitivity limits.

3.1.3 Parkes and ATCA combined H I Maps

In addition to the Parkes and ATCA observations, 1420-MHz H I data has been included from the Staveley-Smith et al. (2003) combined ATCA and Parkes multibeam H I maps. Peaks in the H I spectra indicate the likely systemic velocities of the LMC sources. While some of the sources lie outside these H I regions, they provide supporting evidence for sources which lie in higher density regions of the LMC. For each source in the LMC sample, a spectrum was extracted using a $1'$ region centred on the sources. The resulting spectra have been plotted below the maser spectra in §3.3 to indicate the likely systemic velocity.

3.2 LMC maser results

Four new 1612-MHz circumstellar OH masers have been detected in the LMC (IRAS 04509−6922, IRAS 04516−6902, IRAS 05294−7104, and MSX LMC 807) and wind speeds have been obtained for six others. Thirteen targets have been successfully observed with three discoveries, one serendipitous discovery, and two non-detections; Galactic maser sources (shown in Appendix B) were used to check the pointing. The velocities at the peaks of the maser profile have been used to measure the expansion velocity of these sources with an uncertainty of around 1 km s^{-1}. Additionally observations have successfully observed one target in the 1665-MHz maser transition, IRAS 05280−6910. Before conducting this survey, only five of the known LMC maser profiles were reliable.

For each target, the spectrum for a beam-sized region was extracted using CASA. As systemic velocity information and multiepoch observations exist, significance levels for each peak in the detection would undervalue the significance of the detections, and as a result, have not been included. However each detection has at least one 4σ level peak within the spectra.

Table 3.3: Results of recent maser searches in the LMC.

Object name	$v_{\rm exp}$ (km s^{-1})	Parkes (P) or ATCA (A) epoch	Integration time (h)	Velocity at peaks (km s^{-1})		$F_{\rm int}$ (mJy km s^{-1})		σ (mJy)
				Blue	Red	Blue	Red	
IRAS 04407−7000	8.35	P 2003	8.6	222.8	239.5, 237	9.6	35.5	5.9
		P 2005	1.7		240, 237		89.8	8.8
		Combined	10.2	223?	240, 237		105.8	4.8
IRAS 04498−6842	13.0	P 2003	13.8	246.3		22.9		8.2
		A 2015	4.6	246.3	272.3	8.2	44.5	10.6
		Combined	18.4	246.3	272.3	67.3	6.4	6.3
IRAS 04509−6922	11.4	P 2003	5.0	254.2	274.7	5.1	3.4	10.1
		P 2005	22.7	255.9	278.6	53.3	44.2	3.9
		A 2015	4.1	256		101.5		26.7
		Combined	31.8	255	278.6	75.2	52.1	3.7
IRAS 04516−6902	10.0	P 2003	8.5		287.3		16.0	7.0
		A 2015	12.6		287.3		30.6	3.8
		Combined	21.1	267.1	287.1	13.3	30.4	3.4
IRAS 04537−6922	?	A 2016	10.8					3.7
IRAS 04545−7000	7.7	P 1992	1	258.7	274			6.1
		P 2005	4.5	258.7	274	191.5	37.6	6.1
		Combined	4.5	258.7	274	191.5	37.6	6.1
IRAS 04553−6825	23.8	P 2003	0.8	253.4, 263	281, 300.9	1709, 414	11.7, 8.2	12.7
		P 2005	0.6	253.4, 263	281, 300.9	1346, 289	74.1, 52.6	14.0
		Combined	1.4	253.4, 263	281, 300.9	1417, 272.6	32.3, 21.9	9.8
IRAS 04553−6933	?	A 2016	10.8					3.6
IRAS 05003−6712	?	P 2003	7.2	287?	269.5	87.1		6.7
		P 2005	3.4		269.5	40.5		5.8
		Combined	10.6	243	269.5	65.8		4.2
IRAS 05280−6910	20.6	P 1992	1	255	289	419	398	17

continued ...

. . . continued

Object name	$v_{\rm exp}$ (km s^{-1})	Parkes (P) or ATCA (A) epoch	Integration time (h)	Velocity at peaks (km s^{-1})		$F_{\rm int}$ (mJy km s^{-1})		σ (mJy)
				Blue	Red	Blue	Red	
		A 2016	5.7	258.1	292.6	131.1	147.3	11.5
IRAS 05294−7104	10.3	A 2016	9.8	269.7	290.3	9.6	34.2	5.5
IRAS 05298−6957	10.5	P 1992	1	271	292	519	448	17
IRAS 05346−6949	?	P 2016	1.8					28.3
IRAS 05402−6956	10.5	P 1992	1	263	284	334	181	17
IRAS 05558−7000	8	P 2003	7.7	265	281.5	18.5	11.7	5.7
		P 2005	3.4	265	281.5	68.7	52.5	5.9
		Combined	11.2	265	281.5	70.1	51.0	4.1
MSX LMC 807	8.15	A 2015	9.3	306.4	322.7	19.8	12.1	4.6
MSX LMC 811	8.25	A 2015	9.5	302.4	318.9	151	188	4.3
MSX LMC 815	?	A 2015	14.1					4.5
MSX LMC 1207	?	A 2016	10.8					3.8

This survey has resulted in 13 reliable maser profiles, more than doubling the previous LMC sample. Each will be described in turn in the following subsections. No emission was detected from any source at 1667 or 1720 MHz.

3.3 Individual maser sources

IRAS 04407−7000 The OH maser emission from the dusty AGB star: IRAS 04407−7000 was initially detected with the ATCA (van Loon et al., 1998b). The initial detection showed a single peak at 240 km s^{-1}; now presented are subsequent observations with Parkes (Fig. 3.2). There is a degree of variability between the 2003 and 2005 observations. With the first observation, two peaks at around 237 and 240 km s^{-1} can be seen. With a peak separation of 3 km s^{-1}, it is unlikely a measure of the full expansion velocity, rather substructure within the circumstellar envelope. The spectrum also shows a much smaller peak at 223 km s^{-1} in the 2003 observation. For the much shorter 2005 observation, there are two peaks at 237 and 240 km s^{-1}, flanked by two smaller tentative peaks at 214 and 261 km s^{-1} but an overall increase in noise. When the spectra are combined and weighted by the noise, the dominant profile is that of the 2003 observation. Using a cross-spectrum fitting technique (described in §3.4), the UVES spectrum of IRAS 04407−7000 from the ESO reduced spectra data archive was fitted to that of IRAS 04498−6842 using molecular bandheads around 8440 Å. A systemic velocity of 260 km s^{-1} has been used for IRAS 04498−6842, assumed from its maser profile. From the phase shift, the systemic velocity calculated for IRAS 04407−7000 is 231.6 km s^{-1} (denoted by V_{UVES}), confirming the smaller blue maser peak at 223 km s^{-1} and the maser profiles of both sources (§3.4).

IRAS 04498−6842 IRAS 04498−6842 was observed in 2003 with a clear peak at 246 km s^{-1} (Fig. 3.3). The new observation with the ATCA has confirmed the peak at 246 km s^{-1} and revealed a red counterpart at 272 km s^{-1}. The Parkes multibeam H I data of the target peak around 260 km s^{-1}. As it is expected that the H I comes from the LMC

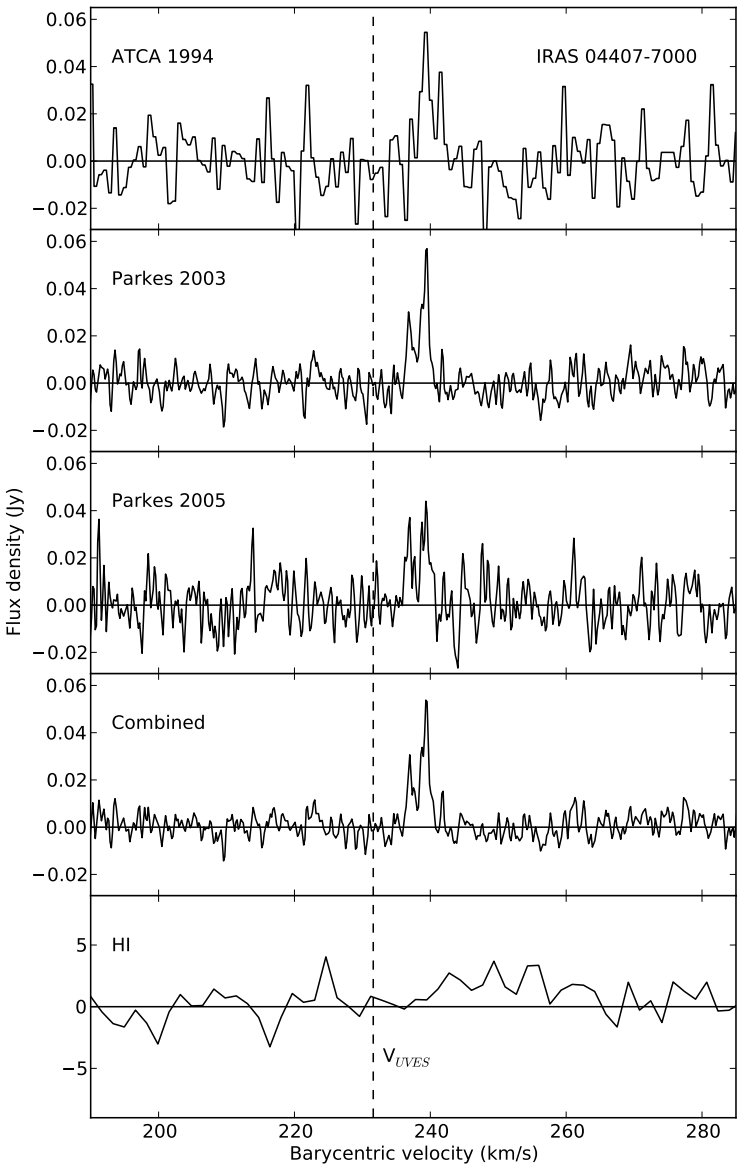

Figure 3.2: OH 1612-MHz maser emission from IRAS 04407−7000 with the velocity derived from cross-spectrum fitting of UVES spectra denoted by V_{UVES}.

disc, and the source is likely to have a similar stellar velocity, this provides evidence for the detection. Additionally, the systemic velocity derived from this source's maser profile (the centre of two maser peaks) has been used as a reference to fit both IRAS 04407−7000 and IRAS 04516−6902, and the velocities of all three maser profiles are consistent with the maser results. IRAS 04498−6842 is one of the more extreme stars within the sample (possibly an RSG, or super-AGB star), with an M10 spectral type (van Loon, Marshall & Zijlstra, 2005) and high luminosity. Thus, it is not surprising that the maser profile yields a high expansion velocity of 13 km s^{-1}.

IRAS 04509−6922 IRAS 04509−6922 is a new detection, with a clear double-peaked profile centred around 268 km s^{-1} (Fig. 3.4). The profile expansion velocity of 11.5 km s^{-1} is also high within the sample but expected, given its low temperature and high luminosity. There is a peak around 255 km s^{-1} over all three observations, but the red component is clear only in the much longer integration in the 2005 observation. The peak in H I at around 260 km s^{-1} supports the detection.

IRAS 04516−6902 IRAS 04516−6902 was observed in 2003, with no clear maser emission. Given the new ATCA data (Fig. 3.5), it seems that the small peak at around 285 km s^{-1} in the Parkes observation is in fact a maser component. There is a much fainter peak in the combined data around 267 km s^{-1}, yielding an expansion velocity of 10 km s^{-1}. Using the same cross-spectrum fitting technique as was adopted for IRAS 04407−7000, a systemic velocity of 278.8 km s^{-1} has been calculated. This velocity lies directly between the two maser peaks, confirming the maser profile. This observation was done using a position switching strategy targeting the two fields shown in Figure 3.6.

IRAS 04545−7000 The maser profile of IRAS 04545−7000 does not seem to vary drastically over the two epochs (Fig. 3.7). The detection has a clear blue-asymmetry, a phenomenon described in Marshall et al. (2004), which has been suggested as a consequence of the contribution of amplified stellar light. While IRAS 04545−7000 is not

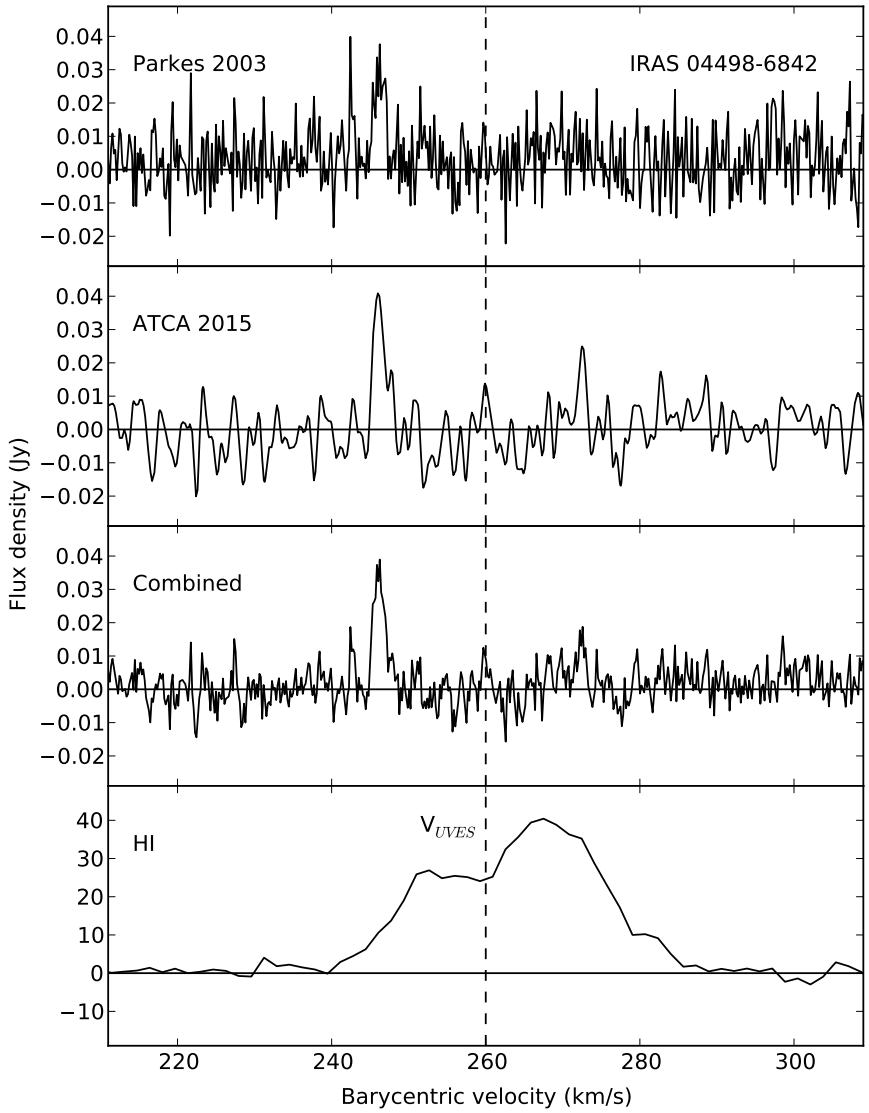

Figure 3.3: OH 1612-MHz maser emission from IRAS 04498−6842 with the velocity used as a model for the cross-spectrum fitting of UVES spectra denoted by V_{UVES}.

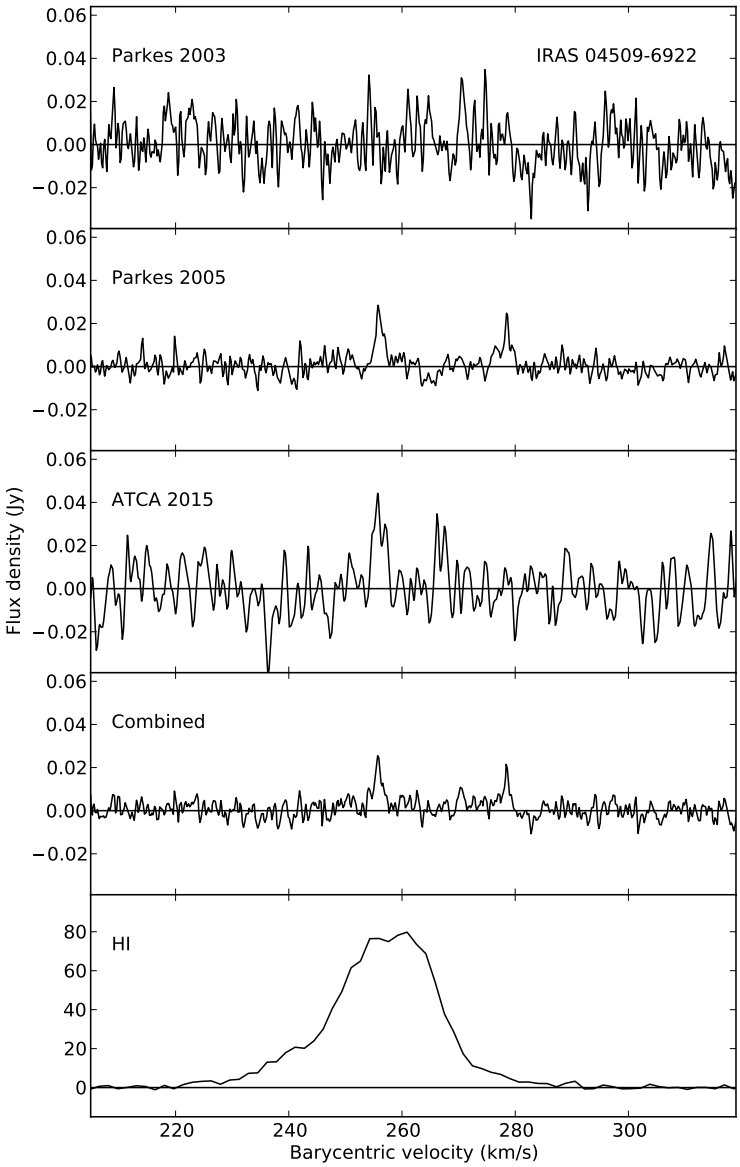

Figure 3.4: OH 1612-MHz maser emission from IRAS 04509−6922.

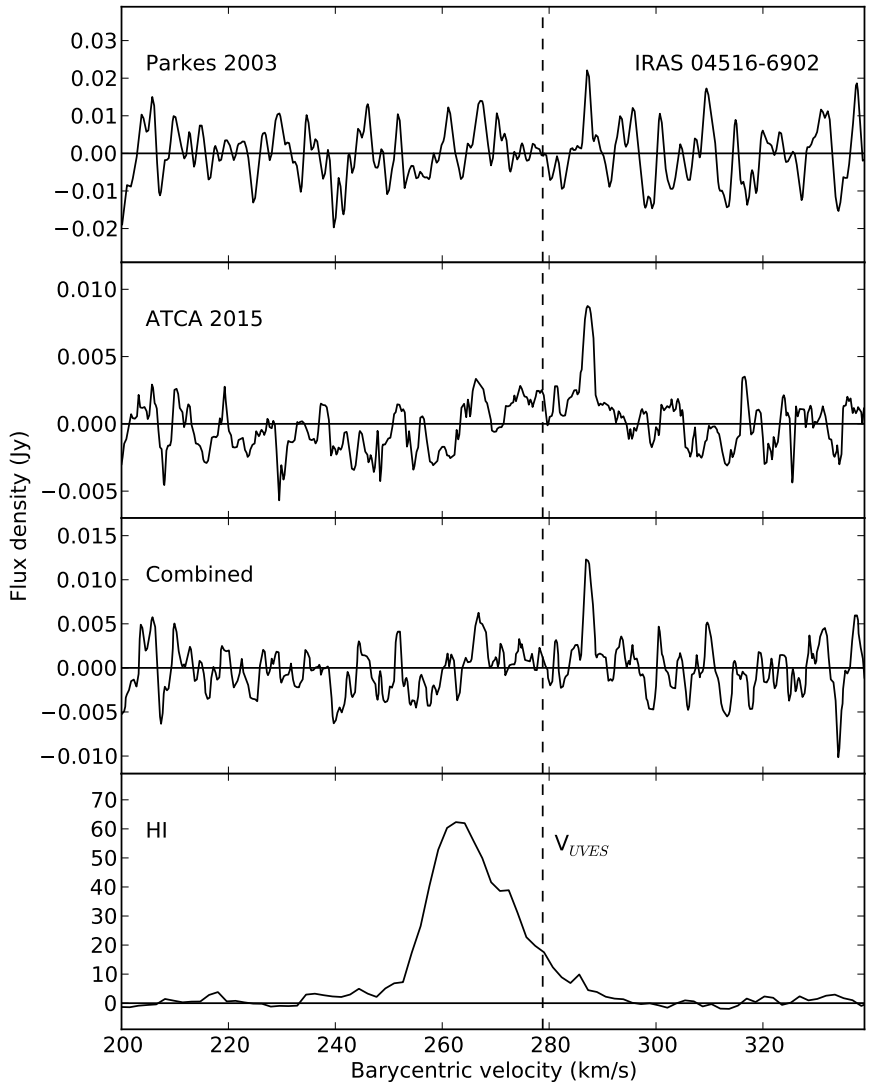

Figure 3.5: OH 1612-MHz maser emission from IRAS 04516−6902 with the velocity derived from cross-spectrum fitting of UVES spectra denoted by V_{UVES}.

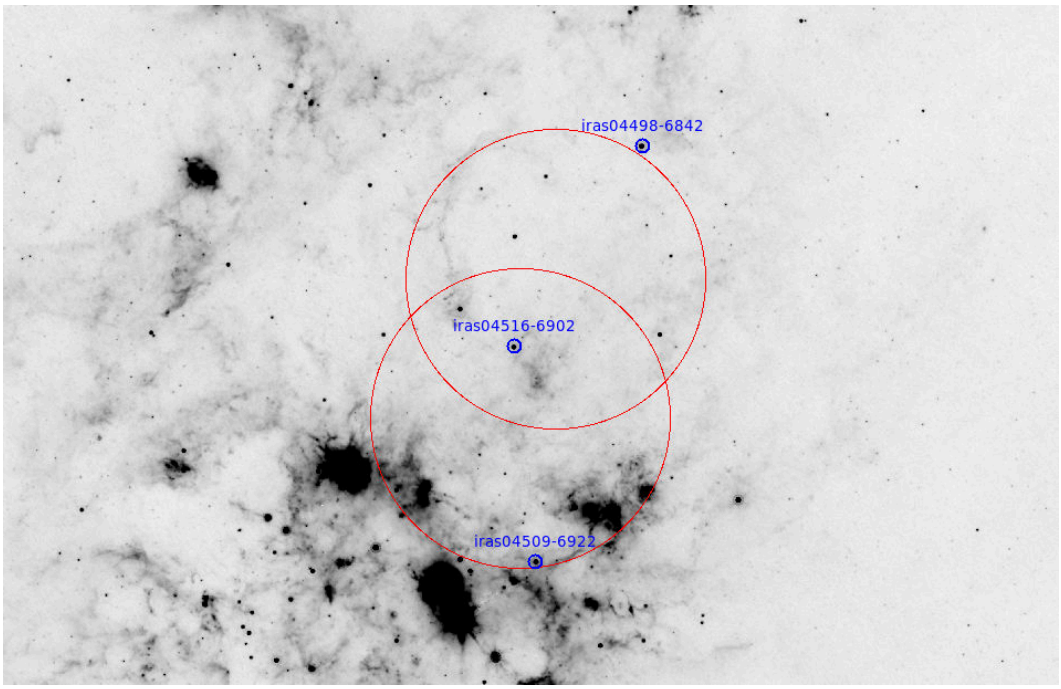

Figure 3.6: A *Spitzer* MIPS 24 μm image of the LMC with the ATCA fields used to target IRAS 04516−6902, IRAS 04498−6842, and IRAS 04509−6922 within the same observation.

a very luminous source, it is one of the most highly reddened sources in the LMC sample with a $(J-K)$ colour of 5.7 mag.

Red supergiant IRAS 04553−6825 IRAS 04553−6825 has shown the most prominent OH maser emission in the LMC with a peak over 600 mJy around 253 km s^{-1} (Fig. 3.8). This RSG is one of the largest known stars, with an estimated radius of 1540 R$_\odot$ (Levesque et al., 2009). This object has been studied in depth, and has been observed in OH (Wood, Bessell & Whiteoak, 1986; Marshall et al., 2004), H_2O (van Loon et al., 1998a), and SiO (van Loon et al., 1996). In addition to its peak at 253 km s^{-1} there are three additional peaks at 262, 281, and 300 km s^{-1}. Given the systematic velocity of 278 km s^{-1} taken from the SiO maser detection, it is likely that the maser profile extends from its prominent blue peak at 253 km s^{-1} to its smallest peak at 300 km s^{-1}. The existence of the two interior peaks has been suggested by Marshall et al. (2004) to be indicative of a second expanding dust shell, flowing primarily in a direction across the

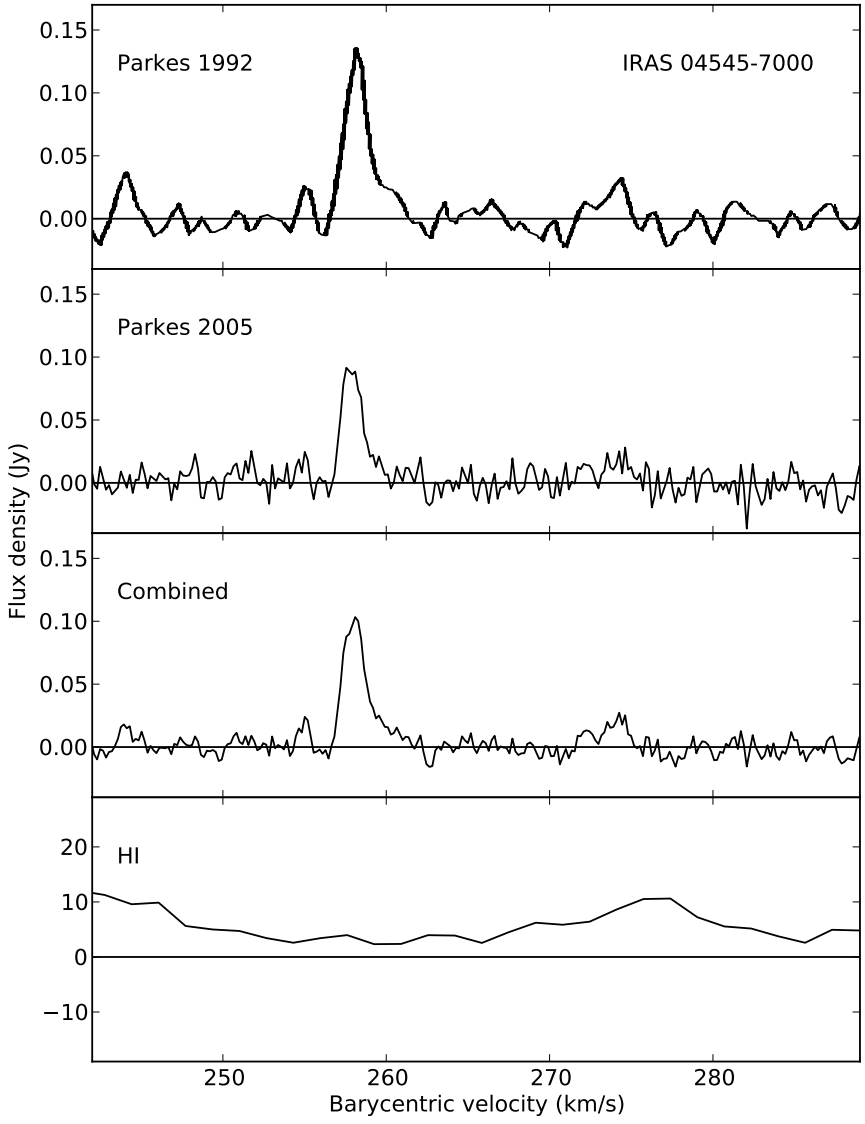

Figure 3.7: OH 1612-MHz maser emission from IRAS 04545−7000.

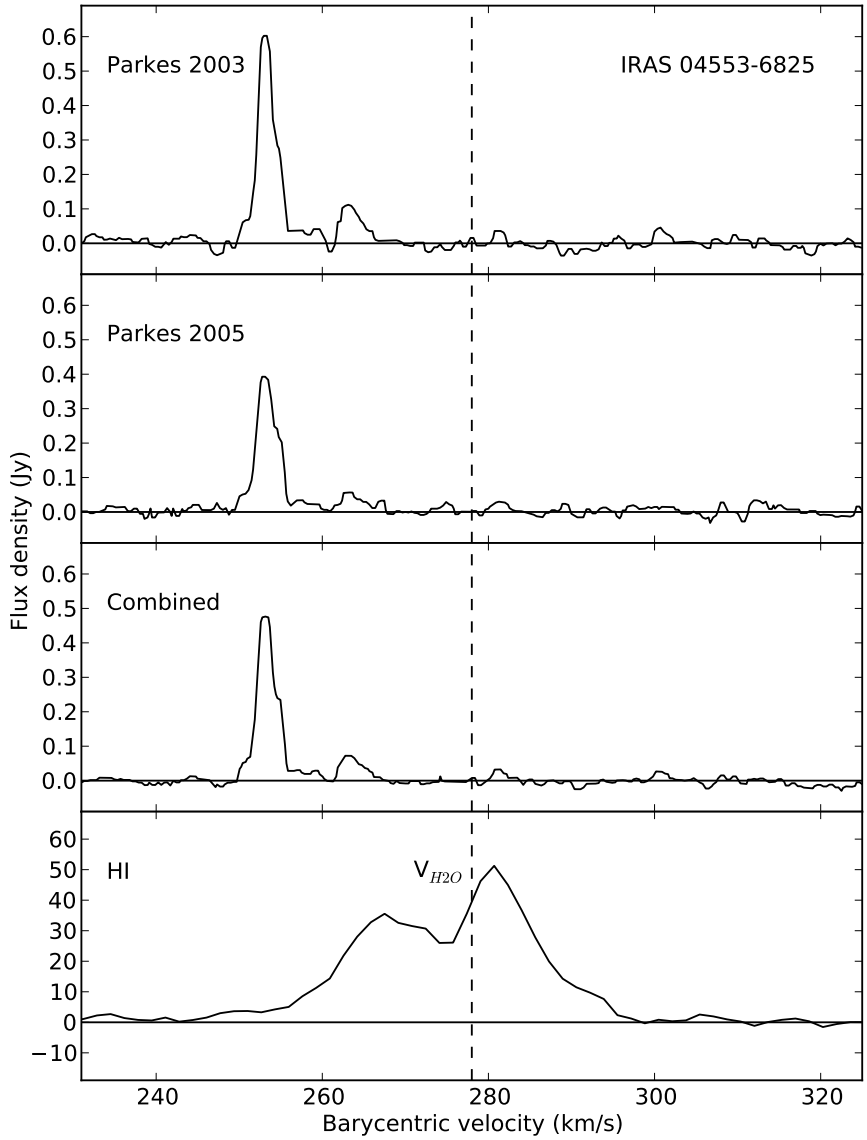

Figure 3.8: OH 1612-MHz maser emission from IRAS 04553−6825 with the H_2O maser velocity from van Loon et al. (2001a) denoted by V_{H2O}.

sky.

IRAS 05003−6712 IRAS 05003−6712 is the least luminous source of the LMC sample (Fig. 3.9). There is a clear peak at 269 km s^{-1} in both epochs, but the second peak is unclear. The source fits all other criteria expected of an OH/IR star, but the

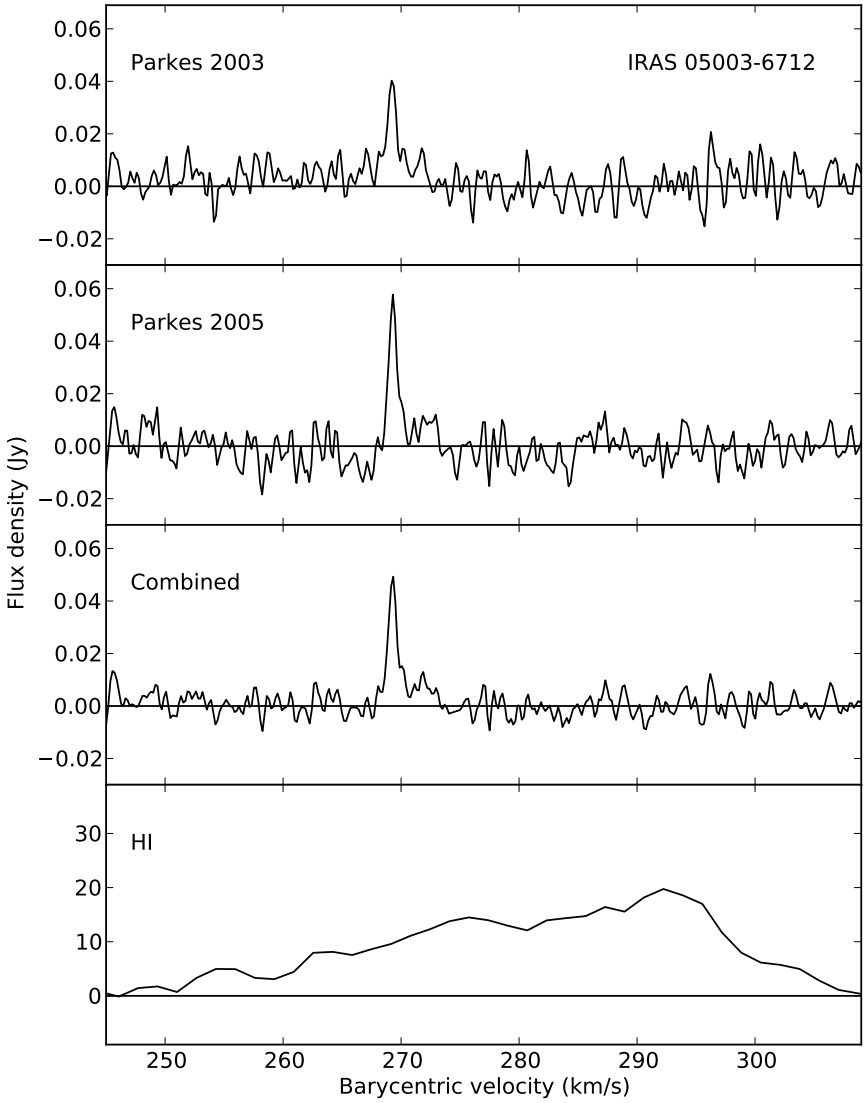

Figure 3.9: OH 1612-MHz maser emission from IRAS 05003−6712.

secondary peak may be below the detection limit of past observations. From SED modelling (explained in Chapter 4), an expansion velocity around 10 km s^{-1} (assuming a metallicity of half solar) is expected. The skewed shape of the peak at 269 km s^{-1} suggests a missing redshifted peak. Nevertheless, the maser profile remains unclear.

Red supergiant IRAS 05280−6910 The maser emission of the RSG: IRAS 05280−6910 was originally observed at 1612 and 1665 MHz with Parkes in 1992 (Wood et al., 1992). The source has since been observed using the ATCA, which has revealed five maser peaks at 1612 MHz and some interesting structure at 1665 MHz (Fig. 3.10). The IR source was originally misidentified as the cluster NGC 1984. High-resolution near- and mid-IR imaging has successfully identified the stellar counterpart (van Loon, Marshall & Zijlstra, 2005). IRAS 05280−6910 is highly obscured and extremely bright in the mid-IR but shows little variability. This source has also shown 22-GHz H_2O maser emission (van Loon et al., 2001b). The lack of symmetry within these maser spectra as well as variability of not only the flux but also of the location of maser components remains puzzling. It is expected that the mainline 1665-MHz detection probes the inner shell of OH and thus lie within the 1612-MHz maser profile. This source will be discussed further in §4.5 and §7.

IRAS 05294−7104 IRAS 05294−7104 was not initially detected during the 2003 observation but has been detected in the more recent longer ATCA observation (Fig. 3.11). It is highly reddened with a $(J - K)$ colour of 2.97 mag, with a long pulsation period lasting 1079 d, and an expansion velocity of 10.3 km s^{-1}. It seems that the initial observation lacked the signal-to-noise ratio required for detection.

IRAS 05298−6957 IRAS 05298−6957 resides in a cluster and thus has a cluster metallicity of 0.4 solar metallicity. This source pulsates with a ΔK of 2 mag, and has an initial mass of 4 $M_\odot$ (van Loon et al., 2001b). The source has a clear double-peaked profile yielding an expansion velocity of 10.5 km s^{-1} (Wood et al., 1992). IRAS 05298−6957 has shown silicate in absorption yet lies in a region of the LMC sample colour–magnitude diagram which is dominated by carbon-rich chemistry (Sargent, Srinivasan & Meixner, 2011). This is a well-known but often ignored issue, which is seen in a number of OH/IR sources (c.f. Zijlstra et al., 1996; van Loon et al., 1997; Trams et al., 1999).

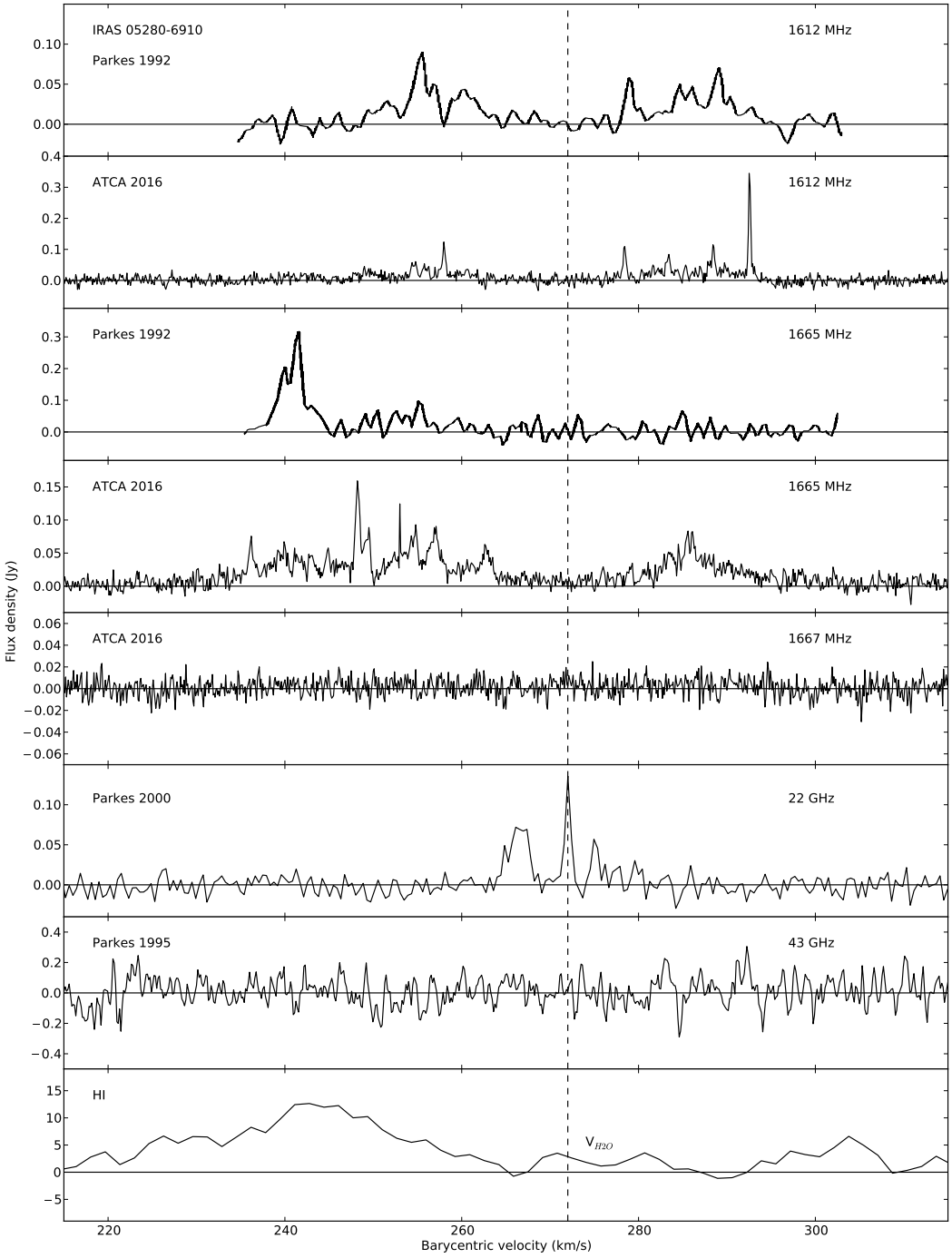

Figure 3.10: OH 1612- and 1665-MHz maser emission from IRAS 05280−6910 with the SiO and H_2O maser detections from van Loon et al. (2001a); the water maser velocity has been plotted and denoted by V_{H2O}.

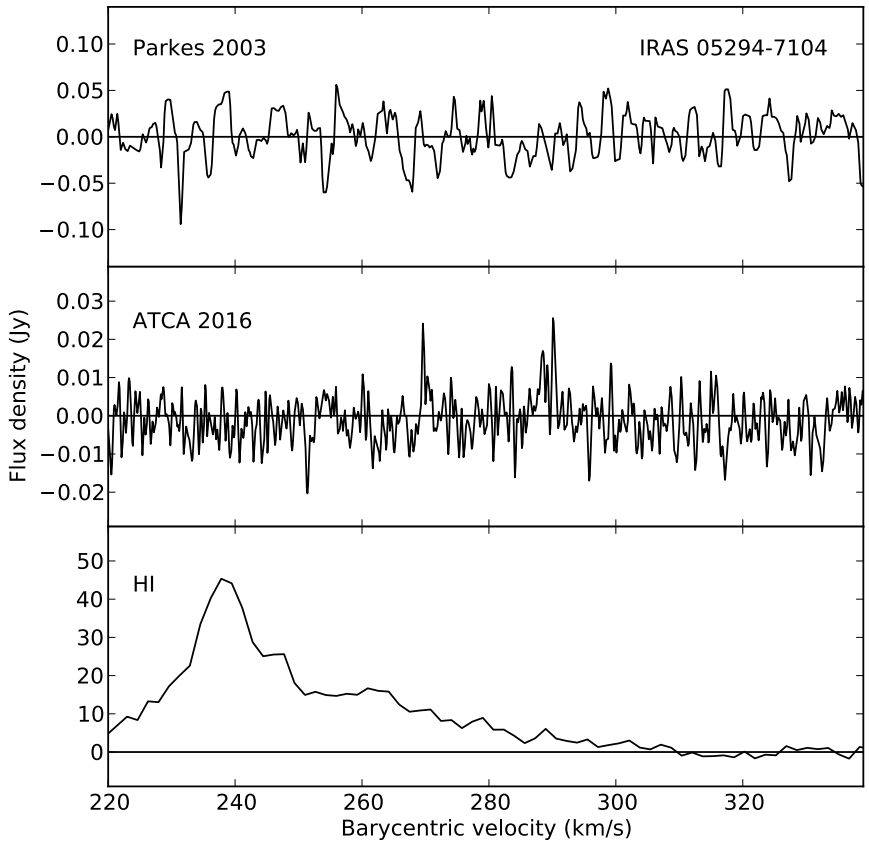

Figure 3.11: OH 1612-MHz maser emission from IRAS 05294−7104.

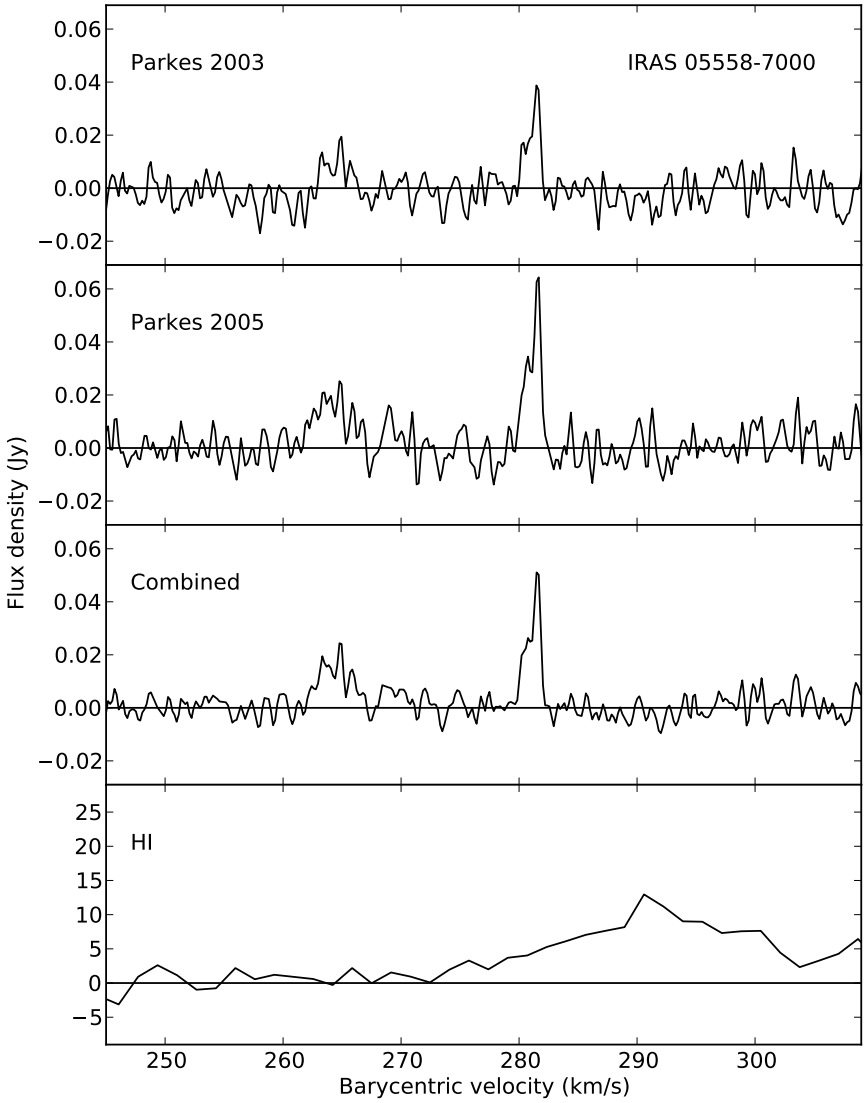

Figure 3.12: OH 1612-MHz maser emission from IRAS 05558−7000.

IRAS 05402−6956 OH maser emission from IRAS 05402−6956 was detected with Parkes in 1992 (Wood et al., 1992), and is known to be within 3′ of an H II region. The expansion velocity from the original observation was 10.5 km s^{-1}, but, as the emission was detected with a low signal-to-noise ratio, it is unclear whether the profile includes the outermost peaks.

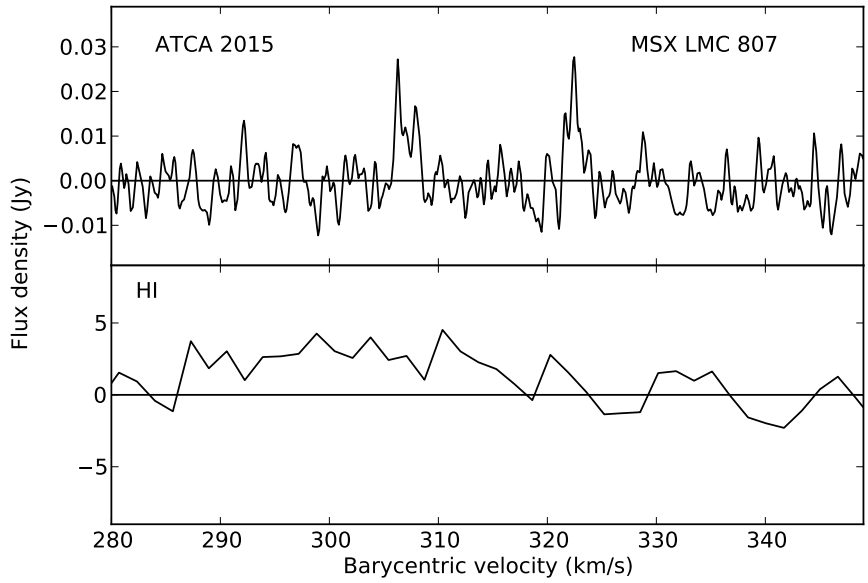

Figure 3.13: OH 1612-MHz maser emission from MSX LMC 807.

IRAS 05558−7000 IRAS 05558−7000 lies at the edge of the LMC. The source has two clear peaks at 265 and 281 km s^{-1}, in both epochs of observation, yielding an expansion velocity of 8 km s^{-1} (Fig. 3.12).

MSX LMC 807 MSX LMC 807 is a dusty O-AGB star with a $(J - K)$ colour of 3.7 mag and $M_{\rm bol} = -6.6$ (Whitelock et al., 2003). This star has shown 10 μm silicate emission (Buchanan et al., 2006) but a low IR luminosity comparable to many C-AGB stars in the LMC (Buchanan et al., 2006). This is one of the new OH maser detections from the recent ATCA observations. A clear double-peaked profile can be seen within the spectrum, which yields an expansion velocity of 8 km s^{-1} (Fig. 3.13).

MSX LMC 811 (IRAS 05329−6708) MSX LMC 811 has been found to be the true counterpart of the maser emission thought to originate from IRAS 05329−6708. While IRAS 05329−6708, MSX LMC 807, and MSX LMC 811 were previously resolved in the IR, the original Parkes observation of IRAS 05329−6708 did not have the resolution to

resolve IRAS 05329−6708 into MSX LMC 807 and MSX LMC 811. Thus the observation yielded partial emission from both MSX LMC 807 and MSX LMC 811 (Fig. 3.14). This can be seen in the four peaks found in the 1992 observation, which show the two similar wind speeds with different systemic velocities. As the *MSX* survey resolved IR sources, this survey has now done the same with the OH maser emission. The star is extremely red with a $(J - K)$ colour of 5.2 mag; the expansion velocity of 8.5 km s^{-1} is also reasonable for the source.

MSX LMC 815 MSX LMC 815 is an M4 O-AGB star with a K-band magnitude of 8.14 and has shown a number of spurious spikes at 1612 MHz but no clear maser profile (Fig. 3.15). H_2O maser emission has been detected at 237 km s^{-1} (LSR) by Imai et al. (2013); yet the H_2O maser detection was a very weak detection, weaker than many H_2O maser detections of RSGs in the Galaxy. This source has a short pulsation period of 590 d typical of the galactic OH/IR sample. It is expected that the 1612-MHz maser flux should peak at close to 25% of the 35-μm flux due to the efficiency of the pumping mechanism (Elitzur, Goldreich & Scoville, 1976; Marshall et al., 2004). As this source has an $F_{24} = 0.22$ Jy, the maser emission would likely be below the observation detection limit.

3.4 Stellar velocities from optical spectra

Systemic velocities have been determined for two LMC sources, IRAS 04407−7000 and IRAS 04516−6902, using UVES-reduced spectra from the ESO data archive. Using a cross-spectrum fitting technique, the molecular bandheads of these two sources have been fitted to that of the UVES spectrum of IRAS 04498−6842 (Fig. 3.16). This technique has been used to determine the best fitting phase difference (or difference in frequency) and the velocity shift. The bright source IRAS 04498−6842 has been used as the model, which has a clear maser profile yielding a systemic velocity of 260 km s^{-1}. The systemic velocities for IRAS 04407−7000 and IRAS 04516−6902 seem to fit well between the

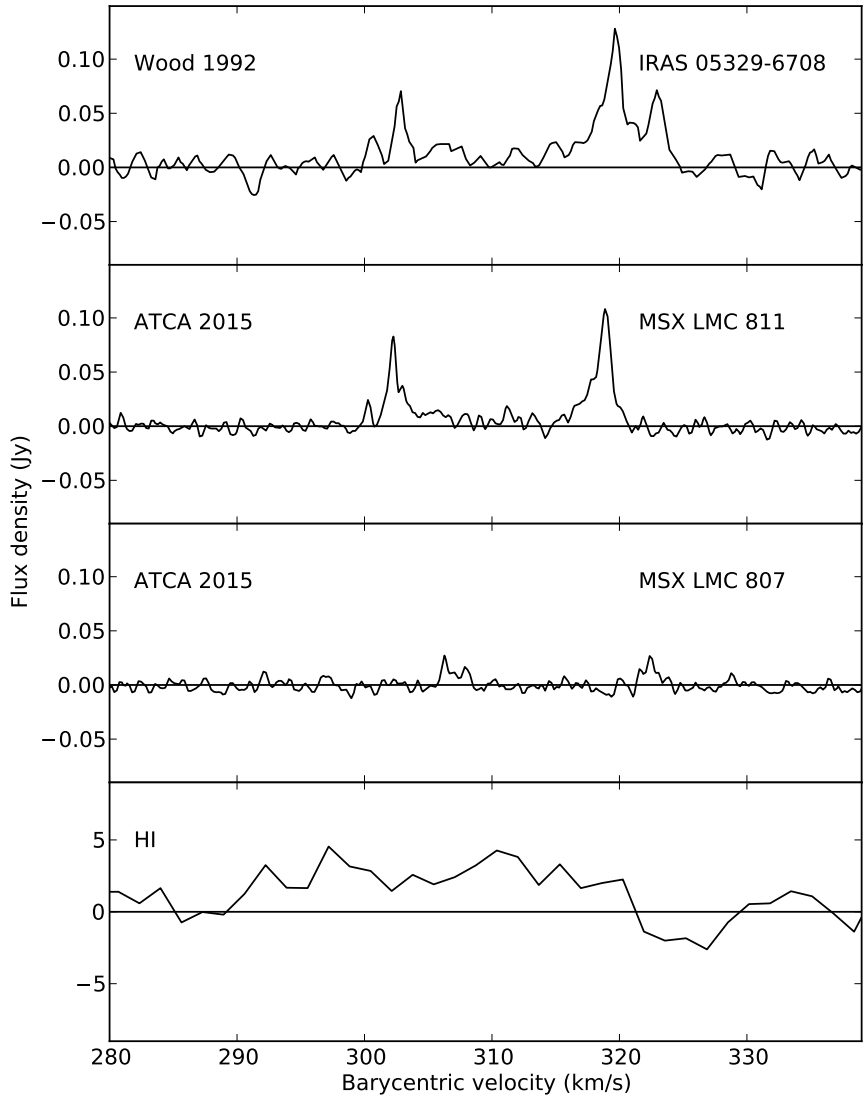

Figure 3.14: OH 1612-MHz maser emission from MSX LMC 811 and the newly discovered MSX LMC 807. Originally thought to originate from IRAS 05329−6708, the true components of the maser emission have now been identified.

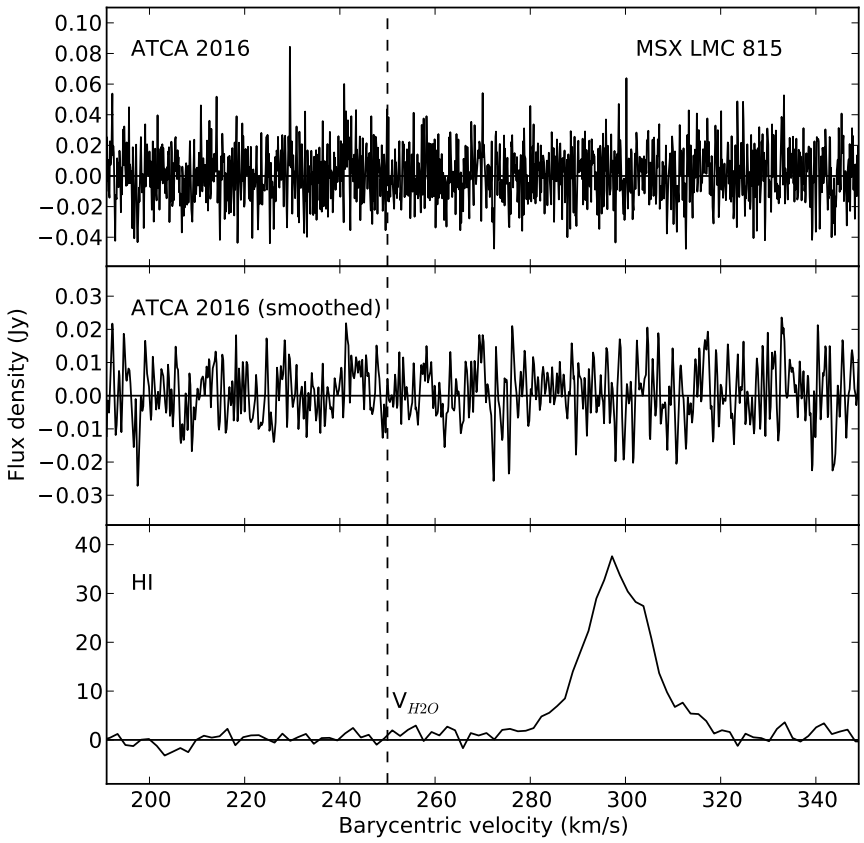

Figure 3.15: OH 1612-MHz nondetection from MSX LMC 815, with the velocity of the water maser detection made by Imai et al. (2013) denoted by V_{H2O}.

maser profiles, corroborating the weaker maser peaks and providing more evidence for all three maser profiles.

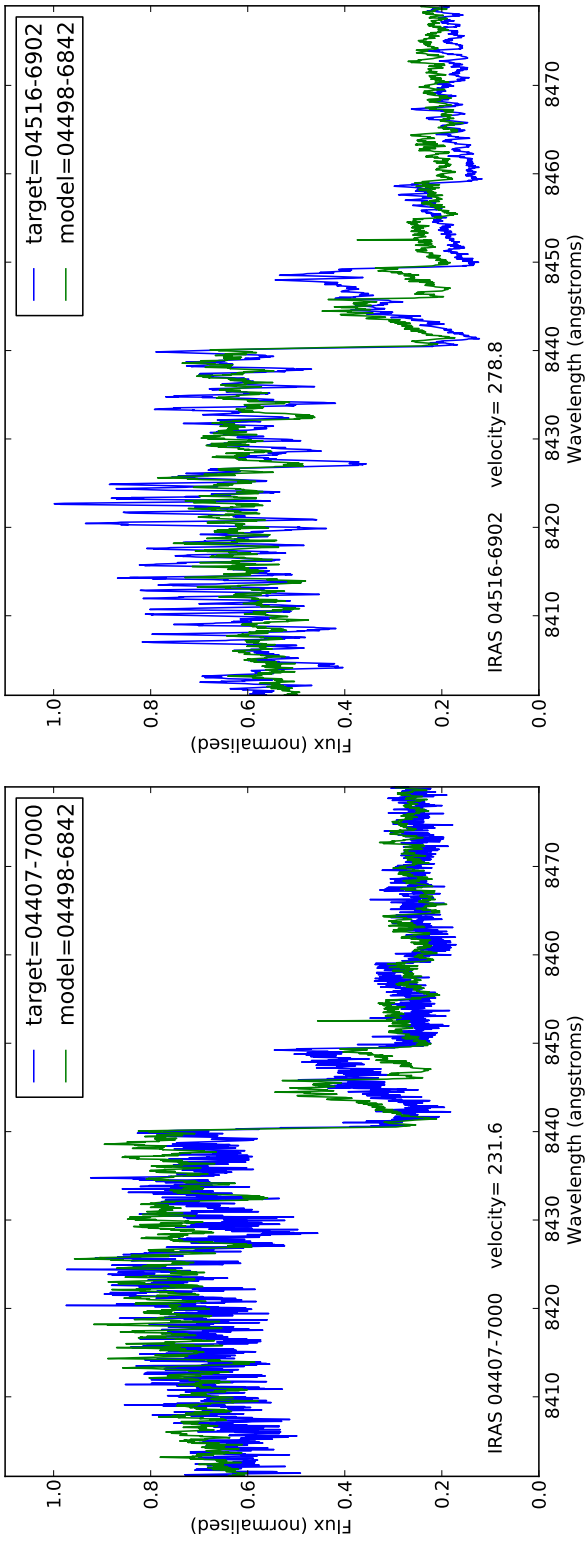

Figure 3.16: The UVES spectra of IRAS 04407−7000 and IRAS 04516−6902 fitted with the UVES spectrum of IRAS 04498−6842 using a cross-spectrum fitting technique. The phase shift has been used to calculate systemic velocities for these sources.

4 Determining the gas-to-dust ratio

4.1 The DUSTY code

The spectral energy distributions of the LMC maser sample have been modelled and fitted using radiative transfer models. The disjointed measures of the infrared and optical light (photometry) from each of these sources has been used to illuminate various aspects of these obscured sources.

Each of the sources have been modelled with radiatively driven wind models produced with the DUSTY 1D radiation transfer code (Elitzur & Ivezić, 2001). Two important outputs from the DUSTY code are the SED of the source modelled and the expansion velocity of the dust-driven wind. The SEDs for the LMC sources are shown in Fig. 4.1, and the model results are listed in Table 4.1. The models use a blackbody for the central star and assume dusty envelopes of warm silicates from Ossenkopf, Henning & Mathis (1992), with varying optical depths, effective temperatures, and inner boundary dust temperatures.

4.2 LMC sample

As these are variable sources, to accurately reproduce the true SED with the models, only one epoch of photometry should be fitted at a time. As a result, the *Spitzer* IRAC and MIPS photometry (Fazio et al., 2004; Rieke et al., 2004), which was taken at the same time and plotted in red, have been fitted with DUSTY models using a χ^2 fitting technique. The available 2MASS JHK photometry are not of the same epoch and are more sensitive to the effects of geometry. As a result, they have been ignored in this source fitting. The fitting technique calculates the best fit of the photometry to 5900 models of varying optical depth, central blackbody temperature, inner dust temperature, and normalisation factor. Luminosities have been calculated for the best-fitting models (plotted in the following figures with dashed lines) assuming a distance of 50 kpc to the

LMC. These luminosities are expected to be more accurate than for Galactic sources because of the well-determined distance to the LMC. These results constrain the derived parameters of the source at the time that the *Spitzer* photometry data were taken (2005 July−November). The current stellar parameters would have fluctuated since as a result of the sources' variability.

For each of the LMC sources, all available photometry has been compiled from 2MASS (Cutri et al., 2003), DENIS (Cioni et al., 2000), *Akari* (Yamamura et al., 2010), MSX (Egan et al., 2003), and IRAS (Beichman et al., 1988), and overplotted on the fitted SED with small open circles; the SED is expected to lie between the stellar variations. Additionally *Spitzer* IRS spectra (Lebouteiller et al., 2011), shown in solid black, have been overplotted. It should be noted that the best-fit DUSTY model was fitted to photometry, independently of the IRS spectra. In most cases, the model successfully fits the photometry and spectra well, which lends credence to the fit solution. The choice of dust optical constants will affect the final result. The dust mineralogy will change as the central star evolves (Dijkstra et al., 2005; Verhoelst et al., 2009) and the inability to compensate for this effect will introduce a degree of uncertainty.

The DUSTY code was run in its radiatively driven wind mode, whereby it solves the hydrodynamical equations for the radial dependence of the density and for the velocities of the gas and dust separately (their difference is the 'drift' speed). It is the velocity of the gas, which dominates the mass by far, which can be measured from the OH maser profiles, but the velocity of the dust can be greater by a factor of a few if the wind density is relatively low. If, however, the drift speed is underestimated, then the SED fitting would yield a dust mass-loss rate which is too low and, assuming the derived gas-to-dust ratio (r_{gd}) is correct, also a total mass-loss rate which is too low. Ramstedt et al. (2008) found a discrepancy between the mass-loss rates derived using DUSTY and those derived from modelling the CO line emission, with the former always yielding lower values. However, if the drift speed was underestimated then the heating of the CO molecules would also have been underestimated and thus CO mass-loss rates would be derived that are too high.

The power of the description of the wind incorporated in DUSTY lies in the

fact that the results can be scaled for different dust contents and luminosities without changing the optical depth according to the following equations (Elitzur & Ivezić, 2001):

$$v_{exp} \propto r_{gd}^{-1/2} L^{1/4} \tag{4.1}$$

$$\dot{M} \propto r_{gd}^{1/2} L^{3/4} \tag{4.2}$$

The latter equation is what determines the shape of the SED. This is, however, a simplification as the shape of the SED (and acceleration of the wind) depends on the distance from the star where the dust forms. This inner radius is set by imposing a fixed dust formation temperature. While it scales with luminosity as $L^{1/2}$, it has a subtle dependency on the temperature of the star as the grain opacity is wavelength dependent (it therefore also depends on the grains' optical properties). Also, the acceleration of the wind will be somewhat different depending on the apparent size of the star whereas it is assumed that all stellar flux arises from one point. These effects mostly affect the emission from the warmest dust at near- to mid-IR wavelengths. An outer limit to the size of the envelope is assumed to be 10^4 times the inner radius, which is typical given these stars are near the end of an extended period of heavy mass-loss. The emission from the coldest dust at far-IR wavelengths depends on this choice but not in a sensitive way.

The photometry have been fitted with models of effective temperatures ranging from $2700 - 3700$ K in steps of 100 K, inner dust temperatures ranging from $600 - 1400$ K in steps of 200 K, each with 100 models spanning a logarithmic range of optical depths from $0.1 - 50$. A comprehensive analysis of the inter-dependency of these inputs has been presented by Ramstedt et al. (2008). Given all the above caveats and assumptions (and departures from spherical symmetry) it becomes clear that a precise error analysis is impractical. The formal errors on the fitting of trends observed between different parameters therefore include both measurement uncertainties and fitting inaccuracies as well as variations in the parameters that are assumed to be fixed. Large sources of

error include asymmetric sources, and inaccurate distances (more important for Galactic sources), which may increase or decrease the derived luminosities, mass-loss rates and gas-to-dust ratios. To a lesser degree, the errors in the fits will also affect these parameters. A non-zero drift speed may result in derived gas-to-dust ratios that are too low and derived gas mass-loss rates that are too high. In trying to asses the goodness of fit, using only the photometric uncertainties for the calculation of the χ^2 value results in seemingly terrible fits. This however does not take into account the assumptions and caveats previously mentioned. As these assumptions cannot easily be quantified, the estimates of the errors, and as a result the goodness of fit, would seem arbitrary and thus they have not been calculated.

Within the LMC sample, silicate is seen in varying degrees of absorption and emission as well as strong attenuation from dust at shorter wavelengths. There are two sources (IRAS 04553−6825 and IRAS 05280−6910) where the models struggle to fit the general SED. This is likely due to a non-spherical symmetry of the dust envelope in these sources. These unique sources are discussed further in §4.4 and §4.5. There are two further sources (IRAS 04553−6933 and MSX LMC 815) where the model struggles to fit both the optical and mid-IR data. Both of these sources show no OH maser emission, and extremely high modelled expansion velocities. These sources may not be optically thick enough for the IR radiation to pump the maser or may in fact be binary systems.

4.3 Galactic samples

In addition to the LMC sample, sources from the Lindqvist et al. (1992) Galactic Centre sample of OH/IR stars, and the Jiménez-Esteban & Engels (2015) Galactic bulge sample of more extreme highly reddened OH/IR stars, have been modelled to serve as comparison samples at higher metallicity; pulsation periods are from Wood, Habing & McGregor (1998) and this work (§5.2) for the Galactic Centre and bulge respectively. Assuming a distance of 8 kpc to these regions, and using a similar modelling method, DUSTY models, and sources of photometry, 70 Galactic Centre and 21 Galactic bulge OH/IR stars have

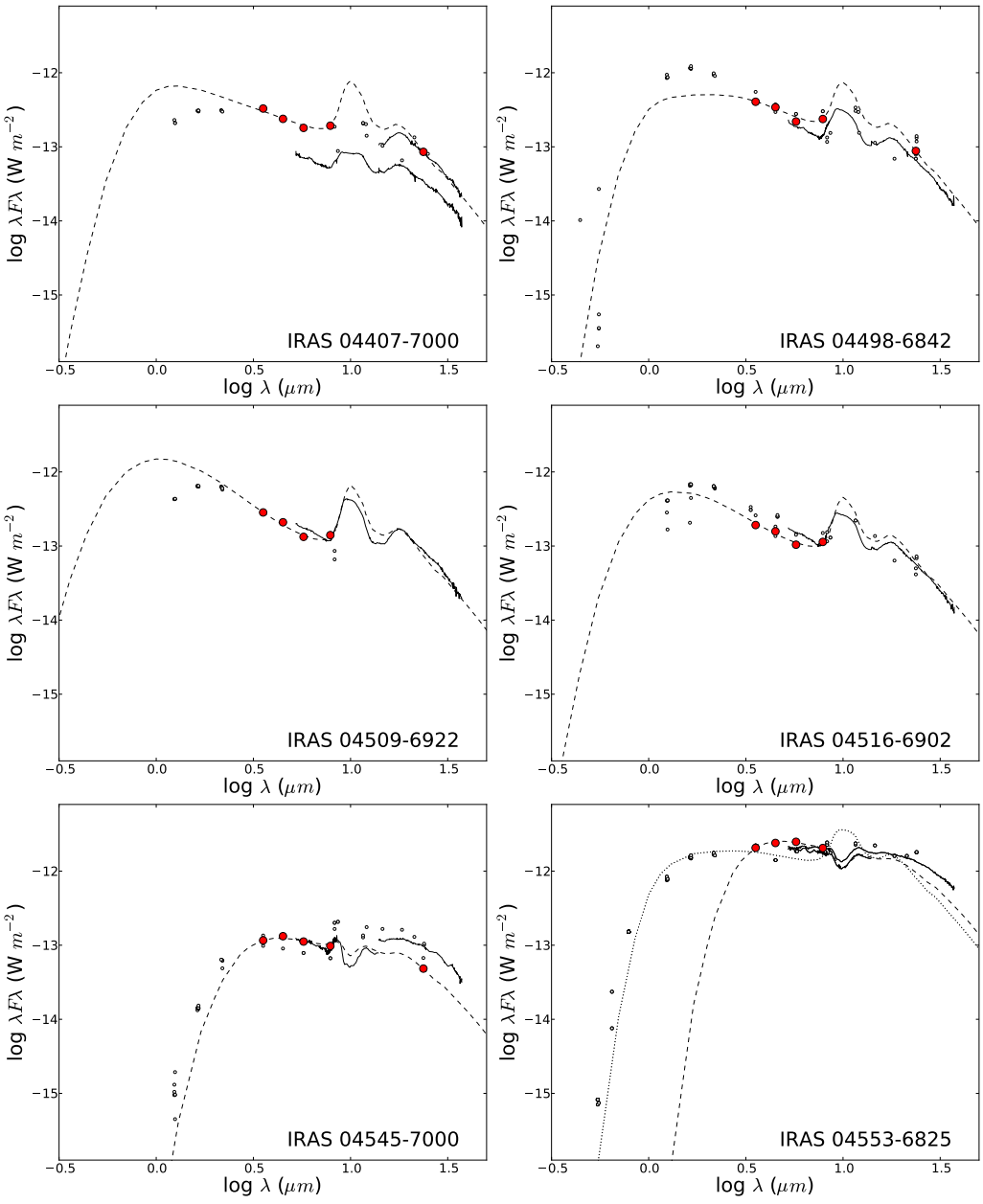

Figure 4.1: The SED fitting of DUSTY models to the LMC sources, with the best-fitting model (dashed line), *Spitzer* IRS spectra (in solid black), *Spitzer* IRAC and MIPS photometry (in red), and the remaining available photometry (small open circles). The large offsets between the IRS spectra and photometry are likely due to variability.

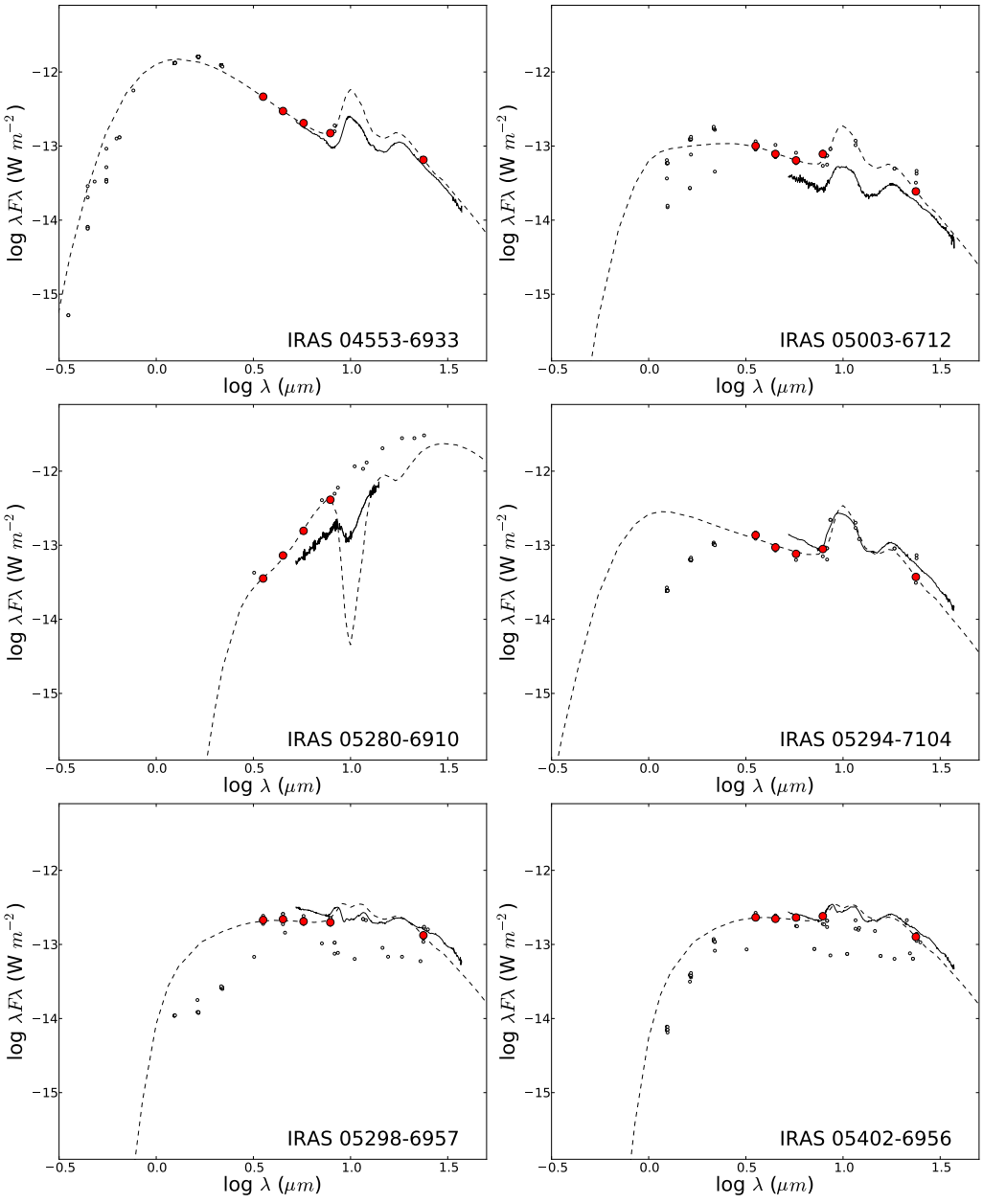

Figure 4.1: continued

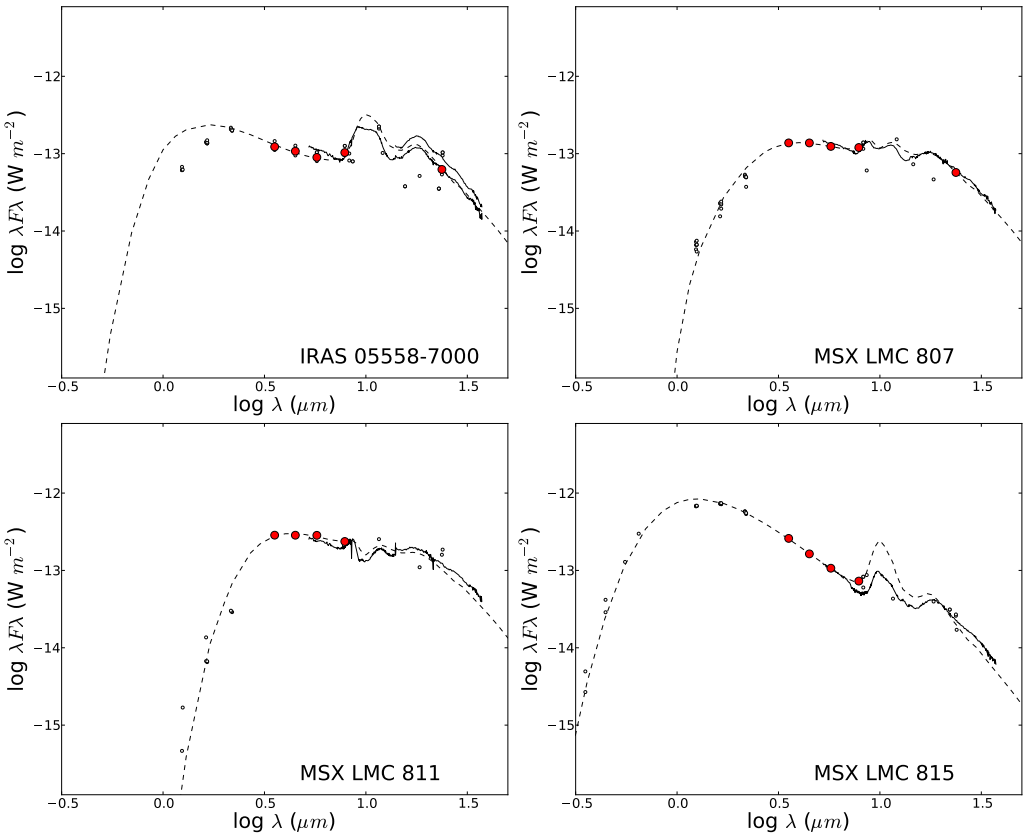

Figure 4.1: continued

successfully been modelled. The distribution of the resulting luminosities is shown along with the values from the LMC in Fig. 1.13. There is a visible void in the histogram where at luminosities between those of the lower luminosity Galactic sources and higher luminosity LMC sources, sources are dominated by carbon-rich chemistry (C stars).

As the photometry is more sensitive to extinction, the SEDs have been fitted using all available photometry, expecting the best-fitting model to fit the median SED. Distances are also less certain for the Galactic sources which will contribute to the uncertainty in the luminosities. For these sources, the Schultheis et al. (2014) extinction maps (from 8 to 8.5 kpc) were used to correct for interstellar extinction. Using the closest value (typically within several arcminutes) for the $(H - K)$ colour excess, the extinction law from Rieke & Lebofsky (1985) was applied using interpolated values to fit the wavelength bands associated with the photometry. This was done for all Galactic bulge and Galactic Centre sources except for IRAS 17030−3053, which was not covered by the extinction maps. As a result, a value of $A_K = 0.15$ mag was assigned, a value adopted by Jiménez-Esteban & Engels (2015). There has been increasing evidence that the reddening law varies within the Galactic Centre (Nataf et al., 2016; Xue et al., 2016); yet, the results are not dramatically affected by this result. This reddening variation is caused by populations of small dust grains and mainly affects shorter wavelength photometry. The results of the DUSTY modelling of the SEDs for the Galactic Centre and Galactic bulge are shown in Figure 4.2.

As the Galactic Centre and some of the Galactic bulge sources lie in crowded fields, a small percentage of photometry points towards shorter wavelengths are expected to come from other sources. The Galactic Centre sources are seen to show a variety of silicate in both emission and absorption. This is a stark contrast to the Galactic bulge sources which all show silicate strongly in absorption, an expectation of this more extreme sample by design. These bulge sources may also be members of the Galactic disc, in the foreground of the bulge. Catchpole et al. (2016) have shown that a number of sources assumed to be members of the bulge have had a wide range of distances. This may introduce a large source of uncertainty in the derived luminosities.

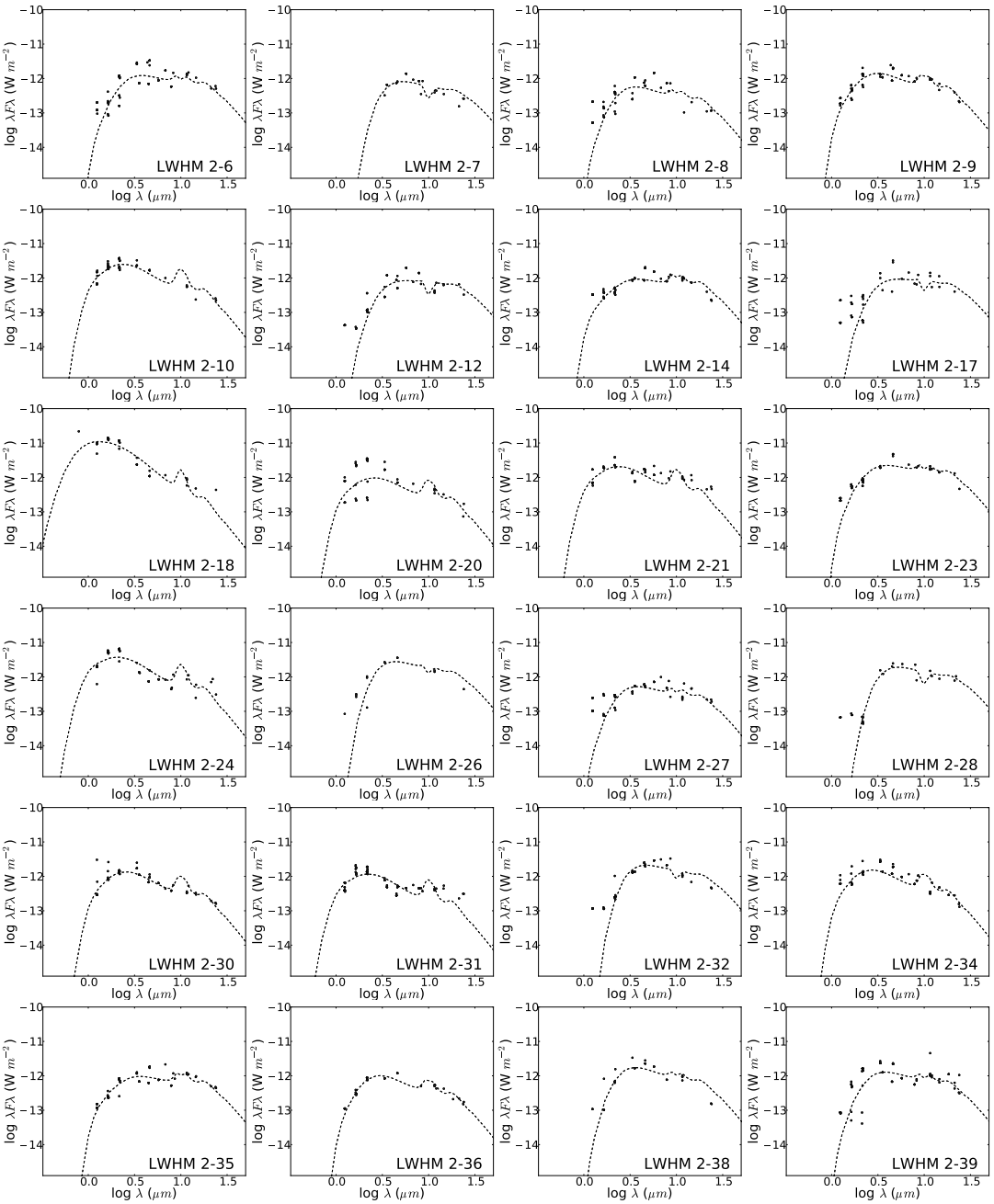

Figure 4.2: The SED fitting of DUSTY models to the dereddened photometry from the Galactic Centre sources.

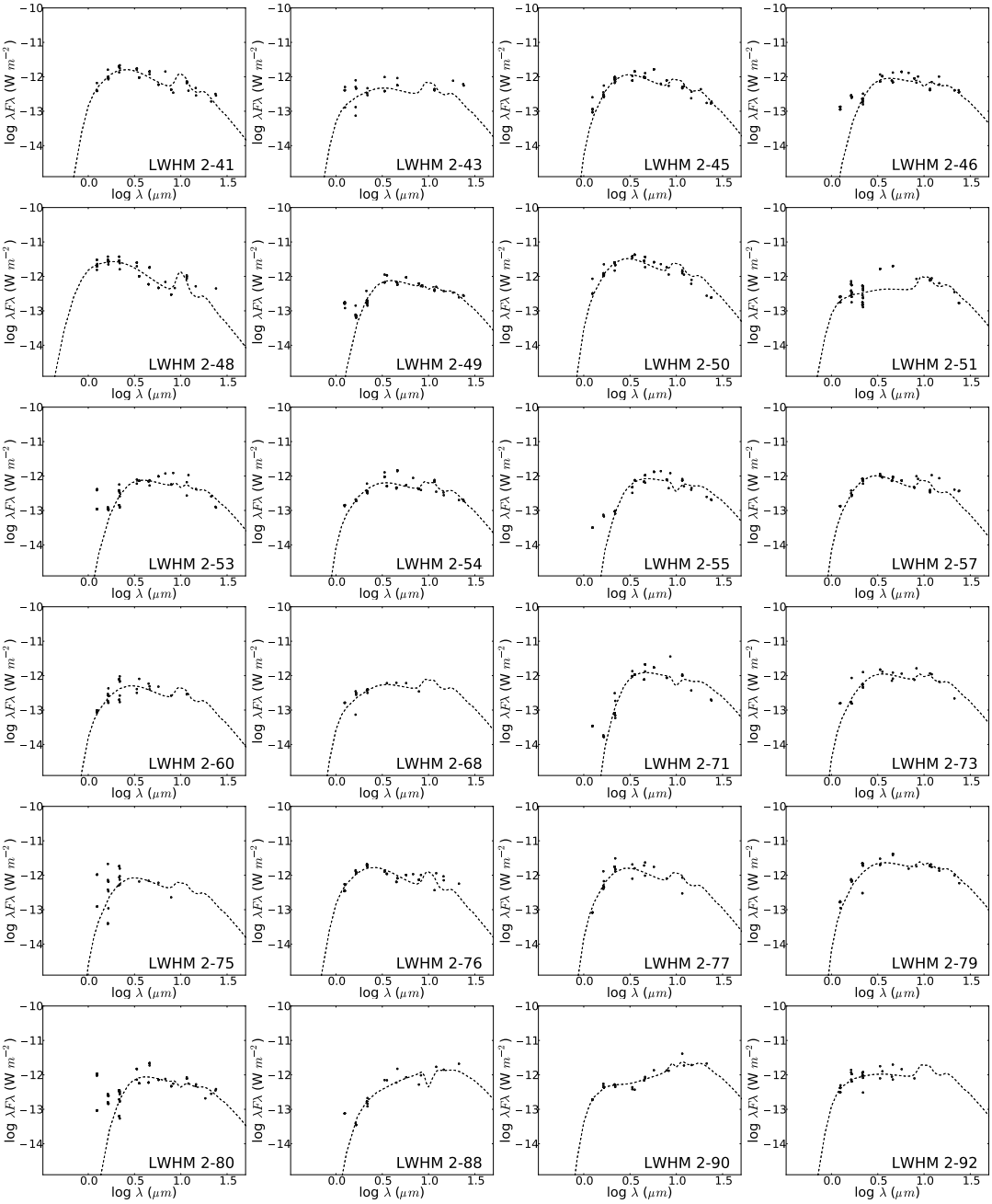

Figure 4.2: continued

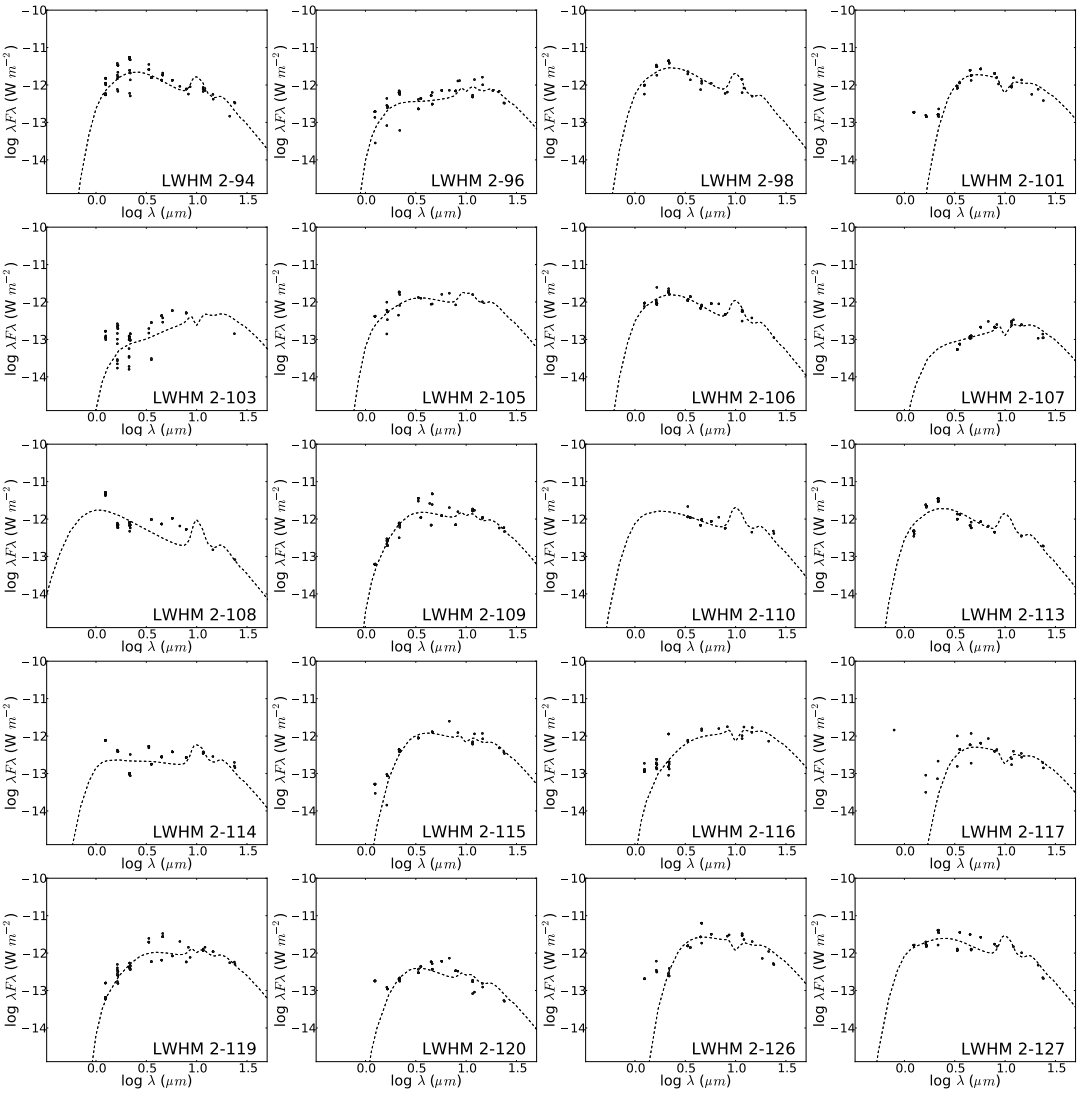

Figure 4.2: continued

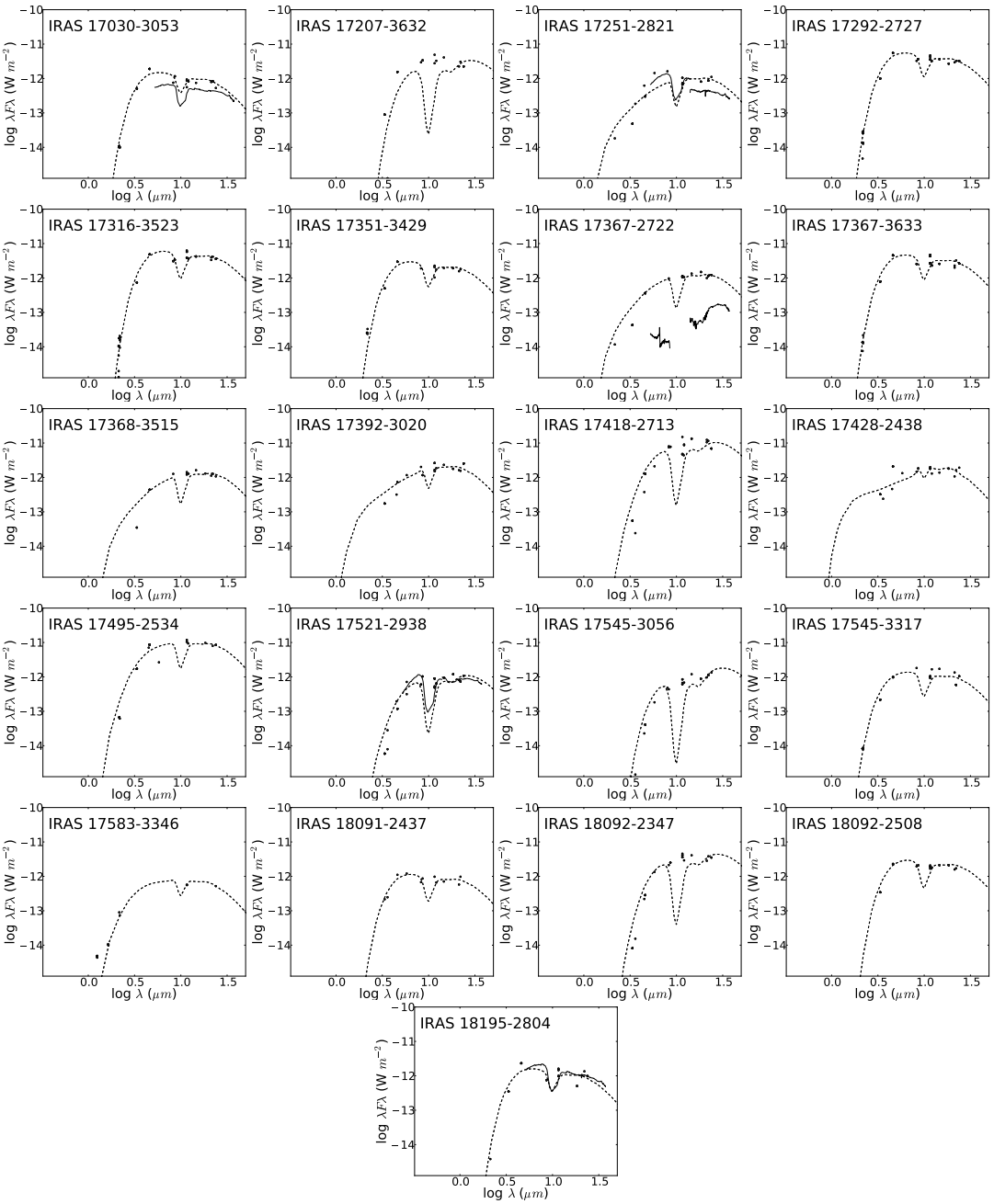

Figure 4.2: The SED fitting of DUSTY models to the dereddened photometry from the Galactic bulge sources; IRS spectra from Golriz et al. (2014) shown in solid black.

4.3.1 Gas-to-dust ratios in the LMC

Values of the expected expansion velocities of the samples have been calculated using the results from SED modelling. These estimates, calculated using the DUSTY code, rely on the assumption that the winds are dust driven and spherically symmetric. Using the measured expansion velocities from OH maser emission, gas-to-dust ratios, assumed by DUSTY to be 200, have been scaled by the square of the ratio between the expected and measured expansion velocities (Eq. 4.1). Using this method, gas-to-dust ratios have been derived for all of the LMC sources shown in Table 4.1.

Table 4.1: The LMC inferred gas-to-dust ratios (r_{gd}) and mass-loss rates ($\dot{M}$) from scaling the resulting DUSTY expansion velocities ($v_{\rm exp,DUSTY}$) to the expansion velocities obtained from circumstellar OH maser profiles ($v_{\rm exp,OH}$). Luminosities (L) and optical depths specified at 10 μm (τ) are derived from the SED fitting of DUSTY models which assume the effective temperature ($T_{\rm eff,DUSTY}$) and inner dust temperature ($T_{\rm inner}$). Mass-loss rates scale in proportion to $L^{3/4}(r_{gd}\rho_{\rm s})^{1/2}$, where the dust grain bulk density (ρ_s) is 3 g cm^{-3}; measured effective temperatures ($T_{\rm eff}$) are from van Loon et al. (2005), unless stated otherwise.

Object name	L (10^3 L$_\odot$)	$T_{\rm eff}$ (K)	$v_{\rm exp,OH}$ (km s^{-1})	$v_{\rm exp,DUSTY}$ (km s^{-1})	$T_{\rm eff,DUSTY}$ (K)	$T_{\rm inner}$ (K)	τ	$\dot{M}$ (M$_\odot$ yr^{-1})	r_{gd}
IRAS 04407−7000	104	3008	8.4	21.4	3400	800	0.4	1.4×10^{-4}	1312
IRAS 04498−6842	97	2500	13.0	22.1	3400	1000	0.7	9.8×10^{-5}	576
IRAS 04509−6922	178	2500	11.4	23.6	3700	600	0.1	9.9×10^{-5}	859
IRAS 04516−6902	75	2667[2]	10.0	16.1	2900	600	0.3	6.5×10^{-5}	519
IRAS 04545−7000	19		7.7	11.2	3200	1200	4.9	7.0×10^{-5}	422
IRAS 04553−6825	340−454	3008	23.8	24.9	3300	1400	8.62	5.8×10^{-4}	218
IRAS 04553−6933	176			21.9	2900	600	0.1	[a]5.9×10^{-5}	
IRAS 05003−6712	23	2667		14.5	3700	1000	0.8	[a]3.3×10^{-5}	
IRAS 05280−6910	225		20.6	13.6	3400	350	13.4	5.4×10^{-4}	84*
IRAS 05294−7104	45	2890	10.3	17.5	3600	800	0.4	5.1×10^{-5}	610
IRAS 05298−6957	50	4000[2]	10.5	11.1	3000	800	2.0	8.6×10^{-5}	224
IRAS 05402−6956	51		10.5	11.3	2700	800	2.2	8.4×10^{-5}	231
IRAS 05558−7000	42	3400[2]	8.0	11.0	2700	600	0.7	5.4×10^{-5}	381

References:
[1]Buchanan et al. (2006)
[2]García-Hernández et al. (2009)

[a] Calculated using assumed gas-to-dust ratio of 400
* Unlikely true gas-to-dust ratio; further explained in §4.5

continued ...

. . . continued

Object name	L (10^3 $L_\odot$)	$T_{\rm eff}$ (K)	$v_{\rm exp,OH}$ (km s^{-1})	$v_{\rm exp,DUSTY}$ (km s^{-1})	$T_{\rm eff,DUSTY}$ (K)	$T_{\rm inner}$ (K)	τ	$\dot{M}$ ($M_\odot$ yr^{-1})	r_{gd}
MSX LMC 807	24		8.2	10.6	2900	1000	3.2	6.2×10^{-5}	336
MSX LMC 811	42		8.3	14.1	2700	1200	5.6	1.5×10^{-4}	586
MSX LMC 815	97	3100[1]		24.9	3000	800	0.1	[a]2.5×10^{-5}	
Sample median values:									
Galactic Centre	5		18.5	8.5	3000	1200	2.8	6.0×10^{-6}	45
Galactic bulge	6		15.7	4.7	3200	800	19.5	2.2×10^{-5}	28
LMC	63		10.3	15.3	3100	800	0.8	7.7×10^{-5}	422

Adding up all of the refractory elements within oxygen-rich dust and scaling to the metallicity of the LMC, gas-to-dust ratio have been calculated to be ~ 500. The interstellar gas-to-dust ratio (r_{gd}) of the LMC has also been shown by Roman-Duval et al. (2014) to be between 380 and 540. The median r_{gd} of 416 agrees well with previous estimates but lies towards the lower end of these estimates. This may be due to a bias towards the most metal rich sources. The highest r_{gd} (lowest metallicity) objects, IRAS 04407−7000 and IRAS 04509−6922, have far lower inferred metallicities than the rest of the sample. All of these sources have quite reliable OH maser detections, with well-fitted SEDs. These stars are within close proximity to each other, lying within the same south-east region of the LMC, towards the Magellanic Bridge. This may be due to either a lower efficiency of dust formation in these stars or they may have formed from lower metallicity gas, possibly originating from the SMC (see Olsen et al., 2011). These are not likely to be members of the small subset of counter-rotating sources found by Olsen et al. (2011); as extreme oxygen-rich sources are rare in the SMC, the counter-rotating subset is a small fraction of the whole LMC population and the kinematics of the three sources are consistent with the rest of the LMC sample.

The majority of stars in the Galactic Centre have metallicities at or above solar, with a small population of low metallicity sources (Do et al., 2015; Wood, Habing & McGregor, 1998). The Galactic bulge has a metallicity typically peaking at a near solar value, with a sharp cutoff just above solar, and a tail towards lower metallicity (Zoccali et al., 2003). It is expected that these extreme sources likely lie towards the higher end of this metallicity range.

Median gas-to-dust ratios of 45 and 28 have been derived for the Galactic Centre and Galactic bulge respectively. Little difference is seen between the results of the Galactic bulge fitting technique and the fitting by Jiménez-Esteban & Engels (2015). Results have shown similar luminosities and mass-loss rates, yet few cases are found where the best-fitting models have similar optical depths. It was suggested by Jiménez-Esteban & Engels (2015) that the existence of these oxygen-rich Galactic bulge sources can be explained if they have metallicities at or above solar metallicity, which is consistent with the derived gas-to-dust ratios. The Galactic sources may be alpha-enhanced, which

would increase the abundance of elements like Si, Ti, and Mg, and thus increase dust production. A bias towards the highest metallicity sources may be magnified by this additional alpha-enhancement.

There is quite a large range of gas-to-dust ratios in the three samples. When these gas-to-dust ratios are compared with respect to luminosity and expansion velocity (Fig. 5.1, shown later) there is a clear difference between the Galactic and LMC samples. Comparing the luminosities and mass-loss rates (Fig. 5.5, shown later), there is a clear trend irrespective of gas-to-dust ratio. The Galactic bulge sources also tend to have higher mass-loss rates than the other two samples, which is expected from this more extreme sample.

The idea that there may be two different OH/IR populations within the Galaxy was originally suggested by Wood, Habing & McGregor (1998), where sources with expansion velocities lower than 18 km s^{-1} were expected to have a metal content 2.1 times lower than sources with higher expansion velocities; these results suggest that this is not the case. A slightly higher median gas-to-dust ratio was derived for the sources targeted in this work, with velocities less than 18 km s^{-1}.

This analysis has provided a useful technique to derive gas-to-dust ratios, given only photometry and a measure of the circumstellar wind speed. While the value comes with a number of caveats and assumptions, this method has successfully calculated gas-to-dust ratios expected from sources in their varying metallicity environments. It is particularly important to note that this method may not be appropriate at lower metallicities. As the drift velocity increases toward lower metallicities, the decoupling of the gas and dust is not represented in this analysis. While this does not appreciably impact the derived gas-to-dust ratios for sources within the Galaxy or LMC, values will become more uncertain towards lower metallicities unless this effect is taken into account.

This SED-fitting technique will be re-visited in Chapter 6 as it has been applied also to the SMC sample. However, gas-to-dust ratios have not been calculated for these sources as they lack measurements of the circumstellar wind speed. Nevertheless, the luminosities and mass-loss rates have provided useful information for the sample.

4.4 The Geometry of WOH G64

IRAS 04553−6825 is known to be highly non-spherical (Roche, Aitken & Smith, 1993; Ohnaka et al., 2008), originally suggested on the basis of its optical brightness and strong silicate feature. This was later suggested by van Loon et al. (1999) on the basis of its maser characteristics. The maser source has been observed in OH, showing four OH maser peaks in the 1612-MHz spectrum. The non-spherical nature of this source makes it quite hard to model, yet work has been done to understand these types sources (Zijlstra et al., 2001). While the 10 μm silicate feature has been successfully modelled in absorption, something that is seen in the *Spitzer* and *ISO* spectra (c.f. Trams et al., 1999; van Loon et al., 1999), the model does not fit the general shape of the SED as well. As a result, a secondary model (plotted with a dotted line) where the general shape of the SED has been fitted (Fig. 4.1). The two models differ slightly in both luminosity and mass-loss, with a luminosity between 340,000 and 454,000 $L_{\odot}$ and a mass-loss rate between $3.1 - 5.8 \times 10^{-4}$ $M_{\odot}$ yr^{-1}. It is expected that the models represent the range of possible luminosities and mass-loss rates of this unique source. Ohnaka et al. (2008) suggested that the source is likely to a have a dusty torus which is being observed pole-on. This explanation is consistent with previous results.

4.5 The Geometry of IRAS 05280−6910

The maser emission from IRAS 05280−6910 is unique. First, the source shows maser emission at 1612 and 1665 MHz but not at 1667 MHz. Secondly, the maser profiles are very irregular with a number of peaks which have changed in amplitude and velocity since 1992. And, thirdly, the 1665-MHz maser profiles, which should probe a region closer to the star (Richards & Yates, 1998), extend (at the blue end) to velocities outside of the 1612-MHz profiles. All of these peculiarities come to heel upon a further investigation of the polarisation data (Fig. 4.3). This source is strongly circularly polarised at 1665 and 1612 MHz, alluding to magnetic activity close to the star. Zeeman splitting is expected

at two locations in the 1665-MHz spectrum centred at 248.9 and 285.8 km s^{-1}. The separation of these bright maser peaks suggests an upper limit of the magnetic fields of around 1.2 and 2.2 mG, respectively. The peaks at 257 and 262.7 km s^{-1} are unlikely to be a Zeeman pair as the resulting magnetic field would be around 10 mG and would result in a ~ 1 km s^{-1} split in the 1612-MHz spectra at this velocity, which is not seen. Stokes $I + V/2$ has been used for RHCP and $I - V/2$ for LHCP (IAU convention), where RHCP is the rotation of the electric field vector in a counterclockwise direction as the wave travels from the source to the observer along the line of sight.

The magnetic activity coupled with the large velocity range of the maser profile may be suggestive of bipolar outflows, collimated by the magnetic fields. The bluest 1665-MHz maser peaks may either be more highly accelerated, localised "bullets" as opposed to the more uniform wind farther out which is probed by the 1612-MHz masers, or they may be associated with interstellar masers as they peak at the H I velocity. The complete absence of 1667-MHz emission must be due to quenching as a result of the strong 1665-MHz masers. Sources like VY CMa and IRAS 04553−6825 have shown similar complex profiles with many maser peaks and asymmetric envelopes (Cohen et al., 1987); yet, IRAS 05280−6910 also has a distinctly unique SED. Studies of VY CMa have shown a number of arcs and knots, which may also be present in this source (Humphreys et al., 2005; Humphreys, Helton & Jones, 2007).

The DUSTY modelling of IRAS 05280−6910 yields an expected expansion velocity of 13.6 km s^{-1}. This is considerably lower than the observed value of 20.6 km s^{-1}. This disparity is expected to come from something more than uncertainty or unrealistic modelling. What may be happening, is that the source may have a near edge-on dusty torus, similar to IRAS 04553−6825 (WOH G64), which is highly obscured along the line of sight. This result would also support the idea that the source has bipolar outflows. These outflows could explain the models' slow calculated expansion velocity (which could be expected along the line of sight), while not necessarily leading to such a low gas-to-dust ratio or high mass-loss rate.

An obvious difference can be seen between the DUSTY models and the IRS spectrum of IRAS 05280−6910. The *Spitzer* IRS spectrum of this source shows silicate

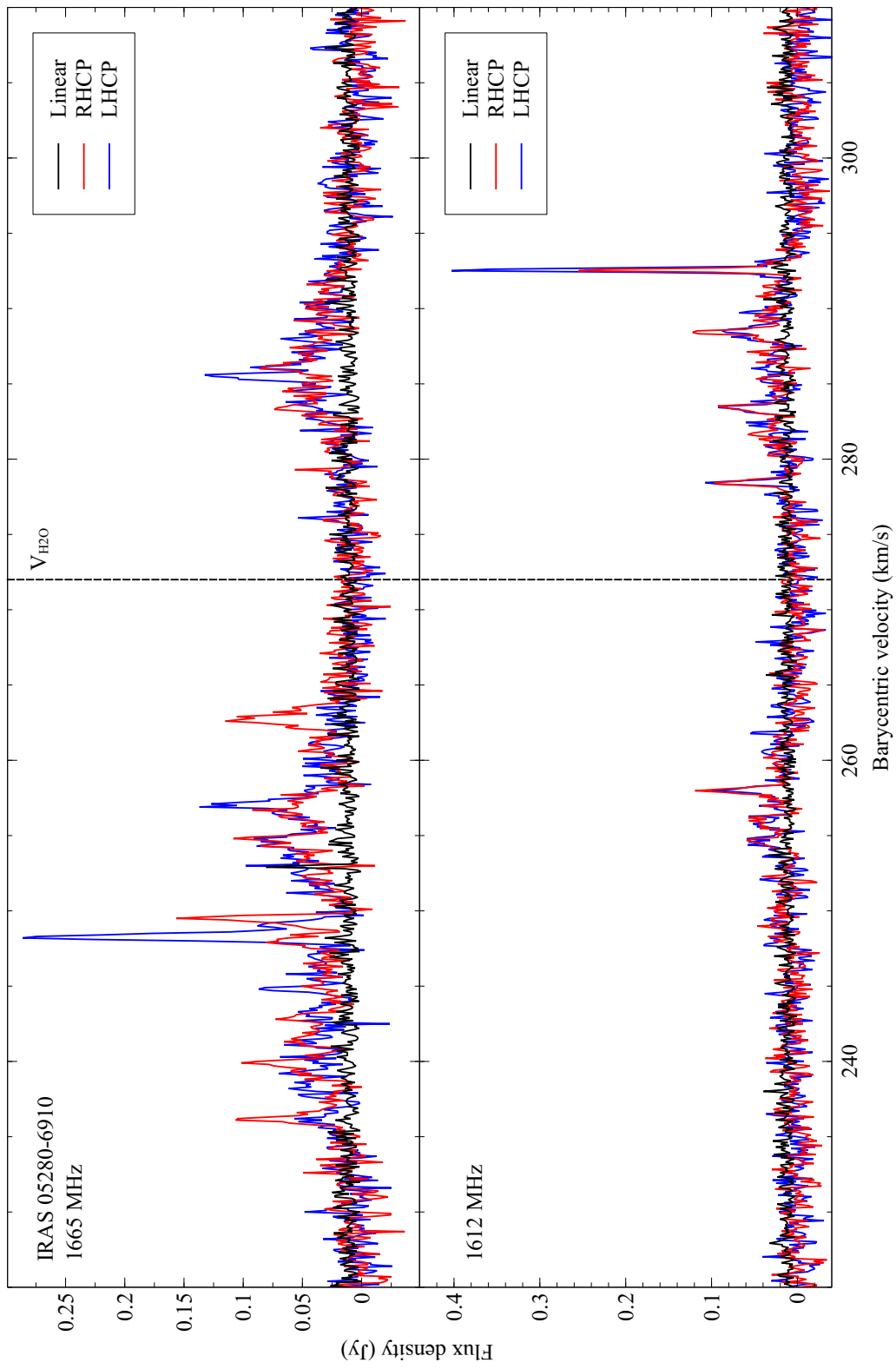

Figure 4.3: The left- and right-hand circular polarisation of the 1665-MHz (top) and 1612-MHz (bottom) maser detections of IRAS 05280−6910; the systemic velocity from the water maser emission from van Loon et al. (2001a) is indicated with V_{H2O}.

in absorption, but not to the same degree as the modelled SED. It was proposed that the observed absorption feature may be partially masked by the nearby RSG WOH G347 (van Loon, Marshall & Zijlstra, 2005), a source which shows silicate in emission. The nature of this source will be revisited in Chapter 7.

5 Wind speeds and mass-loss rates

5.1 Circumstellar wind speed

The stellar wind expansion velocities have been analysed for the sources in the LMC, Galactic Centre, and Galactic bulge samples. In OH/IR stars, the mass-loss process and the outflow acceleration are driven by radiation pressure on dust grains. In these dense environments, the gas is dynamically coupled with dust through friction, and the outflow is assumed to behave like one single fluid. As was discussed in §4, a non-zero drift velocity will affect derived values like the mass-loss rate and gas-to-dust ratio. As these stars produce mainly silicate dust, and the production of silicates is limited by initial metallicity[2], lower metallicity yields a slower wind. It is expected that at lower luminosity there is less radiation pressure to force the dust grains outwards and drive the wind, and therefore a slower expansion velocity; in general, this is observed in both the LMC and Galactic samples, as it was shown by Marshall et al. (2004), as well as the following work.

The LMC and Galactic samples have several differences, including very different luminosities and pulsation periods. The LMC sample is biased towards the most luminous sources as they are distant and obscured, and only the most massive and luminous AGB stars remain oxygen-rich in the heavy mass-loss phase, and are detectable with current instruments. The lower luminosity sources are thus dominated by carbon-rich stars. As a result, a selection bias is expected within the LMC. The LMC sample is also biased towards longer pulsation periods as the OH maser emission is brightest in the most evolved and highest mass-loss sources. The Galactic bulge sample is a collection of the most extreme OH/IR sources in the Galactic bulge and generally lack pulsation periods. Data from the Vista Variables in the Via Lactea (VVV) survey (Minniti et al., 2010) has been used to derive periods for seven of the Galactic bulge sources (§5.4). The Galactic

[2]Contrary to C-stars in which the dredge-up events can enhance the amount of carbon initially available in the atmosphere.

Table 5.1: The resolution of the radio observations of the LMC and Galactic samples.

Sample	Telescope	Spectral resolution (km s^{-1})	Angular resolution
Galactic Centre	VLA	1.36[a]	$6 - 8''$
Galactic bulge	Parkes	0.9[b]	$12'$
	Effelsberg	1.1[b]	$8'$
LMC	Parkes	0.18	$12'$
	ATCA	0.4	$7 - 8''$

References: [a]Lindqvist et al. (1992) [b]te Lintel Hekkert et al. (1991)

Centre sources tend to be lower mass and less extreme but still within the superwind phase of mass-loss. The fact that this is an older population may be contributing to the sample's lack of higher-mass sources, similar to those within the LMC sample. In addition to differences within the sample, there are differences in the quality of the radio observations (Table 5.1). While there is significantly less angular resolution for the Galactic bulge sample, only resolved and reliable maser profiles have been used; all observations have spectral resolutions around 1 km s^{-1}.

At a similar luminosity, the Galactic bulge sources are seen to have lower expansion velocities than those of the Galactic Centre sources (Fig. 5.1). This same effect is seen even more so in the LMC sample with a metallicity (Z) even lower, at half solar. This is consistent with what is expected from simple dust-driven wind theory (e.g., van Loon, 2000). The expansion velocities from the LMC sample have been fitted with respect to their luminosities. The fit ($v_{\rm exp} = 0.118L^{0.4}$) is then scaled to a solar metallicity (a factor of 2) typical of the Galactic samples, which fits well within these samples. These results have been used to derive a new relation for expansion velocity:

$$v_{\rm exp} \propto ZL^{0.4} \tag{5.1}$$

The number of measured wind speeds has been dramatically increased from previous studies, which relied on five accurate wind speeds. Using a larger sample, the updated circumstellar expansion velocity relation: $v_{\rm exp} = 0.118L^{0.4}$, more accurately fits the data

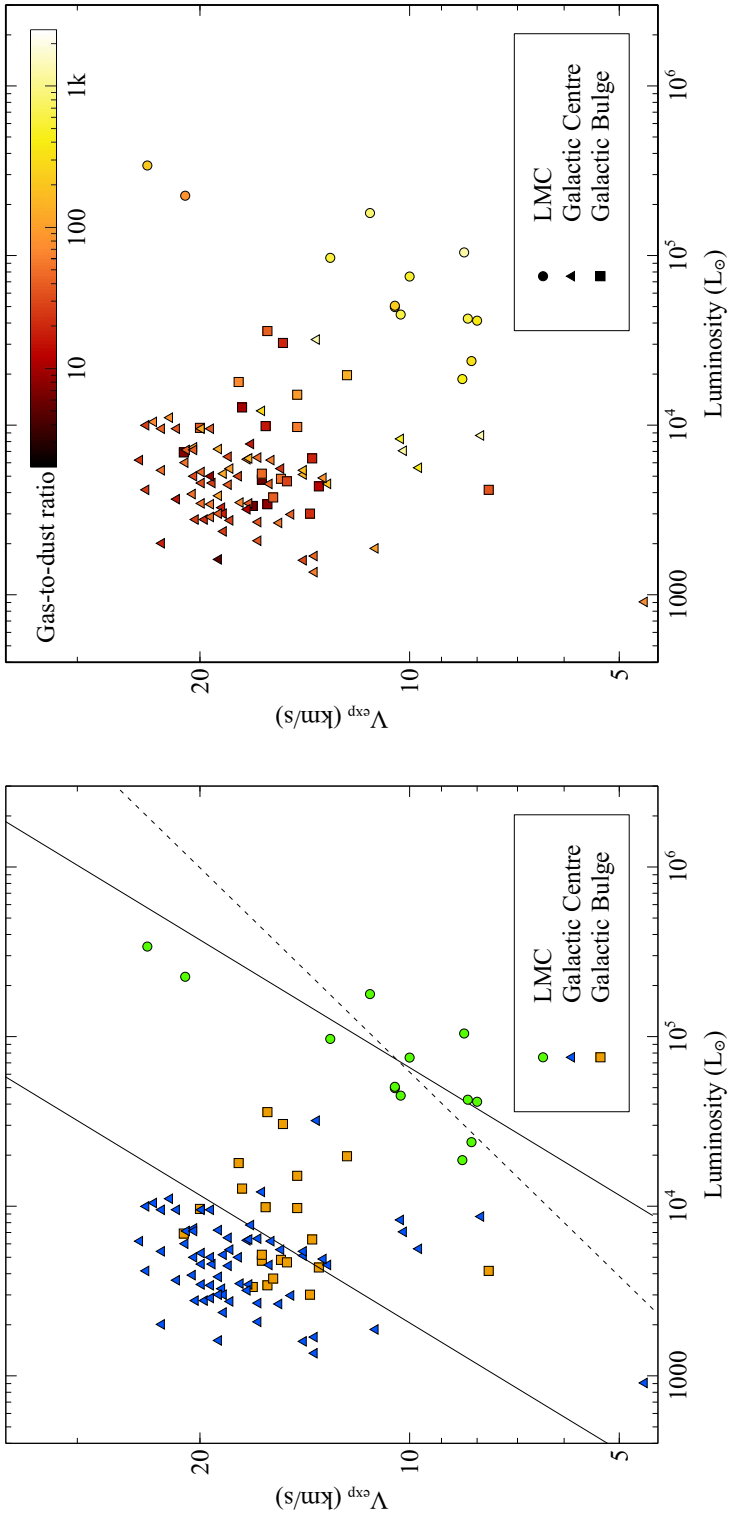

Figure 5.1: ***Left***: The observed wind speed as a function of luminosity for the sample of OH/IR stars in the LMC and Galactic samples. The LMC sample is fitted with a power law ($v_{\rm exp} = 0.118L^{0.4}$). The power law (solid black) is then scaled to a metallicity characteristic of the Galactic sample (a factor of 2). The newly derived relation for circumstellar expansion velocity, fits the samples well. This relation has been compared to that of dust-driven wind theory $v_{\rm exp} \propto r_{gd}^{-1/2} L^{0.25}$ (dotted line). ***Right***: The observed wind speed as a function of luminosity with the gas-to-dust ratio represented in colour, as derived from the scaling of SED models.

than e.q. 4.1, the assumption made by DUSTY (Fig. 5.1). The removal of the two most luminous sources that may exhibit unique geometries does not significantly impact the fit. These results however make several assumptions. It is assumed that the sources are spherically symmetric and that the samples are assumed to have a homogeneous metallicity, which is known not to be the case. It is also expected that the scattering of photons will affect the sources' collective radiation pressure.

The individual effects of different parameters on the expansion velocity is seen more clearly in Fig. 5.2, and 5.3. In Fig. 5.2, the expansion velocity is shown against the gas-to-dust ratios derived from SED fitting (described further in the following section). Results have shown a correlation between the expansion velocity and the gas-to-dust ratio. These samples have been fitted with a power law which is expected to follow: $v_{\rm exp} \propto r_{gd}^{-0.5}$. The actual fit: $v_{\rm exp} \propto r_{gd}^{-0.15}$ is much shallower due to the effects of luminosity on the wind speeds. The higher luminosities of the LMC result in higher LMC wind speeds and a shallower fit. The expansion velocities have been compared to both the mass-loss rates and pulsation periods (Fig. 5.3) but no clear correlation is found. The scatter is mostly due to differences in luminosity and metallicity between and within the samples. This is contrary to the expectations of the DARWIN models (Höfner et al., 2016), which do predict a correlation of expansion velocity and mass-loss rate. Likely, the correlation reflects the evolution along the AGB, whereas the samples are naturally biased towards the endpoints of evolution.

5.2 VVV pulsation periods

Pulsation periods have been derived for seven Galactic bulge stars from the Jiménez-Esteban & Engels (2015) Galactic bulge sample of extreme highly reddened OH/IR stars. Aperture photometry was done on K-band photometry for all of the Galactic bulge sources within the tiles of the Vista Variables in the Via Lactea (VVV) survey (Minniti et al., 2010). A calibrator star was used in each field to derive the relative flux. Fourier analysis was used to fit the period and a least-squares fit was used to calculate the errors.

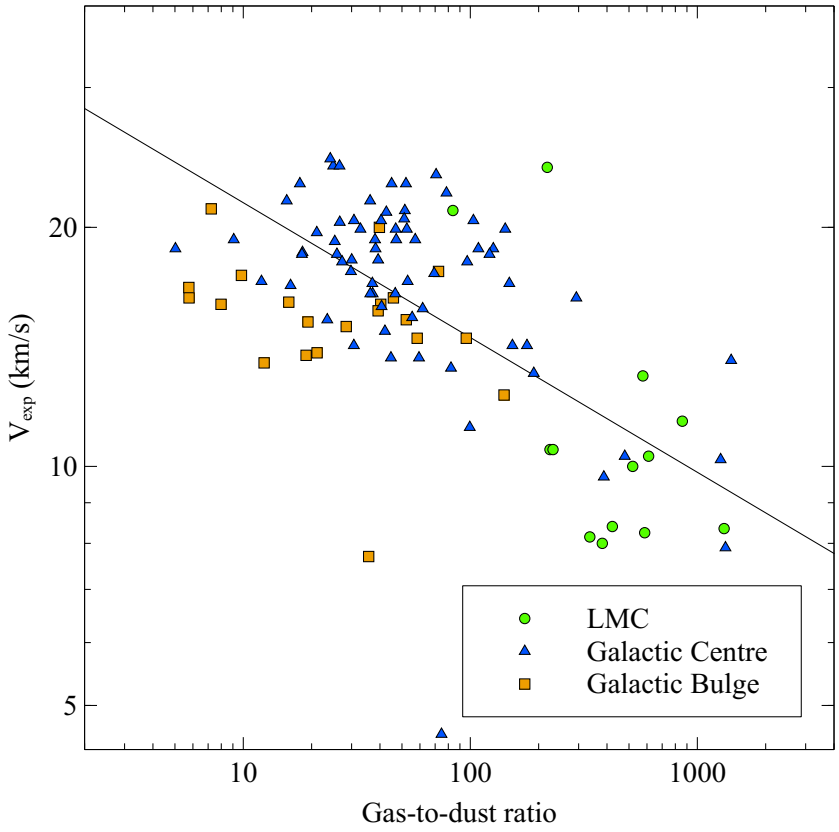

Figure 5.2: The observed wind speed as a function of gas-to-dust ratios derived from SED fitting. The samples have been fitted with a power law which is expected to fit: $v_{\rm exp} \propto r_{gd}^{-0.5}$ (Eq. 1). The actual fit: $v_{\rm exp} \propto r_{gd}^{-0.15}$ is much shallower due to the effects of luminosity on the wind speeds. The higher luminosities of the LMC result in higher LMC wind speeds and a shallower fit.

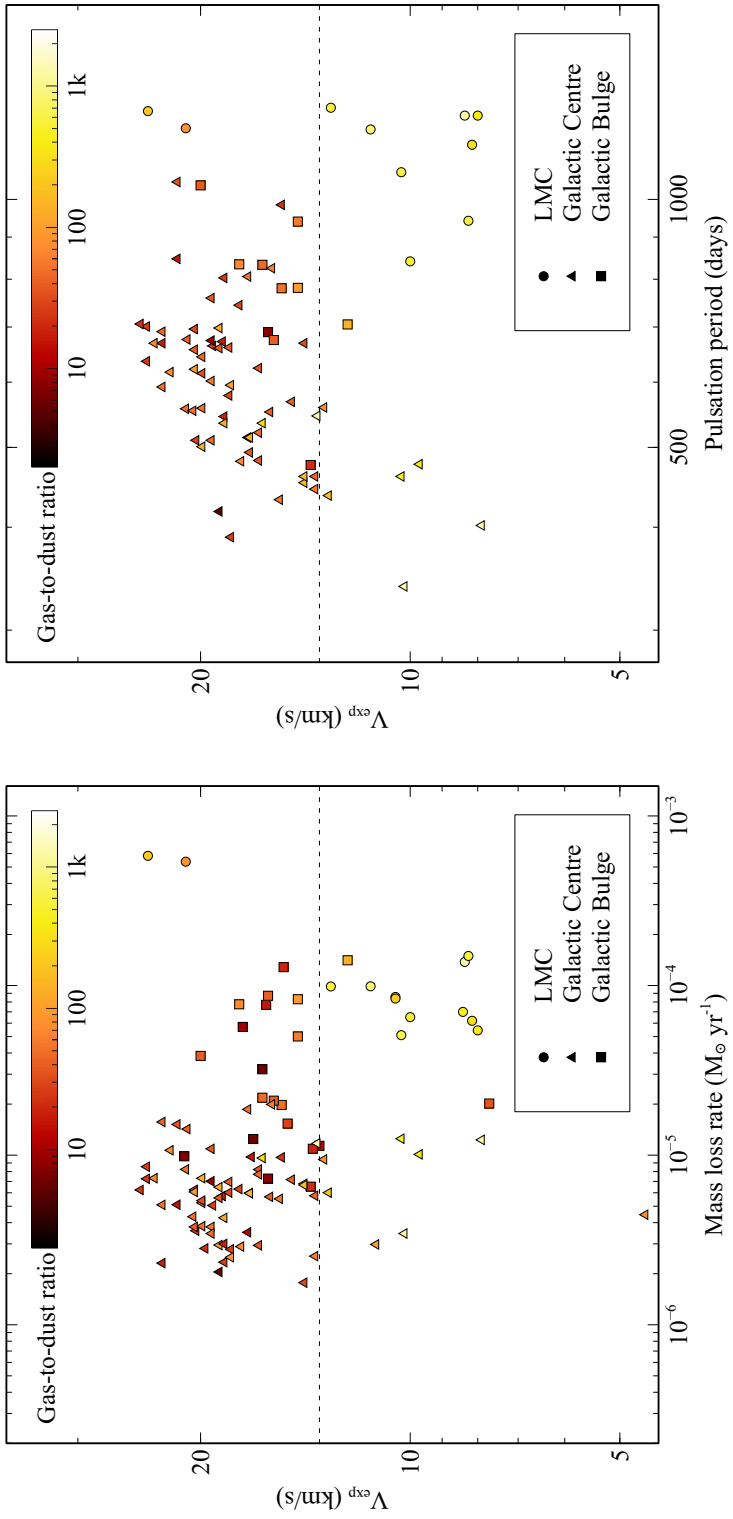

Figure 5.3: The observed wind speed as a function of mass-loss rate (***Left***) and pulsation period (***Right***), with the gas-to-dust ratio represented in colour. Mass-loss rates and gas-to-dust ratios are derived from the scaling of SED models (discussed further in §4.3). The dotted lines indicate the change from the higher to lower metallicity sample, which, as has been shown, will affect the expansion velocities. Looking at the Galactic samples, there does not seem to be any clear correlation between expansion velocity and either mass-loss rate or pulsation period.

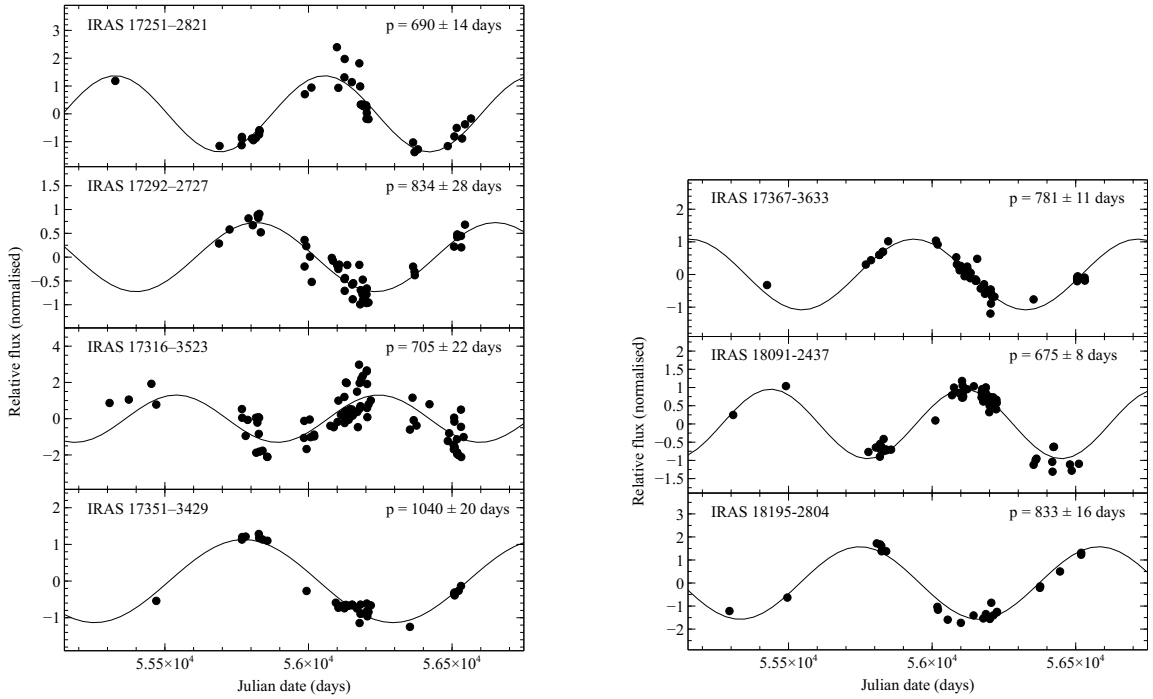

Figure 5.4: Fit pulsation periods of highly evolved stars from the Galactic bulge sample. Aperture photometry was done on tiles from the VVV survey and fitted using a Fourier analysis fitting technique.

Three of the sources have previously derived pulsation periods from van der Veen & Habing (1990). The periods of 690, 781, and 833 d are dramatically different from the values previously derived of 1200, 1500, and 1200, respectively. The inaccuracy of these derived periods has been shown in Whitelock, Feast & Catchpole (1991) and now in this work.

5.3 A new mass-loss prescription

By employing the new gas-to-dust ratios and using equation 4.1, an empirical mass-loss prescription has been derived which includes the luminosity (L), pulsation period (P), and gas-to-dust ratio (r_{gd}): $\dot{M} = 4.2 \times 10^{-11}\, L^{0.9}\, P^{0.75}\, r_{gd}^{-0.03}$ (where luminosity is in $L_{\odot}$ and the pulsation period is in days); normalising this prescription to a typical source, results in the following relation:

$$\frac{\dot{M}}{\mathrm{M}_{\odot}\ \mathrm{yr}^{-1}} = 1.06^{+3.5}_{-0.8} \times 10^{-5} \left(\frac{L}{10^4\,\mathrm{L}_{\odot}}\right)^{0.9\pm0.1} \left(\frac{P}{500\,\mathrm{d}}\right)^{0.75\pm0.3} \left(\frac{r_{gd}}{200}\right)^{-0.03\pm0.07} \tag{5.2}$$

The function for the mass-loss rate has been fitted using a non-linear least-squares-fitting technique, to all sources within the three samples and with complete data. The prescription suggests mass-loss rates of 1.06×10^{-5} $\mathrm{M}_{\odot}$ yr^{-1} for a typical source with a luminosity of 10,000 $\mathrm{L}_{\odot}$, pulsation period of 500 d, and gas-to-dust ratio of 200. This is typical for Mira variables and Galactic sources, but not the LMC sources with higher luminosities, longer pulsation periods, and higher gas-to-dust ratios. Figure 5.5 shows a comparison of the parameter dependence of the mass-loss rates computed with DUSTY, with the parameter dependence of the mass-loss rates from the new formula. There is a general correlation of mass-loss with pulsation period, and a much tighter correlation with luminosity. A Kolmogorov-Smirnov test could have been used here to quantify the correlation and determine the goodness of fit. A strong dependence of gas-to-dust ratio on the mass-loss rate in not seen within the samples. This suggests that the mass-loss is insensitive to metallicity.

Mass-loss prescriptions which include only two of the three mass-loss parameters have also been computed. These prescriptions have been compared to the three-parameter prescription on the basis of their ability to correctly predict the mass-loss rate given by DUSTY; the comparison of these prescriptions is shown in Fig. 5.6. There is little difference between the three parameter prescription and the prescription with only luminosity and pulsation period, again reflecting the insensitivity of mass-loss to gas-to-dust ratio and presumably, to metallicity.

It is possible that no single prescription can accommodate the diversity of all OH/IR stars. Individual samples have also been fitted with all three of the mass-loss parameters but cation should be used in implementing these fits. The limited ranges of the parameters within each of the three samples make these fits much less reliable; the uncertainties on the derived parameters reflect this to some extent, but the fits are overall

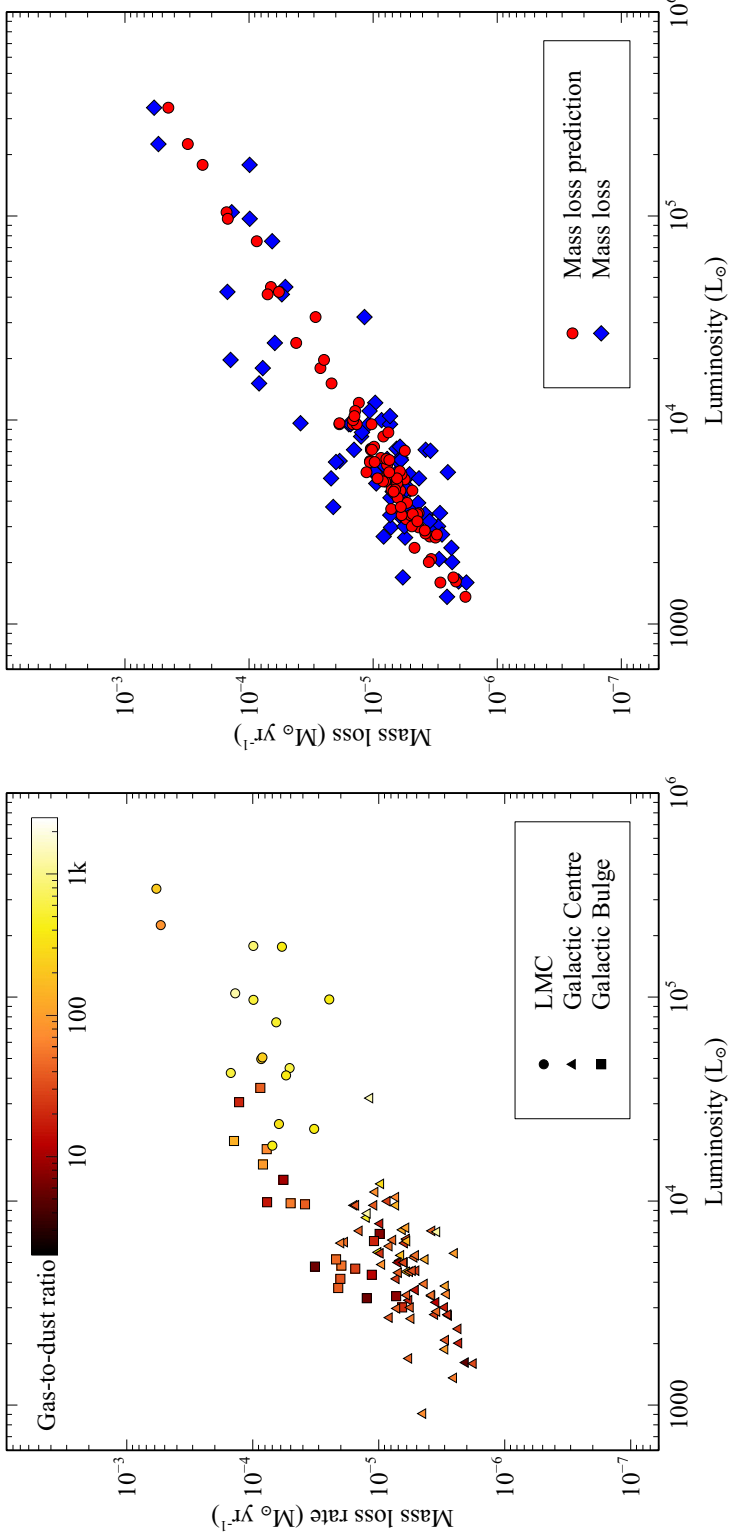

Figure 5.5: ***Left***: The mass-loss rate as a function of luminosity, with the gas-to-dust ratio represented in colour. ***Right***: The predicted mass-loss rates from the newly derived mass-loss prescription (Eq. 3) plotted in red, with mass-loss rates derived by DUSTY for sources with complete data (L, P, and r_{gd}.) in blue.

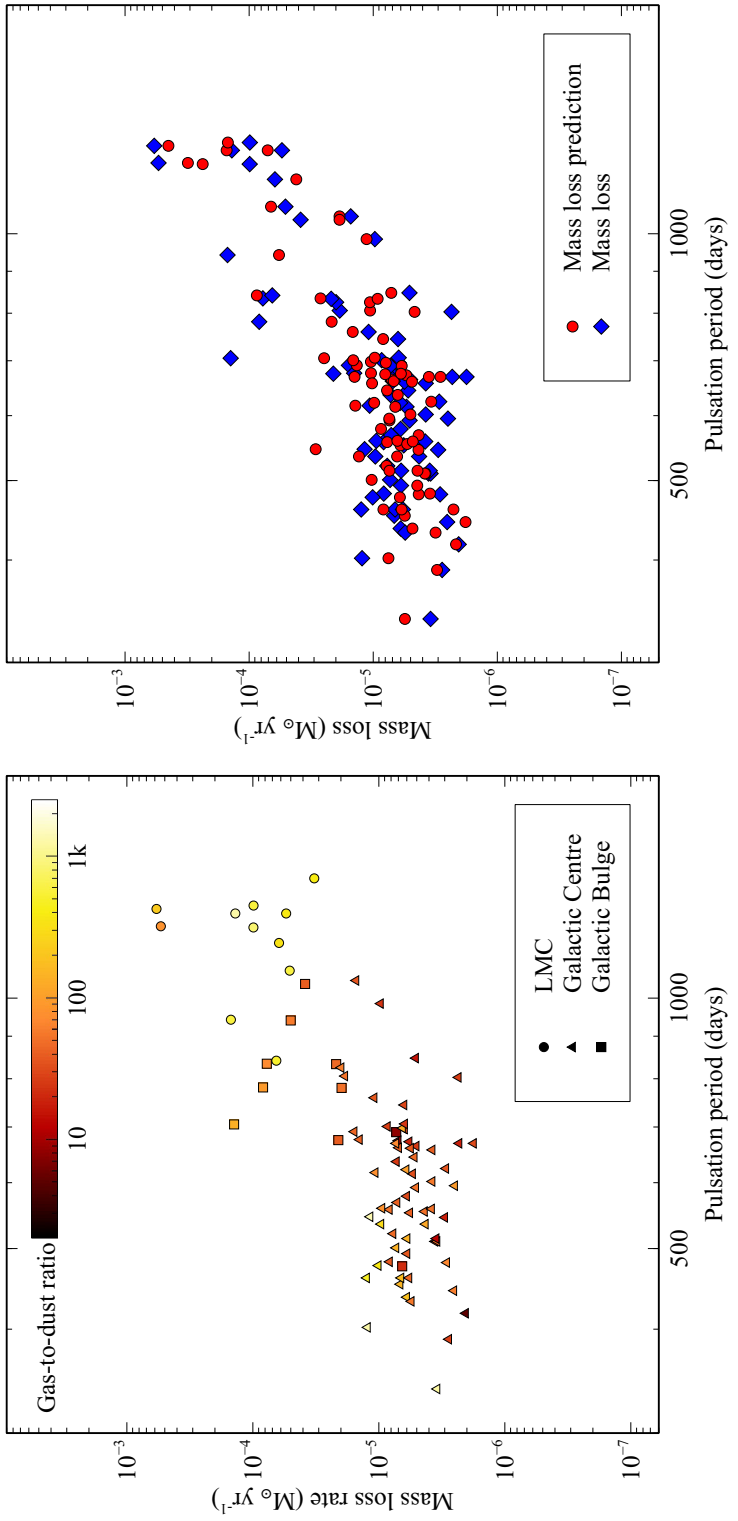

Figure 5.5: continued ***Left***: The mass-loss rate as a function of pulsation period, with the gas-to-dust ratio represented in colour. ***Right***: The predicted mass-loss rate as a function of pulsation period.

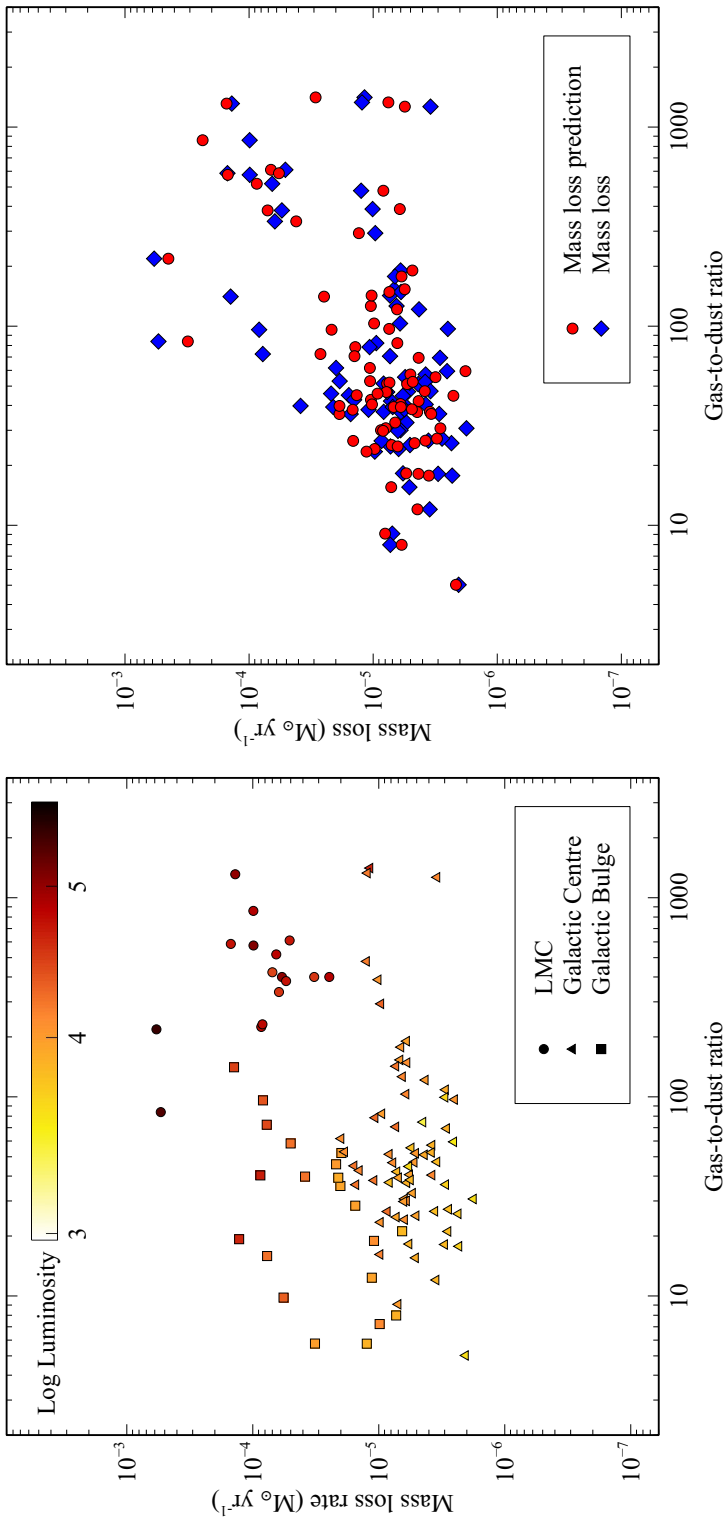

Figure 5.5: continued ***Left***: The mass-loss rate as a function of gas-to-dust ratio, with the gas-to-dust ratio represented in colour. ***Right***: The predicted mass-loss rate as a function of gas-to-dust ratio. The missing sources in the figure (as opposed to the previous figure) stem from a lack of pulsation period measurements in the Galactic bulge sample.

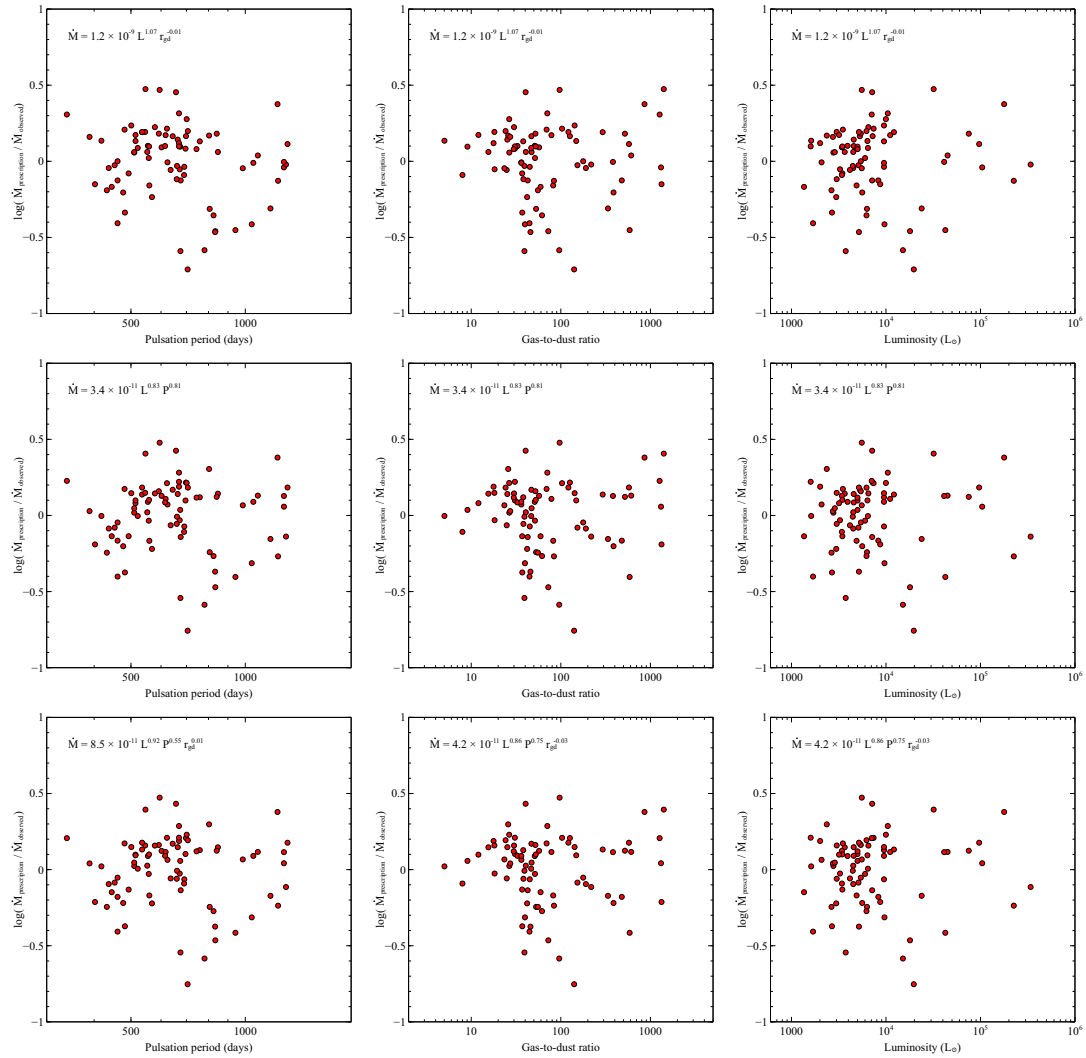

Figure 5.6: A comparison of mass-loss prescriptions. The y-axis in each figure is the log ratio of the prescription listed and the "observed" mass-loss rates derived from DUSTY. In the top two rows are prescriptions which were fitted with only two parameters and in the bottom row is the mass-loss prescription which was fitted with all three. The two-parameter prescriptions show only a slightly larger deviation from the DUSTY mass-loss rates than the three-parameter prescription.

not nearly as convincing as for the combined sample. The dependence on luminosity (the most reliably fit parameter) is very similar between the three samples, although there is a hint of a trend for a weaker luminosity dependence at higher metallicity. The fits are as follows:

$$\mathrm{GC}: \frac{\dot{M}}{\mathrm{M}_\odot\ \mathrm{yr}^{-1}} = 8.8^{+40}_{-7.3} \times 10^{-6} \left(\frac{L}{10^4\,\mathrm{L}_\odot}\right)^{0.6\pm0.1} \left(\frac{P}{500\,\mathrm{d}}\right)^{0.5\pm0.3} \left(\frac{r_{gd}}{200}\right)^{0.05\pm0.07} \tag{5.3}$$

$$\mathrm{GB}: \frac{\dot{M}}{\mathrm{M}_\odot\ \mathrm{yr}^{-1}} = 1.1^{+8.8}_{-1.0} \times 10^{-4} \left(\frac{L}{10^4\,\mathrm{L}_\odot}\right)^{0.8\pm0.1} \left(\frac{P}{500\,\mathrm{d}}\right)^{-0.3\pm0.4} \left(\frac{r_{gd}}{200}\right)^{0.5\pm0.1} \tag{5.4}$$

$$\mathrm{LMC}: \frac{\dot{M}}{\mathrm{M}_\odot\ \mathrm{yr}^{-1}} = 4.4^{+1226}_{-4.3} \times 10^{-5} \left(\frac{L}{10^4\,\mathrm{L}_\odot}\right)^{0.8\pm0.2} \left(\frac{P}{500\,\mathrm{d}}\right)^{-0.4\pm1.1} \left(\frac{r_{gd}}{200}\right)^{-0.4\pm0.2} \tag{5.5}$$

5.3.1 Interpretation of the Goldman et al (2017) mass-loss prescription

The new mass-loss prescription, based entirely on observational data, matches known physical relationships. From the equation for optical depth (equation 1 from van Loon, 2000):

$$\tau(\lambda) \propto \frac{\dot{M}}{r_{gd}\, v_{\mathrm{exp}}\, \sqrt{L}} \tag{5.6}$$

where τ is the optical depth, and from the newly derived relation for the expansion velocity (Eq. 5.1), combining these two yields $\dot{M} \propto L^{0.9}\ \tau(\lambda)\ Z\, r_{gd}$. As metallicity has been shown to be inversely proportional to the gas-to-dust ratio (van Loon, 2000), and τ is a measure of the amount of photon scattering, all that remains is $\dot{M} \propto L^{0.9}$, which is exactly what is derived with the newly derived mass-loss prescription.

The second term in the prescription is pulsation period. Modeling and constraining the pulsation period of evolved stars can be challenging with periods that range between somewhat and very irregular, especially for RSGs (Ireland, Scholz & Wood, 2008). By describing the pulsation as a harmonic oscillation where gravity, g, is the driving force, then it is expected that $2\pi/P \sim 1/t_{\rm freefall} \sim \sqrt{g(R)/R}$, where R is the stellar radius. Based on the results from Schröder & Cuntz (2007), it is found that $\dot{M} \propto 1/g$ (Fig. 5.7). This suggests that $\dot{M} \propto P^2/R$. Describing the star as a polytrope, with MR^3 is equal to a constant, it is expected that $P \propto \sqrt{R/g} \propto M^{-1/2}R^{3/2} = R^3$, and hence $\dot{M} \propto P^{5/3}$. This is a much stronger dependence on pulsation period than the newly derived prescription, $\dot{M} \propto P^{0.75}$; however, it includes the way mass-loss would increase as a result of the star being more luminous, hence larger and thus pulsating with a longer period. The relationship between mass-loss rate and pulsation period is shown in Figure 5.8, where the mass-loss rate is divided by the luminosity to isolate the dependence of pulsation period on the mass-loss rate. At a given stellar effective temperature, $L \propto R^2$, which would suggest $L \propto P^{2/3}$. Within the newly derived prescription, it is found that $\dot{M} \propto L^{0.9}P^{0.75}$. This would then suggest that the newly derived prescription has a total dependence on pulsation period according to $\dot{M} \propto P^{1.35}$. This brings it in closer (albeit not perfect) agreement with the above, simplistic expectation. It is also interesting to note that the Mira period-luminosity relationship has been found not depend on luminosity (Feast, 1996), which is consistent within these results.

Fox & Wood (1982) and Wood (1990) calculated more sophisticated models for pulsating red giants and found that $P \propto R^{1.8}$ (with some dependence on mass). Replacing the above polytrope by this relationship would yield $\dot{M} \propto P^{1.44}$, which is in remarkable agreement with the derived empirical relationship.

The last term in the prescription is the gas-to-dust ratio. The gas-to-dust ratio has been shown to inversely scale with the metal content. Past studies have shown that metallicity has little to no effect on the mass-loss rates within Galactic and Magellanic Cloud AGB and RSG stars (van Loon, 2000; van Loon et al., 2005). the relation of $\dot{M} \propto r_{gd}^{-0.03\pm0.07}$ matches this expectation and thus it can be concluded that the gas-to-dust ratio has little effect on the mass-loss of AGB stars and RSGs within the Galaxy

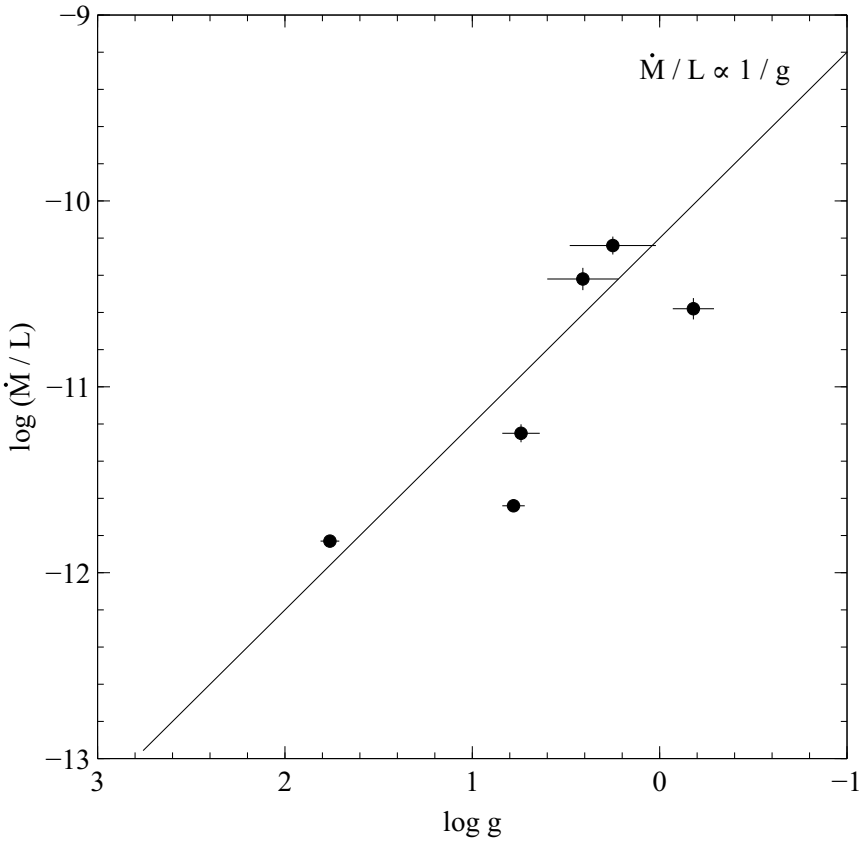

Figure 5.7: A comparison of the values of mass-loss and gravity (g) from the RSG sample from Schröder & Cuntz (2007). Their mass-loss rates have been divided by their derived luminosities, which, as is shown (Eq. 5.6), should be approximately proportional to each other for a given value of gravity. This is done to isolate the dependence of mass-loss rate on gravity.

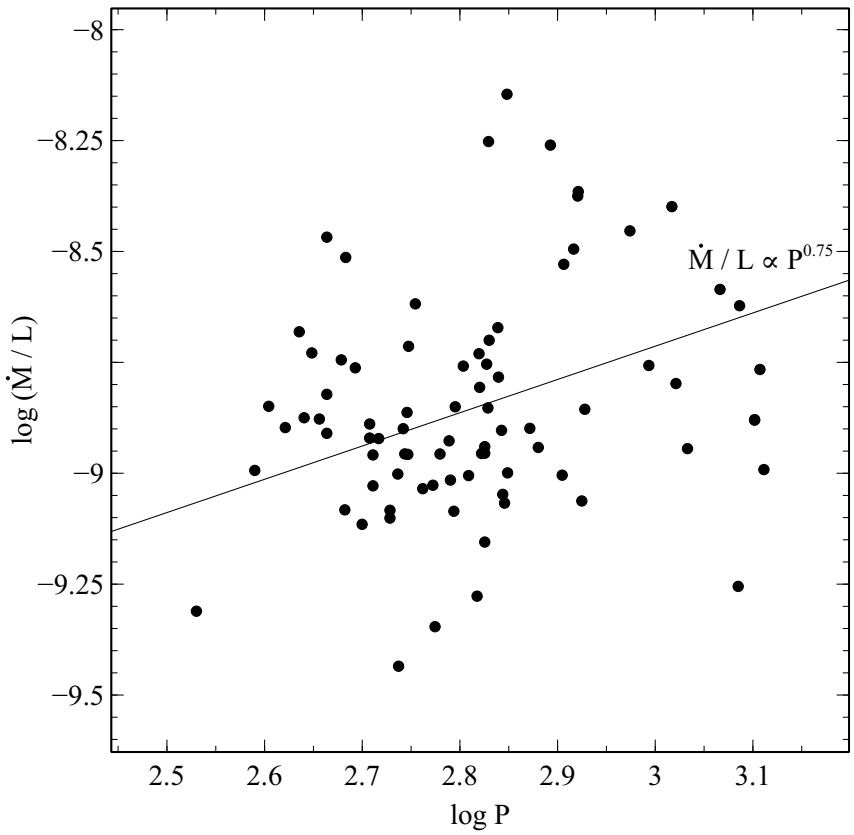

Figure 5.8: A comparison of mass-loss rate against pulsation period. The mass-loss rates have again been divided by their derived luminosities to isolate the dependence of mass-loss rate on pulsation period.

and the LMC. Though the wind is, the mass-loss itself does not appear to be driven by dust; the mass-loss rate is probably set by pulsation and/or other physical mechanisms originating in the stellar photosphere.

The new mass-loss prescription uses three stellar parameters as gauges of physical differences within the sample. In general, luminosity is expected to give a value for the initial mass, gas-to-dust ratio a value for the metallicity, and pulsation period a value for the precise evolutionary stage within the superwind phase. It is expected that all three parameters affect all of these physical differences to some degree.

5.4 Comparison to previous prescriptions

As was discussed in §1.8, most mass-loss prescriptions of AGB and RSG stars typically focus on specific stages of mass-loss, and are derived using observational data. Past mass-loss prescriptions like the Reimers law (Reimers, 1975), and the updated Reimers law (Schröder & Cuntz, 2005) are used to calculate the mass-loss rates in the pre-dust driven wind phase. These are based on the mass-loss of red giant branch stars and use luminosity, stellar radius, and mass; the updated prescription also uses effective temperature and gravity. Other prescriptions like that of van Loon et al. (2005) focus on mass-loss within the superwind phase and are based on the SED modelling of oxygen-rich AGB and RSG stars within the LMC. In-depth comparisons of several previous mass-loss prescriptions have been done by Mauron & Josselin (2011) and Rosenfield et al. (2014).

The values for expansion velocities and mass-loss rates, computed by DUSTY, have been compared with the Galactic RSG sample from Mauron & Josselin (2011), as shown in Figure 5.9 and 5.10. The Galactic RSGs are expected to have gas-to-dust ratio ~ 500 and fit well between the Galactic and LMC samples. The mass-loss rates shown were derived primarily by modelling the wind speeds from CO emission. This excludes the mass-loss rates of α Sco, derived by modelling the H II region (Reimers et al., 2008), of α Ori, derived by fitting C I lines (Huggins et al., 1994), and of VY CMa and μ Cep, derived by fitting the SEDs with DUSTY models (Shenoy et al., 2016). As these were

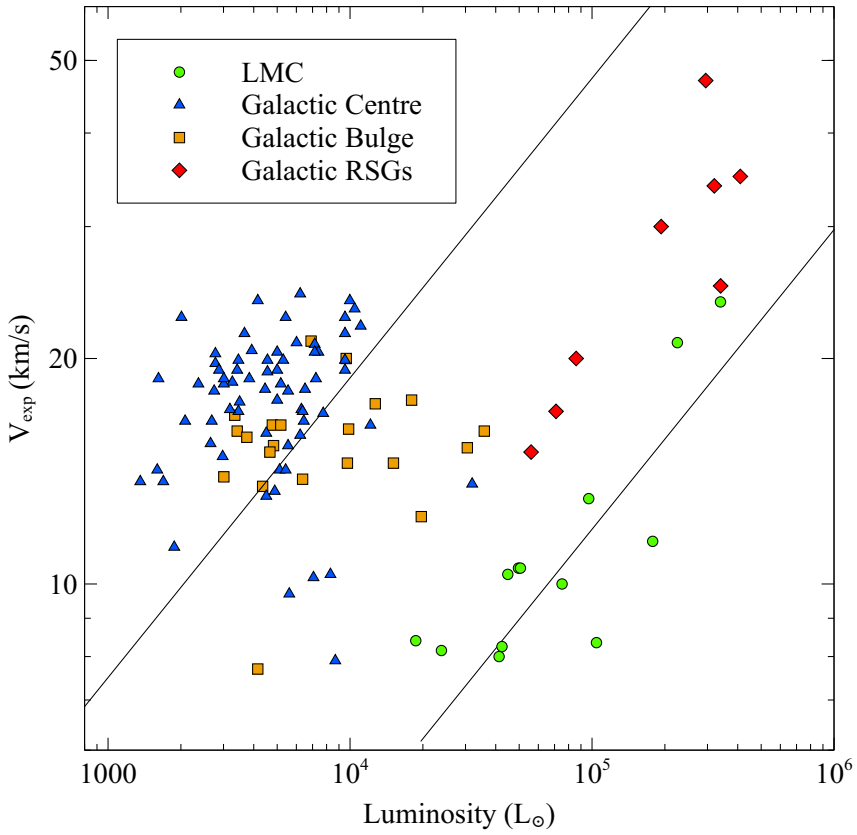

Figure 5.9: The observed wind speed as a function of luminosity as shown in Fig. 5.1 with the Galactic RSG sample from Mauron & Josselin (2011).

derived using various methods and making different assumptions, caution must be used in comparing them individually. However, this sample will be used to understand how red supergiants fit within a more general picture of mass-loss in evolved stars. Also shown are the calculated Galactic RSG mass-loss rates derived using the newly derived mass-loss prescription, in which a gas-to-dust ratio of 500 is assumed; pulsation periods have been taken from Kiss, Szabo & Bedding (2006).

The literature values for mass-loss, which again use different methods of deriving the wind speeds and mass-loss rates, are generally much lower than the prescription values for the mass-loss rates and they have been plotted in Figure 5.10. Along with more accurate distances for the Galactic sources, and thus luminosities and mass-loss rates,

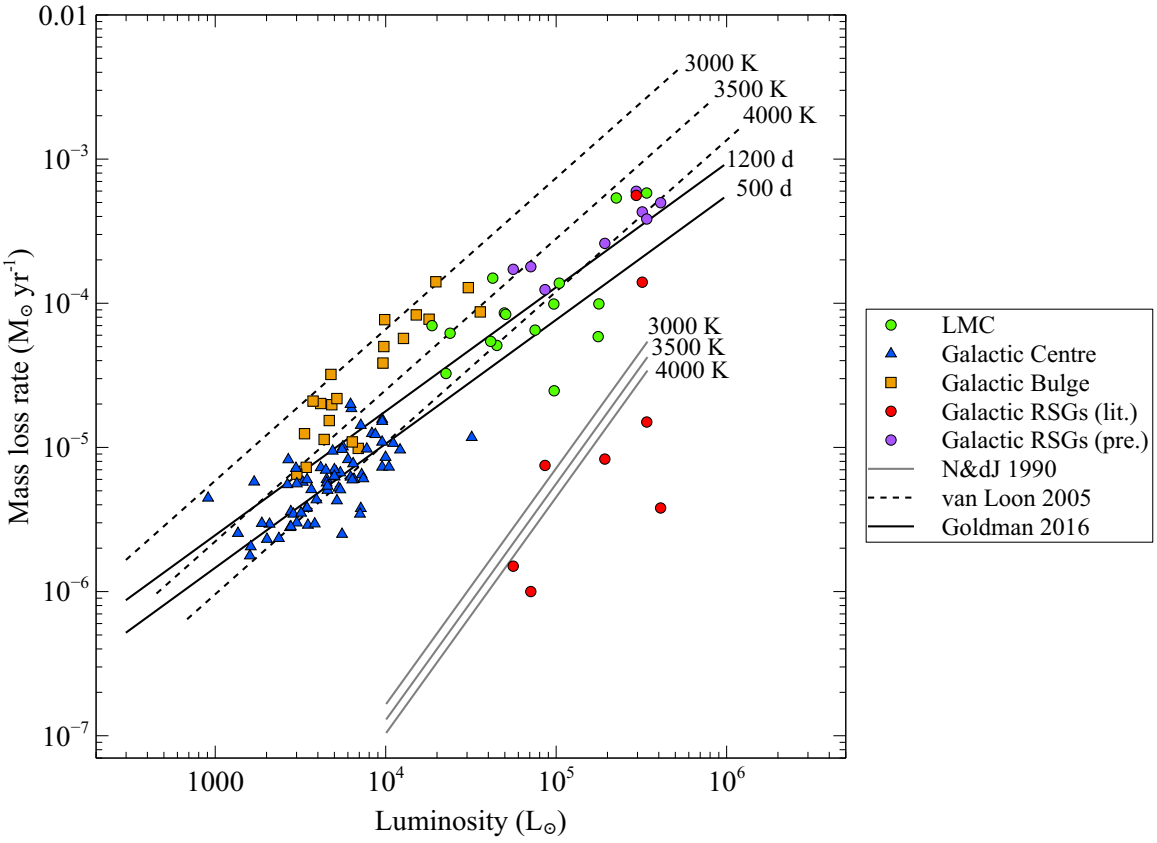

Figure 5.10: The observed mass-loss rates as a function of luminosity as shown in Fig. 5.5, with the Galactic RSG sample from Mauron & Josselin (2011); updated literature mass-loss rates for VY CMa and μ Cep have been used from Shenoy et al. (2016). Literature mass-loss values are shown (Galactic RSGs lit.) as well as the calculated mass-loss rates (assuming an $r_{gd} = 500$) using the mass-loss prescription (Galactic RSGs pre.) and the pulsation periods from Kiss, Szabo & Bedding (2006); NML Cyg pulsation period is from Monnier et al. (1997). Also plotted are the mass-loss prescriptions by Nieuwenhuijzen & de Jager (1990) and van Loon et al. (2005), as well as the newly derived prescription (Goldman 2016), with a range of values for unknown variables (either effective temperature or pulsation period).

new data have allowed for a more accurate measure of the optical depth. More accurate *Spitzer* data have allowed for a better measure of IR excesses as well as a decrease of confusion from contaminating sources within the observing fields. The new mass-loss prescription has also been compared with previous mass-loss prescriptions (Fig 5.10) plotting different values for unknown variables (either effective temperature, expansion velocity, or pulsation period). The comparison suggests that some of the sources within the Galactic RSG sample may not be within the superwind phase of mass-loss. The evolutionary stages of these sources will be discussed further in the following section.

5.5 Fundamental stellar parameters and mass-loss

The current analysis covers highly evolved AGB and RSG stars with a luminosity range from 2,000 to over 300,000 $L_{\odot}$ and a metallicity range of a half to twice solar. This range allows us to draw conclusions about the mass-loss mechanism and how it is affected by fundamental differences within the stars. It is expected that L, r_{gd}, and P are related to mass, metallicity, and evolutionary phase. While the links between luminosity and initial mass, and r_{gd} and metallicity are more established (e.g., Blöcker, 1995; Vassiliadis & Wood, 1993), evidence for a link between pulsation period and evolutionary stage is still unclear (Groenewegen et al., 2007; Sloan et al., 2012). As the stars progress through the superwind stage, stellar pulsation will become stronger and slower. The expectation is that the pulsation period may be able to give us an indication of the source's stage within the superwind phase. Each of these relationships will be discussed in the following sections.

Mass (initial and current): The initial mass will have a dramatic impact on the evolution of these stars. Dredge-up efficiency and hot-bottom burning will vary with initial mass; thus, the C/O ratio of these stars will depend on the initial mass (e.g., Boothroyd, Sackmann & Wasserburg, 1995; Karakas, 2010). In terms of mass-loss, a higher initial mass will allow the star to get to a higher luminosity before the onset of the

superwind phase, thus resulting in a higher mass-loss rate. As these sources reach more advanced stages within the superwind phase, their mass will decrease as their luminosity remains the same. It is expected that a higher luminosity will result in a higher mass-loss rate. In these stars, it is known that the dust-formation zone will depend on luminosity, being farther away for more massive stars. Looking at the ratio of luminosity and current mass (L/M), the higher luminosity RSGs ($\sim 200,000$ $L_{\odot}$) and lower luminosity sources ($\sim 50,000$ $L_{\odot}$) have masses of around 20 and 5 $M_{\odot}$ respectively, and quite similar L/M ratios. Assuming this ratio to be constant within the samples, the ratio of radiation flux and gravity is expected to be independent of radius as both depend on radial distance as r^{-2}. The acceleration is determined by the *difference* between the radiation pressure and gravity, which, at any given radius is larger for more massive (more luminous) stars with the same L/M ratio. However, the wind is driven by dust grains which condense at a distance where the dust grain equilibrium temperature matches the condensation temperature. This happens at a certain photon flux, i.e. farther from a more luminous star by a factor of $R^2 \equiv L$, thus balancing out the larger difference between radiation pressure and gravity at a given distance. But because the area through which the mass flows also increases in proportion to R^2, the total amount of mass flowing through the area should increase accordingly, and thus, $\dot{M} \propto L$. This does not however take into account the complex episodic and clumpy dust formation. Also this requires that larger stars have adequately high number densities at larger radii, which do scale roughly with stellar radius.

As these sources lose mass in the superwind phase and remain at a constant luminosity, L/M will increase, making it easier to drive the wind, whereas the decrease in mass will drive a direct increase in P. The source will then evolve to longer pulsation periods at a constant luminosity; it is expected that this is the case for the extreme Galactic bulge sample. It is still unclear whether the simultaneous increase in pulsation period affects the mass-loss. With longer and larger pulsations, as well as reduced gravity at the surface of a larger star which has lost mass, this should allow stars to levitate more material out to form dust and more easily drive mass-loss. It is expected that L/M affects the mass-loss rate directly, and indirectly through changes in the pulsation period.

However, at this stage, these relationships cannot be actually quantified.

Metallicity: Gas-to-dust ratios have been shown to scale inversely proportionally with metallicity (van Loon, 2000), and thus, can be used to understand the effects of metallicity. Metallicity will have a dramatic impact on the dust production of oxygen-rich AGB and RSG stars as well as the chemical composition of the dust itself (Jones 2013). Unlike carbon stars, these stars can not create the raw materials for dust production. Past studies have shown that while nearby Galactic and Magellanic Cloud oxygen-rich stars have similar total mass-loss rates at higher luminosities, the dust mass-loss rates show a strong dependence on metallicity (Wood, Habing & McGregor, 1998; van Loon, 2000; Lagadec et al., 2008); this is consistent with these results.

Observations of Galactic and Magellanic Cloud carbon AGB stars have been interpreted to show that the quantity of carbon dust produced in both environments is the same. It has also been suggested that LMC carbon stars collectively produce more dust than their oxygen-rich counterparts (Boyer et al., 2011; Matsuura, Woods & Owen, 2013; Sloan et al., 2016). It was suggested by Habing (1996) that carbon-rich LMC AGB stars may have similar gas-to-dust ratios to those of Galactic samples. If this is the case, it also stands to reason that they will have expansion velocities comparable to those of the Galactic samples. However, van Loon et al. (2008) present evidence suggesting that the effect of primary carbon may not be as large, which would mean that also Magellanic carbon star winds are expected to be less dusty, and slower, than solar-metallicity carbon stars.

It was predicted that AGB mass-loss would be dependent on metallicity as an increase in dust optical depth may cause an increase in the number of absorbing and scattering events of photons on dust grains and therefore an increase in the net driving force of the dust-driven wind (Gail & Sedlmayr, 1986). While the dust content and driving of the wind depend on metallicity, there is no evidence to suggest a metallicity dependence on the mass-loss. It is expected that at lower metallicities, the mass is lost in a slower denser outflow (as has been seen in the slower gas wind speeds) with the same

net mass-loss efficiency.

Evolutionary phase: As the sources become more evolved and more extreme, the strength and cycle length of stellar pulsations will increase. In theory the pulsation period at a given luminosity can be used as a gauge of the stage within the superwind phase. As mass decreases due to mass-loss, the pulsation period increases, and reduced gravity at the surface leads to increased mass-loss. As the mass-loss ramps up, the gas-to-dust ratio will also change. As the mass-loss in the sources has been found to be insensitive to metallicity, this implies that the sources are in the superwind phase where they have reached maximal dust formation efficiency.

Stellar pulsations can be affected by chemical differences in the star. The pulsation amplitude of oxygen-rich AGB stars may be affected by metallicity as TiO absorption is affected by metallicity, but it is unclear if the pulsation period will be affected by changes in metallicity as it is determined deeper inside the star. The efficiency of the dust formation will also vary with evolutionary phase which may leave some evolved stars like Betelgeuse with little dust van Loon (2013). However, this source has not entered its superwind phase and would be incompatible with the newly derived mass-loss prescription.

This work has resulted in a new mass-loss prescription derived using several stellar samples selected in the superwind stage of mass-loss. The Galactic RSG sample has also been included for comparison, as these sources seem to follow a similar mass-loss mechanism. However, this sample contains sources not within the superwind phase, and the prescription may not be able to provide a realistic estimation of the mass-loss rate of these sources. In Fig. 5.10, the Nieuwenhuijzen and de Jager prescription fits the bulk of the RSG sample much better. Two of these sources, VY CMa and NML Cyg with mass-loss rates of 5.4×10^{-5} and 1.4×10^{-5} $M_{\odot}$ yr^{-1}, respectively, fit well within the other samples. It is surprising that, given VY CMa shows silicate in emission rather than absorption (Harwit et al., 2001), this source would show such a high mass-loss rate compared to the rest of the sample. However, these sources have some of the highest

luminosities and the lowest effective temperatures of the RSG sample, and may thus be comparable to the sample, whereas the remaining RSGs may be at an early evolutionary stage. A similar gap in mass-loss rates of LMC RSGs of the order of 2 magnitudes or a factor of 100 has been found in the past by van Loon et al. (1999). It should be noted that these types of sources also evolved rapidly with significant changes in mass loss as has been seen in VY CMa in the past century (Decin et al., 2006). It appears that at least within RSGs another parameter is affecting the mass-loss.

5.6 LMC Conclusions

The recent results from a survey of 1612-MHz OH maser emission in the LMC have been presented. Four new sources have been discovered and the number of reliable wind speeds has been increased from five to thirteen. The expansion velocities derived from the maser sources fit well with the updated relation for dust-driven winds. A method of deriving gas-to-dust ratios of OH/IR stars has also been developed using modelled spectral energy distributions and scaling the results with the expansion velocities derived from maser observations. Furthermore these new results have been used to develop an empirical mass-loss prescription that includes the effects of metallicity and luminosity. The results show a correlation of mass-loss rate with pulsation period, with an even tighter correlation between mass-loss rate and luminosity. A clear link is seen between expansion velocity and gas-to-dust ratio, yet the gas-to-dust ratio has little effect on the mass loss of AGB stars and RSGs. This suggests that mass-loss rate is (nearly) independent of metallicity between a half and twice solar within the superwind phase.

6 Extending to lower metallicity environments[9]

6.1 The SMC

As opposed to the LMC at 50 kpc, the SMC lies further at 60 kpc (Feast, 2013; Szewczyk et al., 2009). The SMC also has a much less desirable inclination angle at 62° as opposed to the LMC's more face-on angle between 23 and 37° (Subramanian & Subramaniam, 2009, 2010, 2011). As was discussed in §1.7.2, the Magellanic Clouds have very different SFHs. And the SMC is much smaller in size with a diameter around half that of the LMC. Despite these facts, the SMC has an average metallicity of around [Fe/H] = −0.68 dex (Luck et al., 1998), which corresponds to one fifth solar metallicity and presents us with a suitable nearby environment to further test the effects of metallicity on the circumstellar environment of evolved stars.

6.1.1 Previous searches for oxygen-rich dusty stars in the SMC

Two OH maser studies have targeted SMC circumstellar OH maser emission in the past (discussed further in Appendix D). The deepest observation resulted in a noise level $\sim$ 8 mJy. The Infrared Astronomical Satellite (*IRAS*; Neugebauer et al., 1984), the Midcourse Space Experiment (*MSX*; Price et al., 2001), The Two-Micron All-Sky Survey (*2MASS*) and more recently the *Spitzer Space Telescope* (Werner et al., 2004) have revealed large samples of AGB and RSG stars in the SMC (Wood et al., 1992; Boyer et al., 2011; Kraemer et al., 2017). However the search for deeply embedded sources

[9]The following chapter is based on submitted work entitled '*A dearth of OH/IR stars in the Small Magellanic Cloud*'; Goldman S. R., van Loon J. Th., Goméz J. F., Green J. A., Zijlstra A. A., Nanni A., Imai H., Whitelock P. A., Groenewegen M. A. T. and Oliveira J. M. 2017, arXiv:1710.02184.

All work was conducted by myself.

continues. Based on MSX and 2MASS data, the IR-bright sample from the MSX survey was expected to be composed of one-third carbon stars and one-half OH/IR stars in the SMC. Instead, two-thirds of the sample were found to be carbon stars and no OH/IR stars were detected, with the remaining third composed of RSGs, post-AGB stars, YSOs, PN, and oxygen-rich stars without significant dust. .

Other recent searches have discovered a few candidate OH/IR stars, some of which have been observed in the IR (Jones et al., 2015; Kraemer et al., 2017), and some at radio frequency, but only a few deeply embedded evolved stars like those within the LMC or the galaxy, either carbon- or oxygen-rich, have been found in the SMC (van Loon, Marshall & Zijlstra, 2005; van Loon et al., 2008; Lagadec et al., 2007). It is not a requirement for OH/IR stars to have a high self-extinction, but as the maser luminosity is dependent on the dust, the most luminous maser sources are expected to.

As was noted by Ventura et al. (2016), the most obscured carbon stars in the LMC and SMC have initial masses of $2.5 - 3$ $M_{\odot}$ and ~ 1.5 $M_{\odot}$, respectively, as a result of different SFHs. This has lead to a difference in initial stellar masses in their Thermally-Pulsing AGB (TPAGB) phase in the Magellanic Clouds.

Moving to the higher mass stars, previous searches have found a small sample of dusty RSGs in the SMC, but they are not obscured to the same degree as the OH maser-emitting LMC RSGs (Bonanos et al., 2010). They are both warmer and less dusty than the massive O-rich OH maser-emitting AGB stars and RSGs (called OH/IR stars) in the LMC and the Galaxy. While these stars are few, the results of the Surveying the Agents of Galaxy Evolution in the tidally stripped, low metallicity Small Magellanic Cloud (SAGE-SMC) survey (Gordon et al., 2011) suggest that the small known sample of dusty RSGs within the Magellanic Clouds contributes more dust than the entire sample of optically bright RSGs (Bonanos et al., 2010). Hence it is critically important to obtain measurements of the expansion velocities of these sources to constrain current wind-driving models.

Table 6.1: The most promising maser candidates in the SMC. Listed values are derived bolometric luminosities from SED fitting by DUSTY models (described further in §6.4.5), I-band pulsation periods and amplitudes from Soszyński et al. (2011), $J-K$ colours from 2MASS (Cutri et al., 2003), *Spitzer* MIPS (Rieke et al., 2004) 24 μm fluxes (F_{24}) from Boyer et al. (2011), and spectral types (van Loon et al., 2008, and references therein).

Object name	L (10^3 $L_\odot$)	Pulsation period (d)	Pulsation amplitude (mag)	$J-K$ (mag)	$F_{24\mu m}$ (mJy)	Spectral type
Parkes targets						
IRAS 00483−7347	138	1859	1.7	2.8	660.0	M8
IRAS F00486−7308	41	1062	2.7	1.6	91.1	M4
IRAS 00591−7307	78	1092	1.9	1.3	95.4	M5e
IRAS 01074−7140	34	523	2.8	1.2	396	M5[d]
ATCA sources						
OGLE SMC-LPV-15504	45	543	0.8	1.3	31.6	M3−4[c]
2MASS J01033142−7214072	7	471	1.8	3.7	19.2	
HV 12149	48	769	2.3	1.4	12.7	M8[b]
OGLE SMC-LPV-14322	11	483	1.9	3.5	19.0	
2MASS J00592646−7223417	8			> 4.4	18.9	
BMB-B75	58	761	2.1	1.3	92.0	M6[a]
OGLE J004942.72−730220.4	8	563	0.4	3.9	27.8	
MSX SMC 018	60	897	2.5	2.5	262.0	

References: [a]Blanco, Blanco & McCarthy (1980) [b]González-Fernández et al. (2015) [c]Massey et al. (2007) [d]Whitelock et al. (1989).

6.2 Description of the Sample

Past observations have succeeded in detecting interstellar OH maser emission in the SMC (Breen et al., 2013), but have failed to detect circumstellar OH maser emission (van Loon, 2012). Luminous evolved stars have been targeted to investigate and scrutinize the most promising candidates for circumstellar maser emission to date (Table 6.1). The targets were chosen based on results from Elias, Frogel & Humphreys (1980, 1985); Whitelock et al. (1989); Groenewegen & Blommaert (1998), as well as pulsation periods newly derived from the Optical Gravitational Lensing Experiment (OGLE) (Soszyński et al., 2011).

The observations include four sources targeted for being dusty evolved oxygen-rich sources with the Parkes radio telescope as well as an ATCA survey with four fields spread across the SMC. With Parkes four of the best candidates for OH maser emission in the SMC have been targeted. With the ATCA's FWHM primary beam at 1612 MHz of $29'$, a significant portion of the SMC bar region has been surveyed (Fig. 6.1). Spectra for seven sources have been obtained that are known to be mid−late M-type oxygen-rich sources, one source that is likely to be oxygen-rich (MSX SMC 018), and four sources that are likely carbon stars.

Detectable maser emission was expected in several of the observed sources. The 1612-MHz maser is pumped by IR radiation at 35 μm with a typical efficiency of 23% (discussed further in §6.4). Simplistically assuming this efficiency, the maser flux of the targeted source IRAS 00483−7347 should be over 19 times the noise level of the observation.

6.2.1 Observations

Radial velocities mentioned in this paper are in a barycentric reference frame. The systemic radial velocity of the SMC is ≈ 146 km s^{-1} but radial velocities of stars and gas within the SMC vary by about ± 50 km s^{-1} around this value (Hatzidimitriou et al., 1997; Stanimirovic et al., 1999).

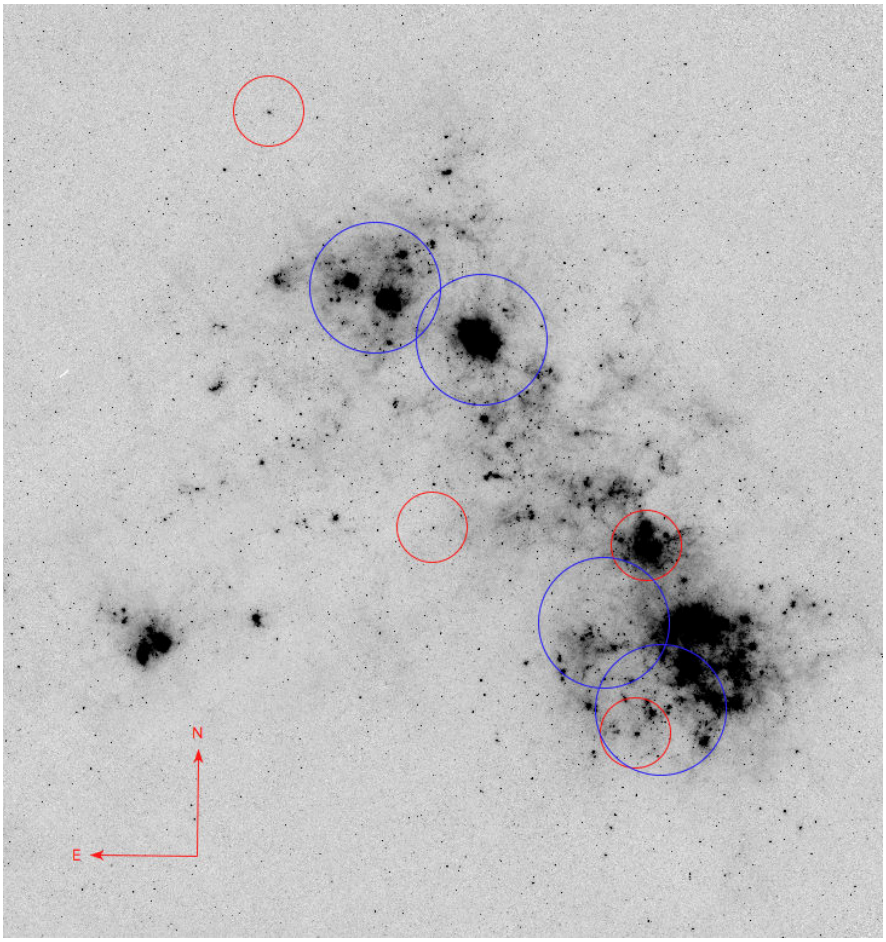

Figure 6.1: The *Spitzer* MIPS 24 μm image of the SMC overlaid with the full width at half-maximum (FWHM) of the primary beam at 1612 MHz of the ATCA interferometric observations (shown in blue) and Parkes single-dish observations (shown in red).

Table 6.2: Results of OH maser searches in the Small Magellanic Cloud. Values for the rms are taken from displayed spectra for Parkes, and calculated over the region of the three-dimensional datacube of which the spectrum was extracted for ATCA.

Target name	RA (J2000)	DEC (J2000)	On-source Integration time (h)	rms (mJy)
Parkes observations				
IRAS 00483−7347	00h 50m 09s	−73° 31′ 29″	58.8	3.7
IRAS F00486−7308	00h 50m 31s	−72° 51′ 30″	31.1	4.5
IRAS 00591−7307	01h 00m 48s	−72° 51′ 02″	10.0	7.7
IRAS 01074−7140	01h 09m 02s	−71° 24′ 10″	61.9	3.4
ATCA observations				
SMC North	01h 03m 60s	−72° 01′ 00″	11.4	8
SMC Centre	00h 59m 00s	−72° 10′ 60″	10.0	9
BMB-B75	00h 52m 13s	−73° 08′ 53″	11.2	10
SMC South	00h 48m 60s	−73° 25′ 60″	8.4	9

Parkes observations

The following section will describe archival (reprocessed) Parkes observations taken in 2003 from August 18 to 20 (Marshall et al., 2004), and new observations taken in 2005 from July 7 to 13 and August 13 to 19, observing the 1612-MHz OH satellite line (Project P433; PI: Jacco van Loon). With the multibeam receiver and multibeam correlator, a dual polarization setup was used with 8-MHz bandwidth and 8192 channels yielding a 0.18 km s^{-1} $channel^{-1}$ velocity resolution; the observations used a frequency-switching calibration technique with a switching frequency of 0.5 MHz (93 km s^{-1} at 1612 MHz) and a 14′ beam. IRAS 00591−7307 was observed in 2003, IRAS F00486−7308 and IRAS 01074−7140 in 2005, and IRAS 00483−7347 in both epochs.

ATCA observations

The data were taken in 2012 between January 1 and January 5 (C2521; PI: Jacco van Loon), and in 2015 on June 12 (C2996; PI: Goldman). Four observations of varying

integration times between 8 and 11 hours were done for each targeted region (displayed in Table 6.2). The observations were done with the CFB 1M-0.5k correlator configuration with zoom-bands (Wilson et al., 2011) and the 6A array configuration, and observed all four OH maser transitions at 18 cm (1612, 1665, 1667, and 1720 MHz). The bandwidth used was 1 MHz, corresponding to zoom-band velocity widths of $\gtrsim 340$ km s^{-1}, and the FWHM of the primary beam of ATCA at 1612 MHz is $29'$. Three of the observations were blind maser searches that targeted two star formation regions in the north and another in the south (Fig. 6.1). These observations used PKS 1934-638 and PKS 0823-500 as flux and bandpass calibrators and PKS 2353-686 and PKS 0230-790 as secondary calibrators. The fourth observation targeted the region covering the evolved star BMB-B75 toward the southern SMC field and used PKS 1934-638 as a bandpass and a flux calibrator and PKS J0047-7530 as a secondary calibrator.

6.2.2 Data reduction

Parkes data reduction

Using the CASA ASAP toolkit (McMullin et al., 2007), spectra were extracted for each of the four targeted sources. Employing a frequency-switching calibration, out-of-band scans were subtracted to ensure a flat baseline. The spectra of IRAS 00483−7347, synthesised from a combination of both epochs, and those of the remaining targets are displayed and discussed in §6.3. The resulting spectra were resampled to a resolution of 0.5 km s^{-1}. This was done to mitigate large spikes from RFI while preserving adequate spectral resolution.

ATCA data reduction

The ATCA data were inspected, flagged, and calibrated using MIRIAD (Sault, Teuben & Wright, 1995). The visibility data were then transformed into three-dimensional data cubes, weighting the visibilities naturally. The source-finding package DUCHAMP (Whiting, 2012) was used to search for maser sources within the FWHM of each of the

fields. For the resulting peaks, the intended targets, and any other potential targets from Boyer et al. (2011), Riebel et al. (2012), or SIMBAD, a spectrum was extracted for a region the size of the synthesized beam ($\sim 7''$). All overlapping fields were mosaicked, and DUCHAMP was used to search within the ATCA's FWHM primary beam, centred between the mosaicked fields. The resulting spectra were resampled to a resolution of 0.5 km s^{-1}, as was done with the Parkes spectra.

6.3 Results

The targeted and blind maser searches within the SMC have yielded no clear OH maser emission. This is the case for the 1612-MHz OH observations (Fig. 6.2), as well as the 1665-, 1667-, and 1720-MHz OH maser observations; all OH mainline observations are shown in Appendix C. The average sensitivities of the 1612-MHz observations are listed in Table 6.2. There are several peaks within the targets' OH maser spectra that may in fact be maser emission, but have low signal-to-noise ratios, most of which are below 3σ. While seemingly unsuccessful, these observations have in fact given us valuable upper limits. In the following sections new limits will be employed to draw conclusions about the SMC, its OH/IR population, and what can be predicted for future maser searches.

The H I column density has shown to be a good indicator of the likely systemic velocities of the sources. In addition to the Parkes and ATCA observations, 1420-MHz H I data from the combined ATCA and Parkes multibeam H I maps (Stanimirovic et al., 1999) has also been included. The survey covers an area of 20 square degrees with a velocity resolution of 1.6 km s^{-1}, a velocity range from $\sim 90 - 215$ km s^{-1}, and an angular resolution of $98''$ (FWHM). For each source in the SMC sample, a spectrum was extracted using a $1'$ region centred on the sources. The resulting spectra have been plotted below each maser spectra. While some of the sources lie outside these H I regions, they provide supporting evidence for sources which lie in higher density regions of the SMC. No indication of maser emission has been found within any of the observations, but each will be discussed in turn remarking on interesting peaks in the spectra to aid in

future maser searches.

Parkes targets

The four Parkes targets are IRAS 00483−7347, IRAS F00486−7308, IRAS 00591−7307, and IRAS 01074−7140. All of these sources have characteristics typical of OH maser sources (Table 6.1) and show 10 μm silicate features in emission, confirming they are oxygen-rich (Groenewegen et al., 1995; Lebouteiller et al., 2011). IRAS 00483−7347 is the best candidate for OH maser emission with an expected mass of $6 - 7$ $M_{\odot}$ (Dell'Agli et al., 2015), and has been found to be the most massive HBB AGB star in the SMC from its large Rb enhancement (García-Hernández et al., 2009). It has been suggested to be a strong candidate for a super-AGB star (Groenewegen et al., 2009), which should not affect the maser emission, but may explain its peculiarity among the other SMC targets. IRAS F00486−7308 has shown strong molecular bands around 3 μm, indicative of an advanced evolutionary stage where the star is cooler with stronger pulsations capable of extending the molecular atmosphere (van Loon et al., 2008). IRAS 01074−7140 is very bright in the IR ($F_{24} = 0.4$ Jy) but does not have a particularly reddened colour or long pulsation period. This source has also shown to be Li-enhanced, indicative of HBB (Whitelock et al., 1989; Smith et al., 1995).

Within the sources' 1612-MHz spectra there is no clear indication of OH maser emission, but several interesting peaks are present in the spectra. In the OH observation of IRAS 00591−7307 a small increase in flux is seen around 132 km s^{-1} which may indicate maser emission. While the integrated flux over this peak is above 2σ, further observations will be needed to confirm this. In the spectrum of IRAS 01074−7140 there is a large negative spike at 237 km s^{-1}, which is a result of off-scan RFI subtracted in the frequency-switching baseline subtraction, but also shows several small peaks at 180 and 200 km s^{-1}, with flux densities above 2σ. These potential features again are mentioned to aid further investigation.

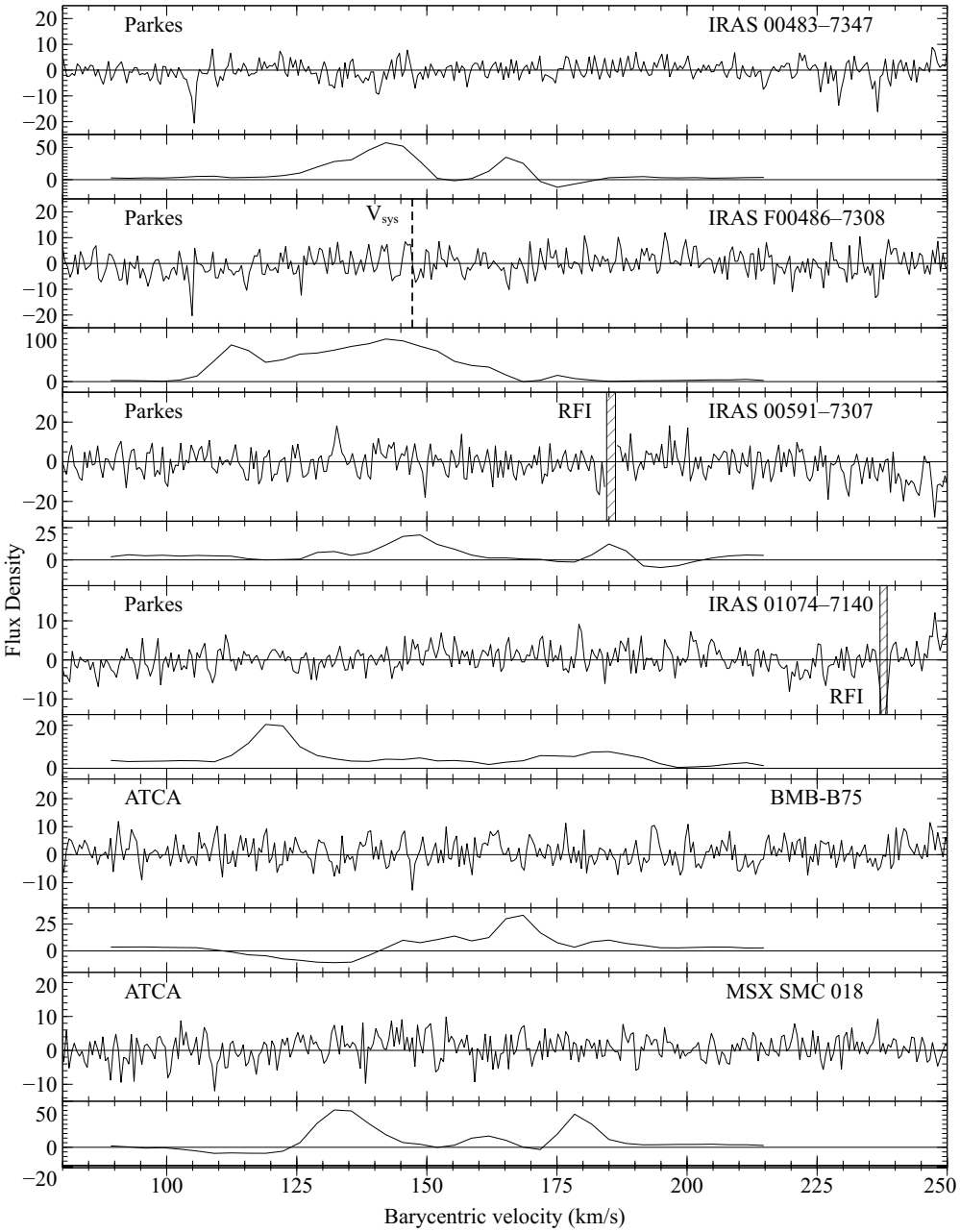

Figure 6.2: OH 1612-MHz maser observations of the SMC targets resampled to a velocity resolution of 0.5 km s^{-1}. Below the maser spectra (flux density in mJy) are H I spectra (flux density in Jy) to indicate the likely systemic velocity of the source. Also shown are measured systemic velocities (V_{sys}) for IRAS F00486−7308 and OGLE SMC-LPV-15504 from González-Fernández et al. (2015) and Massey & Olsen (2003), respectively; areas of Radio Frequency Interference (RFI) are also indicated.

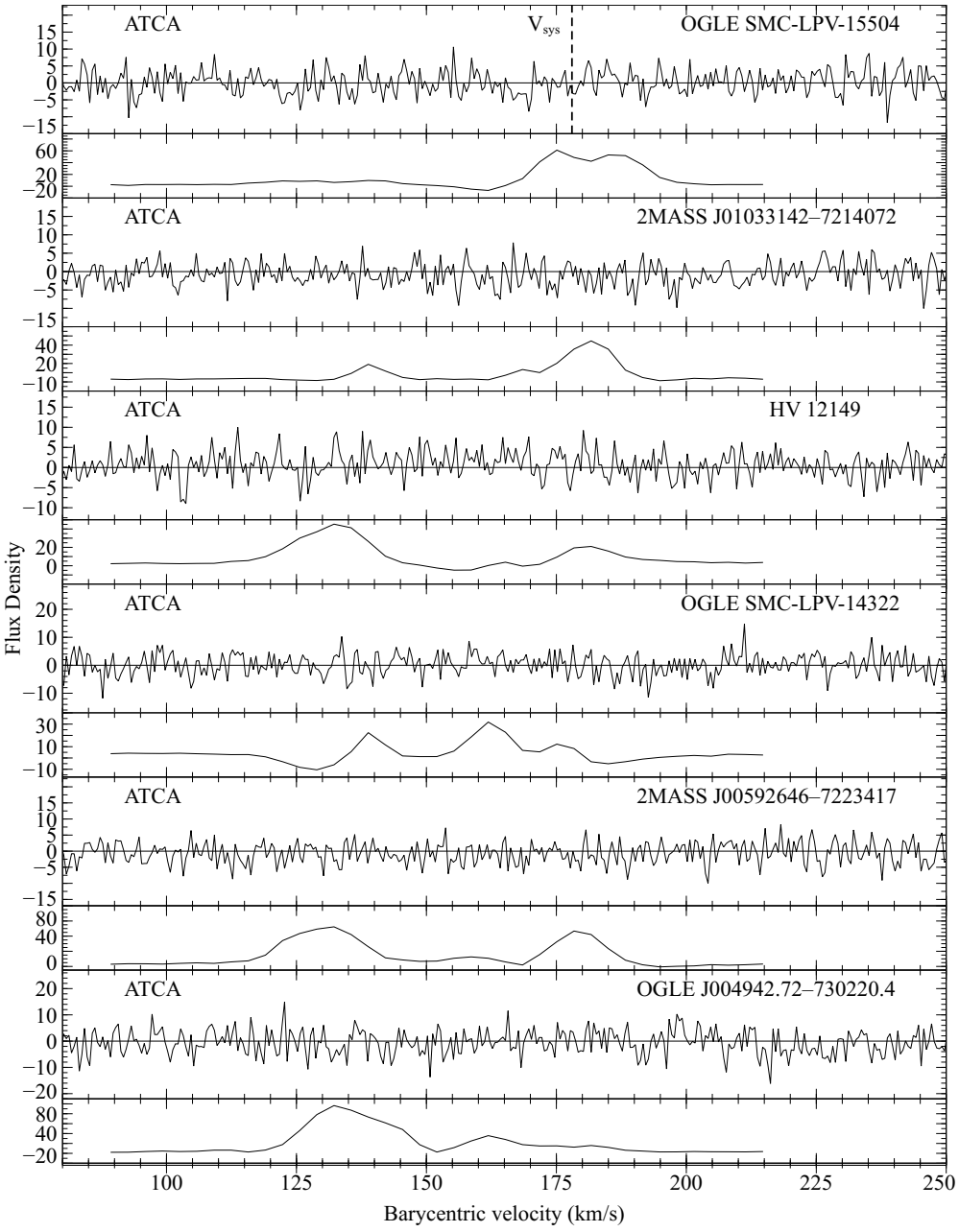

Figure 6.2: continued

ATCA sources

With the ATCA survey of the SMC, spectra have been obtained for eight sources that have been considered good maser candidates. Four of these sources (OGLE SMC-LPV-15504, HV 12149, BMB-B75, and MSX SMC 018) have shown 10 μm silicate features in emission. OGLE SMC-LPV-15504 has a known systemic velocity of 176.8 ± 0.3 km s^{-1} (Massey & Olsen, 2003) from spectroscopic observations of the Ca II triplet, which greatly simplifies the search in velocity space. HV 12149 has an initial mass of around $4 - 5$ M$_{\odot}$, and is likely to have just initiated HBB (González-Fernández et al., 2015; Dell'Agli et al., 2015; Slemer et al., 2017). This source is unique with its late spectral type yet bright K-band flux of $M_K = 8.6$ mag (Cutri et al., 2003), typical of a RSG. After observing BMB-B75, Jones et al. (2015) found that the far-IR emission detected by *Herschel* was due to a spatially coincident galaxy. The mid-IR IRS spectrum of the source shows red-shifted (z ~ 0.16) emission peaks of Polycyclic Aromatic Hydrocarbons (PAHs) at 6.3 and 11.3 μm and Ne III at 12.8 and 15.5 μm from the background galaxy (Lebouteiller et al., 2011; Kraemer et al., 2017), but the silicate emission detected from the source appears unaffected. This source has also been found to have 6 cm continuum (Wong et al., 2012), emission likely emanating from the background galaxy. MSX SMC 018 was categorised as an M-type star by van Loon et al. (2008) who used 3−4 μm spectra for classification, after which a spectral type of M7 was determined by Groenewegen et al. (2009). The source shows deep TiO bands, characteristic of oxygen-rich evolved AGB (as opposed to RSG) stars, and weak crystalline silicate features (Kraemer et al., 2017). The remaining four sources, 2MASS J01033142−7214072, OGLE SMC-LPV-14322, 2MASS J00592646−7223417, and OGLE J004942.72−730220.4, are evolved AGB stars within the observed fields that are likely to be carbon stars (discussed in in §6.4).

Within the spectrum of HV 12149 a possible maser peak is seen at 132.5 km s^{-1} that, even though not sharp, shows significant flux over a number of channels (above 2σ). The peak lies near in velocity to a negative spike in flux at 125.5 km s^{-1}, which may indicate a frequency range compromised by RFI. The spectrum of BMB-B75 shows two peaks at 162.7 and 193.8 km s^{-1}, below 2σ but with significant flux over several channels,

that if attributed to maser emission, would indicate an expansion velocity of 15.6 km s^{-1}. Also visible is a small peak in the 1665-MHz spectrum within this velocity range (see Appendix C). This value is much higher than the value of ~ 3 km s^{-1} predicted for these lower metallicity sources using the newly derived expansion velocity relation (Eq. 5.1). A negative spike at 149 km s^{-1} is also seen within the spectrum. This is close to the systemic velocity of 145.6 km s^{-1} measured for the SMC (McConnachie, 2012) and may indicate interstellar OH absorption. The MSX SMC 018 spectrum has two interesting peaks around this velocity at 153.7 and 149.8 km s^{-1} also near in velocity to the expected systemic velocity of the SMC. A number of interesting spikes in the spectra have been discussed again not to claim detection, but to aid future maser searches.

6.4 Discussion

6.4.1 A dearth of OH masers in the SMC

In trying to understand the lack of maser emission in any of the SMC candidates it is important to first look at the most promising SMC target for maser emission, IRAS 00483−7347. This observation had a 59-hour integration and targets the most luminous SMC candidate. It is possible that the source is uniquely void of maser emission. However, assuming the source is a maser-emitting source, the observation should be able to detect maser emission with a F_{35}-to-F_{OH} pumping efficiency down to 3.6%, given the source's predicted F_{35} (Calculated from the best-fit DUSTY model; described in §6.4.5), and the noise level of the observation. Within the rest of the sample of targeted SMC sources, it is expected that a number of sources should also show OH maser emission. The sample includes oxygen-rich sources slightly less luminous, reddened, and cool, compared to the LMC OH masing sources. In Figure 6.3 it is shown that the SMC sources are typically less reddened at a given luminosity as opposed to the LMC sources, with IRAS 00483−7347 again being the exception. Also included in the figure are PARSEC-COLIBRI stellar isochrones and evolutionary tracks (Marigo et al., 2017) for different stellar ages that

correspond to 2, 4, and 5 solar-mass sources for both Magellanic Cloud metallicities[10]. The point within each evolutionary track where the carbon-to-oxygen ratio becomes greater than one is also marked. Several of the SMC sources lie upon the 5 $M_{\odot}$ SMC track, where the C/O ratio is still less than 1. These sources have also all been spectroscopically confirmed to be oxygen-rich. Four lower-luminosity sources lie between 2 and 4 $M_{\odot}$ at the SMC metallicity indicating that they are likely carbon stars. Only evolutionary tracks for the lower mass regime are shown as the paths of higher mass evolutionary track on the HR diagram are more to difficult model and constrain.

Using the maser efficiency distribution from past maser detections and the noise levels of each targeted SMC observation, a bootstrapping method has been used to predict the likelihood of achieving a maser-pumping efficiency that would result in a 3σ level detection (Table 6.3). By replacing each SMC target with a randomly selected maser efficiency from the Galactic and LMC samples described in previous chapters with one million iterations, the collective probability of not achieving this level in any of the four targeted observation has been calculated to be 0.19%. This suggests that there is likely an underlying reason for the lack of maser emission in the SMC.

The expected SMC maser peak distribution has also been determined using the LMC OH/IR the maser flux peak distribution (Fig. 6.4). The LMC maser spectra have been resampled to 0.5 km s^{-1} resolution to match the SMC spectra. The cumulative density of the peak flux densities of the resulting spectra have been used to estimate the SMC peak maser flux densities. The flux densities have been scaled by 40% for distance, assuming distances of 50 and 60 kpc to the LMC (Feast, 2013) and SMC (Szewczyk et al., 2009), respectively. Assuming the sources are optically thick, the maser emission should depend only on the F_{35} as this value takes metallicity into account. If this is not the case, then the emission will depend on the OH abundance which should scale with metallicity. To compensate for this potential effect all LMC peak flux densities have been scaled down by an additional 40% for the difference in metallicity. The plot

[10]Ages correspond to listed mass and metallicity from the Bressan et al. (2012) PARSEC evolutionary tracks.

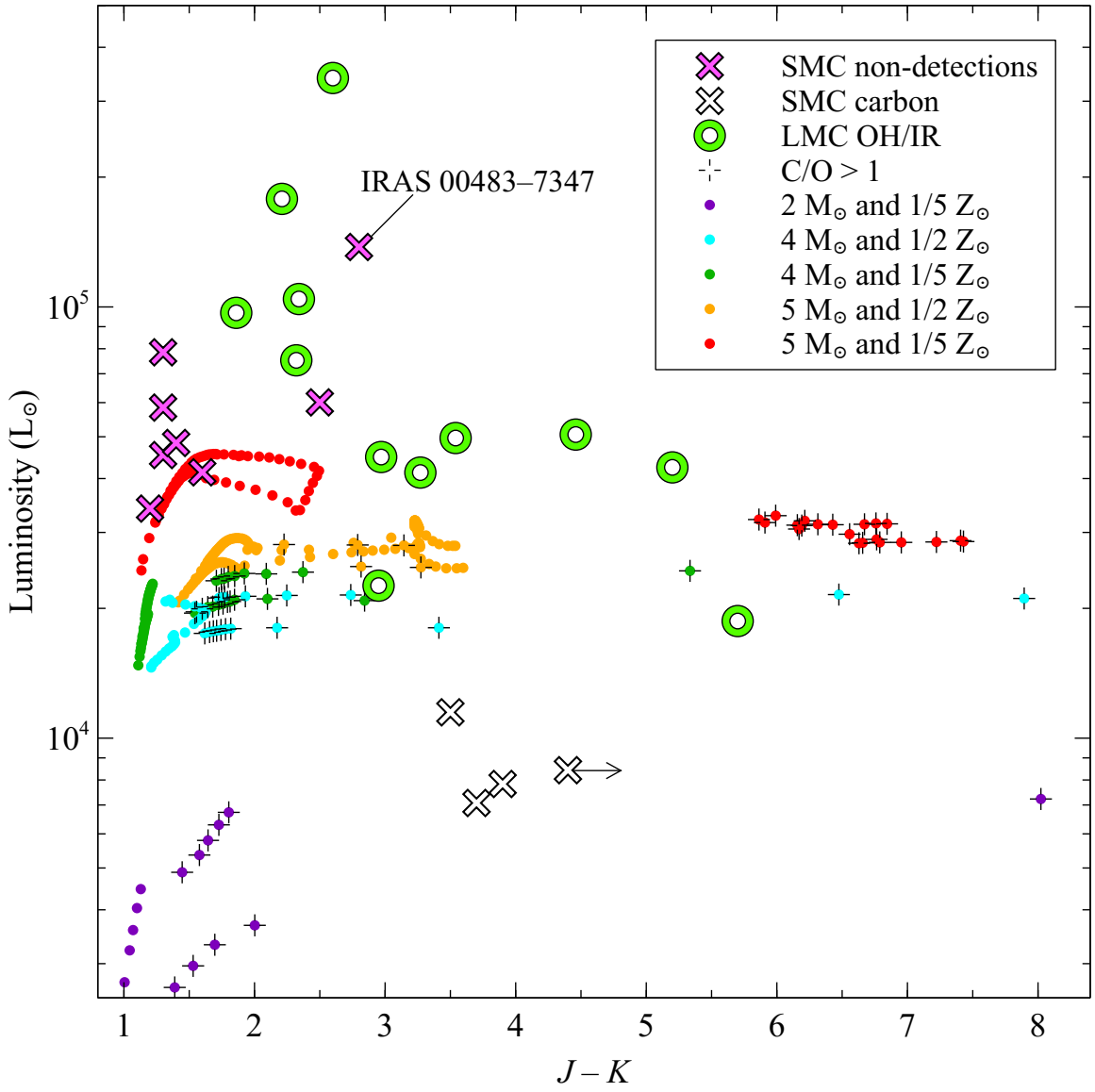

Figure 6.3: The luminosity as a function of $J-K$ colour for the samples in the SMC and LMC. Also shown are PARSEC-COLIBRI stellar evolutionary track (Marigo et al., 2017) corresponding to 2, 4, and 5 solar mass stars in their TPAGB phase for both the LMC and SMC metallicities; also marked on the evolutionary track are the points at which the carbon-to-oxygen ratio is greater than one.

Table 6.3: The flux density upper limits for circumstellar OH maser emission for the SMC targets. Listed values are *Spitzer* MIPS 24 μm flux (F_{24}) from Boyer et al. (2011), predicted 35 μm flux values taken from the best-fit DUSTY model of the source (explained in §6.4.5), predicted OH maser flux ($F_{\mathrm{OH,\,predicted}}$) assuming the median masing efficiency of 23% F_{35} photons to F_{OH} photons and the noise level (σ) of the observation (both combined observations for IRAS 00483−7347. Also shown are the upper limits for maser efficiency (maximum efficiency) and the probability of a 3σ-level detection for each targeted observation calculated with the bootstrapping method using the maser efficiencies of the LMC and Galactic samples previously mentioned.

Object name	$F_{24\mu\mathrm{m}}$ (mJy)	$F_{35\mu\mathrm{m,predicted}}$ (mJy)	$F_{\mathrm{OH,\,predicted}}$ (mJy)	σ (mJy)	Maximum efficiency	Likelihood of detection
Parkes targets						
IRAS 00483−7347	660.0	306.5	70.5	3.7	3.6%	94.2%
IRAS F00486−7308	91.1	39.0	9.0	4.5	34.5%	19.8%
IRAS 00591−7307	95.4	44.3	10.2	7.7	52.1%	10.5%
IRAS 01074−7140	396.0	234.8	54.0	3.4	4.3%	90.7%
ATCA sources						
OGLE SMC-LPV-15504	31.6	13.4	3.1	7.1	158.9%	1.2%
2MASS J01033142−7214072	19.2	8.1	1.9	6.3		
HV 12149	12.7	7.0	1.6	6.5	278.0%	1.2%
OGLE SMC-LPV-14322	19.0	11.1	2.6	7.6		
2MASS J00592646−7223417	18.9	13.1	3.0	6.5		
BMB-B75	92.0	42.9	9.9	9.5	66.5%	7.0%
OGLE J004942.72−730220.4	27.8	14.3	3.3	10.0		
MSX SMC 018	262.0	115.6	26.6	7.2	18.7%	36.1%

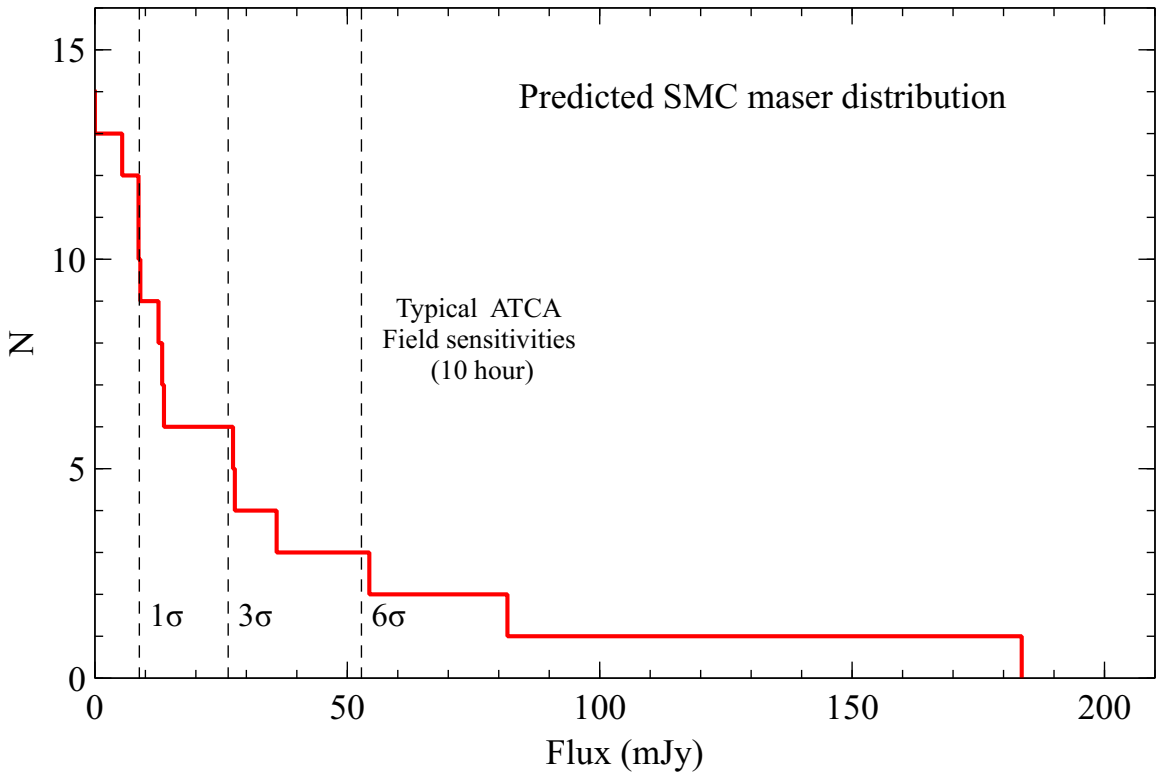

Figure 6.4: The cumulative expected maser peak flux distribution of the SMC sample using the detected LMC maser peak sample and scaling fluxes down by 40% for distance and another 40% for metallicity. Also shown are the typical sensitivities at different significance levels of a 10 hour integration with ATCA ($1\sigma \simeq 8.8$ mJy).

shows that 12 sources with peak maser flux densities above the typical noise level of the ATCA observations are expected, as well as 6 sources with peak flux densities above 3σ. However, this does not account for the difference in SFH in the Magellanic Clouds (see §1.7.2). Using values for the star formation rate for the evolution time of $5-6$ $M_\odot$ stars (100 Myr) of 3 $M_\odot$ yr^{-1} and 0.75 $M_\odot$ yr^{-1} for the LMC and SMC, respectively (Harris & Zaritsky, 2004, 2009), the observations should have detected one fourth of the sources found in the LMC. This gives us an expected detectable maser population of $1-2$ sources above 3σ, whereas none were detect.

6.4.2 OH/IR populations in the Magellanic Clouds

Carbon/Oxygen abundance

The SMC hosts a smaller population of evolved AGB stars than the LMC, and has a higher fraction of carbon-rich evolved AGB stars or carbon stars (Boyer et al., 2011). It has also been observed that evolved AGB stars and RSGs in the SMC have less dust than their LMC counterparts (van Loon, 2000, 2006; van Loon et al., 2008; Bonanos et al., 2010). There are a number of possible explanations for the smaller population of oxygen-rich evolved stars in the SMC, four of which have been proposed by van Loon et al. (2008). The first possibility is that oxygen-rich dust grains are more transparent at near-IR wavelengths, which coupled with a smaller dust content in the SMC, have left few obscured oxygen-rich sources. The second possibility is that higher luminosity oxygen-rich sources, which have undergone Hot-Bottom Burning (HBB), are extended, resulting in more diffuse dust. A third possibility is that the size of the SMC, the initial mass function, and the rapid evolution of higher-mass sources, have left few in this evolutionary phase. A final possibility is that as carbon stars form at lower masses within the Magellanic Clouds (Marigo, Girardi & Bressan, 1999), this has resulted in fewer observable lower-mass oxygen-rich sources.

Warmer evolved red supergiants

For RSGs, studies have shown that while values for $T_{\rm eff}$ and $M_{\rm bol}$ show agreement between Galactic and LMC sources, sources within the SMC show a much larger spread in $T_{\rm eff}$ for a given $M_{\rm bol}$ (Levesque et al., 2006). This is expected as a result of the enhanced effects of rotational mixing at lower metallicity (Maeder & Meynet, 2001). In addition to a larger spread in $T_{\rm eff}$, lower metallicity RSGs have been shown to have earlier spectral types (Elias, Frogel & Humphreys, 1985; Massey & Olsen, 2003). The expectation is that as spectral types are dependent on Titanium oxide (TiO) bands, and lower metallicity stars will have a lower abundance of TiO, this would result in lower metallicity sources being categorised as earlier spectral types. At the same time, lower metallicity RSGs have

also been found to have warmer median $T_{\rm eff}$ (Levesque et al., 2005, 2006, 2009; Massey et al., 2007). As a decrease in the abundance of heavy elements results in a decrease in opacity, and an increase in a star's surface brightness, this results in warmer RSGs at lower metallicity (Levesque, 2013). This would suggest fewer late-type RSGs exist within lower metallicity environments. Yet, observations have shown small populations of late-type RSGs in these lower metallicity environments (Groenewegen & Blommaert, 1998; Massey et al., 2007; Levesque et al., 2007; Bonanos et al., 2010).

6.4.3 Isolating the OH/IR sample

Photometry from the *Spitzer* SAGE-SMC catalogue has been employed to determine the number of sources within the Magellanic Clouds that are capable of OH maser emission (Gordon et al., 2011; Boyer et al., 2011); this photometric data has also been compared to the SAGE-LMC photometry (Blum et al., 2006; Meixner et al., 2006; Bonanos et al., 2009, 2010; Srinivasan et al., 2009; van Loon et al., 2010).

The sources within the LMC circumstellar maser sample were primarily categorized as Far Infrared Objects (FIR) by Boyer et al. (2011) except for IRAS 05280−6910 which was designated as an extreme or x-AGB star (however Boyer et al. (2010) showed that the source is bright at far-IR wavelengths), and IRAS 04553−6825, IRAS 05003−6712, and IRAS 05558−7000, which were not included in the catalogue. In the past, colour-magnitude diagrams (CMDs) have been used to separate different stellar populations within the Magellanic Clouds (Woods et al., 2011). Plotting mid-IR colours against mid-IR flux densities, the red supergiants and massive AGB stars create a distinct branch. Looking at the *Spitzer* IRAC [3.6]−[8.0] colour against the [24] flux density for the LMC OH/IR sample, the sources occupy a similar high position (or "masing zone") on one of these branches (Fig. 6.5). Two CMDs are shown, one with SAGE-LMC sources that fall within the ATCA and Parkes fields (*left*) and one with sources that do not (*right*). This is done to get an overall idea of the fraction of potential maser sources that have not been covered by the maser survey. This has been done also for the sources in the SMC (Fig. 6.6).

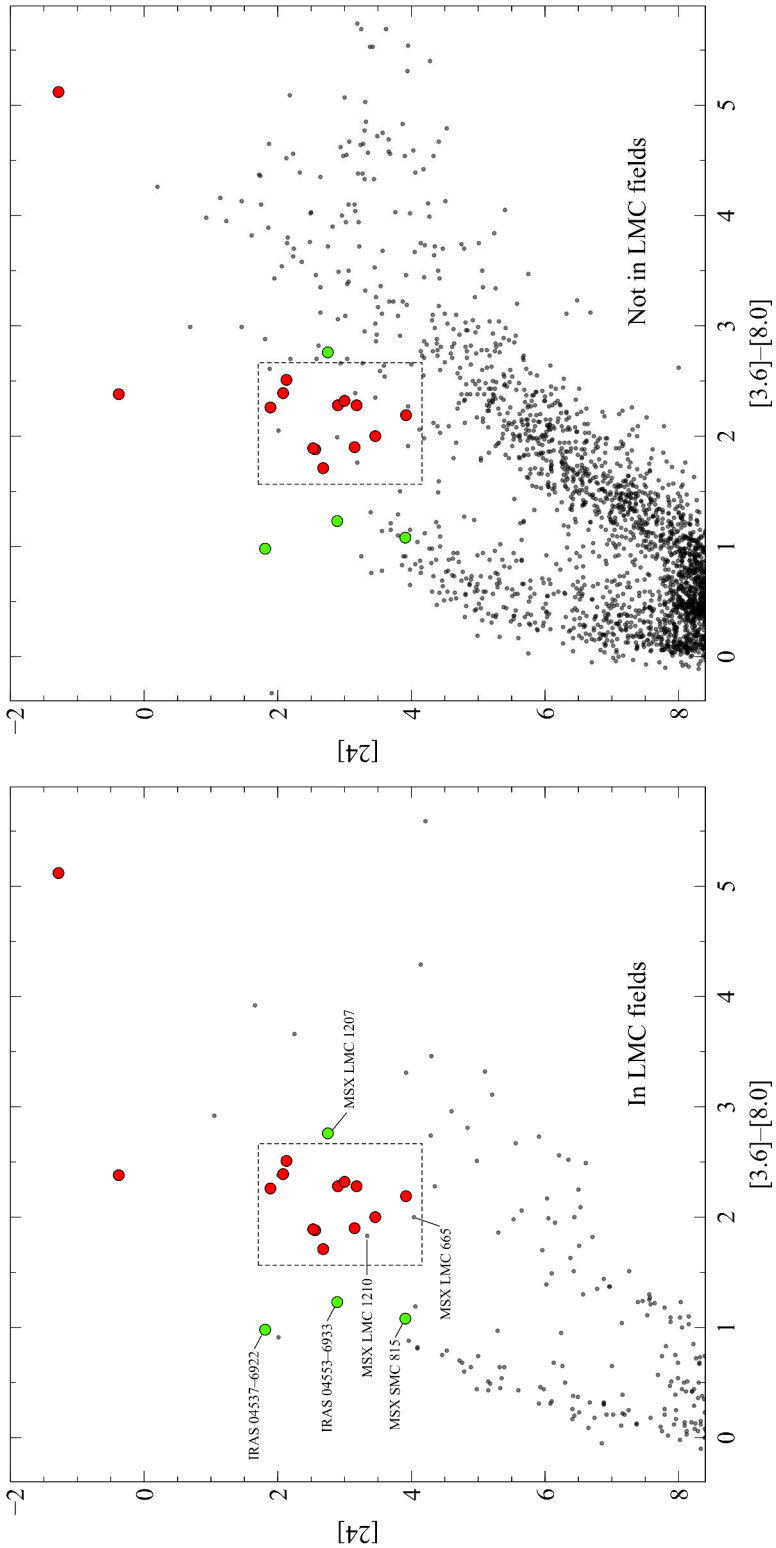

Figure 6.5: The *Spitzer* MIPS 24 μm flux density versus IRAC [3.6]−[8.0] colour for SAGE-LMC sources **IN** (*Left*) or **NOT IN** (*Right*) any of the Parkes or ATCA fields targeting OH, with the LMC OH/IR sample in red, LMC non-detections in green, and remaining sources in black. Also shown is the LMC masing zone (dashed box), a region of the CMD typical of OH masing sources. The [24] for MSX LMC 1207, WOH G64, and IRAS 05280−6910, and is from WISE W4 photometry.

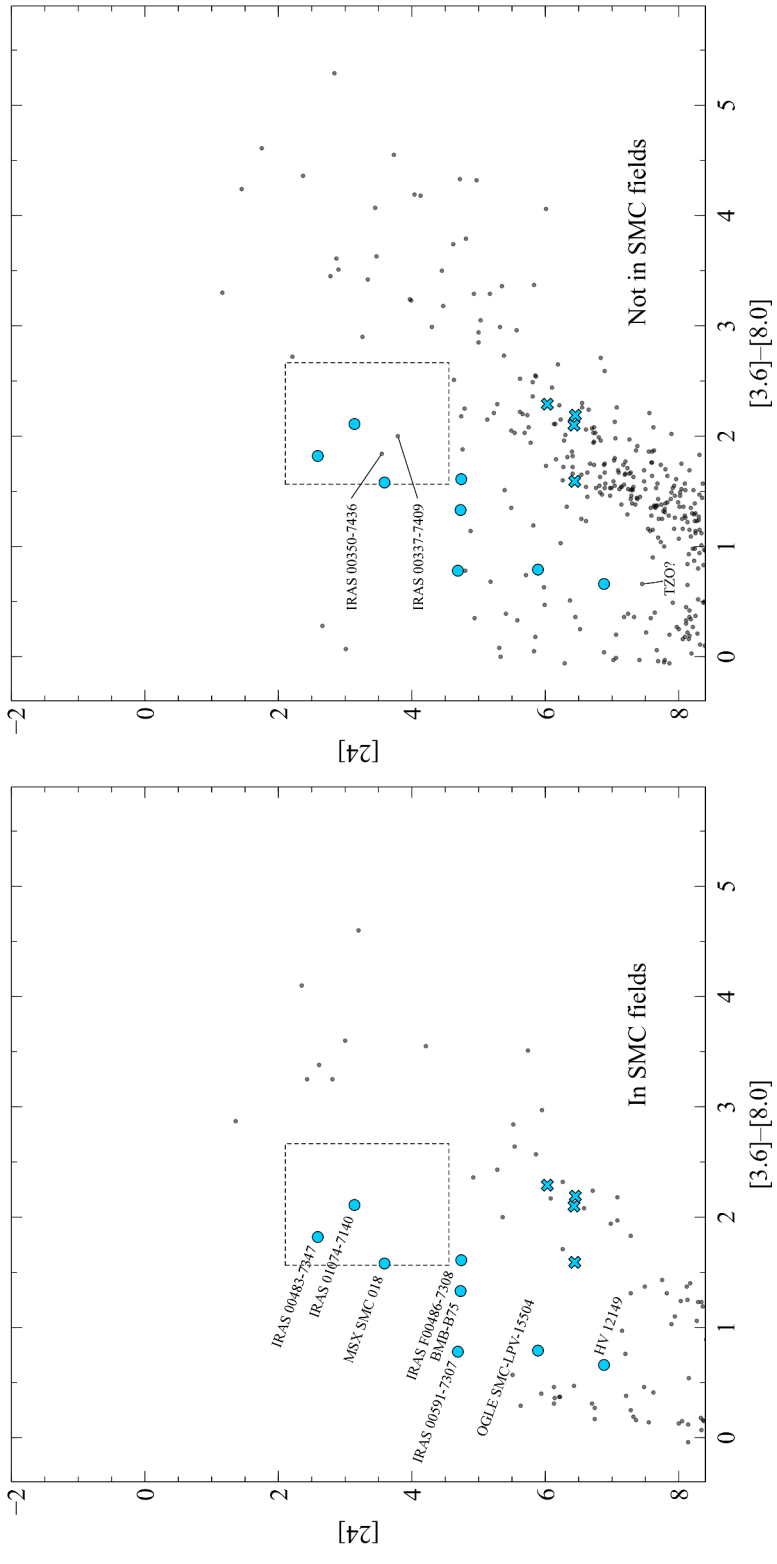

Figure 6.6: The *Spitzer* MIPS 24 μm flux density versus IRAC [3.6]–[8.0] colour for SAGE-SMC sources **IN** (*Left*) or **NOT IN** (*Right*) any Parkes or ATCA fields targeting OH, with the SMC non-detections as blue circles, the SMC sources likely to be carbon stars as blue crosses, and the remaining sources in black. Also shown is the LMC masing zone (dashed box) scaled down by 40% (for distance), for the expected SMC OH/IR population. Also shown is the unremarkable position of the Thorne-Żytkow or super-AGB candidate-star HV 2112 (TZO?), showing the source is not particularly reddened or luminous at 24 μm.

Within the LMC sample, there are two sources in the observed fields that have been identified as AGB stars and lie within the LMC masing zone, but do not exhibit circumstellar maser emission. Within the observed fields are the sources MSX LMC 1210 and MSX LMC 1207, sources that do not exhibit maser emission. The first source, MSX LMC 1210, with a $J - K$ colour of 2.94 mag, is bright at mid-IR ($F_{24} = 387$ mJy), and has a pulsation period of 1050 d (Soszyński et al., 2009). The second source, IRAS 05287−6910, is also bright in the mid-IR (F_{24}=1.1 Jy), exhibits silicate in emission (Lebouteiller et al., 2011), and lies in the cluster NGC 1994 (van Loon, Marshall & Zijlstra, 2005). The cluster has an age of 11.5 Myr (Elson & Fall, 1988) and a metallicity of 0.58 $Z_{\odot}$(Oliva & Origlia, 1998).

Within the masing zone of sources not within the LMC fields are three blue supergiants, three young stellar objects, four emission line stars, two carbon stars, a planetary nebula, and two sources that would be good targets for OH maser emission. The first source, IRAS 04523−7043, has a 24 μm flux density of 3.59 mag, and a pulsation period of 890 d (Soszyński et al., 2009). The second source, 2MASS J05241334−6829587, has a 24 μm flux density of 2.58, a $J - K$ colour of 3.2 mag, a pulsation period of 899 days (Spano et al., 2011).

Within the observed SMC fields, there are three target sources that lie within the scaled LMC masing zone in the CMD: IRAS 00483−7347, IRAS 01074−7140, and MSX SMC 018 (Fig. 6.6). To the right of the region are several young stellar objects and emission line stars (Sewiło et al., 2013). There are also two sources that do not lie in any of the observed fields, IRAS 00350−7436 and IRAS 00337−7409 (HD 3407) within this same masing region. IRAS 00350−7436 has been found to be the most luminous carbon-rich object in the SMC (Whitelock et al., 1989; Srinivasan et al., 2016). In the past the source has been categorized as a carbon star (Ruffle et al., 2015), a post-AGB star (Matsuura et al., 2005) and an interacting binary star (Whitelock et al., 1989). The second source, IRAS 00337−7409, is a foreground star with a radial velocity of 58 km s^{-1} (Florsch, 1972). No other sources within the SAGE-SMC survey lie within the masing zone as defined by the LMC OH/IR sources. This insures that all SMC sources that would be expected to exhibit circumstellar OH maser emission at the current detection

thresholds have been surveyed. Also shown in the figure is the Thorne-Żytkow Object candidate star HV 2112 (Levesque et al., 2014; Tout et al., 2014). These stars, while yet to be confirmed observationally, are thought to be red giants or supergiants with neutron stars at their cores. Alternatively, it has been suggested it could be a super-AGB star (Wood, Bessell & Fox, 1983; Smith & Lambert, 1990; Tout et al., 2014), or even a Galactic foreground S-type star (Maccarone & de Mink, 2016), though its SMC membership seems secure on the basis of the radial velocity of $v_{\rm rad} = 150$ km s^{-1} (González-Fernández et al., 2015) and proper motion (Worley et al., 2016). The position of this source suggests it is not particularly reddened or luminous at 24 μm compared to the other SMC targets.

6.4.4 Maser strength

Now that the expectation of maser detections has been established, the aim will be to understand their absence. Several conditions must be met in order to produce circumstellar OH maser emission. First, as the transition is a population inversion, a dense population of OH with number densities typically $10^{12} - 10^{16}\,\mathrm{m}^{-3}$ is required (Cohen, 1989). The masing environment must have a sufficiently long path length to provide the high column density, needed to amplify the maser (Gray, Howe & Lewis, 2005). Masers can also only occur in a certain radius range of the parent star. If masers occur inside a radius of around several hundred astronomical units (au) from the star, densities are so high that collisional pumping rapidly increases and "quenches" the maser. Outside a few thousand au, lower densities are not enough to sustain the pump rate (Elitzur, 1992; Vlemmings et al., 2006). In addition to having a suitable masing environment, significant IR flux must be present to pump the maser. It is possible that circumstellar environments in the SMC do not adhere to these conditions.

OH abundance

Within oxygen-rich evolved stars, the abundant oxygen allows for the formation of a variety of minerals, CO, and a significant amount of water. A smaller fraction of water

has been found around carbon stars (Melnick et al., 2001; Decin et al., 2010) likely a result of sublimating comets or the Fischer-Tropsch catalysis mechanism which converts CO and H_2 into hydrocarbons and water using iron as a catalyst (Willacy, 2004). In oxygen-rich stars water molecules are transported by stellar pulsation shocks, and the dust-driven wind, out to typical distances of $20 - 80$ au (e.g. Sudou et al., 2002, and references therein). This water is then photodissociated by interstellar UV radiation, creating OH. The abundance of OH will depend on the initial abundance of water but also the efficiency of converting water into OH, i.e. the penetrating strength of the UV radiation within the circumstellar envelope (Lequeux et al., 1994).

The observations and modeling of the conditions in metal-poor dwarf galaxies and nearby globular clusters indicate a much stronger radiation field and more porous molecular gas in lower metallicity environments (Madden et al., 2006; McDonald et al., 2015; McDonald & Zijlstra, 2015; Ward et al., 2017). With more ionized hydrogen and less interstellar dust, the expectation is that the lower opacity will have an impact on chemical abundances in circumstellar environments. This may also be the case with the SMC sources, yet several LMC sources that also lie within clusters (e.g. IRAS 05280−6910 and IRAS 05298−6957) seem unaffected by their cluster environment (van Loon et al., 2001b; van Loon, Marshall & Zijlstra, 2005; Wood et al., 1992).

The source of OH in evolved stars is water, and understanding the abundance of water may lead to a better understanding of the abundance of OH. Past surveys have targeted 22-GHz water maser emission in the SMC (Breen et al., 2013), and while interstellar maser emission has been detected in star forming regions, no circumstellar maser emission has been confirmed. All of the brightest SMC target sources (IRAS 00483−7347, IRAS F00486−7308, IRAS 00591−7307, IRAS 01074−7140, BMB-B75, and MSX SMC 018) have shown water in absorption at ~ 3 μm (van Loon et al., 2008). It was suggested that this may be indicative of an advanced evolutionary stage, yet they also note that the comparison LMC sample does not show strong absorption from these molecular bands. They go on to suggest that it may be possible that less of the water molecules are being locked up in dust or that the population of water molecules may be closer to the stellar surface, increasing the column density as well

as the excitation temperature. This result may hint at a potential difference in the circumstellar environments of the LMC and SMC OH/IR samples. However, the lack of OH maser emission in these sources is not due to a lack of water within their circumstellar environments. A deep survey for water maser emission in the top maser candidates may provide a better opportunity to observe circumstellar maser emission in the SMC.

It is highly possible that a denser circumstellar wind will result in a higher water column density. This higher density would create a more extended water masing region and result in a higher water maser flux density. With water closer to the star, it is less susceptible to external forces like interstellar UV radiation that convert water to OH. Also unlike 1612-MHz OH maser emission, water masers are pumped by both radiation and collisions with H_2 molecules (Babkovskaia & Poutanen, 2006). It is possible that the relative strengths of the maser pumping mechanisms may differ at lower metallicity. With less dust, and as a result lower mid-IR flux, collisional pumping may be more effective at lower metallicity. These facts have led us to the conclusion that the chances of detection within our SMC sample may favour water over OH masers.

Maser pumping

The 1612-MHz maser is a product of a population inversion that results from the pumping by infrared photons of a transition at 35 μm. As a result, the strength of maser emission will depend on the dominant source of IR emission, circumstellar dust. The theoretical maximum pumping efficiency for the 1612-MHz maser transition is 25% (Elitzur, 1992). This assumes the maser is saturated and the maser emission is isotropic. However, results from He et al. (2005) have shown stars with pump rates as low as 0.05, 1/5 of this value. Within the LMC and Galactic samples a large spread in the pumping efficiency is seen that extends far above this theoretical maximum with a median maser efficiency of 23% (Fig. 6.7). It is expected that as the radio and IR measurements were taken at different times, and these sources are highly variable, this has contributed to the large scatter. The median maser efficiencies for the Galactic Centre, Galactic bulge and LMC OH/IR samples from previous chapters have been calculated as 34.8%, 10.5%, and 38.5%,

respectively (see below). It should be noted that these are derived from spectra spanning a range of velocity resolutions between $\sim 0.5 - 1.5$ km s^{-1}, which will introduce some uncertainty. The much lower maser efficiency in the Galactic Bulge sample is surprising as SED fitting has found typically lower gas-to-dust ratio, and dramatically higher optical depth in dust emission than in the Galactic Centre and LMC samples (Table 7.3). This implies a larger supply of IR photons per OH molecule in the Galactic Bulge sources, yet a lower maser efficiency is seen.

Figure 6.7 shows the relationship of maser efficiencies and luminosities of the OH/IR samples. The predicted 35 μm fluxes are from the best-fit DUSTY model of the sources (further explained in §6.4.5). The OH maser fluxes ($F_{\rm OH}$) are the integrated flux of both maser peaks combined for the Galactic samples from Engels & Bunzel (2015), and LMC sample from Chapter 3. Also shown in this figure, are the upper limits of the maser efficiency of the SMC non-detections, as well as the two sources that are here considered the best maser candidates: IRAS 00483−7347 and IRAS 01074−7104, calculated using the ratio of the predicted 35 μm fluxes from the best-fit DUSTY model of the sources (further explained §6.4.5) and three times the noise level. The two best maser candidates are clearly below the expected maser efficiencies of other sources of comparable luminosities except for the unique LMC RSG IRAS 05280−6910, which is suspected to exhibit a unique geometry (Goldman et al., 2017). This again suggests that, while not the case in the LMC, the lower metallicity of the SMC may be a critical factor in determining the presence of maser emission. These pumping efficiencies are comparable to those found in He et al. (2005), yet the values have been expressed in terms of the peak intensity and not photon flux, and the comparative analysis between the Galaxy and the Magellanic Clouds.

OH column density

The minimum OH column density required to pump the 1612-MHz OH maser is around 1.3×10^{19} cm^{-2} (Elitzur, Goldreich & Scoville, 1976). Using the derived DUSTY mass-loss rate (discussed in §6.4.5) and making several assumptions, the expected OH column

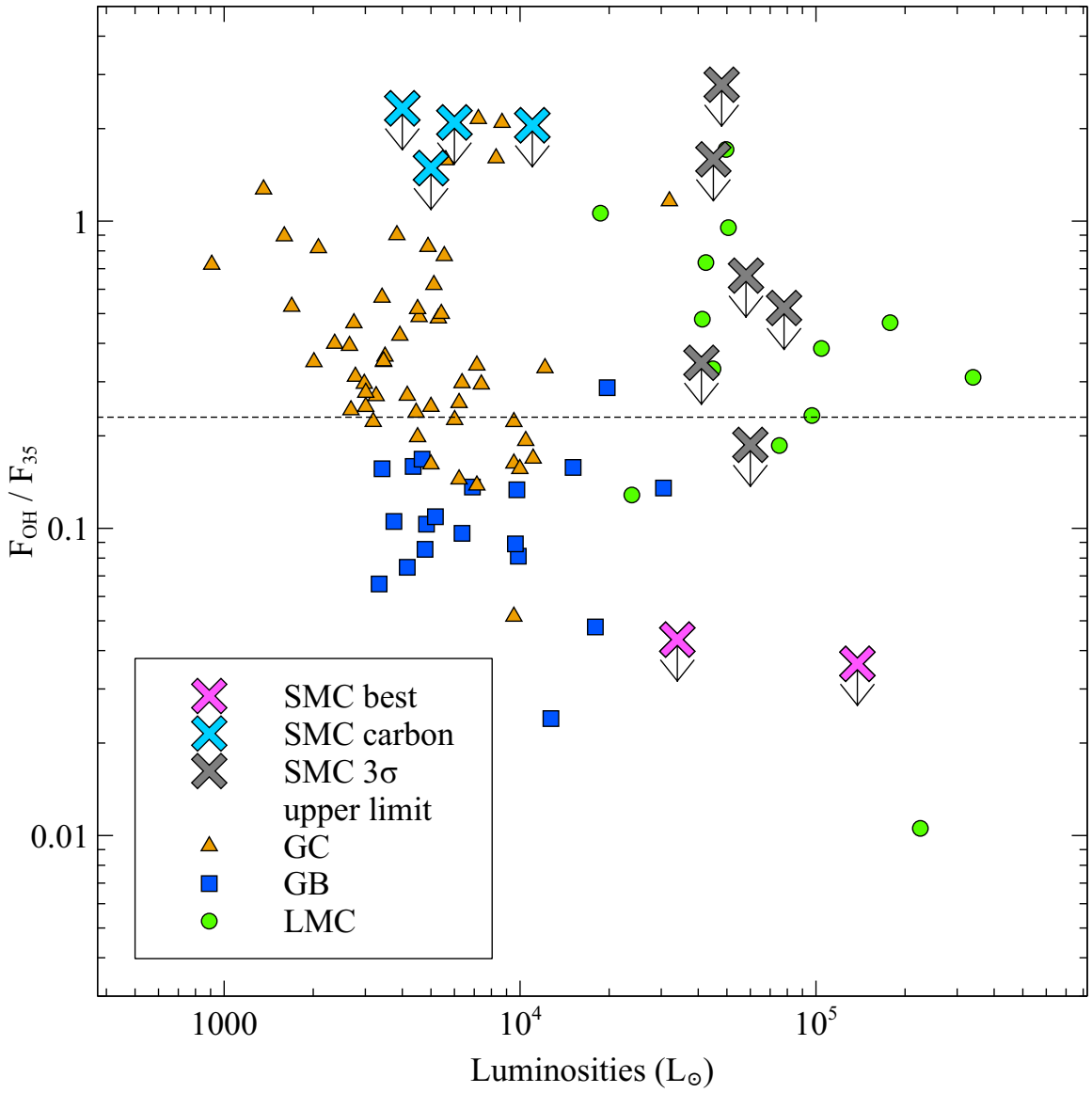

Figure 6.7: Maser efficiency of converting 35 μm photons to 1612-MHz maser photons for the Galactic Centre (GC), Galactic bulge (GB), and LMC samples. The dotted line represents the median efficiency for the three samples of 23%. Also plotted are the 3σ upper limits for the maser efficiencies of the SMC target sample, the best two candidates: IRAS 00483−7308 and IRAS 01074−7104 (SMC best), and the SMC sources likely to be carbon stars (SMC carbon), taken from the ratio of the predicted 35 μm flux to three times the observation noise level.

Table 6.4: The results of SED fitting for the SMC sample. The values are the modelled results from the best-fitting DUSTY models with luminosities (L), effective and inner dust temperatures ($T_{\rm eff,DUSTY}$, $T_{\rm inner}$), optical depths specified at 10 μm (τ), and gas mass-loss rates ($\dot{M}$); mass-loss rates are calculated with the assumption of an SMC gas-to-dust ratio of 1000 (Luck et al., 1998). A discussion of the expected errors can be found in the text. Also listed are the predicted expansion velocities ($v_{\rm exp,Goldman}$) using the new mass-loss prescription (Eq. 5.2) assuming a metallicity of one fifth solar. The grain type used for the fit, either oxygen- or carbon-rich is denoted with an O or C, respectively.

Object name	Grain type	L (10^3 $L_\odot$)	$v_{\rm exp,Goldman}$ (km s^{-1})	$T_{\rm eff,DUSTY}$ (K)	$T_{\rm inner}$ (K)	τ	$\dot{M}$ ($M_\odot$ yr^{-1})
Parkes targets							
IRAS 00483−7347	O	138	5.4	3100	1200	1.31	1.8×10^{-4}
IRAS F00486−7308	O	41	3.3	3700	1000	0.27	3.9×10^{-5}
IRAS 00591−7307	O	78	4.3	2800	600	0.1	3.4×10^{-5}
IRAS 01074−7140	O	34	3.1	3100	350	0.48	5.9×10^{-5}
ATCA sources							
OGLE SMC-LPV-15504	O	45	3.4	2700	1000	0.12	1.5×10^{-5}
2MASS J01033142−7214072	C	4	1.3	3700	1000	0.20	1.2×10^{-5}
	O	7	1.6	3000	1400	1.49	1.8×10^{-5}
HV 12149	O	48	3.5	3000	1400	0.1	1.0×10^{-5}
OGLE SMC-LPV-14322	C	11	2.0	3400	1400	0.20	2.0×10^{-5}
	O	11	2.0	3000	1400	1.09	2.0×10^{-5}
2MASS J00592646−7223417	C	5	1.5	3500	1000	0.24	1.8×10^{-5}
	O	8	1.7	3000	1400	1.31	1.8×10^{-5}
BMB-B75	O	58	3.8	3400	600	0.1	3.5×10^{-5}
OGLE J004942.72−730220.4	C	6	1.5	2800	800	0.15	1.6×10^{-5}
	O	8	1.7	3000	1400	1.8	2.2×10^{-5}
MSX SMC 018	O	60	3.8	2700	600	0.35	7.0×10^{-5}

density of IRAS 00483−7347 has been calculated. Assuming the outflowing material is exclusively H_2 in an r^{-2} distribution and using the inner OH shell radius determined for NML Cyg and VY CMa of 3.0×10^{15} cm (Benson & Mutel, 1979), this yields a value for the H_2 column density. While the radius of NML Cyg has been confirmed using mainline OH maser emission (Etoka & Diamond, 2004), this value has been found to be larger for the more unique source VY CMa (Benson & Mutel, 1982). NML Cyg and VY CMa have derived luminosities and mass-loss rates similar to those of IRAS 00483−7347 listed in §6.4.5 (Mauron & Josselin, 2011; Shenoy et al., 2016), and should have a similar 1612-MHz OH maser shell. Assuming a ratio of 5000:1 for the ratio of H_2 to OH (Olofsson, 2005), and scaling the abundance by 1/5 for metallicity, the fastest expansion velocity that would yield a value above the minimum column density for OH maser emission is 2.8 km s^{-1}. While slow for solar metallicity sources, it is still unclear if this value is realistic for the SMC's lower metallicity sample. From the newly derived expansion velocity relation (Eq. 5.1), the expected value, given the source's luminosity and metallicity is 5.4 km s^{-1}. This may suggest that the column density of the source has dropped below the masing threshold. The ratio of OH-to-H_2 remains the largest uncertainty in this calculation, as Olofsson (2005) describes estimates more as order-of-magnitude approximations. Whether the abundance also scales linearly with the metallicity is also unclear. Regardless, the observations are very near the threshold for maser emission. The determining factor in whether maser emission is seen in the Galactic and LMC maser samples is the supply of IR photons to the system. Within the SMC, it seems that this becomes a two-body problem, where the maser strength drops with the metallicity squared, from a dependence on both the dust emission and the lower abundance of OH with respect to H_2.

6.4.5 Mass-Loss and evolutionary phase

It is expected that metal-poor AGB stars need longer to evolve towards cool temperatures and strong pulsations (Bowen & Willson, 1991). This would result in more massive white dwarfs, as the AGB cores have more time to grow. Yet, observations have shown that

the white dwarf mass functions between the SMC, LMC, and the Galaxy are similar (Villaver, Stanghellini & Shaw, 2004, 2007; Williams, 2007). This would mean that the onset and strength of the dust-driven wind phase is similar within the Galaxy and the Magellanic Clouds (van Loon et al., 2008). However this is only the case for lower-mass AGB stars. The white dwarf mass function does not constrain the strength or duration of the superwind phase in either massive AGB stars or RSGs, which dominate the OH/IR samples in the Magellanic Clouds. A shorter superwind phase should then result in fewer sources exhibiting circumstellar maser emission.

Using the same SED fitting method as has been applied to the LMC sample (see §4.2), SEDs of the SMC sources have been fitted (Fig. 6.8) and luminosities and mass-loss rates calculated for the SMC sample assuming a gas-to-dust ratio of 1000 (Bernard et al., 2008; Bot et al., 2004; Gordon et al., 2009). The results show mass-loss rates $\sim 10^{-5}$ $M_{\odot}$ yr^{-1}, and luminosities typically $\sim 50,000$ $L_{\odot}$, similar to the LMC sample (Table 6.4). Due to the assumptions within the modeling of spherical symmetry, distance, optical properties, and the fact that the model is an idealised system, it would be misleading to quote formal errors for these values. The luminosities are mostly affected by geometry and variability, but are generally accurate to within a factor two. The mass-loss rates are much less certain, and carry a systematic uncertainty of an order of magnitude due to our poor knowledge of the optical properties of the circumstellar grains (Srinivasan, Sargent & Meixner, 2011; Srinivasan et al., 2016). The table also shows expansion velocities calculated using the new expansion velocity relation (Eq. 5.1). While this relation has only been tested in metallicity environments between one half and twice solar, it is expected that the relation should give a good approximation within this metallicity regime. It is possible that at lower metallicity, a different set of dust optical constants may be better suited to reproduce the observed silicate features. However, implementing these changes would compromise the integrity of the comparison of samples, and thus the same set of DUSTY models and dust optical constants as in the LMC analysis have been used.

While there are only three sources (IRAS 00483−7347, IRAS 01074−7140, and MSX SMC 018) with comparable absolute flux densities at 24 μm to the LMC sample,

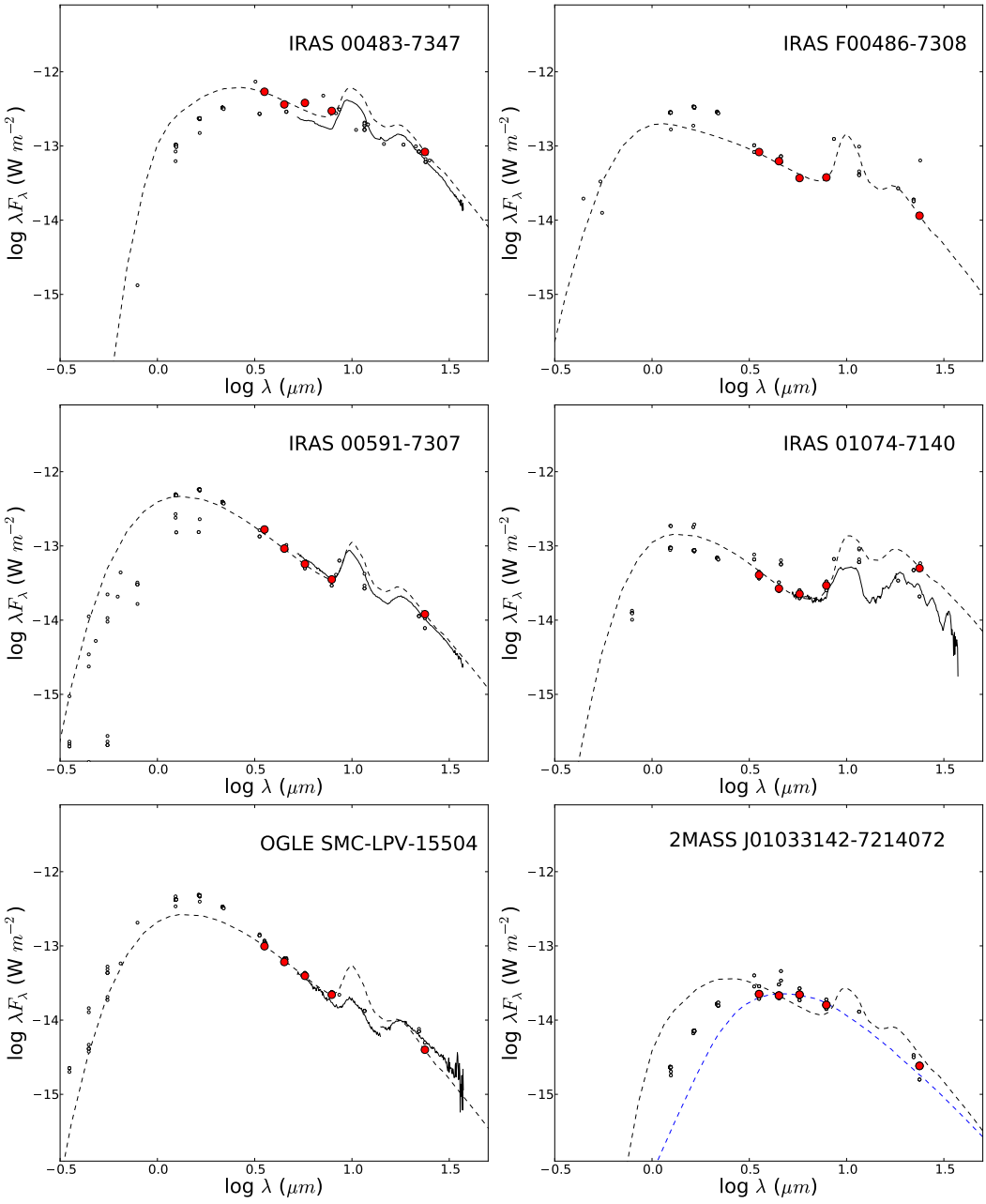

Figure 6.8: The SED fitting of DUSTY models to *Spitzer* IRAC and MIPS photometry of SMC sources (shown in red), with the best-fitting model (dashed line), *Spitzer* IRS spectra (in solid black), and the remaining available photometry (shown with small open circles). Also shown are fits with carbon-rich SED models (shown in blue).

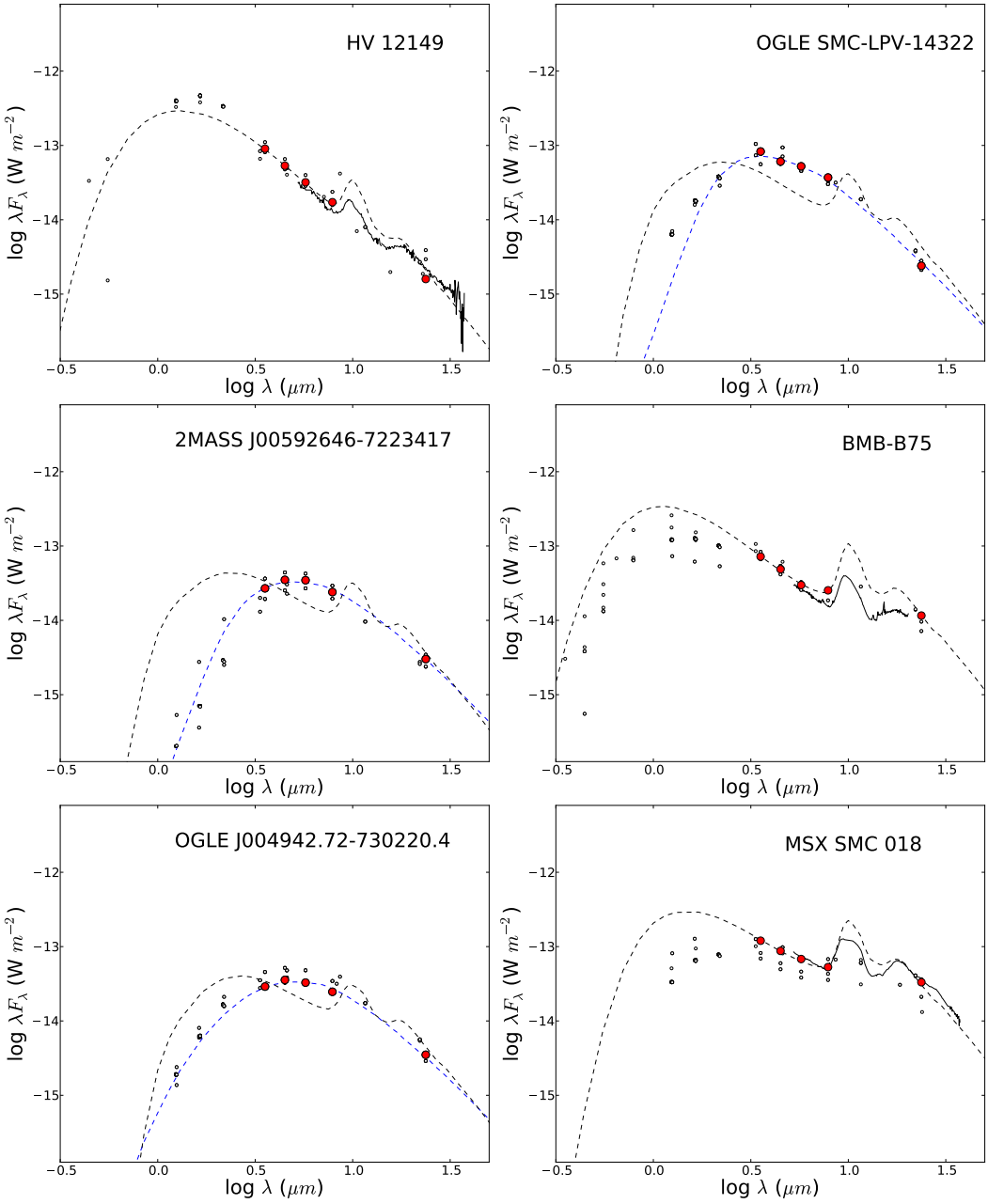

Figure 6.8: continued

there are several sources with comparable luminosities (Fig. 6.9). The most luminous source IRAS 00483−7347 has a long pulsation period, late spectral type, a large Rb enhancement, typical of an AGB star that has undergone HBB. Yet the source has a high luminosity of 138,000 $L_{\odot}$ suggestive of an RSG, which is more likely to indicate that the source is likely a super-AGB star.

When comparing the mass-loss rates and luminosities for the SMC to the LMC samples (Fig. 6.9, 6.10), the higher luminosity SMC sources ($> 2 \times 10^4$ $L_{\odot}$) tend to have a lower mass-loss rate at a given luminosity (except for IRAS 00483−7347). This is not surprising given the SMC sources are not as optically thick as the LMC sources. Also included are the SMC mass-loss rates calculated using the newly derived mass-loss prescription §5.2 designated 'SMC prescription'. The mass-loss rate has been calculated using the prescription and a gas-to-dust ratio of 1000. However this parameter does not significantly affect the calculated mass-loss rate. The values calculated are typically higher than what is calculated from SED fitting, except for several sources that have SEDs that do not conform well to any of the models within the grids (2MASS J01033142−7214072, OGLE SMC-LPV-14322, 2MASS J00592646−7223417, OGLE J004942.72−730220.4). These four sources have been modelled using a similar grid of DUSTY models that use the carbon dust grains from Hanner (1988). The best fit carbon-SED for these sources have been over-layed and it has been found that they better reproduce the observed SED. This along with their position with respect to the PARSEC-COLIBRI evolutionary track (Fig. 6.3) and their low luminosities may signify that they are in fact less evolved non-maser-emitting carbon stars. Within the [3.6]−[8.0] vs. absolute flux density at 24 μm CMD (Fig. 6.6), these less luminous sources occupy an area typical of carbon stars, providing further evidence for this conclusion.

Looking at mass-loss rates versus pulsation period (Fig. 6.10) a spread of values for the SMC is seen that spans the other samples. An increase in the mass-loss rate with pulsation period is also seen for the SMC sample. There are several sources with comparable luminosities, pulsation periods and mass-loss rates, suggesting that the SMC sources are in a similar evolutionary stage within the superwind phase. An example being the SMC source BMB-B75 and the LMC source IRAS 05402−6956, with luminosities of

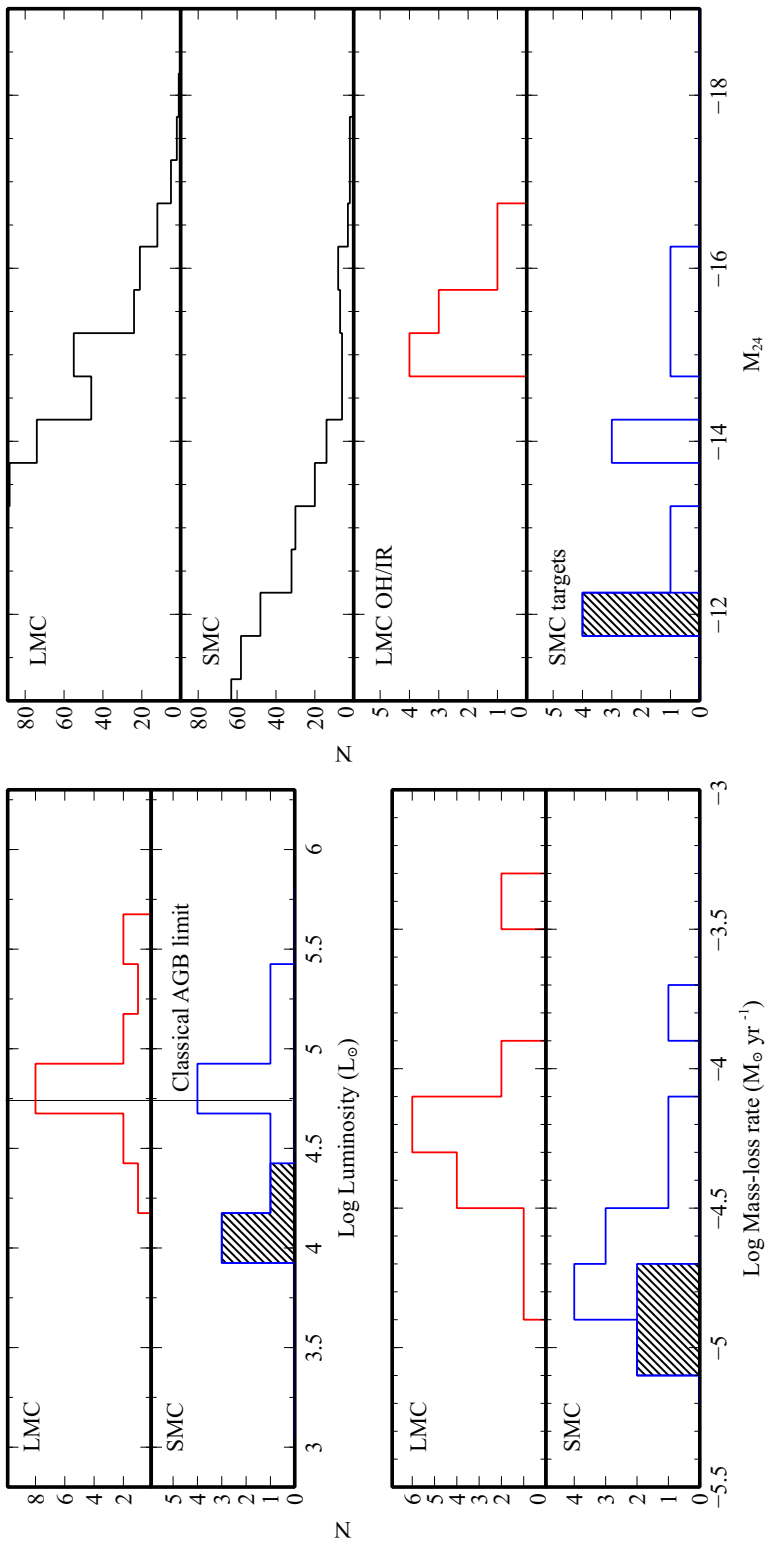

Figure 6.9: ***Left***: Luminosity and mass-loss rate distributions of the SMC targets, and LMC OH/IR stars. ***Right***: The absolute 24 μm flux distribution of the SAGE-LMC and SAGE-SMC samples along with those of the LMC OH/IR and SMC target samples. In both figures, the suspected carbon stars are designated with hatched lines.

Figure 6.10: The mass-loss rate as a function of luminosity (*Left*) and pulsation period (*Right*) for the OH/IR samples in the LMC and SMC. Also shown are the mass-loss rates calculated for the SMC sample using the newly derived mass-loss prescription (Eq. 5.2) designated as 'SMC prescription'. A pulsation period of 500 d is assumed for the calculation of the prescription mass-loss rate for 2MASS J00592646-7223417.

58,000 and 51,000 $L_\odot$, pulsation periods of 1453 and 1393 d, and mass-loss rates of 3.5 and 8.4×10^{-5} $M_\odot$ yr^{-1}, respectively.

From the new relation for the circumstellar expansion velocity (Eq. 5.1), the expected expansion velocities of the SMC target sample has been calculated (shown in Table 6.4) assuming a metallicity of one fifth solar. Typical expansion velocities for these sources are expected around 3 km s^{-1}, yet it is possible that as the strength of radiation pressure wanes, other wind-driving forces take over, resulting in underestimated predictions for the wind speed. SMC sources have also been modelled with DUSTY models calculated with a simple inverse square density distribution (as opposed to the SEDs calculated using a full hydrodynamical solution) and found negligible difference between the results. This may indicate that the material is blown out without the need for pulsation-enhancement. A slower wind should result in more efficient stimulated emission as a result of higher density. This higher rate of collisions may then make it easier to quench the maser. Another scenario worth mentioning is the possibility of binarity in the SMC target sample. While there is no clear evidence to suggest this, symbiotic Miras tend to have weaker maser emission as a result of the decreased coherence within the OH shell (Seaquist, Ivison & Hall, 1995). Disruption of velocity coherence seems to be significant even in less extreme interactions than symbiotics (Howe & Rawlings, 1994). This may provide another possible explanation for a decrease in masing sources within the SMC. We can thus conclude that there is no strong evidence for AGB stars and RSGs in the metal-poor SMC, at ~ 0.2 $Z_\odot$, to experience weaker mass loss than those in the more metal-rich systems, the LMC (~ 0.5 $Z_\odot$) and Galactic Bulge and Centre (~ 0.5–2 $Z_\odot$).

6.4.6 Future prospects

The Galactic Australian Square Kilometre Array Pathfinder (GASKAP) Spectral Line Survey is an upcoming high spectral resolution (0.2 km s^{-1}) ASKAP survey of the 21-cm HI, and 18-cm OH lines, in the Milky Way galactic plane, the LMC, the SMC, and the Magellanic Bridge and Stream (Dickey et al., 2013). GASKAP will survey these

regions with sensitivities better than that of Parkes (around 0.5 mJy with a 200 hour integration). As the entire SMC will fit within the field of view of ASKAP, this is feasible and there is therefore a good chance that GASKAP will detect OH maser emission from the most luminous candidates wherever they reside in the SMC. It was predicted by (Etoka et al., 2015), based on the relation between 1612 MHz OH maser emission and mass-loss rate (Zijlstra et al., 1996), that around two dozen OH maser sources should be detectable in the SMC at a 3-σ sensitivity of 0.1 mJy. Following the same approach, for the range in mass loss parameters listed in Table 4 for our SMC sample of OH maser candidates we would predict 3–29 mJy. We are therefore somewhat more optimistic about the prospects for GASKAP to detect more than a few OH masers in the SMC, or for it to confirm that the maser mechanism breaks down at the metallicity of the SMC. This survey will also be a precursor to much larger surveys using the Square Kilometre Array, which will reveal the full extent of the maser samples in these regions or show that the maser mechanism breaks down at the metallicity of the SMC.

6.5 Conclusions

Using the properties of past OH maser host stars, the brightest SMC sources likely to exhibit circumstellar maser emission have been identified and observed. The new, deep 1612-MHz OH maser observations with single and interferometric instruments have not resulted in any clear maser emission from the targeted or in-field sources, yet a number of maser-emitting sources may still lie below the observation detection thresholds. Assuming the masing mechanism is the same within the Galaxy and Magellanic Clouds, the top two candidates for maser emission have upper limits for maser efficiency (converting F_{35} to $F_{\rm OH}$) of 3.6 and 4.3%. These values are dramatically lower than the typical maser efficiency around 23%. This may point to differences within the circumstellar environments of evolved stars at lower metallicity that may include a low OH abundance or strong interstellar radiation. The effects of metallicity on the strength of circumstellar OH maser emission still cannot be adequately quantified. It is expected that some

of these sources are near the OH column density threshold for maser emission and it is also suspected that maser emission may still lie below the detection threshold. It is also possible that the OH masing phase does not last as long in the SMC as at higher metallicity, at least for massive AGB and RSGs. This could have implications for the contribution from these stars to the total dust budget in the galaxy, and for the contribution in which the RSGs undergo core collapse. Future observation with the GASKAP survey (Dickey et al., 2013) will be able to add clarity to the understanding of circumstellar maser emission and the effects of metallicity.

7 Unveiling the dustiest RSGs in the LMC

As has been stated in previous chapters, dusty evolved red supergiants are major sources of dust in the local group. These types of source are also some of the best candidates for SNe progenitors. However there are several sources like the LMC RSGs IRAS 05280−6910 and IRAS 05346−6949 that do not fit the mould of previous known RSGs in their SEDs or maser properties. IRAS 05280−6910 has 1612-MHz maser emission where IRAS 05346−6949 does not. In order to better understand the nature of these sources as well as their contribution to the LMC, it is critical to have an accurate measure of the optical depth. One of the best methods of doing this is by modeling the SED, focusing specifically on the 10 μm silicate feature, which is sensitive to changes in the optical depth. The superior angular resolution of the Very Large Telescope (VLT) has been employed to target the 10 μm silicate feature and obtain an accurate measure of the mass-loss of the important dust-producing RSG: IRAS 05280−6910, and the nearby RSG: WOH G347. The RSG IRAS 05346−6949 has also been observed in the N-band and at the 1612-MHz OH maser transition. The overall aim of this study however is to understand the feedback and nature of these prominent dust producers.

7.1 IRAS 05280−6910 and WOH G347

IRAS 05280−6910 and WOH G347 lie within the cluster NGC 1984 (van Loon, Marshall & Zijlstra, 2005). The cluster has a metallicity of $0.126^{+0.19}_{-0.08}$ $Z_{\odot}$ (Mackey & Gilmore, 2003), an age of $11.5^{+11.4}_{-5.7}$ Myr (Oliva & Origlia, 1998), and a cluster mass of 1259^{+560}_{-407} $M_{\odot}$ (Elson & Fall, 1988). The low metallicity of this cluster is surprising given the expected metallicity of the LMC at around half solar and the particularly low derived gas-to-dust ratio of IRAS 05280−6910 (§4.5). The locations of the RSGs have been constrained using J- and K-band images from SOFI (details in van Loon, Marshall & Zijlstra, 2005), as well as a WFPC2 0.5 μm image from the HST shown in Figure 7.1. A number of sources within the image are saturated and while WOH G347 is clearly the brightest

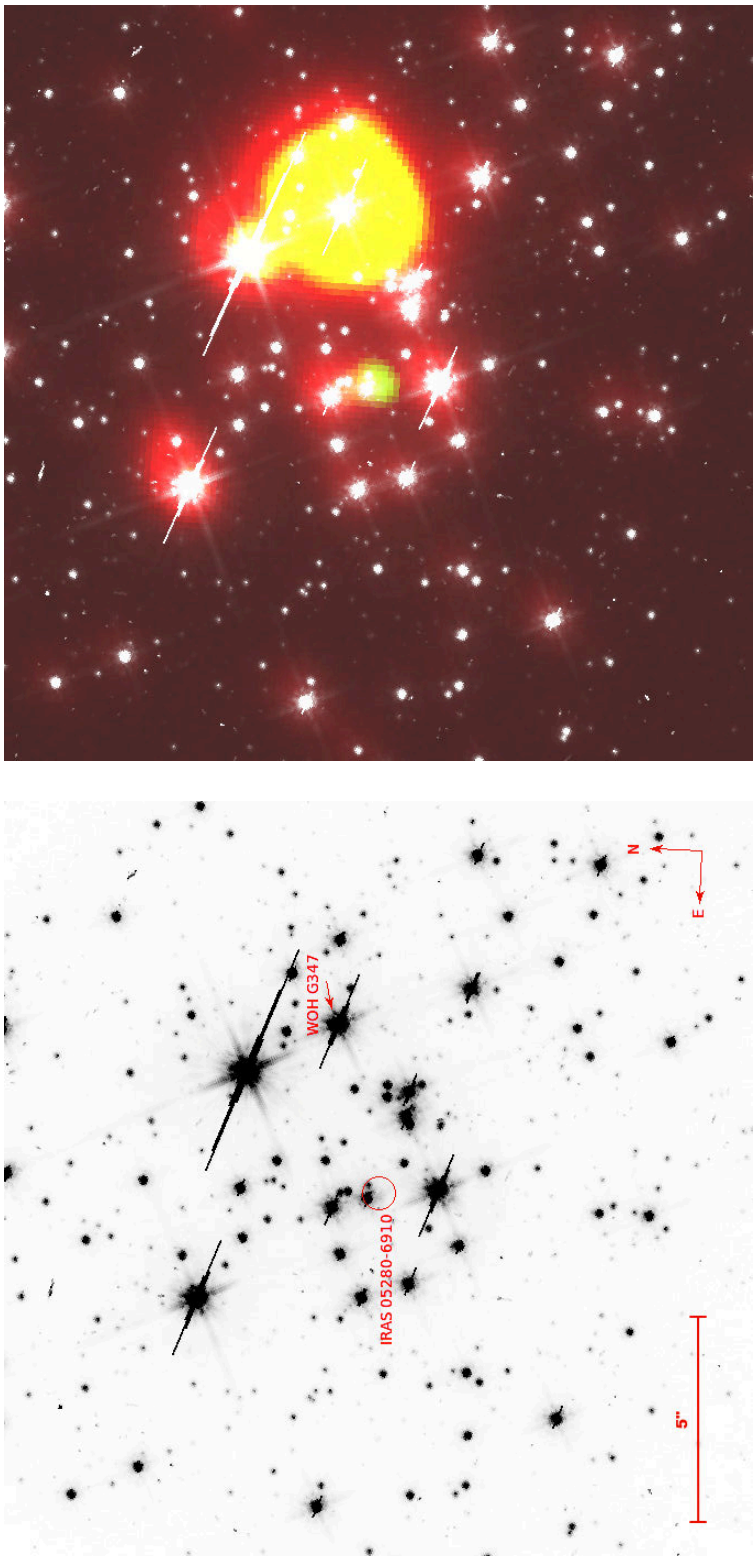

Figure 7.1: ***Left***: An HST 0.5 μm image of the LMC cluster NGC 1984, with the location of WOH G347 and the suspected location of IRAS 05280−6910. ***Right***: SOFI J-band (in red) and K-band (in green) images overlaying the 0.5 μm image.

yellow source on the right of the SOFI image, the location of IRAS 05280−6910 is still unclear. The location has been constrained to the small greenish region within the left side of the image, but IRAS 05280−6910 is not likely visible in the optical as a result of extreme circumstellar dust extinction.

In the past, these sources have been observed at $2.9 - 4.1$ μm with the VLT's ISAAC instrument, with neither source showing strong molecular features at these wavelengths (van Loon et al., 2006a). IRAS 05280−6910 has had previous spectroscopic observations in the near-IR with observations in the N-band using the *Spitzer* Infrared Spectrograph (Kemper et al., 2010) as well as in the far-IR with *Spitzer* MIPS (van Loon et al., 2010) and the *Herschel* PACS and SPIRE instruments (Matsuura et al., 2016). The near-IR results show the 10 μm silicate feature of IRAS 05280−6910 in absorption, indicative of high optical depth, dust content and mass loss. However it was suspected that a contribution from the nearby RSG WOH G347 may be masking the full depth of the silicate feature by (Boyer et al., 2010); fitting the SEDs of the two sources has led to the same suspicion (Fig. 7.2). At far-IR wavelengths, observations have detected both CO and H_2O lines, that were used to calculate a mass-loss rate comparable to previous estimates.

In the radio, circumstellar masers have been detected emanating from IRAS 05280−6910, both at the 22-GHz water maser transition, and 1612- and 1665-MHz OH maser transitions (Wood et al., 1992; van Loon et al., 2001a, §4.5). The results have shown a spectacular array of asymmetric peaks that have changed dramatically over a period of 25 years. The source is also strongly circularly polarized at the 1612- and 1665-MHz maser transitions, indicative of magnetic activity.

IRAS 05280−6910 is the second most luminous OH/IR star in the LMC, second only to the RSG: WOH G64. As has previously been discussed, it is suspected that the two have similar geometries based on observations in the optical, IR, and radio (Roche, Aitken & Smith, 1993; van Loon et al., 1999; Marshall et al., 2004; Ohnaka et al., 2008, §4.5). Ohnaka et al. (2008) used the VLT interferometer to resolve the shell around WOH G64, directly confirming past speculation; the evidence for a torus geometry in IRAS 05280−6910 is still speculative. From the unique spectral energy distributions and maser

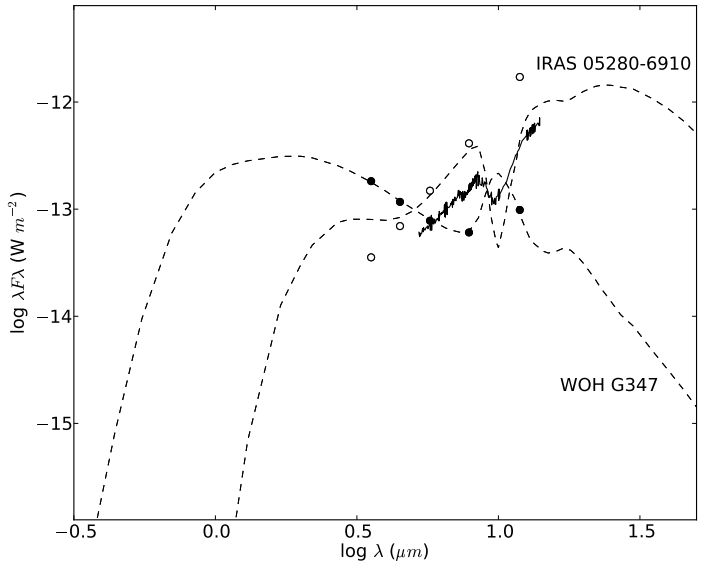

Figure 7.2: The SEDs of both of the RSGs fitted with DUSTY models (dashed lines). Photometry are IRAC@*Spitzer* fluxes and 11.9 μm flux from TIMMI2@ESO3.6m for IRAS 05280−6910 (open symbols) and WOH G347 (closed symbols); the *Spitzer* IRS spectrum (originally thought to have contributions from both sources) is in solid black.

spectra of these sources, they are expected to have dusty tori with bi-polar outflows, where WOH G64 has been observed pole-on and IRAS 05280−6910 nearly edge-on.

7.2 VISIR observations

VISIR is the VLT's mid-IR imager and spectrograph (Lagage et al., 2004), capable of long-slit spectroscopy with resolving powers ranging from 150 to 30,000. The instrument uses a Cassegrain focus and is mounted on the 8.2-metre VLT Melipal telescope (UT3).

The observations (Project 098.D-0272; PI: Goldman) were taken the night of January 15, 2016 and used VISIR's low-resolution spectroscopy mode (and low resolution grating) with a wavelength range of $8 - 13$ μm and a resolving power of 350 at 10 μm. The target field was observed with a 965 second integration and an optical seeing between $0.3 - 0.4''$, corresponding to a spatial resolution of $\sim 0.3''$. The diffraction limit of the telescope ranges from $0.25 - 0.4''$ at the blue and red end of the detector, respectively.

The original observing plan called for a 600 second integration, but this exposure time was increased as the second source could not be seen in the acquisition images.

This observation targeted the two RSGs simultaneously, which lie $\sim 4''$ from each other at an angle of 77.5 degrees west of north. The observation used a slit length of $32''$, a slit width of $1''$, and chopping and nodding to compensate for instrumental effects. Parallel nodding was used with 10 nodding cycles, along with a chopping amplitude of $8''$. The data were reduced using the reflex software (version 2.8.5) VISIR pipeline (version 4.3.1). The resulting spectra were then flux calibrated using the telluric standard eps Psc, taken the night before.

7.3 Results

While previous N-band spectroscopy of IRAS 05280−6910 was done using *Spitzer*, the angular resolution of the observation was not expected to be high enough to disentangle the contribution of sources within the crowded cluster field, yielding an inaccurate measure of the silicate feature at 10 μm. However, the new VISIR spectrum of IRAS 05280−6910 shows little difference from that of the *Spitzer* IRS spectrum (Fig. 7.3, 7.4), indicating this is not the case. The angular resolution of the VLT has insured that the observation has isolated the contribution of the primary target source.

7.3.1 The SEDs of IRAS 05280−6910 and WOH G347

IRAS 05280−6910 is unique in that it has an uncommon SED for a red supergiant. The observed silicate feature in both the *Spitzer* IRS and now VISIR observations is much shallower than is expected from SED modelling. Both of the targets were modelled with the DUSTY 1D radiative transfer code (Elitzur & Ivezić, 2001). Using a similar χ^2 fitting technique as was used in Chapters 4 and 6, SEDs were fitted and the results suggested that the relative contributions of the two sources would likely result in the silicate feature observed. However it has now been confirmed the shallow silicate feature of IRAS

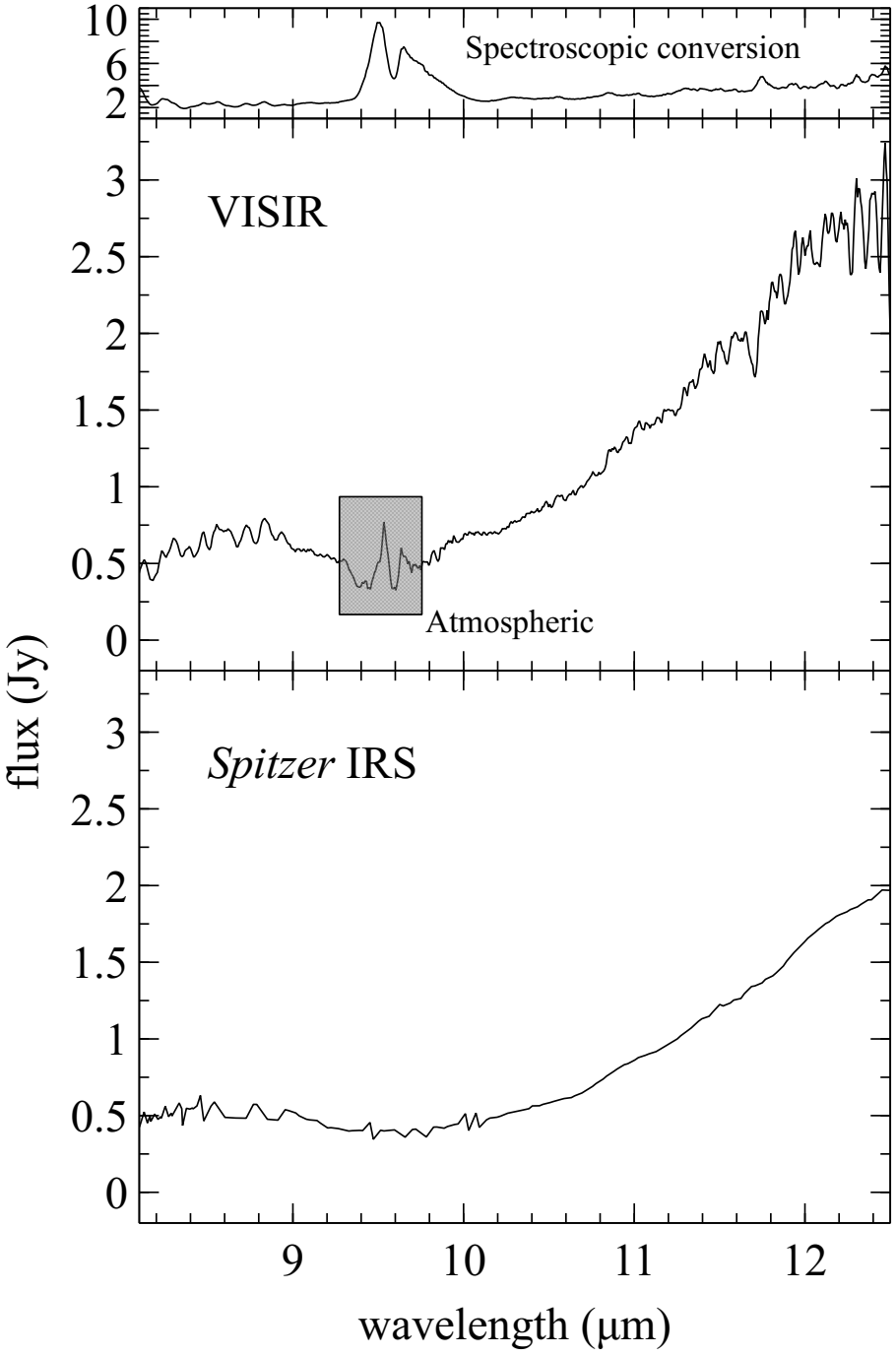

Figure 7.3: The VISIR and IRS N-band spectra of IRAS 05280−6910. The region marked atmospheric is contaminated by telluric features.

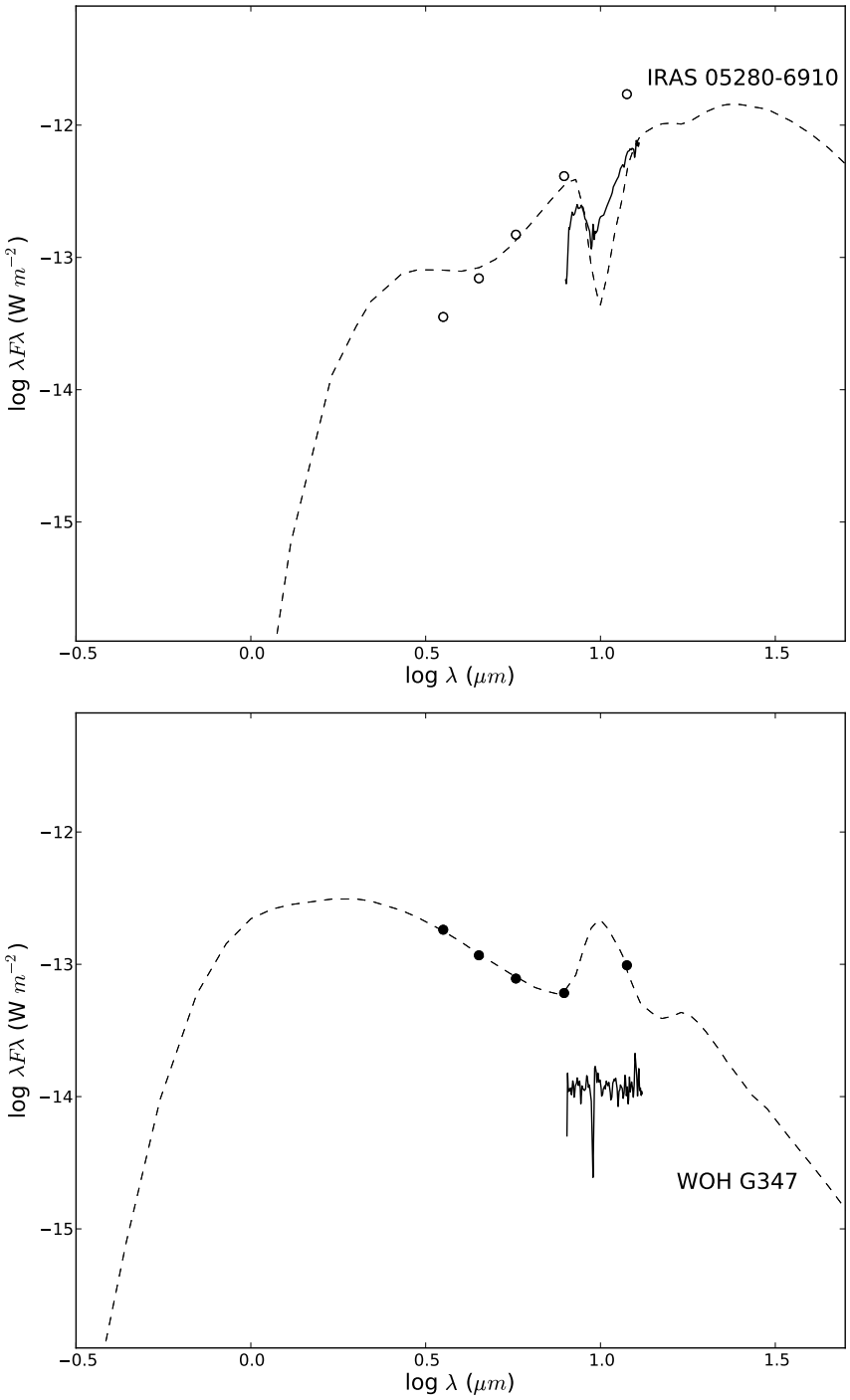

Figure 7.4: The SEDs of IRAS 05280−6910 (*Top*) and WOH G347 (*Bottom*) shown with the best-fit DUSTY model (dashed line). Photometry are IRAC@*Spitzer* fluxes and 11.9 μm flux from TIMMI2@ESO3.6m for IRAS 05280−6910 and WOH G347; the VISIR spectra are shown in solid black.

05280−6910 seems to be unaffected by that of WOH G347. Why the general shape of the SED from photometry and SED models suggests a high optical depth, whereas the observed silicate feature does not, may be a result of the source's unique geometry. This may be a result of another dust component or object within the source. Another possibility is that the source is on the borderline between emission and absorption as has been the case during some epochs for VY CMa (Monnier, Geballe & Danchi, 1998, 1999).

WOH G347 was also detected with VISIR, but the spectrum is not as bright as predicted by the SED. During the observation, WOH G347 was not seen within the acquisition image. It is highly likely that this source was not centred on the slit during acquisition, which has led to a lower flux received by the detector.

7.4 Source location

As has been previously stated, the primary target IRAS 05280−6910 may be visible in the SOFI K-band image, but is likely too obscured to be seen in the HST optical images. However, the position can be further constrained using mid- and far-IR data. Images of the target region from the HST, *Spitzer*, and *Herschel* (Fig. 7.5) suggest a similar picture as that of the SEDs. Two isolated bright sources can be seen clearly in the *Spitzer* 3.6 μm image. This shape can also be seen in the smoothed HST image. As the wavelength increases through the images, the strength of the right source seems to wane as the strength of the left source increases dramatically (ignoring the white saturated pixels). This is seen until the 8 μm image where the two sources are no longer distinguishable from one another.

The best-determined coordinates for IRAS 05280−6910 and WOH G347, for each of the observations, is shown in Table 7.1. The most accurate positions of the two sources are from the HST and SOFI images due to the much higher pointing accuracy and angular resolution of the HST as opposed to the other instruments (Table 7.2). The offset in positions between the VISIR observation and the HST observations is around 3.5″, which is near the pointing accuracy of VISIR at 3″ rms.

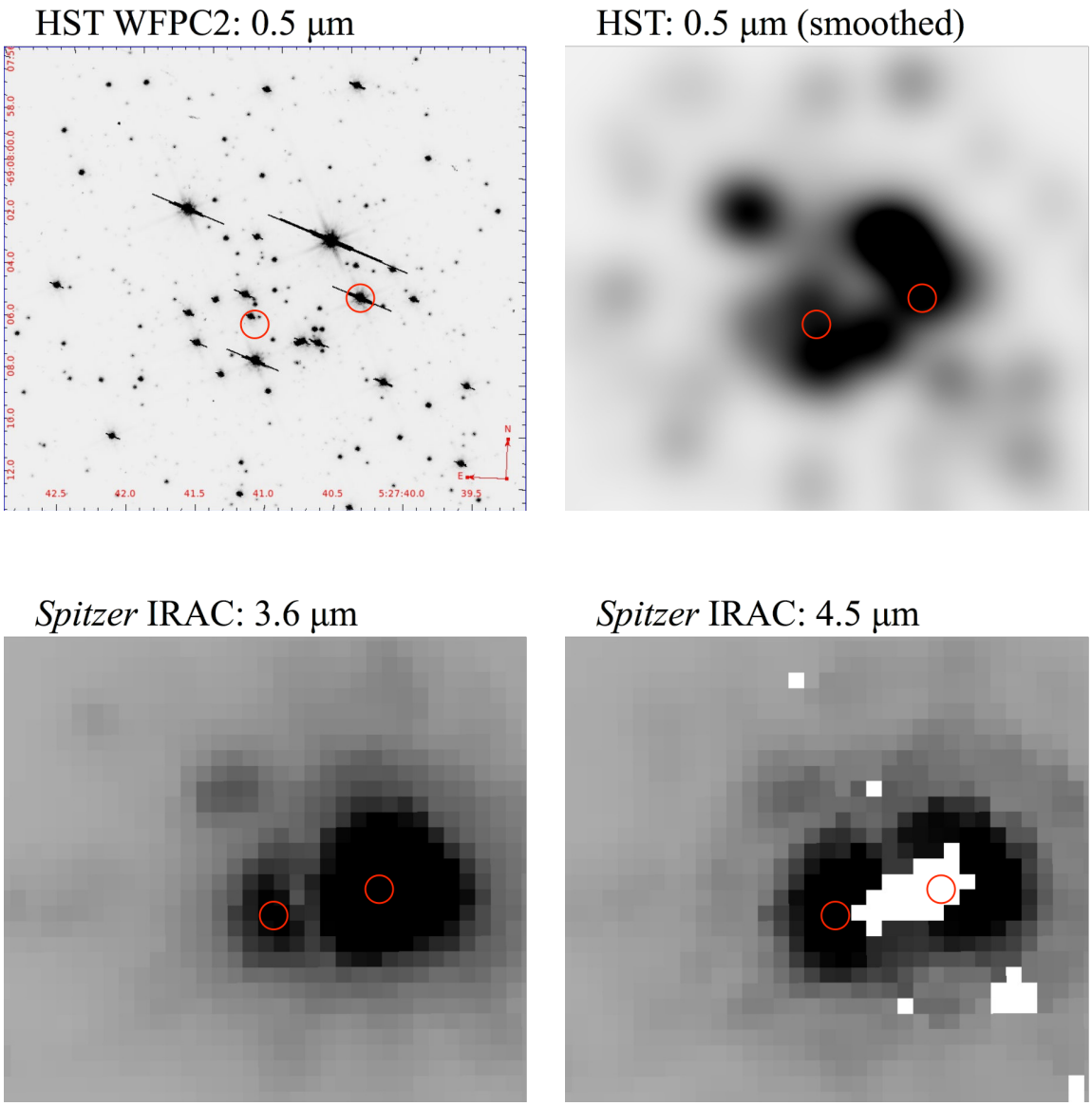

Figure 7.5: Shown are the regions surrounding IRAS 05280−6910 (left red circle) and WOH G347 (right red circle) with images from HST, *Spitzer*, and *Herschel*. The HST image (top left) has been gaussian smoothed with a 50 pixel kernel (top right) to approach the angular resolution of the *Spitzer* images. The diagonal streaks in the HST image and the white pixels in the 4.5, 5.8, and 24 μm images are the result of saturation of the detector.

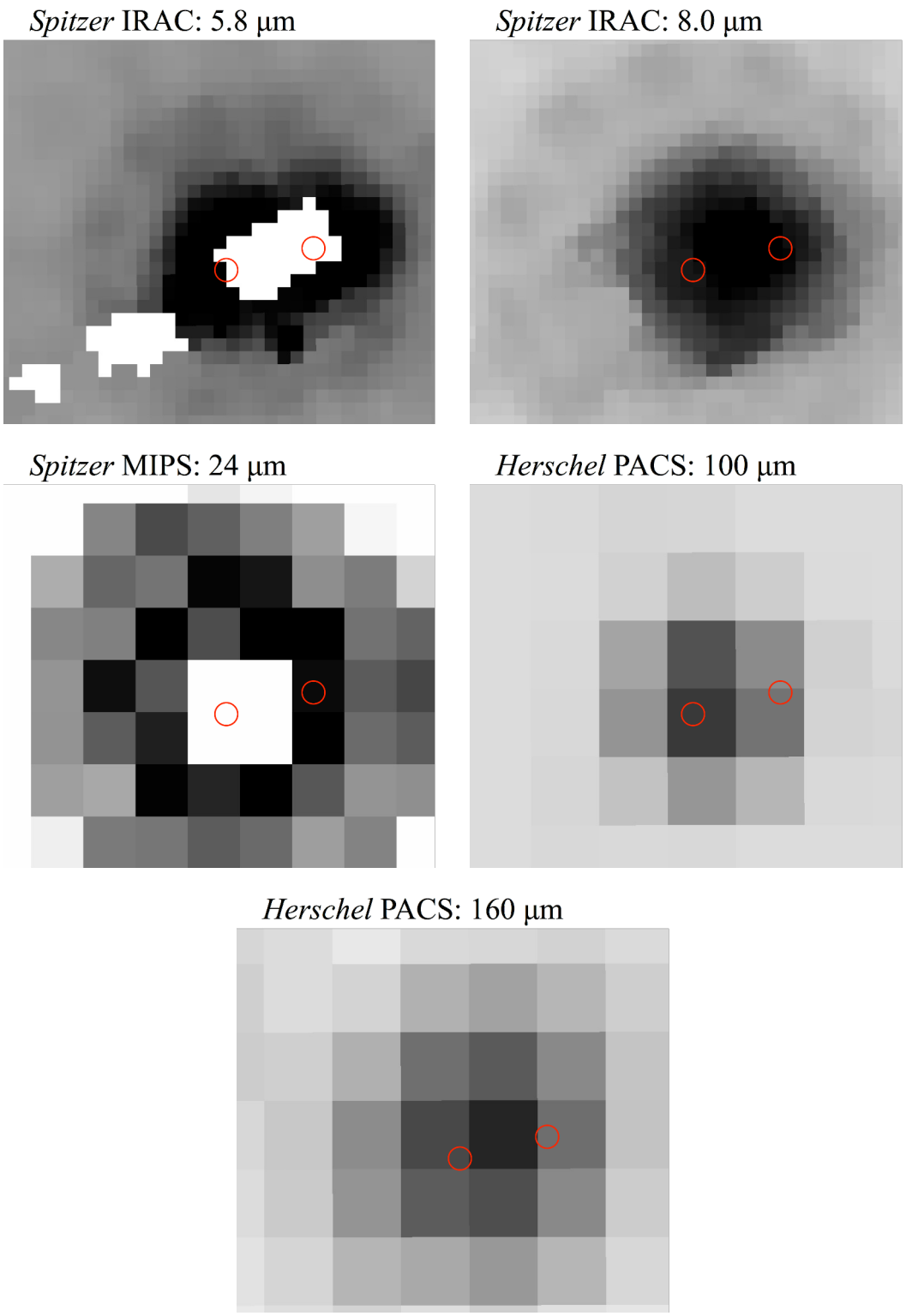

Figure 7.5: continued

Table 7.1: The best-determined J2000 source positions for each observation for VISIR, ATCA, and the suspected position from the combined HST/SOFI image.

Instrument	IRAS 05280−6910		WOH G347	
	RA	Dec.	RA	Dec.
VISIR	05 27 40.2	−69 08 04.8	05 27 39.5	−69 08 03.9
SOFI/HST	05 27 41.1	−69 08 06.0	05 27 40.4	−69 08 04.8
ATCA	05 27 40.9	−69 08 06.9		

Table 7.2: Estimates for the pointing accuracy and angular resolution for the highest angular resolution instruments used to observe IRAS 05280−6910 and WOH G347.

Instrument	Pointing accuracy	Angular resolution
VISIR	3″	0.3″
HST	0.002-0.005″	0.05″
ATCA	2″	7″

Where the optical images have constrained the location of two obscured and reddened sources, the mid-IR images have indicated their identities. The change in strength of the two sources within the IRAC images shows a clear difference between these sources.

7.5 IRAS 05346–6949

The analysis of IRAS 05280−6910 has led to the further study of another LMC RSG: IRAS 05346−6949. The source has a similar unique SED which predicts a much deeper silicate feature in absorption than what has been observed (Fig. 7.6). The sharp increase in flux from 3 to 8 μm ([3.6]-[8.0] = 6.7 mag) is suggestive of heavy extinction. Yet, similar to IRAS 05280−6910, the N-band spectrum from *Spitzer* IRS spectroscopy has shown that this conclusion is not supported by the source's silicate feature. This discrepancy casts doubt on the results of the SED fitting, and the particularly high derived optical depth and mass-loss rate (Table 7.3). To probe the nature of this source

Table 7.3: The LMC RSG derived luminosities (L), predicted expansion velocities assuming a gas-to-dust ratio of 200 ($v_{\rm exp,DUSTY}$), effective temperature ($T_{\rm eff,DUSTY}$), inner dust temperature ($T_{\rm inner}$), optical depths specified at 10 μm (τ), and mass-loss rates ($\dot{M}$), from SED fitting with DUSTY. The mass-loss rates scale in proportion to $L^{3/4}(r_{gd}\rho_{\rm s})^{1/2}$, where the dust grain bulk density (ρ_s) is 3 g cm^{-3}.

Object name	L (10^3 L$_\odot$)	$v_{\rm exp,DUSTY}$ (km s^{-1})	$T_{\rm eff,DUSTY}$ (K)	$T_{\rm inner}$ (K)	τ	$\dot{M}$ (M$_\odot$ yr^{-1})
IRAS 05280−6910	225	13.6	3400	350	13.4	5.4×10^{-4}
WOH G347	45	20.4	3700	1400	0.6	6.4×10^{-6}
IRAS 05346−6949	107	6.7	3000	600	25.1	1.7×10^{-3}

further, it has been targeted at radio frequencies.

IRAS 05346−6949 has been classified as an extremely red object (ERO; Gruendl & Chu, 2009), an extreme-AGB star (Srinivasan et al., 2009), and an RSG (Elias, Frogel & Schwering, 1986; Jones et al., 2015). The source has also shown large variability within data from the VMC survey (Groenewegen, private communication). Given the source's bright IR flux, and other properties typical of maser-emitting evolved stars, it is expected to exhibit bright maser emission, and has been targeted in the past at OH maser frequencies (Wood et al., 1992) as well as SiO and water maser frequencies (van Loon et al., 2001a). These included observations targeting the 86-GHz SiO maser line with Mopra (rms noise level: 0.5 Jy), the 22-GHz water maser transition with Parkes (rms: 11 mJy) and again with Mopra (rms: 4 mJy), and the 1612-MHz OH maser transition with Parkes (rms: $\lesssim$ 50 mJy). Given the high noise level of the previous OH maser observation, and the variability of these sources, the source has been reobserved at 1612-MHz.

On September 2, 2016 the Parkes radio telescope was used to target the 1612-MHz maser line in IRAS 05346−6949 (Project PX032; PI: Goldman). The observation used the H-OH receiver and DFB4 correlator with a dual-polarisation setup with 8-MHz bandwidth and 8192 channels yielding 0.18 km s^{-1} channel^{-1} velocity resolution. The observation used a position switching mode with 15 minutes on-source and 15 minutes off-source to a location 1 degree south of the target.

This source does not show any prominent peaks within its 1612-MHz maser spectrum (Fig. 7.6). Using the predicted 35 μm flux value from the best-fit DUSTY

Figure 7.6: *Left*: The SED fitting of DUSTY models to the IRAS 05346−6949, with the best-fitting model (dashed line), *Spitzer* IRS spectra (in solid black), *Spitzer* IRAC and MIPS, and *Herschel* PACS photometry (in red), and the remaining available photometry (small open circles). ***Right*:** The OH 1612-MHz maser spectrum from IRAS 05346−6949, with the spectrum resampled to 0.5 km s^{-1} (smoothed), and the H I shown for velocity reference.

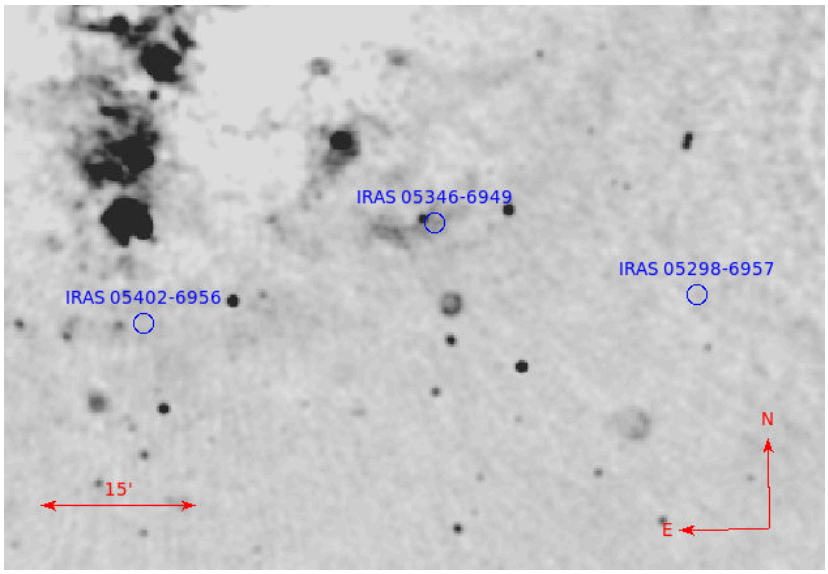

Figure 7.7: The 1420-MHz continuum image of IRAS 05346−6949 from Hughes et al. (2007).

model (9.6 Jy) and the median maser efficiency of the LMC maser sample (38%), the source should have two maser peaks with intensities $\sim$ 0.9 Jy. It is thus surprising that our observation with an rms noise level of around 25 mJy did not detect any emission. Within the 1420-MHz continuum image of the region (Fig. 7.7) from Hughes et al. (2007), several continuum sources lie between IRAS 05346−6949 and the two other nearby masing sources IRAS 05402−6956 and IRAS 05298−6957. An unknown continuum source also lies 1.3′ to the north east of our IRAS 05346−6949 which is unlikely to be contributing flux to the *Spitzer* IRAC photometry, with an angular resolution of $\sim 2''$. As was stated originally by Elias, Frogel & Schwering (1986), the mid-IR colour and lack of spatially coincident continuum emission suggest this source is unlikely to be a YSO. Given what is now known about the source, it remains likely that it is an evolved RSG with an asymmetric geometry, as is also suspected in IRAS 05280−6910 (§4.5), and has been confirmed in WOH G64 (Roche, Aitken & Smith, 1993; van Loon et al., 1999; Ohnaka et al., 2008).

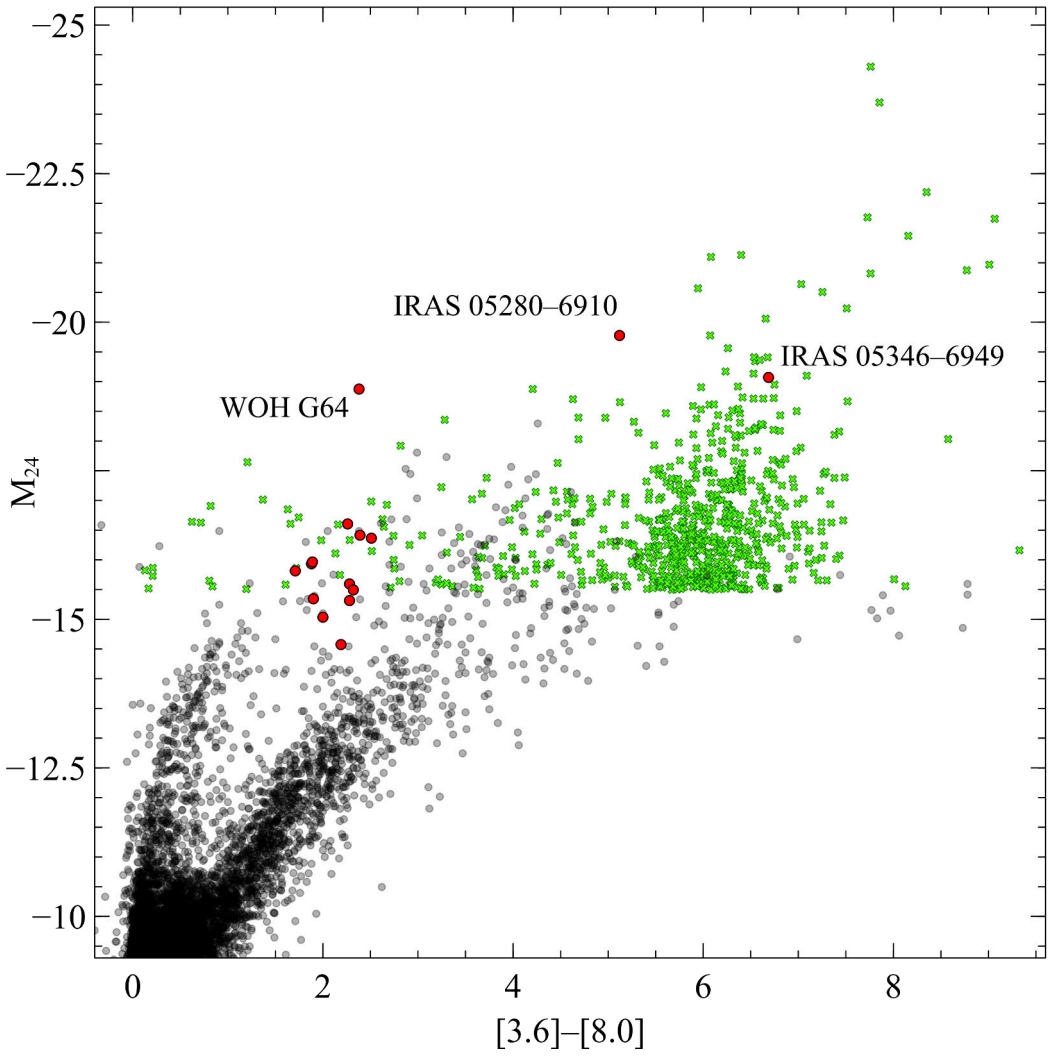

Figure 7.8: The *Spitzer* MIPS 24μm flux density versus IRAC [3.6]−[8.0] colours for the OH/IR sample in the LMC (red) as well as all sources from the SAGE-LMC and SAGE-SMC catalogues (black). Also shown is W4 versus W1−W3 colours for some of the brighter WISE sources (W4 $<$ 2 mag) within a three degree radius of the LMC (green); the M_{24} values for the three labelled RSGs and MSX LMC 1207 are also from WISE W4 photometry.

7.6 The IR colours of the most luminous LMC RSGs

WOH G64, IRAS 05280−6910 and IRAS 05346−6949 have characteristics unlike the rest of the evolved stars within the LMC. The uniqueness of these sources amongst the rest of the LMC OH/IR stars is clear in the *Spitzer* MIPS M_{24} versus IRAC [3.6]−[8.0] CMD of the LMC OH/IR sample, and the rest of the SAGE-LMC and SAGE-SMC sources (Fig 7.8). The MIPS observations of IRAS 05346−6949, WOH G64, and IRAS 05380−6910 were saturated and thus WISE W4 (22μm) fluxes from the WISE all-sky catalogue (Cutri et al., 2012) have been used instead. Some of the brighter LMC sources (W4 $<$ 2 mag, and within a 3 degree radius of the LMC) from the WISE all-sky catalogue have also been included using W4 versus W1 (3.4μm)−W3 (11.6μm) instead to show the region above the limit where the *Spitzer* observations have been saturated. While *Spitzer* has a significantly higher angular resolution than WISE, the WISE photometry have been used here to show the progression of sources with bright 24 μm fluxes and significantly reddened colours. The WISE sources that lie around the position of IRAS 05346−6949 all lie in molecular cloud regions and are expected to be YSOs. No other sources within the SAGE-LMC and SAGE-SMC catalogues or within the brightest WISE LMC sources lie near the positions of WOH G64 and IRAS 05280−6910. Thus it is clear that these sources have unique spectral energy distributions unlike any other evolved stars within the Magellanic Clouds.

7.7 Conclusions

New VISIR *N*-band spectroscopy has been used to constrain the optical depth and mass loss of the RSG: IRAS 05280−6910. HST and SOFI optical images have also been used to confine the locations of the two RSGs, IRAS 05280−6910 and WOH G347, to two regions bright in the SOFI *K*-band image. The source locations have been further matched to their suspected positions using *Spitzer* and *Herschel* mid- and far-IR images.

While the discrepancy between the optical depth suggested by the silicate feature and the overall shape of the SEDs of IRAS 05280−6910 and IRAS 05346−6949 is still puzzling, this is likely a result of geometric effects. Given the reddened colour, long pulsation period, and bright IR flux of the LMC RSG: IRAS 05346−6949, the source was expected to show bright maser emission within the 1612-MHz OH maser line observation. However, the source has shown no clear maser emission. Constraining the mass loss of prominent dust producers like IRAS 05280−6910 and IRAS 05346−6949 will continue to advance the understanding of the dust budget within the Magellanic Clouds and the mass-loss mechanisms within the more luminous regime of evolved stars. Further high angular resolution investigations of these sources with instruments like the VLT's interferometric instrument MATISSE will be needed to further understand these sources.

8 Conclusions

8.1 Discussion

This research has examined and constrained the mass loss and wind dynamics in massive AGB stars and RSGs. Probing sources of varying luminosities and metallicities has allowed for the isolation of important individual stellar relationships. This has led to better constrained empirical links between parameters key to the mechanisms underlying wind-driving and mass loss. The following sections will discuss some of the key relationships studied in this Thesis. The results have implications for the lifetimes of AGB stars and RSGs, the evolutionary path of core-collapse progenitors, stellar transformations within the evolutionary sequence, and origin of gas and dust in the Universe.

8.1.1 How is circumstellar expansion velocity affected by other stellar parameters?

As a result of the survey of circumstellar masers in the Magellanic Clouds conducted in this work, the LMC circumstellar maser sample has been increased significantly, and along with it, the number of derived wind speeds from sources outside of the galaxy. This sample has been used to derive the most robust empirical relation for the link between superwind speeds and the related stellar parameters. The results show a correlation between wind speed and both luminosity and metallicity for evolved stars between a half and twice solar metallicity (Eq. 5.1).

Unlike previous analyses, this work has implemented a new method of determining the dust content of individual sources. Furthermore, these results have been used to refine the relationship between the dust content and wind driving, a parameter which wind driving is expected to be critically influenced by. However, the method of deriving gas-to-dust ratios still needs testing.

These results have led to the expectation that slower wind speeds should exist in

even lower metallicity environments like the SMC. The newly derived empirical relation for the expansion velocity of evolved stars relies on the assumption that the driving force is radiation pressure on dust. At lower metallicity environments the drift velocities between the gas and dust may increase. This may result in highly accelerated localised "bullets" where the dust is quickly blown out as soon as it forms with little accompanying gas. At this point the dust-driven wind may break down. At lower metallicity and luminosity, it is expected that other forces like magneto-acoustic or Alfvén waves may take over in this regime.

8.1.2 How is mass loss affected by other stellar parameters?

The LMC OH/IR sample analysis has found that mass loss is tightly correlated with luminosity. As radiation is the force behind the driving of the wind and mass loss, this is not surprising. The LMC analysis has also found a correlation between mass loss and pulsation period. As larger and longer pulsations levitate more material out to radii where it can condense into dust and drive an outflow, this fits within the current theoretical framework. The fact that luminosity and pulsation period are themselves correlated complicates the relationships. These parameters are also not interchangeable as empirical fits of the product of the two parameters does not fit the samples as well as they do individually. More work will be required to disentangle the dependence of mass loss on these parameters and further constrain the relationships.

The fact that little-to-no correlation is seen between mass loss and gas-to-dust ratio also follows the idea that the net mass transfer will only depend on the driving force: luminosity. These results suggest that while the wind dynamics will be affected by metallicity, the mass-loss mechanism is unaffected by metallicity, at least between a half and twice solar metallicity.

One major assumption made in this work is that the derived mass-loss rates are calculated assuming winds where the gas and dust are dynamically coupled. At lower and lower metallicities, this assumption may not hold. With fewer materials at lower metallicity to act as seed nuclei, and as a result, less dust, there may not be enough dust

to create a uniformly expanding circumstellar wind. Evidence for an unevenly expanding and clumpy wind around a higher meallicity source has been seen around the RSG: VY CMa (Humphreys, Helton & Jones, 2007; Richards et al., 2012). Empirically, uniformly expanding winds are not seen at high resolution, and may occur only in some OH/IR stars.

8.1.3 How does metallicity affect maser emission and the circumstellar environment?

This work has investigated every SMC source likely to exhibit circumstellar maser emission at the current sensitivity limits of the instruments used, and has established the expectation of maser detection within the SMC. The upper limits of the maser efficiency of the best SMC candidates for maser emission point to an underlying change within the circumstellar environment of OH/IR stars at this metallicity, yet how they differ is still unclear. Some sources may lie just below the detection threshold of the observations. An estimation of the required OH abundance for maser emission has led to the conclusion that the SMC sources are also near an OH column density threshold. As the sources become optically thin, the maser emission becomes dependent on both the supply of IR photons and oxygen supply and thus the metallicity squared. This explanation may also apply to the lack of maser emission seen in nearby globular clusters.

Moving forward, the SMC will be further investigated at the 18cm OH maser lines with the upcoming GASKAP survey (discussed in §8.2). However, the survey will not cover the 22-GHz water maser transition. It is possible that the circumstellar environments in the SMC may provide a more suitable environment for water maser emission. As a slower wind may create a denser outflow, this may result in a more extended water masing regions. Considering the water maser transition is also pumped collisionally, it may be more effective at lower metallicity. Observations of the brightest SMC sources in CO line transitions with ALMA may also be able to provide information of the wind kinematics of lower metallicity sources.

8.1.4 An explanation for multiple populations in globular clusters

Studies in nearby globular clusters have illuminated the existence of multiple stellar populations. This has been seen in ω Cen (Lee et al., 1999; Hilker & Richtler, 2000; Bedin et al., 2004; Villaver, Stanghellini & Shaw, 2007), NGC 2808 (Piotto et al., 2007), NGC 1851 (Milone et al., 2008), and NGC 6388 (Piotto, 2008). While the explanation for these populations is still under debate, one explanation is AGB polluter stars. If the circumstellar expansion velocities of evolved stars at these low metallicities are in fact slower, the winds may not be strong enough to escape the globular cluster escape velocity, leading to self-enrichment within the cluster, and multiple stellar populations (Georgiev et al., 2009). The results of this study have provided additional evidence for this explanation.

8.1.5 Constraining the final stages of stellar evolution

The newly derived mass-loss prescription has provided a powerful relation for constraining the final stages of evolution for stars from 1−30 $M_{\odot}$. Quantifying the mass loss and dust production is critically important for understanding the lifetimes of stars, and how they transform into their subsequent evolutionary states.

The initial−final mass relation of AGB stars will depend on the assumed mass-loss rate, and the most significant mass-loss phase is the superwind phase. As RSGs also lose mass within this superwind phase and move toward bluer colours, the calculated mass of the resulting yellow and blue supergiants (or Wolf−Rayet stars) and how they fit along the evolutionary sequence will also depend on the assumed mass-loss rate.

While quantifying the mass loss is important for understanding the transformation of these sources, the mass-loss rate is also important for understanding stellar remnants like white dwarfs, neutron stars, and black holes. It is also especially important in trying to understand the still unclear nature of core-collapse supernova progenitors and the circumburst conditions found around supernova.

Lastly, the overall feedback of gas and dust from these stars, will depend on an assumed mass-loss rate. This rate then has implications for the origin of stellar material and the composition of the interstellar medium.

8.1.6 Open questions

There are still many questions that need to be answered in order to fully understand the contribution and evolution of evolved stars. From within the stars, it is important to continue to develop an understanding of TDU, HBB, convective mixing (Battino et al., 2016), and rotation (den Hartogh et al., 2017). The formation of circumstellar dust (Nanni, 2013), and how it impacts circumstellar outflows is also still unclear. And more work needs to be done in trying to understand the effects of binarity (Ramstedt, Vlemmings & Mohamed, 2015; De Marco & Izzard, 2017) and geometry on the wind-driving and mass-loss mechanisms.

8.2 The next generation of instruments

8.2.1 The Australian Square Kilometre Array Pathfinder

The Australian Square Kilometre Array Pathfinder (ASKAP) is a radio interferometer currently under construction in western Australia. The final instrument will have 36 identical 12 meter dishes with a maximum baseline of 6 km and a 30 square degree field-of-view at 1.4 GHz. The ASKAP's excellent sensitivity and fast surveying speed will provide an important jump forward for radio astronomy. It will also be an important test-of-technology of the Phased Array Feed (PAF) receivers before construction of the much larger Square Kilometre Array (SKA) Telescope.

The GASKAP Survey

The Galactic Australian Square Kilometre Array Pathfinder (GASKAP) Survey is an upcoming high spectral resolution (0.2 km s^{-1}) ASKAP survey of the 21-cm HI, and 18-cm OH lines, in the Milky Way Galactic plane, the LMC, the SMC, and the Magellanic Bridge and Stream (Dickey et al., 2013). GASKAP will survey these regions with sensitivities on the order of a few mJy, matching the sensitivity of current ATCA and Parkes observations in a fraction of the time. Given the number of LMC maser sources recently detected, and the number of SAGE-LMC sources similar to the LMC maser-emitting sample that have yet to be observed at radio frequencies, a number of maser sources are likely to be discovered with this survey.

Initial predictions of the number of detectable maser sources in the SMC (~ 20) predicted by scaling other maser samples, seems to have overestimated this number. Given the sensitivity of the GASKAP survey (around a few mJy) and the SMC target sample already observed, few sources are expected to show maser emission. Given the best candidates for maser emission show nothing at similar sensitivities with Parkes, it is unlikely that other sources will show bright maser emission. It may be the case however that at lower metallicity, a different set of criteria is needed for choosing the best candidates for maser emission. This will be revealed with the GASKAP's blind survey. This survey will be a precursor to much larger surveys using the SKA which will be able to probe these regions even deeper, revealing the full extent of the maser samples in these regions.

8.2.2 MeerKAT

The MeerKAT telescope is another SKA pathfinder instrument that will form the first $\sim$ 1/3 of the Phase 1 dish array of the SKA. It is currently under construction in South Africa, and will eventually have 64 dishes, each 13.5 metres in size, spread over 8 km. While the field of view of MeerKAT is much smaller than ASKAP (1.69 square degrees at 1-GHz as opposed to $\sim$ 30 square degrees), the strength of this telescope over the

ASKAP array is its higher sensitivity as a result of its many dishes. This however comes at the cost of survey speed where ASKAP has a clear advantage.

The ASKAP and MeerKAT instruments complement each other in the same way as the ATCA and Parkes instruments, respectively. The GASKAP will be able to continue the ATCA LMC survey conducted in this work. Conversely, MeerKAT will allow for more sensitive targeted observations of maser candidates as has been done with Parkes in the SMC. Keeping this in mind, the ASKAP will likely be of more use initially in the LMC, where deeper targeted observations with MeerKAT would be more effective in the SMC.

8.2.3 The Square Kilometre Array

The Square Kilometre Array will be a much larger version of the MeerKAT telescope that aims to have a collecting area of one square kilometre. The SKA1 MID (phase 1) telescope will add to the 64 dishes from MeerKAT bringing the number up to around 200 dishes. The array will have a maximum baseline of 150 km, a field-of-view around 1 degree. Unlike previous instruments, in addition to the dramatically increased sensitivity, the SKA1 MID will have a much higher angular resolution ($\sim 0.26''$ at 1612 MHz) than its precursor ($\sim 5''$ at 1612 MHz). This being the case, the SKA will be the first instrument with the angular resolution and sensitivity capable of detecting and resolving maser sources in more distant populations like nearby dwarf spheroidal galaxies and the larger Triangulum (M33) galaxy.

8.2.4 The James Webb Space Telescope

The *James Webb Space Telescope* (JWST) is an instrument set to launch in 2018, that will be the largest space telescope ever constructed. It is an optical to mid-IR telescope with a 6.5 meter segmented mirror and a suite of instruments including near and mid-IR imaging and spectroscopy. The instrument will be incredibly important at examining local group stellar populations and evolved stars at greater distances and lower metallicities. For example, JWST is ideal for investigating regions within larger spiral galaxies like

Andromeda (M31) and M33, more distant dwarf spheroidals like NGC 300, and the even more distant and lowest metallicity galaxies like 1 Zw 18. This will allow for the isolation of additional samples of evolved stars, to further test observable stellar parameters key to the wind-driving and mass loss mechanisms. The JWST will also allow for detailed studies of the Magellanic Clouds, probing deep into the denser molecular cloud regions with high sensitivity and angular resolution. The telescope will be key to opening new paths for studying extragalactic populations and is expected to last for a full 10 year mission.

8.3 Future work

The future of this research will rely on further observational investigations of nearby evolved AGB stars. This will require harnessing the strengths of state-of-the-art instruments like the VLT, HST, SKA and JWST.

8.3.1 Obtaining metallicities for LMC OH/IR stars

In order to further test and constrain the effects of metallicity on the LMC OH/IR sample, the Very Large Telescope (VLT) XSHOOTER spectrograph has been used to obtain optical and infrared spectroscopy of the three most luminous LMC OH/IR stars (Project 097.D-0605; PI: Goldman). Employing the method developed by Davies et al. (2015), metallicities will be derived using J-band spectroscopy, as well as temperatures and systematic velocities from optical spectra. Metallicity measurements will 1). test the gas-to-dust ratio estimates from modeling the targets spectral energy distributions, 2). confirm the metallicity of the lowest metallicity star with detected CO line emission, and 3). give empirical data to test the effects of metallicity and luminosity on the wind-driving mechanism within these stars. These results will be used to further develop an accurate mass-loss prescription that includes the effects of metallicity and luminosity.

8.3.2 Measuring silicate dust in the Galactic bulge

On the night of June 18th 2017, the VLT's UT3 telescope will be used to obtain N-band spectroscopy of the 14 most luminous OH/IR stars in the Galactic bulge (and within the Galactic bulge sample analysed in this work) using the VISIR spectrograph (Project 099.D-0907; PI: Goldman). While N-band spectroscopy has been done on samples of lower mass Galactic Bulge Mira variable stars (e.g. Blommaert et al., 2014), few high-luminosity Galactic OH/IR stars have been observed in the N-band. Within the sample only four sources have N-band spectra. This observation will finally yield data for a sample with a range of luminosities, some of which have comparable luminosities to the LMC OH/IR stars but at higher metallicity. By modeling the observed silicate features at 10 μm with DUSTY models, this will result in accurate measurements of the optical depths which can then be used to calculate more accurate mass-loss rates. The shape of the feature can also be used to understand the geometry and dust mineralogy of the sources. These observations are important for also confirming the significantly deeper predicted silicate features in absorption (found from SED fitting) within some of the Galactic bulge sources (Fig. 4.2). The results will be able to further test and refine dust-driven wind theory and isolate the dependencies of metallicity and luminosity on the mass loss of these stars.

8.3.3 Resolving stellar populations in M31 with Hubble

New observations of the Andromeda galaxy (M31) have been taken as an extension of the Panchromatic Hubble Andromeda Treasury (PHAT) program. These HST observations will be used to investigate the stellar populations of evolved stars within M31. M31 has been found to have a similar metallicity as the Milky Way. Results have shown a metallicity gradient with sources near the centre having around solar metallicity and trailing towards larger radius (Gregersen et al., 2015), as well as an age of around 12 Gyr throughout the bulge (Saglia et al., 2010). The package DOLPHOT (Dolphin, 2000) will be used to obtain point-spread function photometry, and the resulting photometry will

be used to create colour magnitude and colour-colour diagrams to disentangle the stellar populations. The results will then be used with the Bayesian Extinction And Stellar Tool (BEAST) code (Gordon et al., 2016) to constrain a range of important stellar parameters (e.g. $T_{\rm eff}$, L, M, and Z) as well as the extinction, which is key for further studies of the ISM in M31. This will allow for a better understanding of the stellar populations and dust budget of M31. This can then be used to constrain the dust contribution from evolved stars and if and how it differs within local group galaxies.

8.4 SED fitting with a goodness of fit

As was stated in §4, trying to asses the goodness of fit of the DUSTY models with the photometry using only the photometric uncertainties for the calculation of the χ^2 value results in seemingly terrible fits. These are very simplistic models based on a blackbody. In the future, to approach more realistic models, a sample spectrum should be used as the basis of the model. This should allow for more realistic models that should fit more closely with the observational data. While this would still not take into account departures from spherical symmetry, inaccurate distances, non-zero drift velocities, or changes in dust chemistry, this would likely improve the quality of the fits.

8.5 Final remarks

The most important result from this work is the deeper understanding of the mass loss process. This understanding has been aided by a dramatic improvement to the LMC circumstellar maser sample. These new results have reaffirmed the dependence of circumstellar expansion velocity on metallicity and luminosity and greatly constrained their relationships. The new measurements also allow for the further constraining of other important parameters like the dust grain size, shape, and composition, as well as the most realistic dust optical constants to use in stellar models. The further analysis on

the mass loss of these and other sources has indicated that AGB mass loss is likely to be independent of metallicity at least between half and twice solar. These relationships are critically important for determining the lifetimes of AGB and RSG stars, the accuracy of initial masses within stellar models, and understanding the evolutionary paths of core-collapse progenitors. The SMC OH/IR sample analysis has provided a better understanding of lower metallicity circumstellar environments. With GASKAP soon to begin and the SKA on the horizon, the SMC analysis will inform future radio surveys in the Magellanic Clouds. This work will also give more realistic expectations for surveys with the JWST, set to launch in 2018. The VISIR observations of IRAS 05280−6910 also included in this work have constrained the location and mass loss of one of the most prominent dust producers in the Magellanic Clouds. This work will continue as new instruments and technologies reveal more distant stellar populations in the radio and IR, and more is understood of the complexity of evolved stars.

Appendix

A Important mechanisms

Proton-proton chain reaction the chain of nuclear fusion reactions that are the dominant energy source in lower mass stars of temperatures around 18,000,000 K and M $\lesssim$ 1.5 $M_\odot$. First two protons fuse to form diproton ($^2_2$He), which is followed by the loss of a positron in what is called beta-plus decay, leaving deuterium ($^2_1$H). The deuterium then fuses with another proton to form helium (^{3}He). Next two ^{3}He fuse to form ^{4}He. The net effect is the production of ^{4}He from four protons.

CNO cycle the dominant mechanism for producing helium in stars of mass M $\gtrsim$ 1.5 $M_\odot$. The cycle is a catalytic cycle which fuses protons with carbon, nitrogen, and oxygen to produce ^{4}He. First ^{12}C fuses with a proton to form ^{13}N, and then loses a positron (beta-plus decays), producing ^{13}C. Next ^{13}C fuses with two protons (in separate events) to create ^{15}O, and then loses a positron to create ^{15}N. A final fusion of ^{15}N and a proton creates ^{12}C and ^{4}He, where the cycle begins again.

Triple-alpha process the process of nuclear fusion in red giant branch stars with core temperatures above 100,000,000 K, that creates carbon (and some oxygen). After a red giant ceases core hydrogen fusion, and leaves the main sequence, the star will begin to collapse and pressures and temperatures will increase within the core. With high enough temperatures, $^4_2$He will begin to fuse with $^4_2$He to create $^8_4$Be. Due to the short halflife of Be (and Li), these elements will quickly decay. At temperatures higher than 100,000,000 K, fusion reactions are rapid enough for Be and Li to fuse with He before they decay, to create $^{12}_6$C and some $^{16}_8$O.

S-process a process of slow neutron capture that produces heavier elements in stars. This occurs in low-mass AGB stars, relying on free neutrons from ^{13}C, as well as high-mass helium- and carbon-burning stars using ^{22}Ne as the source of free neutrons. Neutron capture increases the atomic mass of an element by one. If the resulting isotope is not stable, this will be followed by a beta-minus decay in which a neutron decays to a proton, an electron is ejected, and the atomic number is increased by 1. This process, while slow, is thought to produce a significant amount of the heavy elements in the Universe.

Third-dredge up a convectively-driven transport mechanism active in AGB stars $\gtrsim$2 $M_\odot$. After a thermal pulse as a result of a helium shell flash, the resulting material is convectively mixed and transported up in the intershell region toward the hydrogen burning shell. At the same time the hydrogen-rich convective envelope penetrates deeper and brings material from within the intershell region to the surface of the star. The net effect is that nuclear processed material such as carbon is brought to the surface, changing the surface composition dramatically.

Hot-Bottom Burning Hot-Bottom burning is proton-capture nucleosynthesis that occurs in higher mass ($\gtrsim 3\ M_\odot$) thermally pulsing AGB stars. It occurs when temperatures reach 40,000,000 K at the base of the outer convective envelope. This provides an environment where the CNO-cycle favours the transformation of C into N. These temperatures also provide the necessary conditions for producing Li through the Cameron & Fowler (1971) mechanism (Mazzitelli, D'Antona & Ventura, 1999).

B Galactic OH maser sources

Eight Galactic maser sources have been observed with Parkes in addition to the LMC sources for pointing checks (Table B1). No noticeable changes in expansion velocity were found when compared with previous observations, but several interesting features

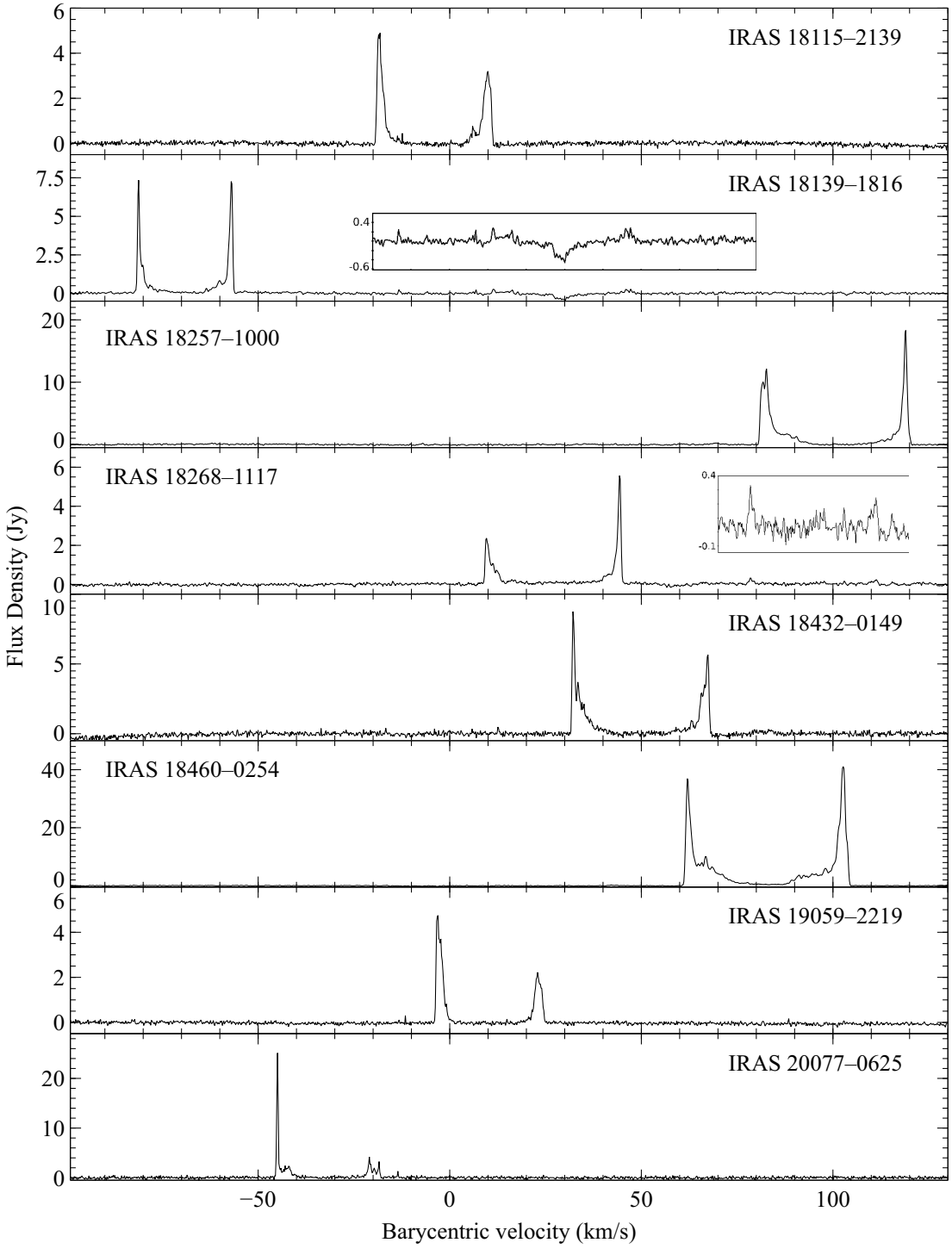

Figure B1: OH 1612-MHz maser emission from the Parkes observations of additional Galactic sources. Sources are from different Galactic samples than those previously mentioned.

have been identified. From the observation of IRAS 18139−1816 an absorption feature around 30 km s^{-1} has been discovered. It is expected that this is a result of absorption within the nearby dust cloud, which can be seen in optical images of the region. A secondary maser source has also been found during the observation of IRAS 18268−1117. This additional maser profile is coming from another source within the $13'$ beam of Parkes. The only potential known sources within around $13'$ are the evolved S-type AGB star, IRAS 18269−1111, and the source IRAS 18272−1117. The S-type source has a carbon-to-oxygen ratio of 1, making it an unlikely candidate for OH maser emission but still within the realm of possibility, especially if it has recently undergone an additional thermal pulse and the OH shell corresponds to a time when it was still an M giant.

Table B1: Results of Galactic maser observations.

Object name	Alternative name	l (°)	b (°)	v_{exp} (km s^{-1})	F_{25} (Jy)	F_{int} (Jy km s^{-1})		Velocity at peaks (km s^{-1})	
				red	blue	red	blue		
IRAS 18115−2139	OH 9.575 −2.032	9.574	−2.031	14.2	60.8	8.85	7.47	−18.4	10.0
IRAS 18139−1816	OH 12.8 −0.9	12.819	−0.901	12.1	16.9	9.21	11.22	−81.1	−56.8
IRAS 18257−1000	OH 21.5 +0.5	21.451	+0.500	18.4	120.5	39.7	30.3	82.4	119.1
IRAS 18268−1117	OH 20.4 −0.3	20.433	−0.344	17.4	30.5	6.15	9.22	9.6	44.4
IRAS 18268−1117 B				16.4		0.82	0.58	78.6	111.4
IRAS 18432−0149	OH 30.7 +0.4	30.715	+0.423	17.5	52.3	15.7	12.5	32.3	67.3
IRAS 18460−0254	OH 30.09 −0.69	30.086	−0.681	20.3	279.9	116.4	131.2	62.1	102.7
IRAS 19059−2219	V* V3880 Sgr	14.662	−13.610	13.0	211.6	8.23	4.5	−3.0	23.0
IRAS 20077−0625	V* V1300 Aql	36.356	−20.415	12.6	1061.0	18.9	8.46	−44.9	−19.8

C Mainline OH spectra

Each of the ATCA observations described in §3.1 and §6.2 observed multiple OH maser lines. In addition to the 1612-MHz OH satellite line, the observations also targeted the 1665- and 1667-MHz OH mainlines, which probe regions closer to the star, and the 1720-MHz OH line, primarily found in SNR interactions with molecular clouds. The only observation that was found to show mainline emission was IRAS 05280−6910 (described in §4.5), and no observation detected 1667- or 1720-MHz OH maser emission. The spectrum for each of the LMC and SMC targets was reduced and extracted in the same manner as the 1612-MHz data, and is shown in the following figures. Each of the mainline spectra have been resampled to 0.5 km s^{-1}. Also shown is the average of the 1665- and 1667-MHz mainline emission. It is known that the 1612-MHz maser dominates at longer path lengths (Gray, Doel & Field, 1991). The 1665-MHz mainline emission can come from the OH being located in a high density region (close to the star). High densities ($\gtrsim 10^7$ cm^{-3}) suppress the 1667-MHz emission compared to the 1665-MHz emission. In normal lower mass-loss Mira variables both main line masers are often comparable in strength, a result of lower densities. As either mainlines will not have a reduced intensity as a result of competitive gain with the other, and the sources are likely to have similar line profiles, the average of the main line emission may provide a clearer view of the interiors of these envelopes. Shown first are the SMC sources: IRAS 00483−7347, MSX SMC 018, and BMB-B75 and then the LMC maser sample. The much more sensitive Parkes observation of IRAS 00483−7347 is shown for the 1612 MHz spectrum.

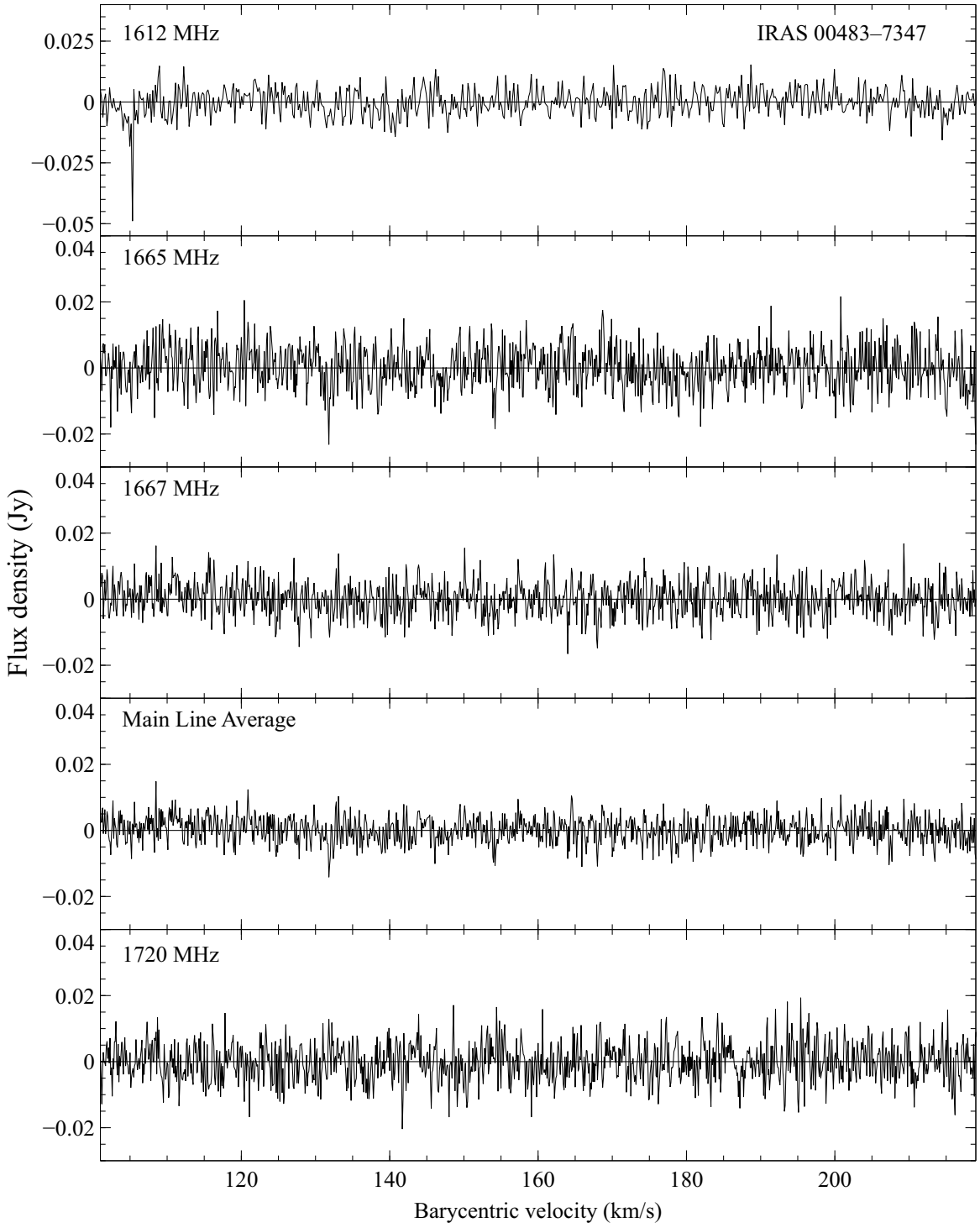

Figure C1: 1612-, 1665-, 1667-, and 1720-MHz OH maser observations of IRAS 00483−7347.

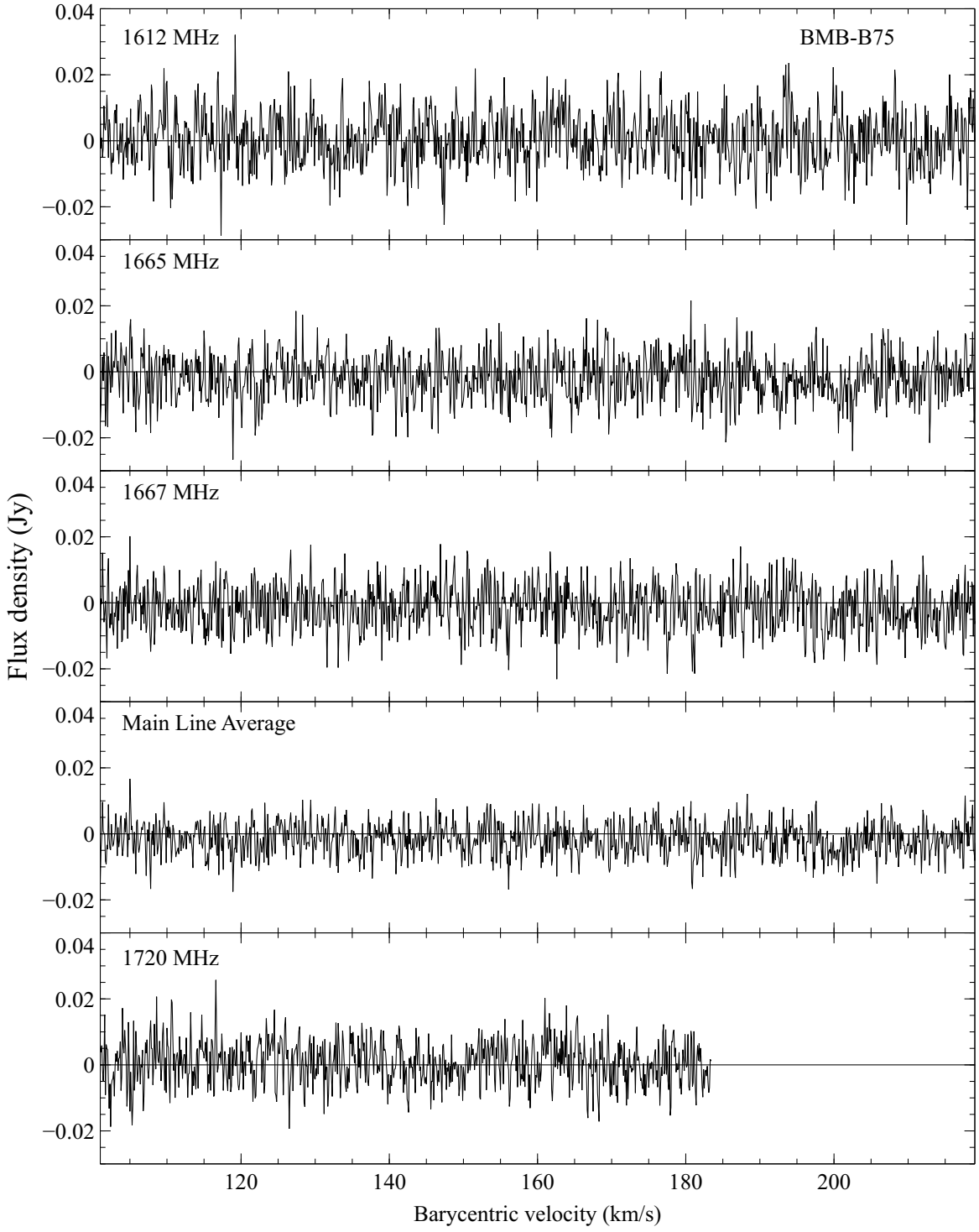

Figure C2: 1612-, 1665-, 1667-, and 1720-MHz OH maser observations of BMB-B75. The missing data $\gtrsim 180$ km s^{-1} in the 1720-MHz spectrum is due to a correlator block failure.

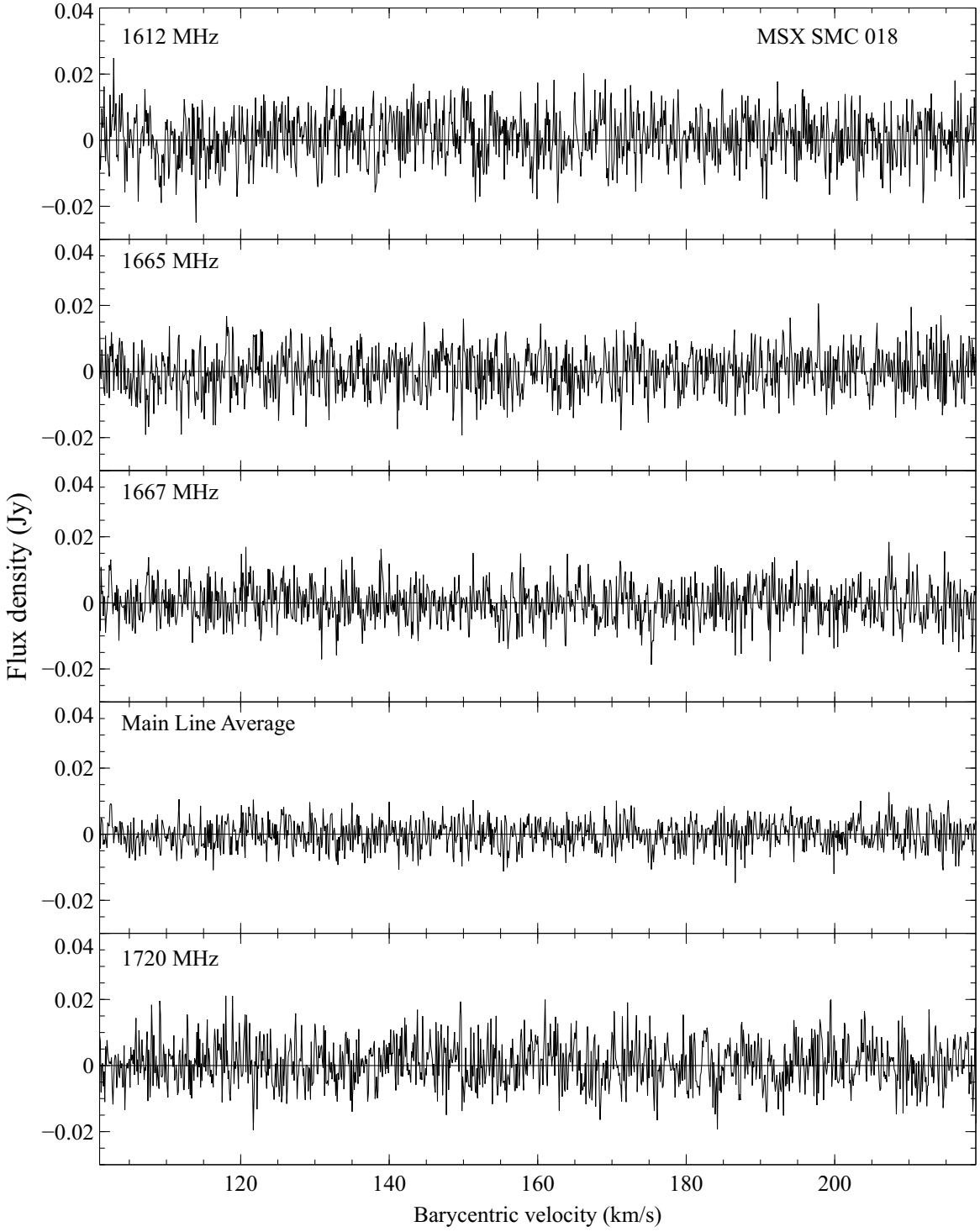

Figure C3: 1612-, 1665-, 1667-, and 1720-MHz OH maser observations of MSX SMC 018.

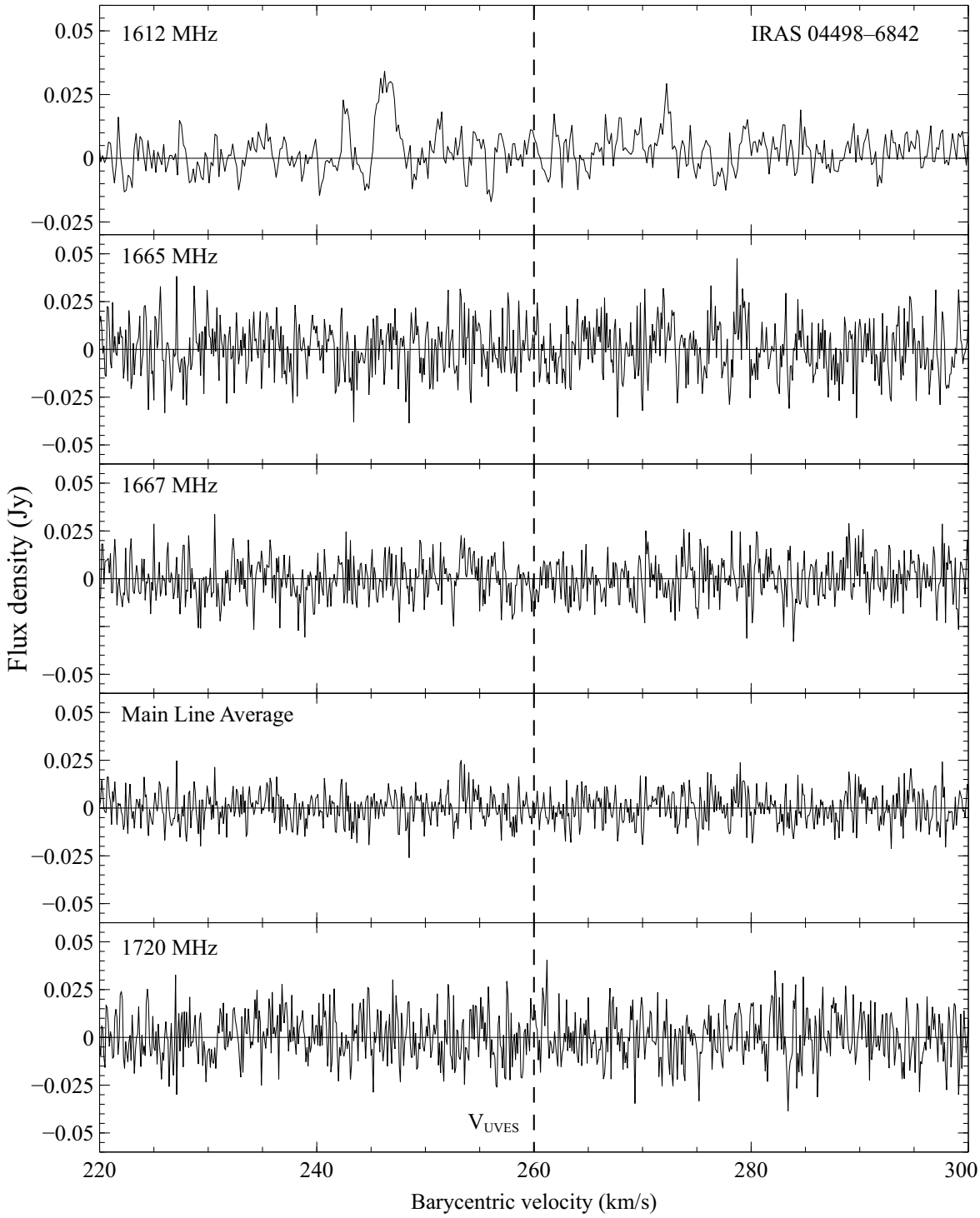

Figure C4: 1612-, 1665-, 1667-, and 1720-MHz OH maser observations of IRAS 04498−6842 with the velocity derived from cross-spectrum fitting of UVES spectra denoted by V_{UVES}.

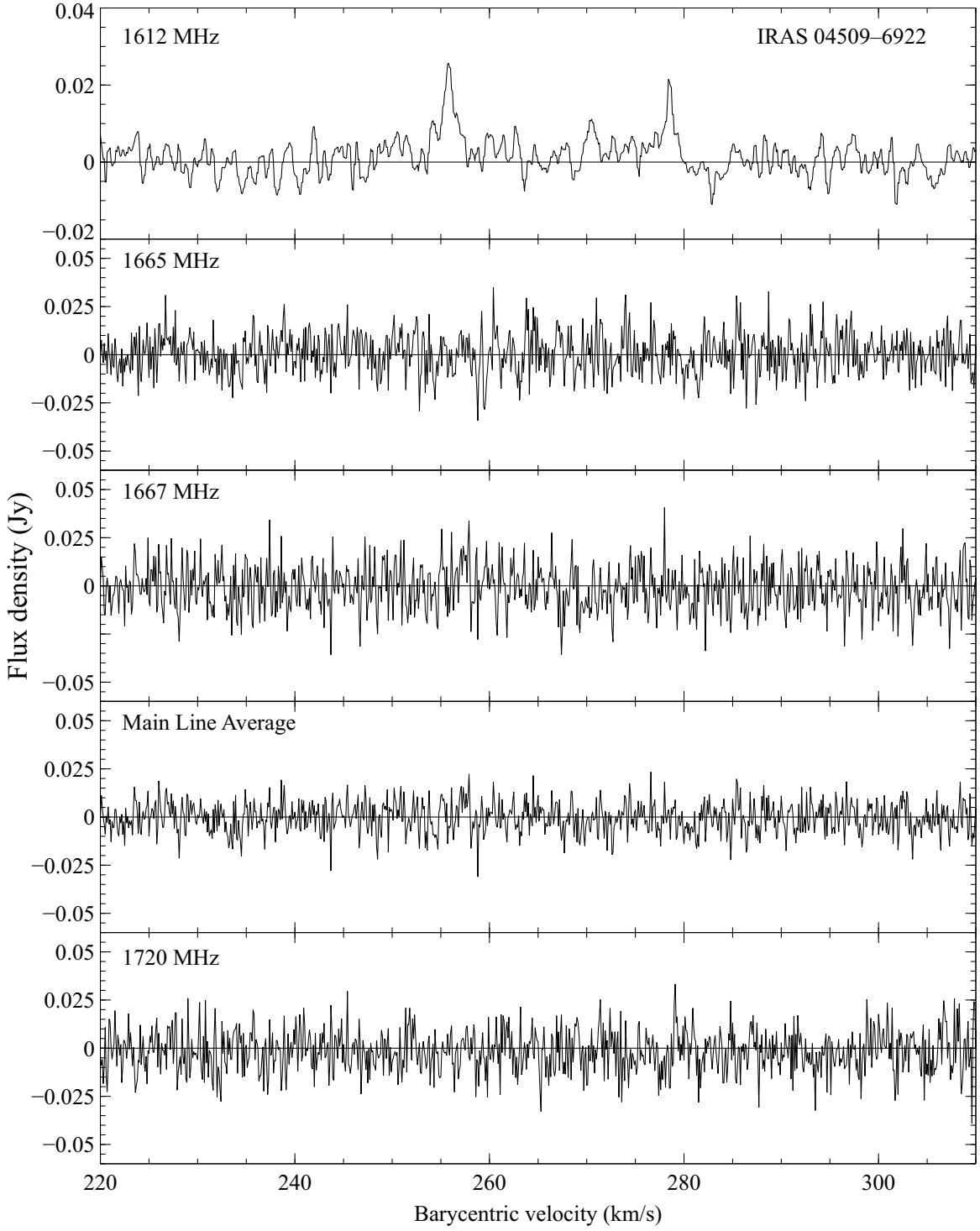

Figure C5: 1612-, 1665-, 1667-, and 1720-MHz OH maser observations of IRAS 04509−6922.

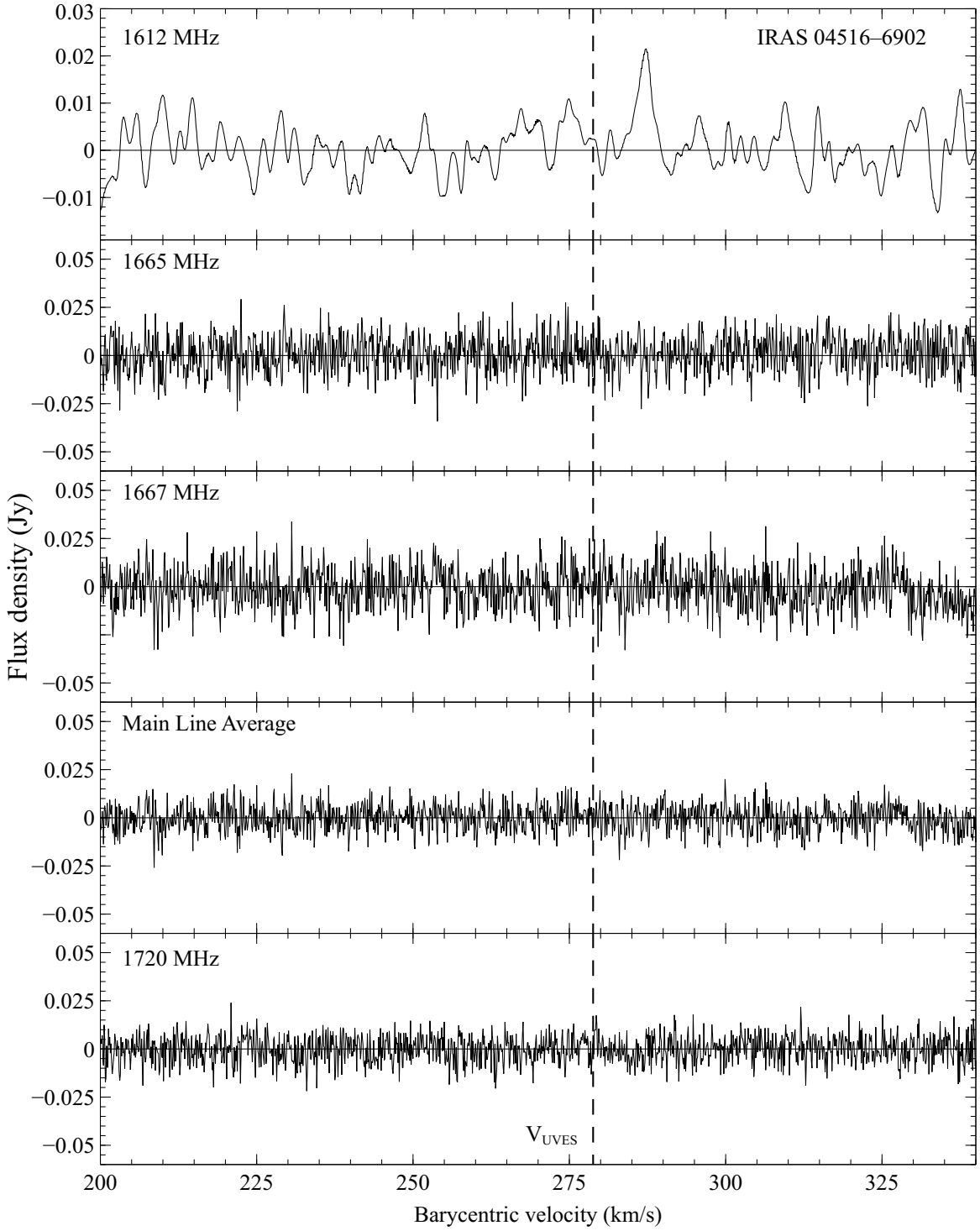

Figure C6: 1612-, 1665-, 1667-, and 1720-MHz OH maser observations of IRAS 04516−6902 with the velocity derived from cross-spectrum fitting of UVES spectra denoted by V_{UVES}.

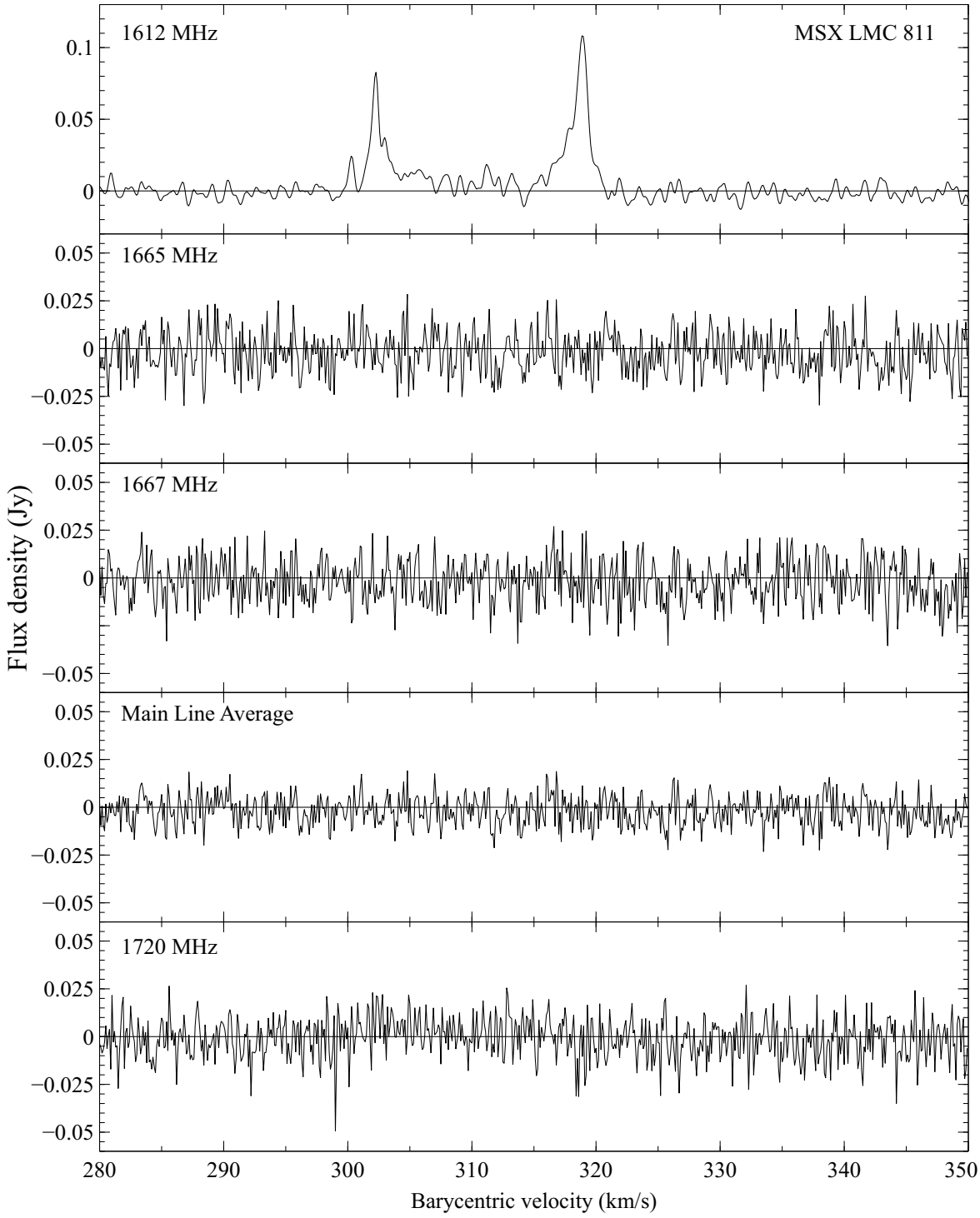

Figure C7: 1612-, 1665-, 1667-, and 1720-MHz OH maser observations of MSX LMC 811.

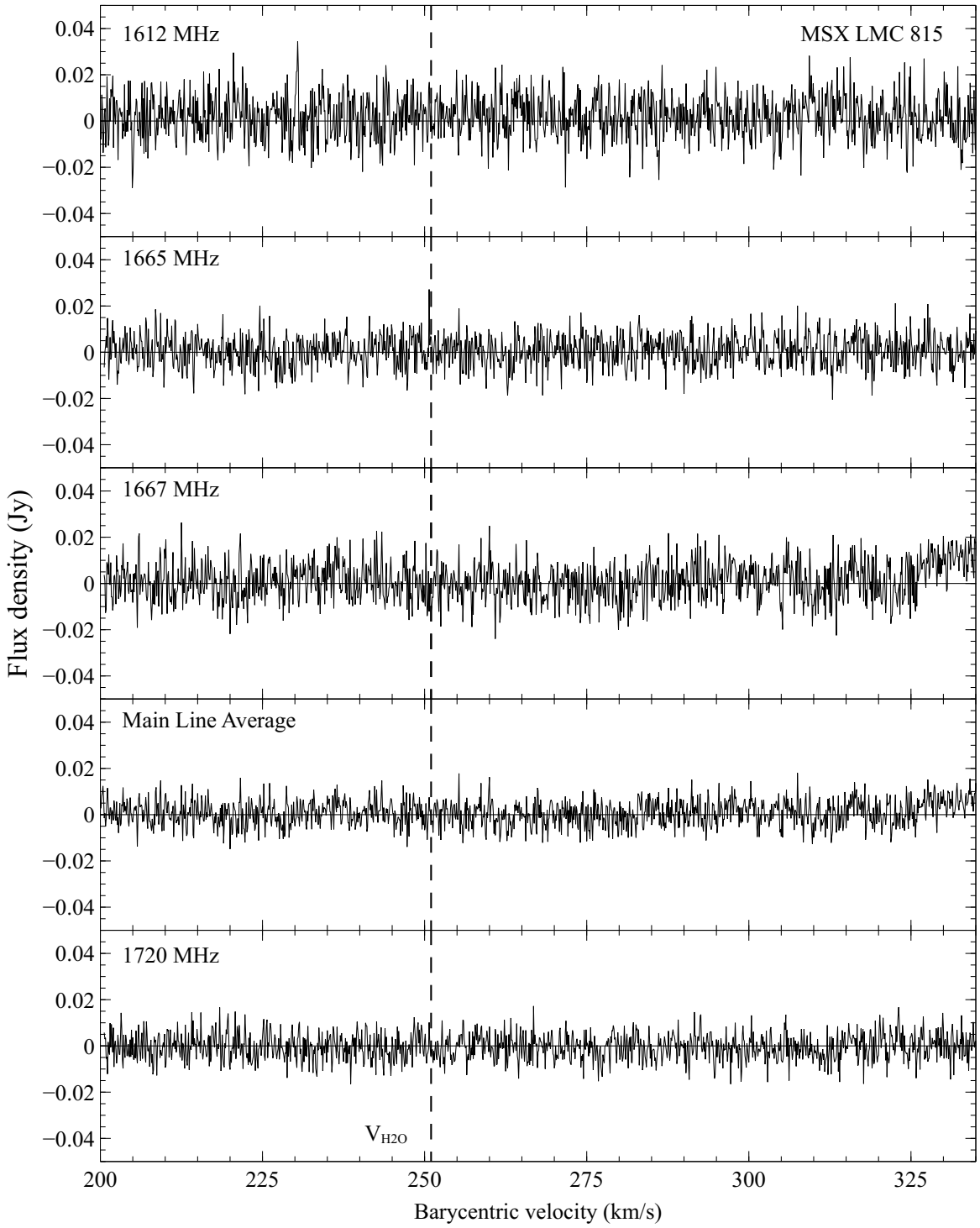

Figure C8: 1612-, 1665-, 1667-, and 1720-MHz OH maser observations of MSX LMC 815 with the velocity of the water maser detection made by Imai et al. (2013) denoted by V_{H2O}.

D Past SMC maser targets

There have been two previous 1612-MHz maser surveys in the SMC conducted by Marshall et al. (2004) and Wood et al. (1992). The observations by Marshall et al. (2004) targeted two sources, IRAS 00483−7347, which has been re-observed with a higher sensitivity, and IRAS 00591−7307 which have been reprocessed to present a complete and uniform dataset. The observations by Wood et al. (1992) focused on 15 sources targeted for having high IRAS 25 μm flux densities and that fit the criteria: $0.0 < \mathrm{Log}(F_{25}/F_{12}) < 0.5$. These observations achieved noise levels typically $\sim$ 40 mJy and did not result in any clear maser detections in the SMC. This is dramatically higher than the noise level achieved in recent Parkes observations which were expected to observed 1−2 MSC masers sources above 3σ with noise levels around 3 mJy. The 15 targets are composed of an evolved AGB star, a Seyfert 2 Galaxy, a star forming region, 2 foreground stars, 2 YSOs, 3 H II regions, and 5 sources whose identity is still unclear (Table D1). New observations have been presented for the re-observed AGB star, HV 12149. The foreground sources are the red giant IRAS 00542−7334 (CM Tuc) (Prévot et al., 1983; González-Fernández et al., 2015), and the F star IRAS 00490−7125 (HD 5028) (Gontcharov, 2006). The unknown source IRAS 00435−7339 lies near a star-forming region. The IR flux coming from the unknown source IRAS 01208−7532 was likely a contribution from the nearby galaxy: 2MASX J01215707-7516248. The Seyfert 2 galaxy that was observed is the well studied peculiar source IRAS 00521−7054 (Véron-Cetty & Véron, 2010; Ricci et al., 2014), which has shown a uniquely strong and broad feature at 6 keV (Tan et al., 2012). None of the unknown sources, or the source IRAS 00477−7322 have 2MASS counterparts. IRAS 00477−7322, IRAS 005177240 and IRAS 005537317 also show nothing visible in any of the *Spitzer* IRAC or MIPS images.

Within this sample, the only source that is still a good candidate for maser emission is the AGB star HV 12149. However, the typical characteristics of these sources have only recently been constrained. At the time of the survey (in 1987), little was known about the nature of these sources.

Table D1: Targets from the 1612-MHz OH maser survey by Wood et al. (1992).

Target	Type	Reference
HV 12149	AGB (SpT = M8.5)	González-Fernández et al. (2015)
IRAS 00430−7326	YSO	van Loon et al. (2010)
IRAS 00435−7339	?	
IRAS 00466−7322	H II region	Pellegrini et al. (2012)
IRAS 00477−7322	?	
IRAS 00477−7343	H II region	Indebetouw, Johnson & Conti (2004)
IRAS 00490−7125	F-type star	Gray et al. (2006)
IRAS 00517−7240	?	
IRAS 00521−7054	Seyfert 2 galaxy	Elias & Frogel (1987)
IRAS 00542−7334	Foreground AGB	González-Fernández et al. (2015)
IRAS 00553−7317	?	
IRAS 01039−7305	YSO	van Loon et al. (2008)
IRAS 01126−7332	Star-forming region	Breen et al. (2013)
IRAS 01208−7532	?	
IRAS 01228−7324	H II region	Testor & Pakull (1985)

E YSO OH maser spectra

After the Parkes observations in 2005, it was found that two sources within the SMC maser survey fields were in fact YSOs. These sources were suggested as YSO candidates by van Loon et al. (2008) and then confirmed by Oliveira et al. (2013). Present here are the 1612-MHz spectra for the sources IRAS 01039−7305 and IRAS 01042−7215. They were observed for 7.4 and 6.3 hours, respectively. YSOs are expected to have the strongest OH maser emission in their mainline transitions, but will also exhibit maser emission at 1612 MHz. No clear maser emission in seen in either source but there are several large narrow spikes, likely a result of RFI.

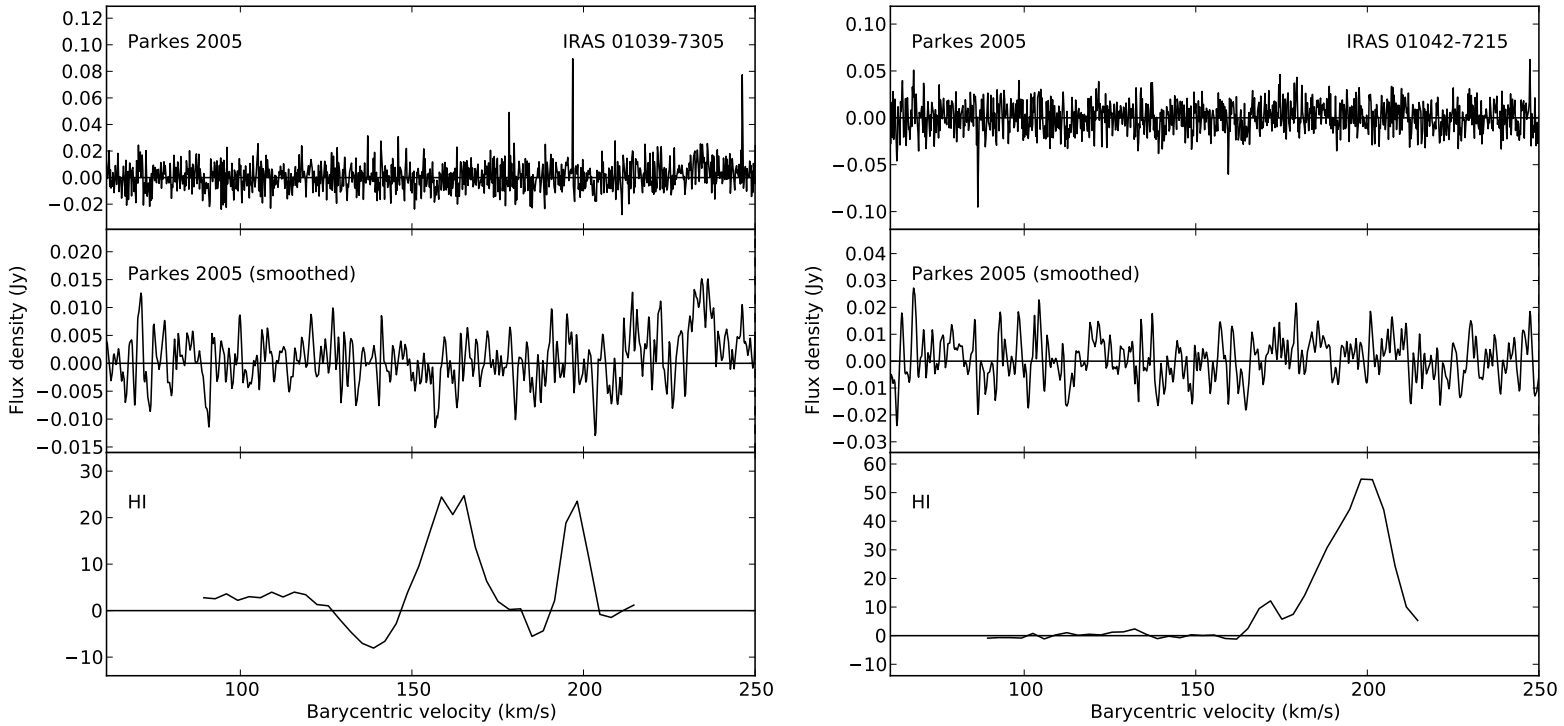

Figure E1: Parkes 1612-MHz OH maser observations of IRAS 01039−7305 and IRAS 01042−7215. As has been done for the previous 1612-MHz spectra, the H I spectra are presented for velocity reference.

Bibliography

Arnett W. D., 1980, ApJ, 237, 541

Babkovskaia N., Poutanen J., 2006, A&A, 447, 949

Battino U. et al., 2016, ApJ, 827, 30

Baud B., Habing H. J., 1983, A&A, 127, 73

Bedin L. R., Piotto G., Anderson J., Cassisi S., King I. R., Momany Y., Carraro G., 2004, ApJ, 605, L125

Beichman C. A., Neugebauer G., Habing H. J., Clegg P. E., Chester T. J., 1988, Infrared astronomical satellite (IRAS) catalogs and atlases. Volume 1, 1

Benson J. M., Mutel R. L., 1979, ApJ, 233, 119

Benson J. M., Mutel R. L., 1982, ApJ, 253, 199

Benson P. J., Little-Marenin I. R., 1996, ApJS, 106, 579

Bernard J.-P. et al., 2008, AJ, 136, 919

Bianchi S., Schneider R., 2007, MNRAS, 378, 973

Bladh S., Höfner S., Nowotny W., Aringer B., Eriksson K., 2013, A&A, 553, A20

Blanco V. M., Blanco B. M., McCarthy M. F., 1980, ApJ, 242, 938

Blöcker T., 1995, A&A, 297, 727

Blommaert J. A. D. L. et al., 2014

Blum R. D. et al., 2006, AJ, 132, 2034

Bonanos A. Z. et al., 2009, AJ, 138, 1003

Bonanos A. Z. et al., 2010, AJ, 140, 416

Boothroyd A. I., Sackmann I. J., Ahern S. C., 1993, ApJ, 416, 762

Boothroyd A. I., Sackmann I. J., Wasserburg G. J., 1995, ApJ, 442, L21

Bot C., Boulanger F., Lagache G., Cambresy L., Egret D., 2004, A&A, 423, 567

Bowen G. H., 1988, ApJ, 329, 299

Bowen G. H., Willson L. A., 1991, ApJ, 375, L53

Boyer M. L. et al., 2010, A&A, 518, L142

Boyer M. L. et al., 2011, AJ, 142, 103

Breen S. L., Lovell J. E. J., Ellingsen S. P., Horiuchi S., Beasley A. J., Marvel K., 2013, MNRAS, 432, 1382

Bressan A., Marigo P., Girardi L., Salasnich B., Dal Cero C., Rubele S., Nanni A., 2012, MNRAS, 427, 127

Buchanan C. L., Kastner J. H., Forrest W. J., Hrivnak B. J., Sahai R., Egan M., Frank A., Barnbaum C., 2006, AJ, 132, 1890

Bujarrabal V., Guibert J., Nguyen-Q-Rieu, Omont A., 1980, A&A, 84, 311

Cameron A. G. W., Fowler W. A., 1971, ApJ, 164, 111

Catchpole R. M., Whitelock P. A., Feast M. W., Hughes S. M. G., Irwin M., Alard C., 2016, MNRAS, 455, 2216

Cherchneff I., 2013, in Proceedings of The Life Cycle of Dust in the Universe: Observations, p. 18

Chevalier R. A., 1976, ApJ, 207, 872

Choudhury S., Subramaniam A., Cole A. A., 2016, MNRAS, 455, 1855

Cimerman M., Scoville N., 1980, ApJ, 239, 526

Cioni M.-R. et al., 2000, A&AS, 144, 235

Cohen R. J., 1989, Reports on Progress in Physics, 52, 881

Cohen R. J., Downs G., Emerson R., Grimm M., Gulkis S., Stevens G., Tarter J., 1987, MNRAS, 225, 491

Cutri R. M. et al., 2012, VizieR On-line Data Catalog, 2311

Cutri R. M. et al., 2003, VizieR On-line Data Catalog, 2246

Davies B., Kudritzki R.-P., Gazak Z., Plez B., Bergemann M., Evans C., Patrick L., 2015, ApJ, 806, 21

De Beck E., Decin L., de Koter A., Justtanont K., Verhoelst T., Kemper F., Menten K. M., 2010, A&A, 523, A18

de Jager C., Nieuwenhuijzen H., van der Hucht K. A., 1988, A&AS, 72, 259

De Marco O., Izzard R. G., 2017, PASA, 34, e001

Decin L. et al., 2010, Nature, 467, 64

Decin L., Hony S., de Koter A., Justtanont K., Tielens A. G. G. M., Waters L. B. F. M., 2006, A&A, 456, 549

Decin L. et al., 2017, in Braun R., ed., Science with Parkes at 50 years young, arXiv:1704.05237

Dell'Agli F., García-Hernández D. A., Ventura P., Schneider R., Di Criscienzo M., Rossi C., 2015, MNRAS, 454, 4235

den Hartogh J., Battino U., Hirschi R., Pignatari M., Herwig F., 2017, in Proceedings of the 14th International Symposium on Nuclei in the Cosmos (NIC2016), Astrophysics Group, Keele University, Keele ST5 5BG, U.K.; Nugrid collaboration,; BRIDGCE U.K. Network,, Journal of the Physical Society of Japan, p. 020904

Dickey J. M. et al., 2013, PASA, 30, e003

Dijkstra C., Speck A. K., Reid R. B., Abraham P., 2005, ApJ, 633, L133

Do T., Kerzendorf W., Winsor N., Støstad M., Morris M. R., Lu J. R., Ghez A. M., 2015, ApJ, 809, 143

Doherty C. L., Gil-Pons P., Siess L., Lattanzio J. C., Lau H. H. B., 2015, MNRAS, 446, 2599

Dolphin A. E., 2000, PASP, 112, 1383

Dunne L., Eales S., Ivison R., Morgan H., Edmunds M., 2003, Nature, 424, 285

Dupree A. K., Hartmann L., Avrett E. H., 1984, ApJ, 281, L37

Dwek E., 2004, ApJ, 607, 848

Egan M. P. et al., 2003, VizieR On-line Data Catalog, 5114

Eisenhauer F., Schödel R., Genzel R., Ott T., Tecza M., Abuter R., Eckart A., Alexander T., 2003, ApJ, 597, L121

Elias J. H., Frogel J. A., 1987, Star formation in galaxies, 2466

Elias J. H., Frogel J. A., Humphreys R. M., 1980, ApJ, 242, L13

Elias J. H., Frogel J. A., Humphreys R. M., 1985, ApJS, 57, 91

Elias J. H., Frogel J. A., Schwering P. B. W., 1986, ApJ, 302, 675

Elitzur M., 1982, Reviews of Modern Physics, 54, 1225

Elitzur M., 1992, Astronomical masers. Kluwer, Dordrecht

Elitzur M., Goldreich P., Scoville N., 1976, ApJ, 205, 384

Elitzur M., Ivezić Z., 2001, MNRAS, 327, 403

Elson R. A., Fall S. M., 1988, AJ, 96, 1383

Engels D., Bunzel F., 2015, A&A, 582, A68

Etoka S., Diamond P., 2004, MNRAS, 348, 34

Etoka S., Engels D., Imai H., Dawson J., Ellingsen S., Sjouwerman L., van Langevelde H., 2015, Advancing Astrophysics with the Square Kilometre Array (AASKA14), 125

Fazio G. G. et al., 2004, ApJS, 154, 10

Feast M. W., 1992, Koninklijke Nederlandse Akademie van Wetenschappen. Verhandlingen, 18

Feast M. W., 1996, MNRAS, 278, 11

Feast M. W., 2013, Planets, 829

Feltzing S., Chiba M., 2013, New Astronomy Reviews, 57, 80

Florsch A., 1972, Publ. Obs. Astron. Strasbourg, 2

Fox M. W., Wood P. R., 1982, ApJ, 259, 198

Gail H. P., Sedlmayr E., 1986, A&A, 161, 201

Gail H. P., Sedlmayr E., 1999, A&A, 347, 594

Gail H.-P., Sedlmayr E., 2014, Physics and Chemistry of Circumstellar Dust Shells

García-Hernández D. A. et al., 2009, ApJ, 705, L31

Gehrz R., 1989, in Interstellar Dust: Proceedings of the 135th Symposium of the International Astronomical Union, p. 445

Georgiev I. Y., Hilker M., Puzia T. H., Goudfrooij P., Baumgardt H., 2009, MNRAS, 396, 1075

Goldman S. R. et al., 2017, MNRAS, 465, 403

Goldreich P., Scoville N., 1976, ApJ, 205, 144

Golriz S. S. et al., 2014, MNRAS, 443, 3402

Gomez H. L. et al., 2012, MNRAS, 420, 3557

Gontcharov G. A., 2006, Astronomy Letters, 32, 759

González-Fernández C., Dorda R., Negueruela I., Marco A., 2015, A&A, 578, A3

Gordon K. D. et al., 2009, ApJ, 690, L76

Gordon K. D. et al., 2016, ApJ, 826, 104

Gordon K. D. et al., 2011, AJ, 142, 102

Gray M., 2012, Maser Sources in Astrophysics

Gray M. D., Doel R. C., Field D., 1991, MNRAS, 252, 30

Gray M. D., Howe D. A., Lewis B. M., 2005, MNRAS, 364, 783

Gray R. O., Corbally C. J., Garrison R. F., McFadden M. T., Bubar E. J., McGahee C. E., O'Donoghue A. A., Knox E. R., 2006, AJ, 132, 161

Gregersen D. et al., 2015, ApJ, 150, 189

Groenewegen M. A. T., Blommaert J. A. D. L., 1998, A&A, 332, 25

Groenewegen M. A. T., Oudmaijer R. D., Ludwig H. G., 1997, MNRAS, 292, 686

Groenewegen M. A. T., Sevenster M., Spoon H. W. W., Pérez I., 2002, A&A, 390, 511

Groenewegen M. A. T., Sloan G. C., Soszyński I., Petersen E. A., 2009, A&A, 506, 1277

Groenewegen M. A. T., Smith C. H., Wood P. R., Omont A., Fujiyoshi T., 1995, ApJ, 449, L119

Groenewegen M. A. T. et al., 2016, A&A, 596, A50

Groenewegen M. A. T. et al., 2007, MNRAS, 376, 313

Gruendl R. A., Chu Y.-H., 2009, ApJS, 184, 172

Habing H. J., 1987, in IN: Circumstellar matter; Proceedings of the IAU Symposium, Leiden, Rijksuniversiteit, Sterrewacht, Netherlands, pp. 197–213

Habing H. J., 1996, A&ARv, 7, 97

Hanner M., 1988, In NASA

Harris J., Zaritsky D., 2004, AJ, 127, 1531

Harris J., Zaritsky D., 2009, AJ, 138, 1243

Hartmann L., MacGregor K. B., 1980, ApJ, 242, 260

Harvey P. M., Bechis K. P., Wilson W. J., Ball J. A., 1974, ApJS, 27, 331

Harwit M., Malfait K., Decin L., Waelkens C., Feuchtgruber H., Melnick G. J., 2001, ApJ, 557, 844

Hatzidimitriou D., Croke B. F., Morgan D. H., Cannon R. D., 1997, A&AS, 122

He J. H., Szczerba R., Chen P. S., Sobolev A. M., 2005, A&A, 434, 201

Herwig F., 2005, ARAA, 43, 435

Hilker M., Richtler T., 2000, A&A, 362, 895

Höfner S., 2008, A&A, 491, L1

Höfner S., 2015, in Why Galaxies Care about AGB Stars III: A Closer Look in Space and Time. Proceedings of a conference held 28 July-1 August 2014, pp. 333–

Höfner S., Bladh S., Aringer B., Ahuja R., 2016, A&A, 594, A108

Howe D. A., Rawlings J. M. C., 1994, MNRAS, 271, 1017

Huggins P. J., Bachiller R., Cox P., Forveille T., 1994, ApJ, 424, L127

Hughes A., Staveley-Smith L., Kim S., Wolleben M., Filipović M., 2007, MNRAS, 382, 543

Humphreys R. M., 1978, ApJ, 38, 309

Humphreys R. M., Davidson K., Ruch G., Wallerstein G., 2005, AJ, 129, 492

Humphreys R. M., Helton L. A., Jones T. J., 2007, AJ, 133, 2716

Iben I., Renzini A., 1983, ARAA, 21, 271

Imai H., Katayama Y., Ellingsen S. P., Hagiwara Y., 2013, MNRAS, 432, L16

Indebetouw R., Johnson K. E., Conti P., 2004, AJ, 128, 2206

Ireland M. J., Scholz M., Wood P. R., 2008, MNRAS, 391, 1994

Jiménez-Esteban F. M., Engels D., 2015, A&A, 1504, 5712

Jones O., 2013, PhD thesis, University of Manchester

Jones O. C. et al., 2012, MNRAS, 427, 3209

Jones O. C., Kemper F., Srinivasan S., McDonald I., Sloan G. C., Zijlstra A. A., 2014, MNRAS, 440, 631

Jones O. C., Meixner M., Sargent B. A., Boyer M. L., Sewiło M., Hony S., Roman-Duval J., 2015, ApJ, 811, 145

Jones S. et al., 2013, ApJ, 772, 150

Jørgensen U. G., Johnson H. R., 1992, A&A, 265, 168

Judge P. G., Stencel R. E., 1991, ApJ, 371, 357

Jura M., 1986, ApJ, 303, 327

Karakas A. I., 2010, MNRAS, 403, 1413

Kemper F. et al., 2010, PASP, 122, 683

Kerschbaum F., Olofsson H., 1999, A&AS, 138, 299

Kim D. W., Protopapas P., Bailer-Jones C. A. L., Byun Y. I., Chang S. W., Marquette J. B., Shin M. S., 2014, VizieR On-line Data Catalog, 356

Kiss L. L., Szabo G. M., Bedding T. R., 2006, MNRAS, 372, 1721

Kraemer K. E., Sloan G. C., Wood P. R., Jones O. C., Egan M. P., 2017, ApJ, 834, 185

Krause O., Birkmann S. M., Rieke G. H., Lemke D., Klaas U., Hines D. C., Gordon K. D., 2004, Nature, 432, 596

Lagadec E., Zijlstra A. A., Matsuura M., Menzies J. W., van Loon J. T., Whitelock P. A., 2008, MNRAS, 383, 399

Lagadec E., Zijlstra A. A., Mauron N., Fuller G., Josselin E., Sloan G. C., Riggs A. J. E., 2010, MNRAS, 403, 1331

Lagadec E. et al., 2007, MNRAS, 376, 1270

Lagage P. O. et al., 2004, The Messenger (ISSN0722-6691), 117, 12

Lakićević M. et al., 2015, ApJ, 799, 50

Lebouteiller V., Barry D. J., Spoon H. W. W., Bernard-Salas J., Sloan G. C., Houck J. R., Weedman D. W., 2011, ApJS, 196, 8

Lee Y. W., Joo J. M., Sohn Y. J., Rey S. C., Lee H. C., Walker A. R., 1999, Nature, 402, 55

Lépine J. R. D. et al., 2011, MNRAS, 417, 698

Lequeux J., Le Bourlot J., Pineau des Forets G., Roueff E., Boulanger F., Rubio M., 1994, A&A, 292, 371

Levesque E. M., 2013, EAS, 60, 269

Levesque E. M., Massey P., Olsen K. A. G., Plez B., 2007, ApJ, 667, 202

Levesque E. M., Massey P., Olsen K. A. G., Plez B., Josselin E., Maeder A., Meynet G., 2005, ApJ, 628, 973

Levesque E. M., Massey P., Olsen K. A. G., Plez B., Meynet G., Maeder A., 2006, ApJ, 645, 1102

Levesque E. M., Massey P., Plez B., Olsen K. A. G., 2009, AJ, 137, 4744

Levesque E. M., Massey P., Żytkow A. N., Morrell N., 2014, MNRAS, 443, L94

Lindqvist M., Winnberg A., Habing H. J., Matthews H. E., 1992, ApJS, 92, 43

Luck R. E., Moffett T. J., Barnes T. G. I., Gieren W. P., 1998, AJ, 115, 605

Maccarone T. J., de Mink S. E., 2016, MNRAS, 458, L1

Mackey A. D., Gilmore G. F., 2003, MNRAS, 338, 85

Madden S. C., Galliano F., Jones A. P., Sauvage M., 2006, A&A, 446, 877

Maeder A., Meynet G., 2001, A&A, 373, 555

Marigo P., Girardi L., Bressan A., 1999, A&A, 344, 123

Marigo P. et al., 2017, ApJ, 835, 77

Marshall J. R., van Loon J. T., Matsuura M., Wood P. R., Zijlstra A. A., Whitelock P. A., 2004, MNRAS, 355, 1348

Mason R., Wong A., Geballe T., Volk K., Hayward T., Dillman M., Fisher R. S., Radomski J., 2008, Observatory Operations: Strategies, 7016, 70161Y

Massey P., Levesque E. M., Olsen K. A. G., Plez B., Skiff B. A., 2007, ApJ, 660, 301

Massey P., Olsen K. A. G., 2003, AJ, 126, 2867

Matsuura M. et al., 2011, ApJ, 333, 1258

Matsuura M. et al., 2016, MNRAS, 462, 2995

Matsuura M., Woods P. M., Owen P. J., 2013, MNRAS, 429, 2527

Matsuura M. et al., 2005, A&A, 434, 691

Mauron N., Josselin E., 2011, A&A, 526, 156

Mazzitelli I., D'Antona F., Ventura P., 1999, A&A, 348, 846

McConnachie A. W., 2012, AJ, 144, 4

McDonald I., van Loon J. T., 2007, A&A, 476, 1261

McDonald I., Zijlstra A. A., 2015, MNRAS, 448, 502

McDonald I. et al., 2015, MNRAS, 453, 4324

McIntosh G. C., Predmore C. R., Moran J. M., Greenhill L. J., Rogers A. E. E., Barvainis R., 1989, ApJ, 337, 934

McMullin J. P., Waters B., Schiebel D., Young W., Golap K., 2007, Astronomical Data Analysis Software and Systems XVI ASP Conference Series, 376, 127

Meixner M. et al., 2006, AJ, 132, 2268

Meixner M. et al., 2013, AJ, 146, 62

Melnick G. J., Neufeld D. A., Ford K. E. S., Hollenbach D. J., Ashby M. L. N., 2001, Nature, 412, 160

Middelberg E., Bach U., 2008, Reports on Progress in Physics, 71, 066901

Milone A. P. et al., 2008, ApJ, 673, 241

Minniti D. et al., 2010, New Astronomy, 15, 433

Monnier J. D. et al., 1997, ApJ, 481, 420

Monnier J. D., Geballe T. R., Danchi W. C., 1998, ApJ, 502, 833

Monnier J. D., Geballe T. R., Danchi W. C., 1999, ApJ, 521, 261

Nanni A., 2013, PhD thesis, SISSA

Nanni A., Bressan A., Marigo P., Girardi L., 2013, MNRAS, 434, 2390

Nataf D. M. et al., 2016, MNRAS, 456, 2692

Ness M., Freeman K., 2015, PASA, 33, 22

Neugebauer G. et al., 1984, ApJ, 278, L1

Nieuwenhuijzen H., de Jager C., 1990, A&A, 231, 134

Ohnaka K., Driebe T., Hofmann K. H., Weigelt G., Wittkowski M., 2008, A&A, 484, 371

Oliva E., Origlia L., 1998, A&A, 332, 46

Oliveira J. M. et al., 2013, MNRAS, 428, 3001

Olofsson H., 2005, Astrochemistry: Recent Successes and Current Challenges, 231, 499

Olofsson H., González Delgado D., Kerschbaum F., Schöier F. L., 2002, A&A, 391, 1053

Olsen K. A. G., Zaritsky D., Blum R. D., Boyer M. L., Gordon K. D., 2011, ApJ, 737, 29

O'Neil K., 2002, Single-Dish Radio Astronomy: Techniques and Applications, 278, 293

Ossenkopf V., Henning T., Mathis J. S., 1992, A&A, 261, 567

Pellegrini E. W., Oey M. S., Winkler P. F., Points S. D., Smith R. C., Jaskot A. E., Zastrow J., 2012, ApJ, 755, 40

Pierce M. J., Jurcevic J. S., Crabtree D., 2000, MNRAS, 313, 271

Piotto G., 2008, Memorie della Società Astronomica Italiana, 79, 334

Piotto G. et al., 2007, ApJ, 661, L53

Prévot L., Martin N., Rebeirot E., Maurice E., Rousseau J., 1983, A&AS, 53, 255

Price S. D., Egan M. P., Carey S. J., Mizuno D. R., Kuchar T. A., 2001, AJ, 121, 2819

Ramstedt S., Schöier F. L., Olofsson H., Lundgren A. A., 2008, A&A, 487, 645

Ramstedt S., Vlemmings W. H. T., Mohamed S., 2015, in Why Galaxies Care about AGB Stars III: A Closer Look in Space and Time. Proceedings of a conference held 28 July-1 August 2014, pp. 187–

Reimers D., 1975, Mémoires of the Société Royale des Sciences de Liège, 8, 369

Reimers D., Hagen H. J., Baade R., Braun K., 2008, A&A, 491, 229

Ricci C., Tazaki F., Ueda Y., Paltani S., Boissay R., Terashima Y., 2014, ApJ, 795, 147

Richards A. M. S., Etoka S., Gray M. D., Lekht E. E., Mendoza-Torres J. E., Murakawa K., Rudnitskij G., Yates J. A., 2012, A&A, 546, A16

Richards A. M. S., Yates J. A., 1998, IAJ, 25, 7

Riebel D. et al., 2015, ApJ, 807, 1

Riebel D., Srinivasan S., Sargent B., Meixner M., 2012, ApJ, 753, 71

Rieke G. H., Lebofsky M. J., 1985, ApJ, 288, 618

Rieke G. H. et al., 2004, AJSS, 154, 25

Roche P. F., Aitken D. K., Smith C. H., 1993, MNRAS, 262, 301

Roman-Duval J. et al., 2014, ApJ, 797, 86

Rosenfield P. et al., 2014, ApJ, 790, 22

Rubele S. et al., 2015, MNRAS, 449, 639

Ruffle P. M. E. et al., 2015, MNRAS, 451, 3504

Saglia R. P. et al., 2010, A&A, 509, A61

Salasnich B., Bressan A., Chiosi C., 1999, A&A, 342, 131

Salpeter E. E., 1977, In: Annual review of astronomy and astrophysics. Volume 15. (A78-16576 04-90) Palo Alto, 15, 267

Sargent B. A., Srinivasan S., Meixner M., 2011, ApJ, 728, 93

Sault R. J., Teuben P. J., Wright M. C. H., 1995, Astronomical Data Analysis Software and Systems IV, 77, 433

Schröder K. P., Cuntz M., 2005, ApJ, 630, L73

Schröder K. P., Cuntz M., 2007, A&A, 465, 593

Schultheis M. et al., 2014, A&A, 566, A120

Seaquist E. R., Ivison R. J., Hall P. J., 1995, MNRAS, 276, 867

Sewiło M. et al., 2013, ApJ, 778, 15

Shenoy D. et al., 2016, AJ, 151, 51

Sivagnanam P., Diamond P. J., Le Squeren A. M., Daigne G., Biraud F., Ortega-Molina A., Graham D. A., 1988, A&A, 194, 157

Skibba R. A. et al., 2012, ApJ, 761, 42

Slemer A. et al., 2017, MNRAS, 465, 4817

Sloan G. C. et al., 2016, ApJ, 826, 44

Sloan G. C., Kraemer K. E., Wood P. R., Zijlstra A. A., Bernard-Salas J., Devost D., Houck J. R., 2008, ApJ, 686, 1056

Sloan G. C. et al., 2012, ApJ, 752, 140

Smartt S. J., 2009, ARAA, 47, 63

Smith V. V., Lambert D. L., 1990, ApJL, 361, L69

Smith V. V., Plez B., Lambert D. L., Lubowich D. A., 1995, ApJ, 441, 735

Soszyński I. et al., 2009, AA, 59, 239

Soszyński I. et al., 2011, AA, 61, 217

Spano M., Mowlavi N., Eyer L., Burki G., Marquette J. B., Lecoeur-Taibi I., Tisserand P., 2011, VizieR On-line Data Catalog, 353

Srinivasan S., Boyer M. L., Kemper F., Meixner M., Sargent B. A., Riebel D., 2016, MNRAS, 457, 2814

Srinivasan S. et al., 2009, AJ, 137, 4810

Srinivasan S., Sargent B. A., Meixner M., 2011, A&A, 532, 54

Stanimirovic S., Staveley-Smith L., Dickey J. M., Sault R. J., Snowden S. L., 1999, MNRAS, 302, 417

Staveley-Smith L., Kim S., Calabretta M. R., Haynes R. F., Kesteven M. J., 2003, MNRAS, 339, 87

Subramanian S., Subramaniam A., 2009, A&A, 496, 399

Subramanian S., Subramaniam A., 2010, A&A, 520, A24

Subramanian S., Subramaniam A., 2011, ApJ, 744, 128

Sudou H., Omodaka T., Imai H., Sasao T., Takaba H., Nishio M., Hasegawa W., Nakajima J., 2002, PASJ, 54, 757

Szewczyk O., Pietrzynski G., Gieren W., Ciechanowska A., Bresolin F., Kudritzki R.-P., 2009, AJ, 138, 1661

Takaba H., Ukita N., Miyaji T., Miyoshi M., 1994, PASJ, 46, 629

Tan Y., Wang J. X., Shu X. W., Zhou Y., 2012, ApJ, 747, L11

te Lintel Hekkert P., Caswell J. L., Habing H. J., Haynes R. F., Norris R. P., 1991, A&AS, 90, 327

Temim T., Dwek E., Tchernyshyov K., Boyer M. L., Meixner M., Gall C., Roman-Duval J., 2015, ApJ, 799, 158

Testor G., Pakull M., 1985, A&A, 145, 170

Thompson A. R., Moran J. M., Swenson, Jr. G. W., 2001, Interferometry and Synthesis in Radio Astronomy, 2nd Edition

Tout C. A., Żytkow A. N., Church R. P., Lau H. H. B., Doherty C. L., Izzard R. G., 2014, MNRAS, 445, L36

Trams N. R. et al., 1999, A&A, 346, 843

Udalski A. et al., 2008, AA, 58, 89

Valiante R., Schneider R., Bianchi S., Andersen A. C., 2009, MNRAS, 397, 1661

van Aarle E., Van Winckel H., Lloyd Evans T., Ueta T., Wood P. R., Ginsburg A. G., 2011, A&A, 530, A90

van der Veen W. E. C. J., Habing H. J., 1990, A&A, 231, 404

van der Veen W. E. C. J., Rugers M., 1989, A&A, 226, 183

van Loon J. T., 2000, A&A, 354, 125

van Loon J. T., 2006, ASPC, 353, 211

van Loon J. T., 2012, arxiv, arXiv:1210.0983

van Loon J. T., 2013, EAS, 60, 307

van Loon J. T., Cioni M. R. L., Zijlstra A. A., Loup C., 2005, A&A, 438, 273

van Loon J. T., Cohen M., Oliveira J. M., Matsuura M., McDonald I., Sloan G. C., Wood P. R., Zijlstra A. A., 2008, A&A, 487, 1055

van Loon J. T. et al., 2003, MNRAS, 338, 857

van Loon J. T., Groenewegen M. A. T., de Koter A., Trams N. R., Waters L. B. F. M., Zijlstra A. A., Whitelock P. A., Loup C., 1999, A&A, 351, 559

van Loon J. T., Hekkert P. T. L., Bujarrabal V., Zijlstra A. A., Nyman L.-A., 1998a, A&A, 337, 141

van Loon J. T., Marshall J. R., Cohen M., Matsuura M., Wood P. R., Yamamura I., Zijlstra A. A., 2006a, A&A, 447, 971

van Loon J. T., Marshall J. R., Zijlstra A. A., 2005, A&A, 442, 597

van Loon J. T., McDonald I., Oliveira J. M., Evans A., Boyer M. L., Gehrz R. D., Polomski E., Woodward C. E., 2006b, A&A, 450, 339

van Loon J. T., Oliveira J. M., Gordon K. D., Sloan G. C., Engelbracht C. W., 2010, AJ, 139, 1553

van Loon J. T., Zijlstra A. A., Bujarrabal V., Nyman L. A., 1996, A&A, 306, L29

van Loon J. T., Zijlstra A. A., Bujarrabal V., Nyman L. A., 2001a, A&A, 368, 950

van Loon J. T., Zijlstra A. A., Kaper L., Gilmore G. F., Loup C., Blommaert J. A. D. L., 2001b, A&A, 368, 239

van Loon J. T. et al., 1998b, A&A, 329, 169

van Loon J. T., Zijlstra A. A., Whitelock P. A., Waters L. B. F. M., Loup C., Trams N. R., 1997, A&A, 325, 585

Vassiliadis E., Wood P. R., 1993, ApJ, 413, 641

Ventura P., Karakas A. I., Dell'Agli F., García-Hernández D. A., Boyer M. L., Di Criscienzo M., 2016, MNRAS, 457, 1456

Verhoelst T., Van der Zypen N., Hony S., Decin L., Cami J., Eriksson K., 2009, A&A, 498, 127

Véron-Cetty M. P., Véron P., 2010, A&A, 518, A10

Villaver E., Stanghellini L., Shaw R. A., 2004, ApJ, 614, 716

Villaver E., Stanghellini L., Shaw R. A., 2007, ApJ, 656, 831

Vlemmings W. H. T., Diamond P. J., van Langevelde H. J., Torrelles J. M., 2006, A&A, 448, 597

von Steiger R., Zurbuchen T. H., 2016, ApJ, 816, 13

Ward J. L., Oliveira J. M., van Loon J. T., Sewiło M., 2017, MNRAS, 464, 1512

Weaver H., Williams D. R. W., Dieter N. H., Lum W. T., 1965, Nature, 208, 29

Weisz D. R., Dolphin A. E., Skillman E. D., Holtzman J., Dalcanton J. J., Cole A. A., Neary K., 2013, MNRAS, 431, 364

Werner M. W. et al., 2004, AJSS, 154, 1

Whitelock P., Feast M., Catchpole R., 1991, MNRAS, 248, 276

Whitelock P. A., Feast M. W., Menzies J. W., Catchpole R. M., 1989, MNRAS, 238, 769

Whitelock P. A., Feast M. W., van Loon J. T., Zijlstra A. A., 2003, MNRAS, 342, 86

Whiting M. T., 2012, MNRAS, 421, 3242

Willacy K., 2004, ApJ, 600, L87

Williams K. A., 2007, 15th European Workshop on White Dwarfs ASP Conference Series, 372, 85

Wilson W. E. et al., 2011, MNRAS, 416, 832

Wittkowski M., Boboltz D. A., Ohnaka K., Driebe T., Scholz M., 2007, A&A, 470, 191

Woitke P., 2006, A&A, 460, L9

Wong G. F. et al., 2012, Serbian Astronomical Journal, 184, 93

Wood P. R., 1990, in IN: Confrontation between stellar pulsation and evolution; Proceedings of the Conference, Mount Stromlo and Siding Spring Observatoires, Canberra, Australia, pp. 355–363

Wood P. R., Bessell M. S., Fox M. W., 1983, ApJ, 272, 99

Wood P. R., Bessell M. S., Whiteoak J. B., 1986, ApJ, 306, L81

Wood P. R., Habing H. J., McGregor P. J., 1998, A&A, 336, 925

Wood P. R., Whiteoak J. B., Hughes S. M. G., Bessell M. S., Gardner F. F., Hyland A. R., 1992, ApJ, 397, 552

Woods P. M. et al., 2011, MNRAS, 411, 1597

Worley C. C., Irwin M. J., Tout C. A., Żytkow A. N., Fraser M., Izzard R. G., 2016, MNRAS, 459, L31

Xue M., Jiang B. W., Gao J., Liu J., Wang S., Li A., 2016, AJSS, 224, 23

Yamamura I., Makiuti S., Ikeda N., Fukuda Y., Oyabu S., Koga T., White G. J., 2010, VizieR On-line Data Catalog, 2298

Yi J., Booth R. S., Conway J. E., Diamond P. J., 2005, A&A, 432, 531

Zaritsky D., Harris J., Thompson I. B., Grebel E. K., 2004, AJ, 128, 1606

Zijlstra A. A., Chapman J. M., te Lintel Hekkert P., Likkel L., Comeron F., Norris R. P., Molster F. J., Cohen R. J., 2001, MNRAS, 322, 280

Zijlstra A. A., Loup C., Waters L. B. F. M., Whitelock P. A., van Loon J. T., Guglielmo F., 1996, MNRAS, 279, 32

Zoccali M. et al., 2003, A&A, 399, 931